Convective precipitation simulated with ICON over heterogeneous surfaces in dependence on model and land-surface resolution

Zur Erlangung des akademischen Grades eines
DOKTORS DER NATURWISSENSCHAFTEN
von der KIT-Fakultät für Physik des
Karlsruher Instituts für Technologie (KIT)

genehmigte

DISSERTATION

von

Shweta Singh
aus Deoria (Indien)

Tag der mündlichen Prüfung: 24.04.2020
Referent: Prof. Dr. Christoph Kottmeier
Korreferent: Prof. Dr. Corinna Hoose

Abstract

The impact of land-surface properties like vegetation, soil type and soil moisture, and the orography on the atmosphere is manifold. On the one hand, these features determine the evolution of the atmospheric boundary layer, in particular, the convective conditions and further the exchange of mass, momentum, heat, and humidity with the free troposphere. Subsequently, the land surface also influences the pre-convective environment. On the other hand, land-surface heterogeneity results in the spatial variability of the land-surface parameters, which often leads to thermally-induced circulations and associated convergence zones in the convective boundary layer. These, in turn, act as trigger mechanisms for convective clouds and precipitation. That means in simulations, the distribution and amount of clouds and subsequent precipitation depend on the resolution of land-surface and model grid spacing (Δ_h) alike. Therefore, the focus of the study is to (i) compare areal mean precipitation for different model grid spacings and land-surface resolutions, (ii) analyse reasons for their differences, (iii) investigate spatial precipitation patterns, and describe relevant trigger mechanisms of convection.
The impact of model grid spacing and land-surface resolution on convective precipitation is investigated within the framework of the HD(CP)^2 project (High Definition Clouds and Precipitation for advancing Climate Prediction). For that purpose, geographical areas with different types of complexity in the orography and considerable number density of lightning strikes (deep convection) are selected. The areas are: the flat terrain near Berlin (A1), the isolated Harz mountain range in central Germany (A2), and the complex terrain, the Black Forest mountains (A3). Six suitable days with weak large-scale forcing but a considerable number of lightning strikes are chosen. ICOsahedral Nonhydrostatic (ICON) simulations in large eddy model setup have been performed using six model grid spacings: Numerical Weather Prediction (NWP) mode ($\Delta_{5000\,m}$, $\Delta_{2500\,m}$), Large Eddy Simulation (LES) mode ($\Delta_{1250\,m}$, $\Delta_{625\,m}$, $\Delta_{312\,m}$ and $\Delta_{156\,m}$) in a nested domain setup (control runs). The $\Delta_{156\,m}$ control run is the reference run. The impact of land-surface resolution on areal mean precipitation and precipitation patterns

has been deduced by reducing the resolution of land-surface properties, e.g. vegetation, soil type, and the orography. The differences in simulated areal mean precipitation are explained through heat and moisture budget calculations. Variations in the precipitation patterns are analysed by investigating relevant triggering mechanisms. The source regions of the convective precipitation are identified by applying a backward trajectory model. To diagnose the turbulent sensible and latent heat fluxes at the Earth's surface in the source regions of convection, their dependence on parameters like orography, soil moisture index, transpiration area index, and net radiation is determined using the standardised multiple regression techniques.

The results show that the areal mean accumulated precipitation amount for most of the cases decreases systematically across the LES grid spacings from Δ_{1250m} to Δ_{156m}. The relative precipitation difference normalised by the precipitation in the reference run is in the range of -26 to 400 % with the 75th percentile of 155 %. In four out of the six days, Δ_{1250m} results in intenser precipitation patterns and an earlier onset of precipitation by 1 to 2 hours in comparison to the reference run. The modification of land-surface resolution from 156 m to 1250 m leads to variability in the mean precipitation in the range of 17 to 37 % with the 75th percentile of 7 % which increases to a range of -17 to 49 % and the 75th percentile of 22 % with the land-surface resolution of 5000 m. The land-surface sensitivity experiments show a negligible impact on the onset time of precipitation and the precipitation patterns. Thus, the modification in land-surface resolution results in much smaller variability in the areal mean precipitation amount in comparison to the model grid spacing.

To understand the differences of areal mean accumulated precipitation and onset of precipitation between the control runs, the heat and moisture budgets are analysed in detail for one day, for which the relative difference in the mean precipitation by Δ_{1250m} and Δ_{156m} is $\simeq$175 %. Unlike Δ_{1250m}, Δ_{156m} first shows intensive evaporative cooling due to the formation of numerous small clouds. Evaporative cooling is generated at the edge and shell regions of the small clouds. As a result, the clouds often dissolve before they could grow deep enough to precipitate. In the subsequent hours cloud aggregation is a crucial step causing precipitation generation in Δ_{156m}.

Concerning initiation of convection, overall the LES grid spacings show the similar thermally- and orographically-induced circulations in all areas (A1, A2, and A3). However, as demonstrated for A1 considerable differences in triggering could occur when the land-surface resolution is reduced down from 156 m to 5000 m. This finding holds when the resolution of 5000 m smoothed out those land-surface heterogeneities (e.g. lake breezes and urban heat island) which are responsible for convection initiation at 156 m land-surface resolution.

Contents

1. Introduction and motivation

Clouds are complex bodies because they consist of numerous droplets interacting through a variety of cloud-physical processes. For example, its growth and dissolution due to evaporation are very complex and take place at a very fine scale. On the global scale, clouds are one of the largest uncertainties in the climate projection by models (Bony and Dufresne, 2005; Boucher et al., 2013) and NWP models (Zhang et al., 2019). Numerical models provide opportunities to study the different multi-scale processes and their interactions. As the NWP models at high resolution can resolve the deep convection, the parametrization of deep convection is not required for model grid spacings of a few kilometres and finer (Weisman et al., 1997). The convection-resolving simulations of short-range NWP (Weusthoff et al., 2011) and longer-range projections (Hohenegger et al., 2008), explicitly resolve the governing nonhydrostatic processes of deep convective storms. Hence, they perform better than convection-parametrizing simulations. However, the resolved convection and the resulting precipitation on kilo- and hectometre scale may vary depending upon the embedded resolved (and unresolved) processes.

Therefore, the selection of suitable model grid spacings to study deep convection, clouds, and precipitation is a difficult task as it poses questions about the extensive usage of the computational power and the complexity of resolved and other parameterized processes like turbulence and cloud-microphysics. Convective precipitation is one of the difficult phenomena to capture in the model simulation. There are several challenges in the forecast of precipitating convective events, e.g. the onset time and the precipitation patterns that could be dependent on the model grid spacing, parameterization schemes, initial and boundary conditions, land-surface resolution, etc. Model simulations are sensitive to the factors mentioned above; therefore, it should be chosen carefully based on the applications. With this, the forecasting systems using kilometre to hectometre resolution provide insights into the scalar dispersion, city ventilation, cloud modelling and wind energy production (Liu et al., 2011; Zhu et al., 2010; Taylor et al., 2016).

Concerning moist convection, the processes of Convective Boundary Layer (CBL) are quite decisive. The CBL properties determine the convection initiation, which are, e.g. represented by parameters like Convective Available Potential Energy (CAPE) and Convective Inhibition (CIN). The spatial heterogeneities of the CBL often generate mesoscale circulations which then act as trigger mechanisms for convection. The state of the CBL, in turn, is determined by the surface fluxes, i.e., how the available energy at the Earth's surface is partitioned into the sensible and latent heat flux. This partitioning in turn depends on the land-surface conditions (Kalthoff et al., 1999; Western et al., 2002; Koster et al., 2004). Land-surface heterogeneity results from the variations in land cover and land use across a range of length scales, i.e. the evolution of moist convection are strongly coupled with the characteristics of land-surface types (Avissar and Chen, 1993).

The aforementioned factors and processes influence the distribution and amount of convection, clouds, and precipitation. But the question of characteristic model grid spacing in conjunction with an optimal land-surface resolution to study the moist convection processes is still difficult to address as their relative sensitivity to convective precipitation over scale of a kilometre and hectometre is not well known. With this overview, the scientific objectives addressed in this thesis are as follows:

1. To investigate the impact of model grid spacing and land-surface resolution on clouds and precipitation.

2. To monitor the processes causing different precipitation behaviour across the model grid spacings.

3. To identify the triggering mechanisms over the grid spacings resulting in different precipitation patterns.

To achieve the above goals the ICON model has been used in this thesis which is a crucial motivation of this thesis and allows to test the capability of the new ICON model. This study focuses on the inter-comparison of locally induced convective precipitation simulated in ICON over a range of model grid spacings and land-surface resolutions. ICON is a unified model system which is now operational at Deutscher Wetterdienst (DWD) since January 2015. This model has been developed in collaboration with DWD and Max-Planck-Institute for Meteorology (MPI-M). It can be run in three different modes depending upon the

application of the users. These modes are: ICON-ECHAM, ICON-NWP, and ICON-Large Eddy Model (LEM). The details of the general configuration and model setup are discussed in Chapter 4. ICON atmospheric model in LEM mode has been used in this study. LEM is a setup in limited area mode with LES turbulence.

Convective precipitation is often localised, intense, and short-lived in nature. To identify the hot spot areas of deep convection, the number density of lightning strikes for the summer period (MJJAS) from 2000 to 2018 is investigated, lightning being a proxy of deep convection (Leary and Ritchie, 2009). The lightning data is retrieved from Siemens lightning information service (BLIDS), which is a part of the European Cooperation for Lightning Detection (EUCLID). The details of the used lightning data are discussed in Chapter 3. Deep convection preferably occurs over orographically complex terrain (Kottmeier et al., 2008; Kalthoff et al., 2011; Barthlott and Kalthoff, 2011). Therefore, depending upon the complexity of the orography and the associated number density of lightning strikes, three areas turn out to be most suitable which are: the flat terrain near Berlin (A1), the isolated mountain range, Harz mountains (A2) and the complex terrain, the Black Forest (A3).

As the impact of land-surface resolution is expected to be most prominent for locally induced circulation, the conditions with weak large-scale forcing over the above-selected areas are chosen. In total six cases are chosen, two for each area, in this study (Chapter 3). These days have been analysed by performing the ICON simulations (See Chapter 5 for details of the configuration of ICON simulations). An overview of the relative impact of model grid spacings and land-surface resolution on convective precipitation is presented (Chapter 6). The reasons for differences have been analysed using the heat and moisture budgets. The budget components have been implemented in ICON in online mode. The budgets infer the role of heat and moisture in regulating the processes of mass, momentum, heat and moisture exchange between the Earth's surface and CBL, and further to free troposphere activated at a particular grid spacing. Furthermore, to identify the source areas of this triggered moist convection, the backward trajectories are calculated using the trajectory model LAGrangian ANalysis TOol (LAGRANTO) (Wernli and Davies, 1997). LAGRANTO has been adapted for ICON model fields (for details of LAGRANTO see Section 5.6). The backward trajectories facilitate the

understanding of the conditions of the source region resulting in the formation of convective clouds (Chapter 7).
To understand the impact of land-surface resolution on precipitation, the sensitivity simulations have been performed where the combinations of model grid spacing (Δ_h), land-surface properties (L)- and orography (O)- resolution are used in a way that addresses their relative importance to convective precipitation. This way, the study contributes to the second phase of the Federal Ministry of Education and Research (BMBF) project "HD(CP)^2 " which stands for High Definition Clouds and Precipitation for advancing Climate Prediction. This project focusses on cloud processes by combining current low-resolution global climate simulations and regional high-resolution simulations. The high-resolution simulations facilitate the process-based comparisons with observations, which should give an added value to the understanding of cloud processes. The current work is a synthesis part of the project HD(CP)^2 . In this part, the land-surface heterogeneity will assess and reduce the uncertainties of climate models caused by non-resolved subsurface processes and its feedback to the CBL, the exchange processes between CBL and the free troposphere including the cloud development, convection initiation, and precipitation. In the HD(CP)^2 framework, the present thesis contributes to the investigations about the impact of the land including sub-surface, vegetation and anthropogenic structures on the regional climate of central Europe with a focus on cloud and precipitation development, intensity, and distribution (Stevens et al., 2020).
This study is not a model evaluation but a model inter-comparison. Nevertheless, the assessment concerning the plausibility and the more realistic ICON simulations are based on qualitative comparison with observational data.

To summarize the outline: in the next chapter, the literature synthesis of the various aspects of model strategies and their limitations are presented (Chapter 2). In Chapter 3, the details of the selection of suitable areas and cases are discussed. Chapter 4 describes the ICON model system (physics, dynamics and their coupling) along with its most interesting and related aspects used in this thesis. Chapter 5 presents the details of the ICON model simulations performed in this study. It also describes the developed simulation strategy and the trajectory model LAGRANTO. The results from these simulations are split into two chapters: Chapter 6 discusses the first aim of this thesis which is to investigate

the impact of model grid spacing and land-surface heterogeneity on clouds and precipitation. Chapter 7 addresses the identified important triggering mechanisms at the most appropriate grid spacing from all the cases and areas. Ultimately, the findings are summarised together with an overall conclusion in Chapter 8.

2. Literature synthesis

This chapter provides a literature synthesis of the studies analysing clouds and precipitation at different grid scales, especially in the numerical simulations. Atmospheric processes occur at different length scales. Even with the advent of advanced numerical models with much improved representation of physical processes, it is a challenge to decide the optimum model grid spacing, land-surface resolution, and suitable parameterization schemes which solve the closure problem of the equation of motion entirely efficiently. The atmospheric and land-surface based processes play crucial roles in the evolution of convection. Therefore, modelling and understanding the processes of clouds and precipitation require the selection of a suitable grid scale. According to the scale definition of Orlanski (1975), the relevant scales in this study belong to the meso-β, meso-γ, and micro-α, i.e., the atmospheric processes with a characteristic horizontal scale of $\sim$ 20 km, 2-20 km, and 200 m - 2 km, respectively whose time scale ranges between a diurnal period to few hours (Figure 2.1).

Further, Inoue et al. (2008) uses the global cloud-resolving model (Nonhydrostatic icosahedral atmospheric model (NICAM)) and resolve clouds at a grid spacings of 3.5 km and 7 km. A thorough comparison of cloud properties against Japanese geostationary meteorological satellite (MTSAT-1R) proves that the overall cloud size distribution simulated in 3.5 km grid spacing is closer to the observation in contrast to 7 km. However, 3.5 km underestimates the number of small clouds and is incapable of producing very large clouds. Moreover, these processes are parameterized in the conventional climate models, which is examined as a major source of the model errors and uncertainty in the climate projections (Henderson-Sellers et al., 1993; Déqué et al., 2007). The approach of explicitly simulating the crucial processes at hecto- or kilometre scale is already in practice by the operational institutes and the scientific community. For example, the studies using Convection-Permitting Models (CPMs) like Prein et al. (2015) prove that the horizontal grid spacing $\leq$ 4 km not only outperforms the traditional Large-Scale Models (LSMs) (horizontal grid spacing $>$ 10 km) and present more realistic in-

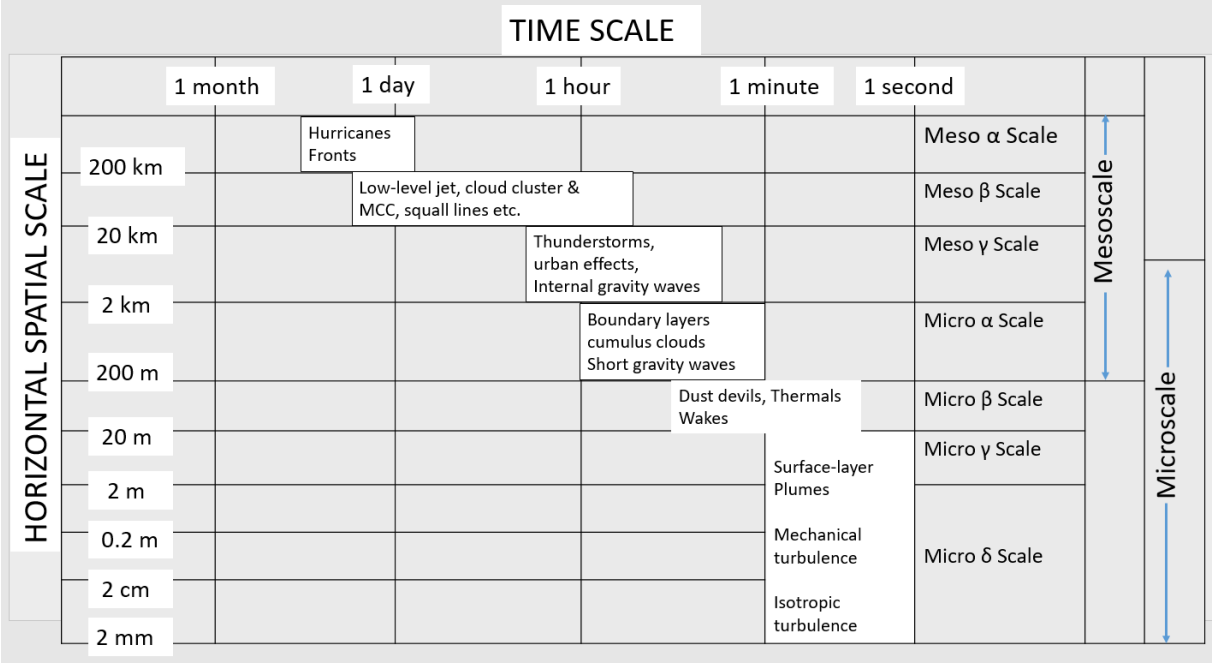

Figure 2.1.: Scale definition and the characteristic time and horizontal scales of different processes (adapted after Orlanski (1975))

sights on climate and regional scales. The modes of explicitly resolving convection at a kilometre and finer-scale were already adapted more than twenty years back (Weisman et al., 1997). All in all, the atmospheric mesoscale models are now actively used across an extended range of spatial scales with tens of kilometre to $<$ 1 km (Chow et al., 2006; Leung et al., 2006; Knote et al., 2010). But even at hecto- or kilometre scale the processes like turbulence, cloud microphysics are not resolved. Therefore, they have to be parameterized (Bryan et al., 2003). In this regards LES runs have been examined for studying clouds (Mellado et al., 2018). Moreover, the question is how fine grid spacing is enough to represent above small-scale processes, how are they represented in the models, and how much uncertainty can be expected over a range of grid spacings in LES.

Several studies are comparing the behaviour of cloud properties across deca-, hecto- to a few kilometre scales and provide possible limitations over these scales. Chow et al. (2019) addresses the importance of scale-aware parameterization schemes to study the cross-scale interactions occurring in complex terrain within the grey zone continuum (convection, turbulence and topography) at a scale ranging from $\sim$ 10 km to $\sim$ 10 m. The grey zone, which is also referred as *terra incognita*, corresponds to the grid resolutions where certain features are partly re-

solved and subgrid (Wyngaard, 2004). The scale-aware parameterization enables a consistent representation of subgrid (turbulence) and grid-scale processes with the refinement of grid spacings. For example, a smooth transition from NWP to LES-type turbulence closure will be enabled in the so-called scale-aware parameterization schemes (Chow et al., 2019). Exclusively, the uncertainties in these models may come from initial and lateral boundary conditions, incomplete set of parameterized physical processes, or the numerical methods themselves, which influences the Convection Initiation (CI), onset and distribution of clouds and precipitation (Barthlott et al., 2011).

Another crucial component is the representation of land surface in these models. The main land-surface characteristics can be categorised as land-surface properties like vegetation, soil type, soil moisture, and orography. The land surface is an integral component to represent in the atmospheric models because of their intensive impact at different length scales. Land-surface properties and orography directly influence the surface temperature and moisture distribution and therefore, the partitioning of available energy into sensible and latent heat flux. The heterogeneity of land surface and its associated energy exchange results into a differential heating of the CBL and may modify the atmospheric state by inducing secondary circulations which further influences the turbulent transport of heat and energy in the CBL and the free troposphere (Avissar and Liu, 1996; Taylor et al., 2007). That means the clouds and convection are interactively coupled with the underlying land surface, which also impacts the initiation and evolution of convective systems (Banta, 1990; Weckwerth, 2000). The studies based on in-situ observations and NWP runs address the importance of land surface-based triggering mechanisms in the modulation of atmospheric systems (Entekhabi et al., 1996; Taylor et al., 2007; Garcia-Carreras et al., 2011; Wulfmeyer et al., 2011; Khodayar et al., 2013). The land surface-induced thermal and radiant energy exchange processes which occur when there is differential heating caused by land-surface heterogeneity, for example, thermally-driven wind system in complex terrain (Zardi and Whiteman, 2013). Over flat terrain, the impact of variability of land-surface properties on convection and turbulence is intensively studied using observations (Pielke Sr, 2001; Maurer et al., 2016) and NWP and LES models (Shao et al., 2001; Adler et al., 2011; Khodayar and Schädler, 2013; Maurer et al., 2016; Liu et al., 2017). The horizontal extent of land-surface anomalies

is an important factor for the development of secondary circulation systems. For example, the soil-moisture anomalies having a horizontal length scale in the order of 2.5 to 10 km tend to generate thermally-driven circulations, for example, the atmospheric flows at meso-β and meso-γ scales (Figure 2.1) (Shuttleworth, 1991; Taylor et al., 2007; Gantner and Kalthoff, 2010). As the interactions between the soil and overlying atmosphere are crucial to the climate and weather system over a spectrum of spatial and temporal scales (Pielke Sr, 2001; Koster et al., 2004), the initial state of soil moisture fields must be estimated correctly (Van Weverberg et al., 2010; Barthlott and Kalthoff, 2011). The positive soil moisture-precipitation feedback has been consistently proven in observation and model studies (Findell and Eltahir, 1997; Schär et al., 1999; Pal and Eltahir, 2001). The wide range of precipitation response over the complex terrain has been systematically studied using high-resolution simulations (Schneider et al., 2018; Baur, 2019). The model resolution up to 500 m allows to capture thermally-induced circulations occurring at micro-α to meso-γ scales. Especially under fair weather conditions, the onset time and precipitation amount shows considerable improvement in the high-resolution simulations (Schneider et al., 2018). Moreover, the field campaigns like International H2O Project (IHOP)_2002 (Weckwerth, 2000), Convective Storm Initiation Project (CSIP) (Browning et al., 2007), Convective and Orographically-induced Precipitation Study (COPS) (Kottmeier et al., 2008; Wulfmeyer et al., 2011) were conducted especially to understand the line of processes leading to convective precipitation in complex terrain. The low-level convergence zones, heat and moisture distribution show significant impact on CBL resulting in deep convection (Wilson and Schreiber, 1986; Kalthoff et al., 2009).

Therefore, LES is well-suited option to study these small scale processes from micro-scale turbulence to the organised mesoscale structures specifically dependent upon atmospheric stability, land-surface heterogeneity and orography (Deardorff, 1972; Courault et al., 2007; Gantner et al., 2017; Imamovic et al., 2017). On one hand, the diversity of the small-scale processes leads to the complexity of their mutual interaction, on the other hand, the inclusion of corresponding optimised parameterization schemes are computationally expensive. For example, in the case of turbulence parameterization, the 1D TKE-based NWP and 3D classical Smagorinsky LES comprehend differently as per the applicative area of study. The differences on the impacts of convection due to the different turbulence closure are

analysed in several studies, for example, Simon et al. (2019). This study shows that the onset time of convection between 1D TKE and 3D Smagorinsky differs almost by 2 hours. Their research also introduced the Dynamic Reconstruction Model (DRM), a mixed model using explicit filtering and reconstruction technique, a turbulence closure which results into a shorter extent of the grey zone.
The intriguing scenario is that over heterogeneous land surfaces and for a given model grid spacing, the representation of land-surface heterogeneity is less apprehended which leads to inaccuracies like the aggregation effect and the dynamical effect (Giorgi and Avissar, 1997; Mahfouf et al., 1987; Avissar and Schmidt, 1998). The aggregation effect, which is the result of highly nonlinear subgrid-scale processes, primarily affects the surface sensible and latent heat fluxes, the dynamics of soil moisture, intercepted water and runoff. The dynamical effect results when the heterogeneity induced circulations are not explicitly resolved by a model. It influences the CBL structures, evolution of clouds, precipitation occurrence and vertical exchange of energy, heat and moisture up to the free troposphere. Shao et al. (2001) studied the behaviour of these effects by performing numerical experiments using the flow model FOOT3D (Brücher, 1997) at atmospheric resolution of 1 - 4 km in combination with varying soil model resolution (1 - 4 km). The results show that at a given atmospheric model resolution, the higher land-surface resolution leads to improved or more variable representation of surface energy and momentum fluxes and vice versa. That means the land-surface induced subgrid variations in surface energy fluxes needs to be taken into account in subgrid closure schemes. Furthermore, averaging these local variations of the land cover has a much smaller impact on the surface fluxes over homogeneous land surfaces in comparison to that over heterogeneous surfaces due to the nonlinear nature of processes and the extended-spectrum of scale variations over heterogeneous surfaces (Heinemann and Kerschgens, 2005).

Moreover, the present study uses ICON-LES, which has the unstructured horizontal grid structure and an added value to study the multi-scale interactions. This study discusses the land surface-induced circulations and compares the impact of land-surface heterogeneity and the resolution of the atmosphere on clouds and precipitation. In long term perspective, the incorporation of an optimum land-surface resolution in climate models will assess and reduce the uncertainty caused

by subgrid subsurface processes, and its mutual relation with CBL, CI, cloud development, and precipitation.

3. Selection of suitable areas and cases for convective precipitation

This chapter describes the approach of selecting suitable areas and the meteorological case studies formulated in this thesis. Lightning in thunderstorms can be taken as an equivalent to deep convection (Mansell et al., 2007; Leary and Ritchie, 2009). It gives the general estimate of the occurrence and temporal evolution of convective systems. Lightning is defined as the discharge, which could occur as cloud-to-cloud (IC), cloud-to-ground (CG), and cloud-to-air (CA). In general, CG lightning has a significant impact on our daily lives, in terms of life and property loss, power outages and also natural calamities like forest fires.

Lightning

The lightning data used here are obtained from the Siemens BLIDS detection system, which is a part of the EUCLID network (Schulz et al., 2016). EUCLID is a collaboration among the national lightning detecting networks in Europe. It aims to identify and detect lightning by using 148 sensors throughout Europe. The application of the EUCLID product is not only limited to the meteorology but actively in insurance, hydrology, communications, forestry, defence, aviation, and hydrology. According to Pohjola and Mäkelä (2013), the implementation of a low-frequency (LF) (30 - 300 kHz) lightning detection system results into a significantly lower detection efficiency of cloud-to-cloud (IC) lightning. The detection efficiency has been confirmed to be 96% for flashes with a peak current of $\approx$2 kA while the CG lightning strikes can be detected with an accuracy of $\approx$100 m (Schulz et al., 2016; Piper and Kunz, 2017). Therefore, only cloud-to-ground (CG) lightning has been considered in further calculations, and both polarity and current have not been taken into account (Kunz et al., 2018).

To identify the areas with hotspots of Deep Convection (DC), the lightning density during the summer period (MJJAS) of 2000-2018 is investigated. Lightning density is defined as the mean daily flash total within a specified grid

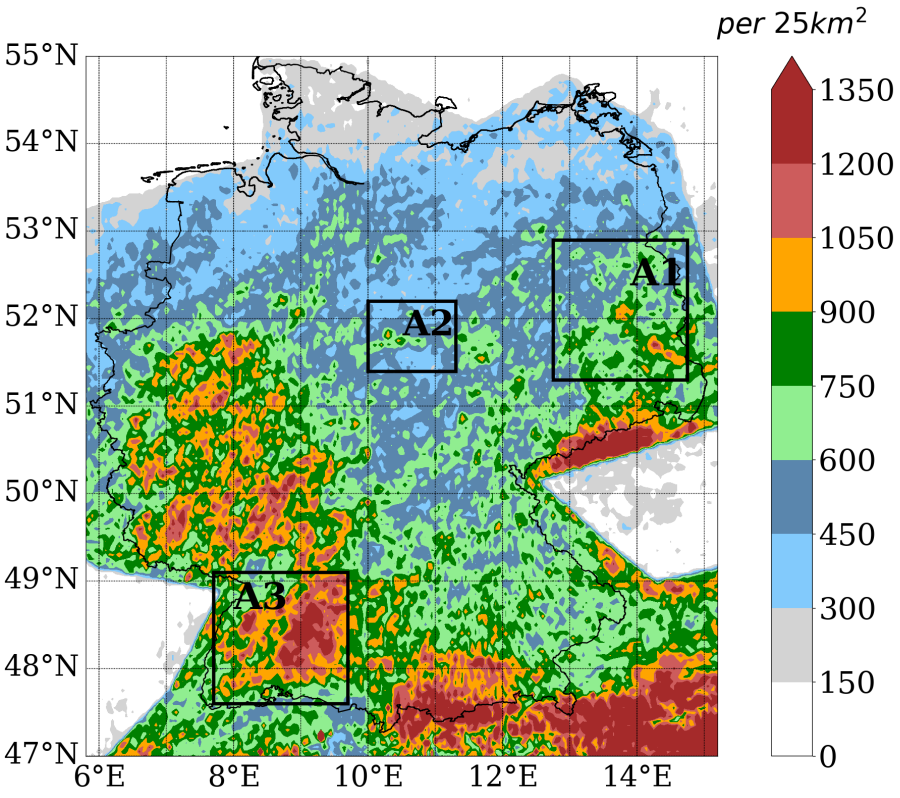

Figure 3.1.: Total lightning density over Germany during the summer period (MJJAS) of 2000 - 2018.

cell (Piper and Kunz, 2017). Figure 3.1 shows Germany wide lightning density per 25 km^2 during the summer period (MJJAS) of 2000 to 2018.

The higher lightning density over the mountainous or complex terrain like the Black Forest, Alps mountains, and Thuringian forest is considerably higher in comparison to the surrounding flat region. This may be attributed to the orographically induced deep convective systems. Additionally, there are smaller areas near the southwestern part of Berlin and Harz mountains with the strong number density of lightning strikes. Based on the lightning density (Figure 3.1) and the different types of orographic complexity scale (Figure 6.1), three distinct geographical areas have been chosen, namely: A1: the flat terrain near Berlin, A2: the isolated mountain range called as Harz mountains with the peak height of 1140 m, and A3: the Black Forest mountain range.

As locally triggered convection is of major interest for this study, two criteria are applied to detect the suitable days, that is (i) having a weak large-scale synoptic forcing and (ii) a considerable number of lightning strikes over the respective

areas. As a proxy for weak synoptic forcing, we used a threshold of <10 ms^{-1} at 850 hPa. For the selection of suitable days, the number of lightning strikes and the horizontal wind at 850 hPa from ECMWF Re-Analysis (ERA)-Interim (Berrisford et al., 2011; Dee et al., 2011) dataset are used. Figure 3.2 shows a typical example of the outcome of the above criteria calculated over A1 where the set of markers represent the different years, and the numbers are the days of the summer period (MJJAS) showing considerable lightning density. Similarly, using this criterion,

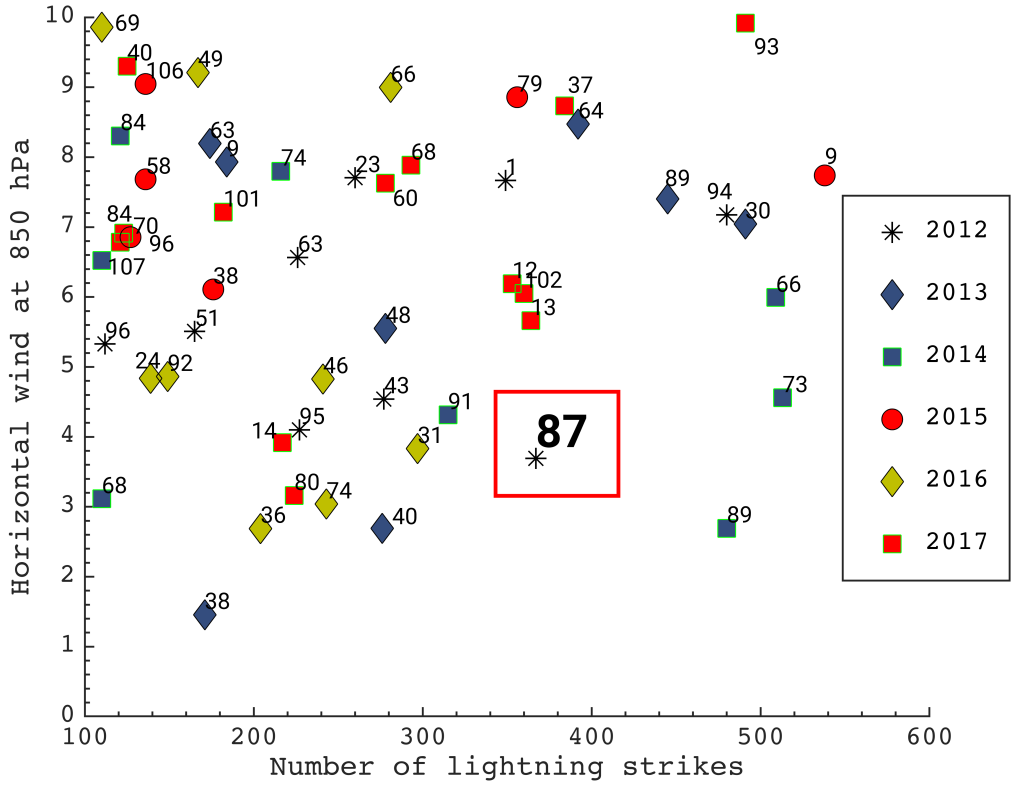

Figure 3.2.: Distribution of summer days (MJJAS) over A1 in the period 2012 - 2017 on the basis of areal mean horizontal wind speed at (at 850 hPa) and the number of lightning strikes. The number indicates the days in the summer period (e.g. 1 indicates 01 May). Number 87 represents one of the selected case, dated 26 July 2012.

two suitable cases are chosen for each area, that means, in a total of six cases. To get an impression of the observed precipitation patterns on the investigated days,

the Radar Online Adjustment (RADOLAN) RW composites are shown in the following section. However, notably, this study focuses on the inter-comparison of simulated precipitation for different model grid spacings and land-surface resolution, not on their validation against the observation. As the name suggests, RADOLAN from the DWD is a forum which provides Radar-based quantitative precipitation estimation products which are of exceptionally high temporal (5 minutes) and spatial resolution (1 x 1 km^2) covering all hydrological catchment areas of Germany. The high spatio-temporal resolution provides data input to flood risk management and is used for other hydro-meteorological and climatic applications (Bartels et al., 2004). The precipitation products in RADOLAN RW products have been used in this study. These products are based on the combination of quantitative measurements with C-band Doppler radar and hourly rain gauge measurements. Here, RW denotes hourly adjusted radar data.

In the following section, the general synoptic situation of one example case from each area is briefly discussed using the composites of the observed daily-lightning density and accumulated precipitation. The other cases are shown in the appendix (Figure B.2, B.3, B.4).

3.1. A1: Flat terrain

Case: 26 July 2012

The spatial distribution of daily lightning density per 25 km^2 and accumulated precipitation (in mm) from RADOLAN RW on 26 July 2012 over A1 are shown in Figures 3.3a and 3.3b. This day has scattered but intensive precipitating cells restricted mainly in the east and southeast of Berlin. The high lightning density indicates that the precipitation result of deep convection.

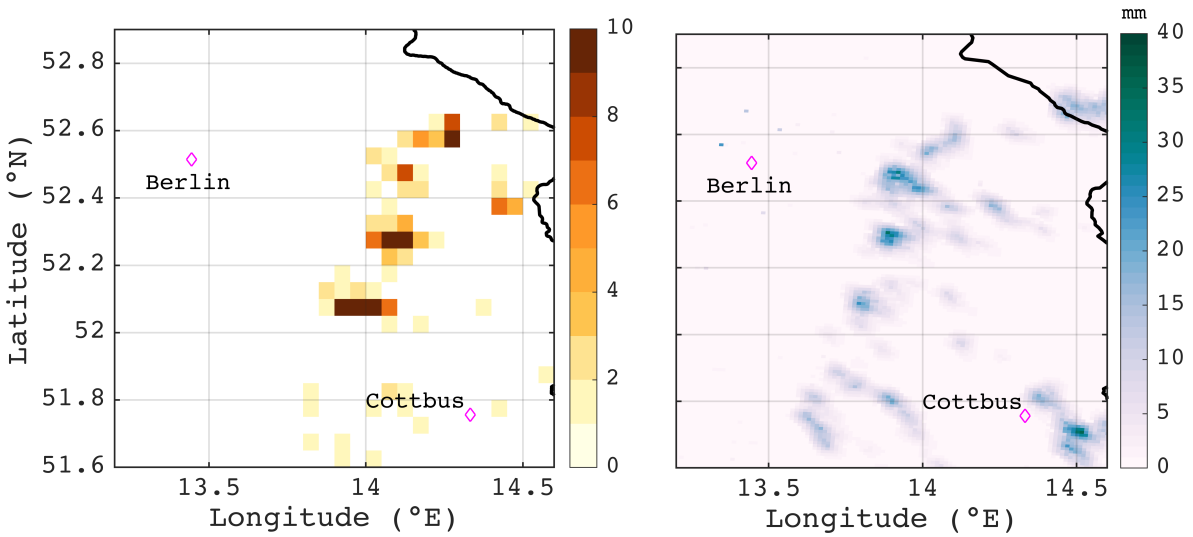

(a) (b)

Figure 3.3.: Horizontal distribution of lightning density (a) and observed (RADOLAN RW) daily accumulated precipitation (b) over A1 on 26 July 2012.

3.2. A2: Isolated orography

Case: 09 June 2018

This day is characterized by a locally induced precipitating system over A2 (Harz mountains) (Figure 3.4a and 3.4b). There are mainly two sets of convective systems observed over this region. The first system was formed along the Harz mountains around 1100 UTC and the second subsequent system was formed in the southwestern part of Harz mountains around 1300 UTC. Both of the systems show intensive lightning density indicating deep convective activity.

3.3. A3: Complex terrain

Case: 12 Aug 2015

The composites of daily lightning density per 25 km^2 and accumulated precipitation (in mm) from RADOLAN RW on 12 Aug 2015 over A3 are shown in (Figure 3.5a and 3.5b). It shows the intensive precipitating cells formed over the peaks of the Black Forest, especially over the southern Black Forest, the precipitating cells are convective and intense.

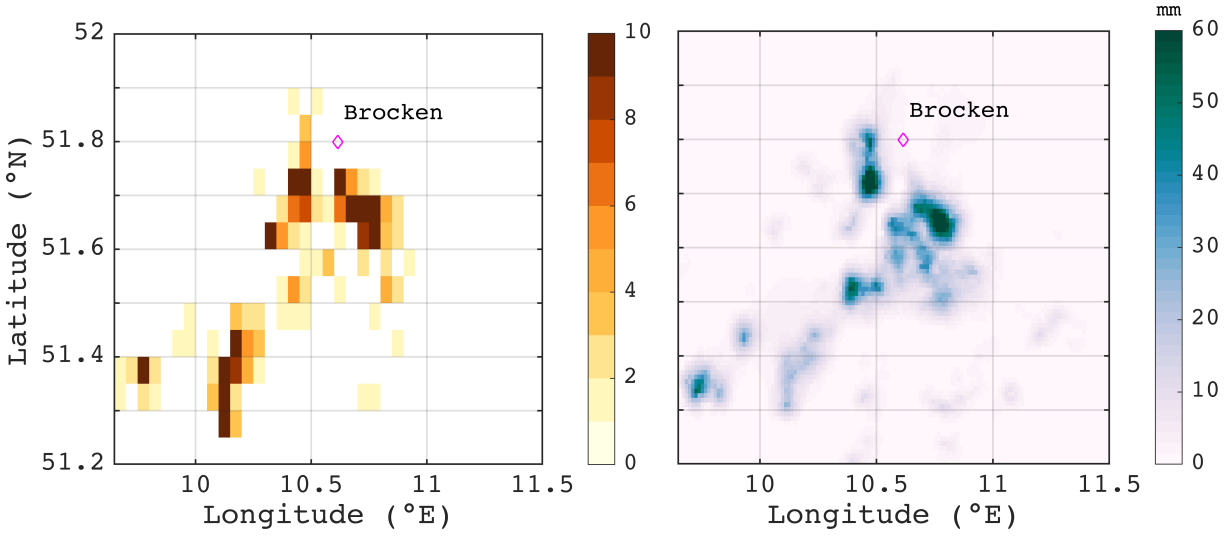

Figure 3.4.: Same as Figure 3.3 but over A2 on 09 June 2018.

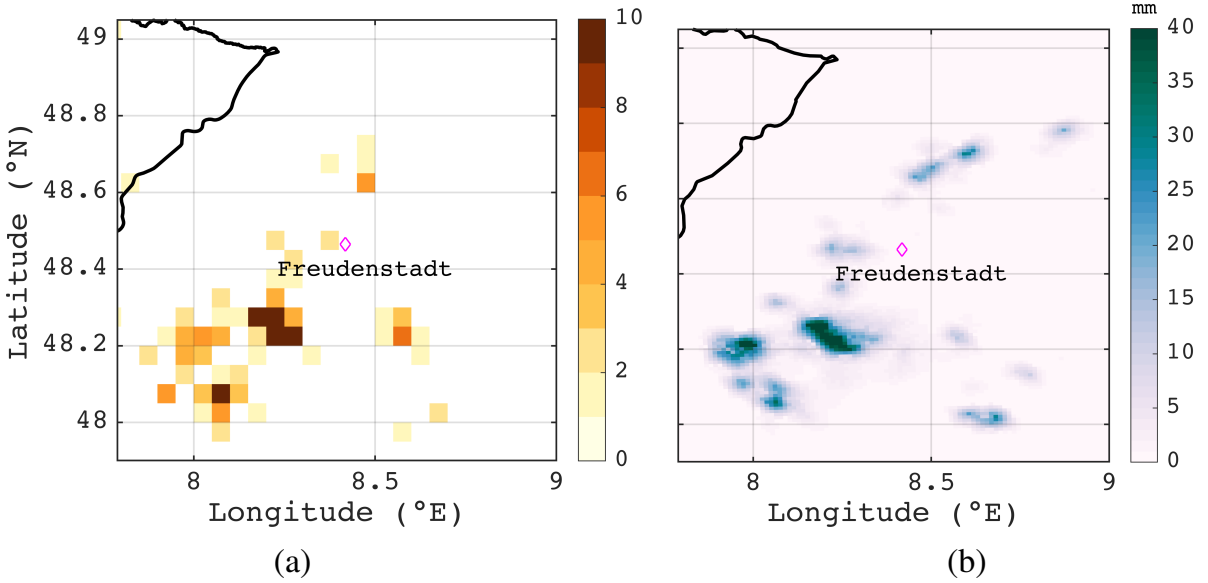

Figure 3.5.: Same as Figure 3.3 but over A3 on 12 Aug 2015.

4. ICOsahedral Non-hydrostatic (ICON) Model: description of its key features

This chapter describes the general features of the ICON model. The ICON is a nonhydrostatic fully compressible general circulation model that has been developed at German Weather Services (DWD) and MPI-M (Zängl et al., 2015). ICON is used at DWD operationally as a global numerical weather prediction model since January 2015. Different communities for the assessment of the uncertainty in the representation of mesoscale circulations in comparison to other NWP models (Heinze et al., 2017). The authors also aim at high resolution, regional LES and idealised (Dipankar et al., 2015; Silvers et al., 2016) simulations to study the subgrid forcing of the physical processes, for example, turbulence, cloud-based processes. ICON also intends to a better representation of the exchange processes between different air masses along with an improved representation of the land surface and subgrid-scale heterogeneities. Depending upon the applications and scale study, ICON is further designed in three basic packages; namely, i) Climate predictions (ICON-Global), ii) Numerical weather prediction (ICON-NWP) and iii) Large-eddy-simulations, (ICON-LES), which is also called as ICOsahedral Nonhydrostatic - Large Eddy Model (ICON-LEM).

ICON-LEM uses physics designed for LES in Limited Area Mode (LAM) usually at the scale of $\mathcal{O}$(100m). The LES physics package was introduced in ICON (Dipankar et al., 2015) within the framework of HD(CP)^2 which stands for *High Definition Clouds and Precipitation for Climate Prediction* project. HD(CP)^2 aimed at the improvement of representation of clouds, convection and precipitation processes in the climatic prediction by utilising very high $\mathcal{O}$(100m) resolution simulations. These simulations provide a better understanding of embedded and complicated resolved processes which are parametrized in the coarser model simulations. Furthermore, ICON-LEM model simulations also provide lateral boundary conditions for other limited area forecasts which are used in the nested simulations for a better representation of boundary and environmental flows.

ICON follows the sets of equations of prognostic variables suggested by Gassmann and Herzog (2008) and the two dimensional Lamb transformations which transform the nonlinear horizontal momentum advection into a vector invariant form as explained in Zängl et al. (2015). These set of equations describe a two-component system which consists of dry air and all the three phases of water. The prognostic equations are solved for horizontal velocity components normal to the triangular edges v_n, the vertical wind component w, the total density of the air mixture ρ, virtual potential temperature θ_v and the specific masses and number densities of tracers q_i ($i = 1,2,3,..,N_t$, where N_t is the total number of traces). According to Zängl et al. (2015), the basic equations system used in ICON are as follows:

$$\frac{\partial v_n}{\partial t} + \frac{\partial K_h}{\partial n} + (\zeta + f)v_t + w\frac{\partial v_n}{\partial z} = -c_{pd}\theta_v\frac{\partial \Pi}{\partial n} + F(v_n), \tag{4.1}$$

$$\frac{\partial w}{\partial t} + v_h.\nabla w + w\frac{\partial w}{\partial z} = -c_{pd}\theta_v\frac{\partial \Pi}{\partial z} - g, \tag{4.2}$$

$$\frac{\partial \rho}{\partial t} + \nabla.(v\rho) = 0, \tag{4.3}$$

$$\frac{\partial \rho\theta_v}{\partial t} + \nabla.(v\rho\theta_v) = \tilde{Q}. \tag{4.4}$$

For a simplified numerical treatment of the terms representing vertical sound wave propagation, the equation 4.4 can be also written as:

$$\frac{\partial \Pi}{\partial t} + \frac{R_d}{c_{vd}}.\frac{\Pi}{\rho\theta_v}\nabla.(v\rho\theta_v) = \tilde{Q}, \tag{4.5}$$

where $K_h = \frac{1}{2}({v_n}^2 + {v_t}^2)$ is the horizontal component of kinetic energy per mass unit, v_t is the reconstructed tangential velocity component, ζ is the vertical vorticity component, f is Coriolis parameter, g is the acceleration due to gravity, $F(v_n)$ is the source term for horizontal momentum, v_h is horizontal velocity component, v is the full three dimensional wind vector, Π is the Exner function, R_d is the gas constant of dry air, c_{pd} and c_{vd} are specific heat capacities of dry air at constant pressure and volume, respectively, and $\tilde{Q}$ is the diabatic heat source term (Wan et al., 2013; Zängl et al., 2015). Moreover, the derivative, $\frac{\partial}{\partial n}$ denotes a horizontal derivative in edge-normal direction. In ICON, local mass conservation is achieved through flux form of equation 4.3 and 4.4. For time integration, a two-

time level predictor-corrector scheme is used, which is explicitly done except for the terms describing sound-wave propagation (for details see Zängl et al. (2015)). To achieve a mass-consistent tracer transport, the air mass fluxes are aggregated over the small-time steps in the dynamical core and then passed to the transport scheme. This tracer transport is done using a flux-form semi-Lagrangian scheme (Miura, 2007).

The ICON grid system comprises of horizontal grid (as described in Section 4.1) and the vertical grid setup (see Section 4.2). According to Linardakis et al. (2011) the horizontal grid discretises the sphere surface on a triangular or hexagonal grid, and the vertical grid is discretised using a set of horizontal layers along the sphere radius.

4.1. Horizontal grid

The horizontal grid of ICON is one of the most featured advantages of this model. The first step to create the horizontal grid is projecting a regular icosahedron onto the sphere in such a way that two vertices fall onto North and South Poles (Figure 4.1). Figure 4.1 shows an example of the regional limited ICON grid where the light blue grid indicates the icosahedron defined base grid, which comprises of 20 triangular faces, 13 edges and 12 vertices. The first refinement of this root grid is the dark blue grid where the edge centres form the new vertices. There is another refinement done only for the northern hemisphere (green grid) and based on this grid, another mesh refinement is done over the European region (red grid).

The desirable resolution is achieved by triangulating the triangular faces of the icosahedron (cf. Figure 4.2a), which is called Delaunay-Voronoi triangulation method, which is nothing but a repeated subdivision of the triangular cells of a spherical icosahedron (cf. Figure 4.2b) into smaller cells. This results into the division of each great circle arc of a projected icosahedron face into n arcs of equal length (cf. Figure 4.2c) and each icosahedron face into ${n_r}^2$ small triangles. For details, see Sadourny et al. (1968). This process is called root division, and the resulting mesh is grid level 0. With the further mesh refinement (by bisecting each spherical triangle edge, k) and connecting the midpoints by great circle arcs, it leads to '*RnBk*' grid (Figure 4.2). Figure 4.2d,e show the two examples of $R2B0$ and $R2B2$ grids.

Figure 4.1.: The icosahedral grid of the ICON model. The grid level 0 or icosahedron base grid (light blue lines) has 20 triangular faces, 30 edges and 12 vertices. The first horizontal grid refinement is shown by dark blue lines. The green grid shows the refinement done over the northern hemisphere, and the third one is done over Europe, shown by red lines (Source Giorgetta et al. (2017)).

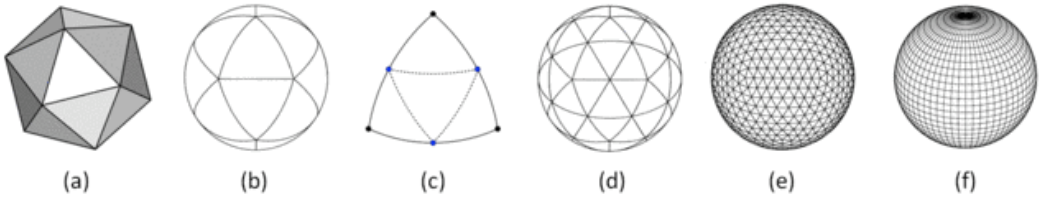

Figure 4.2.: Construction of ICON horizontal grid. The icosahedron (a) is constructed on a sphere (b). The triangle edges are bisected into n equal sections. The new edge points are connected great circle arcs to generate n^2 spherical triangles within the root triangle (c). After further mesh refinement, the aimed grid is obtained (e). (f) compares the occurrence of polar singularities of latitude-longitude grids against the complete avoidance of it in (e) for the ICON grid construction (Source Linardakis et al. (2011)).

Figure 4.2e highlights the advantage of triangular grid in ICON. It removes the polar singularities of latitude-longitude grids and allows a consistent uniformity in resolution over the globe (for further advantages of the triangular grid, see Gassmann (2011)).

There is an interesting distinction and definition of the term ‘resolution’ in ICON. According to Heinze et al. (2017), the resolution in ICON is defined as the square root of the average cell area of the icosahedral grid of ICON, which is approximately 1.5 times the resolution on a corresponding regular grid. This means that for

the resolution R_nB_k, the total number of cells (n_c) , edges (n_e) and vertices (n_v) will be:

$$n_c = 20n^2 4^k,\ n_e = 30n^2 4^k,\ n_v = 10n^2 4^k + 2. \tag{4.6}$$

Further, the effective mesh size $\overline{\Delta x}$ is:

$$\overline{\Delta x} = \sqrt{\bar{a}_c} = \sqrt{\frac{\pi}{5}} \frac{r_e}{n2^k}, \tag{4.7}$$

where $\bar{a}_c$ is the average cell area and r_e is the radius of the Earth (Zängl et al., 2015). Altogether, the definition of effective mesh size or grid resolution could be also based on the square root of the area of the triangle, the length between the two cell-centres, or the edge length of the cell. According to Dipankar et al. (2015), the approximate relation between the triangle edge length (Δ_l) and the grid resolution (Δ) following the above definitions will be: $\Delta_1 = 0.67\Delta_l$, $\Delta_2 = 0.58\Delta_l$, $\Delta_3 = \Delta_l$, respectively, where $\Delta_3 > \Delta_1 > \Delta_2$.
But there are also slightly different definitions of 'resolution' in ICON used by other researchers. According to Wan et al. (2013), in the grid level 0, there are only 12 icosahedrons which are surrounded by five triangles, also called as pentagon points, the rests are surrounded by six triangular cells. This grid distribution results in inequality in the cell areas and the edges of triangles. Quantitatively the reason is that the average cell centre distances are smaller by a factor of about $\sqrt{\frac{4}{3}}$ on a triangular grid because every grid cell point has only three nearest neighbours. For the present study, the grid resolution is taken as the triangle edge length which is termed as 'model grid spacing' (Δ_h) (this should not be confused with the model resolution). Furthermore, C-staggering is applied to the triangular cells by putting mass and temperature at the circumcenters of triangles (Bonaventura and Ringler, 2005; Wan et al., 2013; Giorgetta et al., 2015; Linardakis et al., 2011) (Figure 4.3).

4.2. Vertical grid

The vertical grid of ICON comprises of a set of layers which possess the horizontal two-dimensional grid structure, shown in Figure 4.4. It employs a Lorenz-type staggering where the vertical velocity is defined at the boundaries of lay-

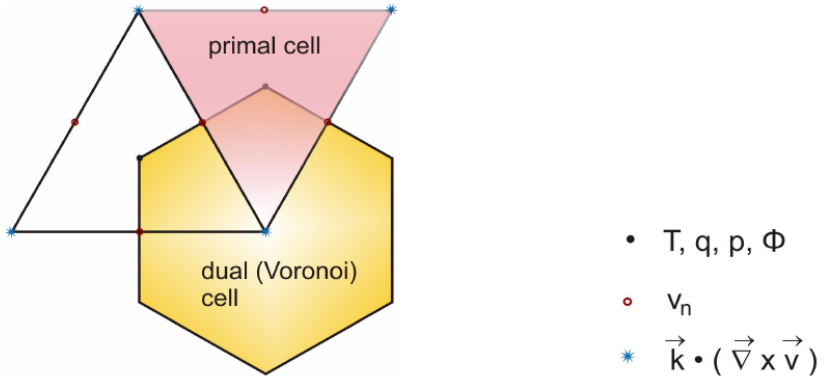

Figure 4.3.: Positioning of prognostic variables on ICON horizontal grid with primal cell (triangular) and dual cell (hexagonal). The dual edges are bisect and orthogonal to the primal edges (Source: Linardakis et al. (2011)).

ers (half levels). At the same time, other prognostic variables are placed in the centre of the layers (full levels). ICON has a height-based terrain-following hybrid structured vertical coordinate system and the smooth level vertical coordinate implementation (SLEVE) (Leuenberger et al., 2010). The conventional Gal-Chen and Somerville (1975) formulation is also available alternatively. The main advantage of this vertical coordinate system is that it allows a faster transition to smooth levels in between the upper troposphere and lower stratosphere in comparison to the traditional height-based Gal-Chen coordinate system. Depending

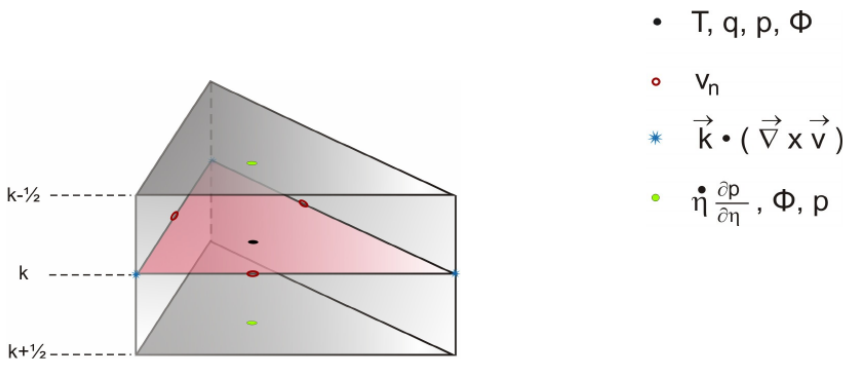

Figure 4.4.: Illustration of the vertical structure of the primal cells. As shown, the half levels ($k \pm 1/2$) correspond to η vertical levels (Source: Linardakis et al. (2011)).

upon the specified model top height, the number of height levels and the stretch-

ing factor, ICON defines the set of vertical levels. These definitions of vertical grid staggering are controlled by the use of the respective namelist parameters (number of levels, stretching factor, model top height, minimum layer thickness, flat height (the height above which the vertical coordinate surfaces are flat) (Namelist Overview, 2015). The stretching factor controls the thickness and therefore, the distribution of vertical levels. One example of the vertical level distribution of ICON-LEM simulations performed in this study is shown in Figure 4.5. The detailed model configuration is discussed in Section 5.

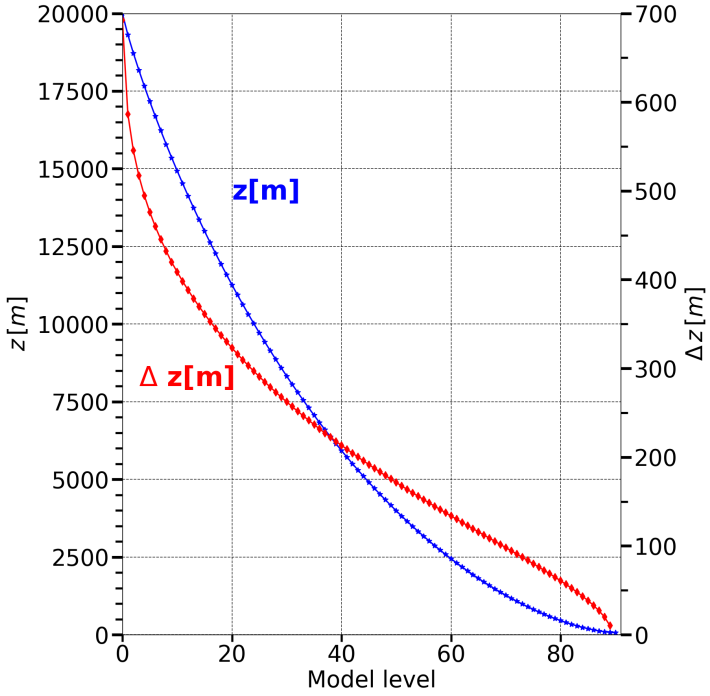

Figure 4.5.: Distribution of vertical half levels (blue) and the layer thickness (red) in one of the ICON simulations performed over flat terrain (A1).

4.3. ICON physics, dynamics and their coupling

In ICON, the physical processes are categorised as slow- and fast- physics forcing depending upon how frequently they are called in the simulation. In other words, the processes whose time scale is comparable or relatively shorter (longer) than

the model time step are called as fast (slow)-physics processes. The examples of fast physics are saturation adjustment, surface transfer, land/lake/sea-ice based parametrization, turbulent diffusion and microphysics. Slow physics are convection, cloud cover, radiation, non-orographic gravity wave drag and sub-grid-scale orographic drag. Since the slow physics tendencies are called less frequently, they are stored to be integrated with the governing equation. In contrast, the fast physics are called every model time step so that it updates the prognostic variables sequentially and therefore, they do not need to provide the tendencies terms to the model governing equations (Zängl et al., 2015; Dipankar et al., 2015; Heinze et al., 2017). Since ICON is designed to solve prognostic equations based on the Exner function (Π) rather than temperature (T), the temperature tendencies have to be converted into tendencies of Π first. Also, the moisture tendencies are not treated as a forcing term during the tracer advection but in a split manner and then further added to the newly updated moisture variables.

4.4. Land-Soil Model TERRA_ML

The atmosphere and the underlying land-surface is strongly coupled, which is represented in numerical models as surface fluxes. In ICON, the soil-vegetation-atmosphere-transfer component TERRA_ML (Schrodin and Heise, 2002; Heise et al., 2006) is used for the exchange of momentum-, heat-, moisture-, mass-fluxes between land-surface and atmosphere. It forms the boundary condition for the atmospheric part of ICON. TERRA_ML is the multi-layer version of the soil model TERRA. It considers the physical processes like radiation, biophysical control of evapotranspiration, heat and soil-water transport, snow formation and the coupling with the atmosphere based on a multi-layer concept for the soil. Usually, most of the characteristic parameters of the soil model, for example, heat and water storage capacity, porosity, are strongly coupled with the soil texture. With this categorisation in TERRA_ML, it gives eight different soil types. The multi-layer version not only makes the layer thickness independent of the respective soil type but also avoids the different soil layer designation into the thermal and hydrological section of the model (for details see Doms et al. (2011))

4.5. ICON-LEM standard setup

As stated before, ICON-LEM is the LES setup of ICON designed for very high-resolution simulation, which is especially done in LAM. Besides having high potential in a line of improving the understanding of moist convective processes and their parameterization in climate models (Heinze et al., 2017), ICON has proven its eddy-resolving abilities (Dipankar et al., 2015). However, the implementation of a three-dimensional turbulence scheme on a triangular grid on a conservative basis is described as a non-trivial step because many interpolation operations have to be performed. Additionally, there are new approaches mandatory for the representation of the subgrid-scale turbulence and other complicated microphysical, cloud-based processes (Dipankar et al., 2015). The adaptation of the simulations using the standard ICON-LEM setup is described in detail in the next chapter 5.

5. Adaptation of ICON for sensitivity simulations

5.1. Domain configuration

This chapter describes the ICON simulations performed in this study. The ICON simulations are performed in LEM mode, with the model grid spacings ($\Delta_{5000\,m}$, $\Delta_{2500\,m}$, $\Delta_{1250\,m}$, $\Delta_{625\,m}$, $\Delta_{312\,m}$ and $\Delta_{156\,m}$) for a comparison of the impact of different model grid spacing (Δ_h) and land-surface resolution on moist convection. The six model grid spacings (Δ_h) are used in a nested setup, starting from the parent domain of grid size 5000 m, going to a grid size of 156 m, in the ratio of two. A typical example of the domain configuration for a case simulated over flat terrain (A1) on 26 July 2012 is shown in Figure 5.1. The setup uses 90 vertical levels with the model top height at 20,000 m, and the lowermost minimum layer thickness as 10 m which results into the stretching factor of model levels that equals to 0.9 (Figure 4.5).

5.2. Model physics setup

There are limited studies which address the suitable resolution when there is a transition from 1D turbulence scheme of NWP to 3D turbulence scheme of LES (Honnert and Masson, 2014; Cuxart, 2015). According to Honnert and Masson (2014) the criterion of an optimal horizontal grid spacing (Δ_h) scaling should be based on the size of thermal plumes which is equal to the sum of boundary layer height h and the depth of cloud layer h_c. This study proposed two separate critical resolution for free and forced CBL which is $\Delta x \leq 0.5(h+h_c)$ and $\Delta x \leq 3(h+h_c)$, respectively. However, ICON-LES turbulence scheme (3D Classical Smagorinsky scheme) assumes isotropic turbulence which is not a good approximation especially for shear-driven turbulence and therefore a scale adaptive turbulent scheme is recommended. The choice of physics packages in this study is based on a few tests and for a broader range of comparison of the grid spacings (Δ_h). Therefore, the transition in turbulence closure is done for $\Delta_{1250\,m}$ and the finer grid spacings,

which are referred as LES model grid spacings. This scale covers the atmospheric flows ranging from mesoscale γ to microscale α. Mesoscale simulations still do not explicitly resolve the atmospheric motions (and turbulence) occurring over an hourly or lower time range. But the chosen LES model simulation range explicitly resolve most of the deep convection and turbulent eddies. The selection of LES turbulence for model grid spacing from $\Delta_{1250\,m}$ to $\Delta_{156\,m}$ allows us to compare the sensitivity of model grid spacing on deep convection over a broader range with a simple and uniform setup.

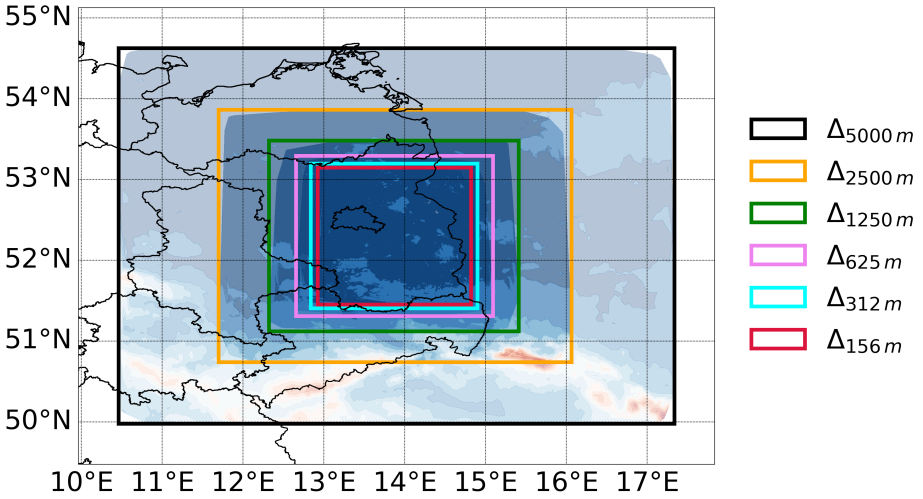

Figure 5.1.: Model domain for the case over flat terrain, area near Berlin, dated 26 July 2012. This is a setup of one way nesting starting from $\Delta_{5000\,m}$ nested down to $\Delta_{156\,m}$.

Since these packages are designed for studying the eddy-resolving as well as also subgrid-scale processes, there are two sets of processes which have to be explicitly and implicitly represented in the model simulation. Firstly, the explicit physical processes are categorised into the following physics packages. For example, convective schemes, subgrid-scale orographic effects (this controls blocking and gravity wave drag formation), non-orographic gravity wave drag. The second category is for the processes, which need to be parametrized, and which are called under the following physics packages:

- Cloud microphysics scheme: Double-moment microphysics scheme based on Seifert and Beheng (2001)

- Subgrid-scale turbulence scheme:
  - Prognostic Turbulent Kinetic Energy (TKE) COnsortium for small-scale MOdelling (COSMO) (for NWP) (Raschendorfer, 2001)
  - 3D Smagorinsky diffusion scheme (for LES) based on Smagorinsky (1963) with the modifications by Lilly (Lilly, 1962) in order to consider the thermal stratification (buoyancy along-with wind shear)

- Cloud cover scheme:
  - Diagnostic Probability Density Function (PDF) cloud cover scheme (for NWP)
  - 'All-or-nothing' which is also called a grid-scale cloud cover scheme (for LES)

- Land-soil model: TERRA-ML (Schrodin and Heise, 2002). It consists of eight irregularly spaced soil levels and eight soil types. In the current model setup, $ntiles = 1$ has been used, which means that the tile approach is turned off and only the dominating land-surface type of a grid cell has been taken into account.

- The ICON simulations performed in this study do not use a lake or sea-ice model.

The Rapid Radiation Transfer Model (RRTM) scheme is applied for radiation (Mlawer et al., 1995). TERRA_ML is used as multi-layer surface scheme (Doms et al., 2011). This is the version without subgrid land-cover variability, and in this configuration, the vertical interpolation of soil variables are needed. Land-use data, orography and soil type are taken from the high-resolution observational dataset, which is also interpolated on respective ICON grid. The details of these external parameters are given in Section 5.3.

5.3. External parameter: EXTPAR

At the step of initialising the surface fields, NWP models need to generate the geographically localised dataset for example terrain height, plant cover, land use. External Parameter for Numerical Weather Prediction and Climate Application (EXTPAR) is a software tool used in COSMO and ICON to perform this task. It takes the raw input dataset and interpolates it on the target grid (here, ICON).

Parameter	Dataset	Source	Resolution
Land use	Globcover 2009 (GlobCover, 2009)	European Space Agency (ESA)	10” (300 m)
Orography	Advanced Spaceborne Thermal Emission and Reflection Radiometer (ASTER) (ASTER, 2011)	Ministry of Economy, Trade, and Industry of Japan (METI) / National Aeronautics and Space Administration, United States (NASA)	1” (30 m)
Soil-type	Harmonized World Soil Database (HWSD) (Fischer et al., 2008)	FAO/IIASA/ISRIC/ISSCAS/ JRC	30” (900 m)

Table 5.1.: Input raw datasets for ICON

In this way, the different raw datasets are aggregated to the target grid, by considering all the raw data elements, which lie within the target grid element. For details see Asensio et al. (2018). The source-raw datasets of some of the external parameters and their resolution is tabulated in Table 5.1.

5.4. Initial and boundary conditions

The initial and lateral boundary conditions for ICON simulations are taken from different types of models. Out of the six cases, one case over flat terrain (A1) 26 July 2012 is initialised using the surface fields from COSMO-DE and atmospheric fields from ECMWF-Integrated Forecasting System (ECMWF-IFS).

COSMO-DE is a NWP model having a spatial resolution of 2.8 km and 50 vertical levels. Here, DE refers to its domain setup over Germany, Switzerland, Austria and parts of some other neighbouring countries (for details see Deutscher Wetterdienst (DWD) (2016)). The ECMWF-IFS model operational analysis dataset is with a horizontal resolution of ≈9 km. With this, the ICON-LEM is relaxed towards six-hourly ECMWF-IFS analysis in a 20 km wide nudging zone. The nudging zone width of the nested domains is 8 grid points wide (cf. Heinze et al. (2017)).
The other cases use the operational ICON analysis product ICON-Europe (ICON-EU) for initial and boundary conditions having a resolution of 6.5 km and 60 vertical layers. The boundary of the parent domain (Δ_{5000m}) is relaxed towards three hourly ICON-EU assimilation forecast products. ICON-EU products are available to registered users via DWD's PArallel MOdel data REtrieve from the Oracle Databases (PAMORE) service (for details see DWD-PAMORE (2015))

The above-listed model products need to be interpolated on the corresponding ICON grid in order to be used as initial and boundary conditions. For this purpose ICON-tool from DWD is used (for details see Prill (2014)). For example ICON-EU data has been interpolated on the respective ICON-LEM grids by using a Radial Basis Function (RBF) interpolation method (Peixoto and Barros, 2014).

These six different days are simulated each for 24 h periods (00-24 Coordinated Universal Time (UTC)). A summary of the days, with some important notations and differences, is shown in Table 5.2.

5.5. Simulation strategy

The general structure of the set of simulations is discussed in section 5.1, 5.3 and 5.4. This part discusses the simulation strategy of all the cases, along with their sensitivity simulations (see Figure 5.2). In all the cases, Δ_{156m} of the set of control runs is taken as the reference run. The control run simulations have been performed for all six cases. Along the control run line, the model grid spacing (blue) and land-surface resolution (green) have been changed simultaneously (shown along the diagonal line, Figure 5.2). Furthermore, the sensitivity simulations have been performed by keeping the land-surface resolution (<res>: 5000 m and 1250 m) constant and only changing the model grid spacing. Here, land-surface parameters can be broadly categorised into groups. The first group com-

Areas	A1 Flat terrain	A2 Isolated mountain range	A3 Complex orography
Cases	26.07.2012 17.09.2017	09.06.2018 17.09.2017	12.08.2015 29.05.2017
Model resolution	5000 m, 2500 m, 1250 m, 625 m, 312 m, 156 m		
Duration	00-24 UTC	00-24 UTC	00-24 UTC
Initial condition	COSMO-DE and ECMWF-IFS ICON-EU	ICON-EU ICON-EU	ICON-EU ICON-EU
Boundary condition	ECMWF-IFS ICON-EU	ICON-EU ICON-EU	ICON-EU ICON-EU

Table 5.2.: Outline of simulated cases

prises of parameters related to land-surface properties (denoted as L) for example plant cover, land use, the fraction of land and lake, roughness length. The second group consists of the parameters related to orography (denoted as O) for example terrain height, slope angle, slope azimuth. This way, the sensitivity simulations have been done further in three ways, firstly the land surface properties and orography parameters are modified altogether (denoted as LO_<res>). Secondly, the land-surface properties are only modified, but the resolution of orography-related parameters are the same as the corresponding model grid spacing (denoted as L_<res>). Thirdly, the orography-related parameters are modified, but the resolution of land-surface properties are used as the corresponding model grid spacing (denoted as O_<res>).

That means the land-surface properties and orographic parameters are coarsened sequentially while the atmospheric variables are used at high resolution. This modification is done by interpolating the land surface parameters from 5000 m to the finer resolution 2500 m, 1250 m, 625 m, 312 m, 156 m in the case of LO_5000 m, L_5000 m and O_5000 m and from 1250 m to 625 m, 312 m, 156 m in the case of LO_1250 m, L_1250 m and O_1250 m. This modification is done by using the DWD-ICON-tools. The interpolation is done using the option of Barycentric interpolation algorithm. The main advantage of this interpolation method is that it interpolates the data from triangular grid exactly on the target triangular grid. Therefore there is no over- and undershoots of the resulting interpolated paramet-

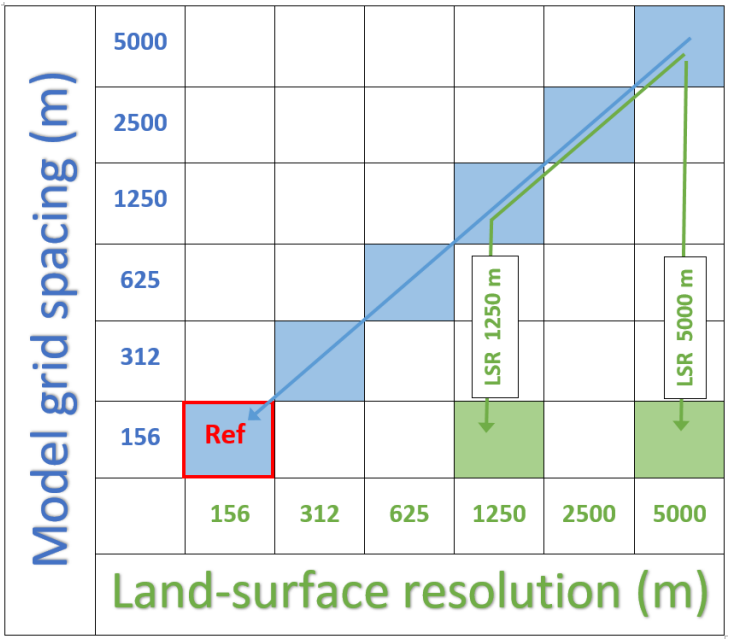

Figure 5.2.: ICON-LEM simulation strategy. Terms in blue colour represent model grid spacing (Δ_h) and in green colour represent land-surface resolutions (LSR). Ref (in red) which is 156 m control run, denotes the reference run.

ers, which happened to be the case with other interpolation methods (RBF and Nearest-Neighbour method) (for details see Prill (2014)).

5.6. LAGRANTO: LAGRangian ANalysis TOol

LAGRANTO stands for LAGRangian ANalysis TOol (Wernli and Davies, 1997). It is a tool designed essentially to calculate forward and backward trajectories of air parcels to identify the flow structures of air masses. This tool is frequently used in the study of extratropical storm tracks, tropical cyclones, warm conveyor belt, identification of atmospheric blocking, dispersion of pollutants and in the characterisation of other transport regimes (Sprenger and Wernli, 2015; Steinfeld and Pfahl, 2019; Babić et al., 2019). The essential theory of the trajectory calculation in LAGRANTO is the same as used in other trajectory tools, for example FLEXTRA trajectory model (Stohl, 1999), Hybrid Single Particle Lagrangian Integrated Trajectory model (HYSPLIT) (Draxler and Hess, 1998) etc. The basic trajectory equation, which they solve numerically is:

$$\frac{D\mathbf{x}}{Dt} = \mathbf{u}(\mathbf{x}), \tag{5.1}$$

where $\mathbf{x} = (\lambda, \phi, p)$, $\mathbf{u} = (u, v, \omega)$. $\mathbf{x}$ is the position vector in the respective geographic coordinate and $\mathbf{u}$ represents 3-D wind field. Though LAGRANTO differs in terms of spatial discretisation, treatment of lower boundary and also its flexible objective criteria of selection of trajectories. It also allows the user to calculate some diagnostic parameters like potential vorticity, diabatic heating rate, divergence and potential temperature etc. LAGRANTO is flexible in the sense that it allows the user to calculate forward and backward trajectories for different global and NWP models (European Centre for Medium-Range Weather Forecasts (ECMWF), COSMO, Weather Research and Forecasting (WRF) and UK Met Office Unified Model (MetUM)).

In this study, LAGRANTO is used to identify the source region of the convective system. To achieve that the backward trajectories starting from the cloud base or inside the cloud itself are calculated. The adaptation of the LAGRANTO 2.0 version has been done for the ICON model with the assistance of M. Sprenger from ETH Zürich. The version LAGRANTO-ICON works on horizontal regular latitude-longitude. Therefore, the required trajectory fields are interpolated from ICON to regular latitude-longitude grid. LAGRANTO uses 3-D wind fields namely (zonal wind u (in $m\ s^{-1}$), meridional wind v (in $m\ s^{-1}$) and vertical wind ω (in $Pa\ s^{-1}$)). Additionally, it needs surface pressure (PS) (in *hPa*) for the configuration of a level type, which further calculates the full 3-D pressure (P) on the model fields and identifies the trajectory points intersecting the underlying orography. To study the local triggering, the vertical coordinate in meters is intended. Therefore, LAGRANTO needs the information of orography and the 3-D geopotential height (*z_mc*) for all grid points. The new version is adapted to work also with a very high temporal resolution of model fields (which in this study is up to 1 to 10 minutes). With the above adaptations and the required trajectory fields, LAGRANTO - ICON is used extensively in this study. This flexibility of LAGRANTO makes it a novel choice for research doing the calculation of air parcel trajectories. For details of the different functionalities and their usage in LAGRANTO see Sprenger and Wernli (2015).

6. Impact of model grid spacing and land-surface resolution on clouds and precipitation

The first aim of this study is to investigate the impact of model grid spacing (Δ_h) and land-surface resolution on convective precipitation using ICON. In the first step, the selected areas are classified based on land-surface heterogeneity using the parameters representing orography, soil type, and vegetation (Section 6.1). It gives an overview of the impact of model grid spacing (Δ_h) and land-surface resolution on convective precipitation (Section 6.2) analysed for the six simulated cases (selected as described in Section 3). Moreover, it also describes the responsible factors and processes which may cause the differences across LES model grid spacings ($\Delta_{1250\,m}$ to $\Delta_{156\,m}$).

6.1. Classification of land-surface heterogeneity

The criteria for selecting the suitable geographical areas and an overview of the cases and their synoptic is discussed in Chapter 3. Figure 6.1 shows the horizontal snapshot of the orographic structures of these areas located in three different regions of Germany. Considering the different physical characteristics of the specified region, the land-surface heterogeneity can be categorised broadly into two groups, namely, the land-surface properties, for example, vegetation (Leaf Area Index (LAI), plant cover), and the orography (Meißner et al., 2007). Figure B.1 shows the spatial pattern of modelled orography, Transpiration Area Index (TAI) and soil type across the six chosen model grid spacings ($\Delta_{5000\,m}$, $\Delta_{2500\,m}$, $\Delta_{1250\,m}$, $\Delta_{625\,m}$, $\Delta_{312\,m}$ and $\Delta_{156\,m}$) of each area (A1, A2 and A3). The orography shown here is a model output (Figure B.1a-c). Notably, the ICON model output orography is usually produced by digital filtering with a ∇^2-diffusion operator. But in the simulations performed in this study, there is no smoothing applied to the orography. That means the original orography interpolated on the respective model grid spacing (Δ_h) is used (Figure B.1a-c). Furthermore, TAI (Figure B.1d-f) which is the product of plant cover and maximum LAI is a good represent-

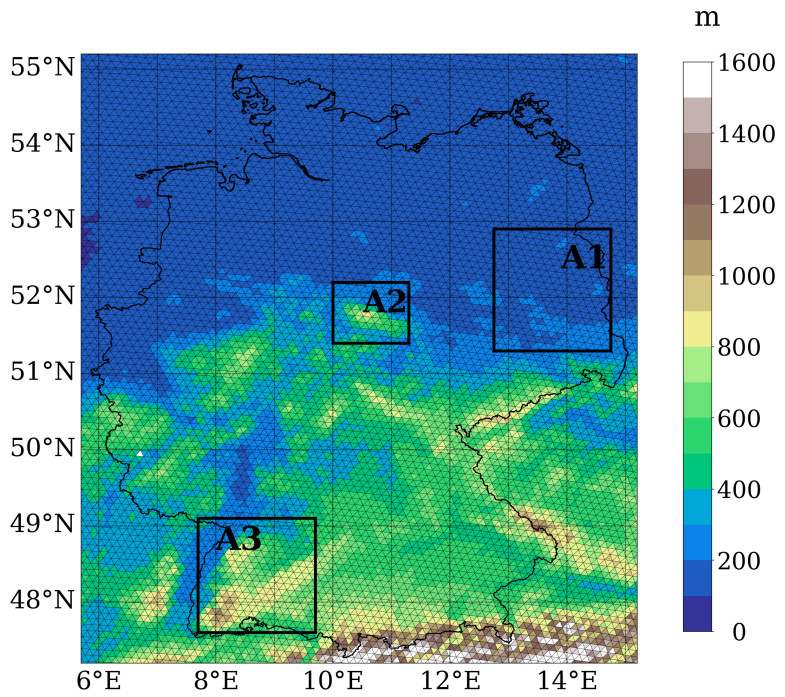

Figure 6.1.: Orography map (colour coded) with the selected areas: A1 (flat terrain), A2 (isolated mountain range), and A3 (complex terrain). The thin solid line marks the national boundary of Germany.

ative of vegetation. Lastly, the third characteristic parameter shown here is the soil type (Figure B.1g-i). There are eight different soil types used in TERRA - Multi Layer (TERRA-ML) (Schrodin and Heise, 2002), which are: ice, rock, sand, sandy loam, loam, loamy clay, clay, peat (seawater and sea ice) which are denoted over a scale from 1 to 8, respectively (Section 4.4).

The flat terrain area, A1, in Eastern Germany is mainly characterised by a variety of land-surface properties, for example, a set of soil type composition (10.5 % sand, 40 % sandy loam, 41.5 % loam, 0.4 % clay, 6 % peat, and 1.7 % water) and TAI. The second area, A2, up-rises on the orographic-complexity level and possesses a higher elevated mountain range, called Harz mountains and also the heterogeneous soil type (52.6 % sand, 0.9 % sandy loam, 45 % loam, 0.8 % loamy clay, 0.7 % peat, and 0.3 % water) located close to its highest mountain peak (1132 m), called Brocken. The third area, A3, which is a complex mountain range, called the Black Forest, located in south-west Germany and has the highest peak of 1484 m (Feldberg). A3 consists of a range of orographic as well as vegetation ranging from Rhine valley, parts of Swabian Jura and Black forest mountain ranges. A3

also has heterogeneous soil type composition with 18 % sand, 3 % sandy loam, 71 % loam, 1 % loamy clay, 6 % clay and 0.5 % water.

Now, in order to quantify this spatial variability of land-surface heterogeneity across the model grid spacings, the areal mean Coefficient of Variation (CV) of three physical parameters (orography, soil type and TAI) (Figure 6.2) of the three selected geographical areas is calculated. CV is a measure of relative variability of a parameter and can be expressed as the ratio of its standard deviation (σ) to the mean value (μ). Therefore, CV for any parameter (P) over an area ($A_{i=1,2,3}$) at a grid spacing (Δ_h) will be:

$$\mathrm{CV}_{P|A_i} = \frac{\sigma_{P|A_i}}{\mu_{P|\mathbb{A}}} * 100\%, \tag{6.1}$$

where $\mu_{P|\mathbb{A}}$ is the mean value of a given parameter (P) over all the three areas ($\mathbb{A}$). CV is expressed as a percentage value. The higher the CV of the given parameter (orography, TAI and soil type), the larger the deviation around the mean value and vice versa. Higher CV means more resolved structures at a particular model grid spacing (Δ_h) for the respective areas. A steeper slope of the curve means a more considerable variability of the parameter across the range of model grid spacings (Δ_h). All in all, it gives the variability of a parameter in terms of the resolved (or unresolved) physical structures at the given model grid spacing (Δ_h).
Figure 6.2 illustrates the CV of orography (a), soil type (b) and TAI (c) of A1, A2 and A3, respectively. The inter-variability of resolved orography (Figure 6.2a) among the areas is lowest for A1 ($\approx$2%) and highest for A3 ($\approx$33%). That means A3 contains more disperse orographic structures than A1. The sequential arrangement of the mean CV curves for the given set of model grid spacings of the three areas (A1, A2 and A3) follows the orography hierarchies arranged in the order of ascending mean terrain height of the regions. Here, A3 has a more significant slope of 15.8° than that of A2 (slope of 11.3°) and A1 (slope of 3.4°) which means that the variability across the model grid spacings (from $\Delta_{5000\,m}$ to $\Delta_{156\,m}$) for orography is largest for A3 and lowest for A1. Thus most of the orographic features are already resolved at $\Delta_{5000\,m}$ in A1 whereas $\Delta_{5000\,m}$ in A3 contains a relatively high number of unresolved features which are yet to resolve at finer grid spacings. Furthermore, A1 at $\Delta_{1250\,m}$, $\Delta_{625\,m}$, $\Delta_{312\,m}$, and $\Delta_{156\,m}$ grid spacings show higher values of mean CV for soil type (Figure 6.2b) in comparison to A2 and A3, which

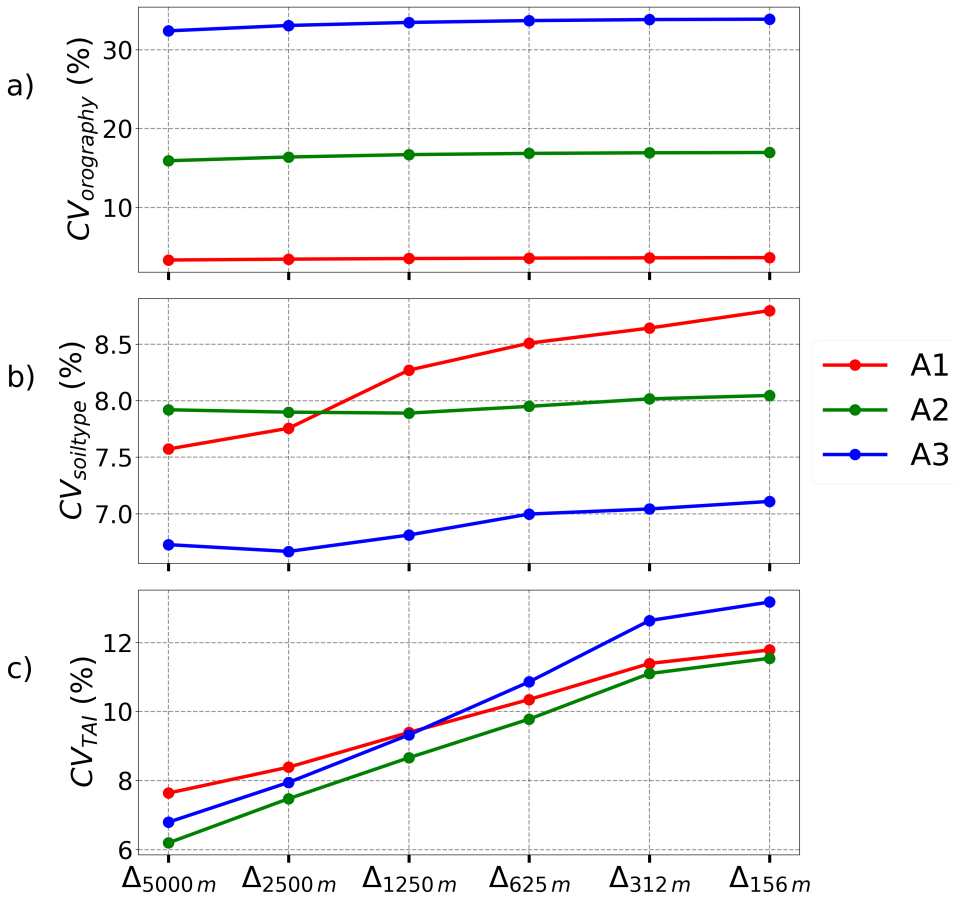

Figure 6.2.: Classification of the three areas and different model grid spacings based on areal mean Coefficient of Variation (CV) of orography (a), soil type (b), and TAI (c).

means that the soil type heterogeneity is more prominent over the flat terrain (A1) than the other two areas (A2 and A3) except at the scales of $\Delta_{5000\,m}$ and $\Delta_{2500\,m}$ where A2 shows slightly higher CV in comparison to A1. This is because A2 at $\Delta_{5000\,m}$ has a relatively larger deviation (0.4 %) of soil type (54 % sand, 0.85 % sandy loam, 43.7 % loam, 0.85 % loamy clay and 0.71 % peat) around the mean value whereas $\Delta_{5000\,m}$ in A1 is dominated with similar soil type varieties (11 % sand, 41.2 % sandy loam, 42.8 % loam, clay 0.4 % and 4.7 % peat) but smaller deviation. Finally, A1 has the largest slope of 14.5° compared to A2 (1.7°) and A3 (5.3°) which means that the soil type based variability in terms of unresolved/resolved soil types within a scale range from $\Delta_{5000\,m}$ to $\Delta_{156\,m}$ is higher for the flat terrain (A1) compared to that over A2 and A3 region. As such, small

lakes and the areas with soil type peat are not resolved at $\Delta_{5000\,m}$ over A1, but only at the finer grid spacings ($\Delta_{1250\,m}$ to $\Delta_{156\,m}$).
Similarly, the variability associated with TAI (Figure 6.2c) at $\Delta_{156\,m}$ is highest for A3 ($\sim$ 13.5%) compared to that of A1 (11.9%) and A2 (11.8%) which means $\Delta_{156\,m}$ in A3 resolves a higher number of heterogeneous vegetated surfaces. A3 has the highest slope of 53.6°, hence the highest difference in variability, whereas A2 and A1 with the slope of 47.9°, 41.3° show a relatively lower level of disperse vegetation resolved across the given model grid spacings. Despite the relative differences, the range of variability of TAI across the model grid spacings remains significantly large for all the areas.

From the above classification, it would be interesting to see whether this substantial modification of TAI values across the model grid spacing has a considerable impact on the spatio-temporal behaviour of precipitation, in comparison to orography and soil type. Moreover, as the selected days (Chapter 3) are characterised by locally induced precipitation, the triggering may vary significantly depending upon the resolved land-surface properties and the orography at the different grid spacings. This dependence is discussed in detail in Chapter 7.

6.2. Convective precipitation in control runs and sensitivity experiments

This section investigates the sensitivity of spatial patterns and the areal mean of precipitation to different model grid spacing and land-surface resolution is studied.

Spatial pattern of daily accumulated precipitation in control runs

Figure 6.3 and 6.4 show the horizontal snapshots of total accumulated precipitation until 2000 UTC from the control runs of the cases simulated over A1 (flat terrain), dated 26 July 2012 and A3 (complex terrain), dated 12 Aug 2015, respectively (details of numerical simulations and used physics are described in Chapter 5). In Figure 6.3, the reference run ($\Delta_{156\,m}$ of the control run) produces clustered, and non-uniform precipitation patterns in the east and southeast of Berlin whereas $\Delta_{1250\,m}$ and the other LES grid spacings form dispersed, but relatively uniform-sized precipitating cells throughout the East of Berlin. Similarly, in Figure 6.4, the reference run results into clustered precipitation patterns in the North-

ern Black Forest along with a few small-sized precipitating cells in the south-western part of the Black Forest, while, $\Delta_{1250\,m}$ produces many much bigger and almost uniform sized precipitating cells in most of the area.
Considering the comparison across model grid spacings (Δ_h) with the same physics, Figure 6.3c-f is one example showing the different behaviour of precipitation patterns across LES grid spacings simulated over A1, case: 26 July 2012. $\Delta_{1250\,m}$ produces intense precipitating cells in comparison to other finer LES model grid spacings which is a consistent model behaviour found in the precipitation patterns simulated for other cases (see Section 3 for details of cases) except in A2 (17 Sept 2017) and A3 (29 May 2017) where $\Delta_{156\,m}$ produces stronger precipitation cells than other coarser LES model grid spacings (Δ_h) (Figure B.5, B.6, B.7, B.8).
Furthermore, the total precipitation patterns differ considerably between NWP ($\Delta_{5000\,m}$, $\Delta_{2500\,m}$) and LES set of model grid spacings ($\Delta_{1250\,m}$, $\Delta_{625\,m}$, $\Delta_{312\,m}$ and $\Delta_{156\,m}$) in both of the cases (Figure 6.3 and 6.4). In A1, NWP model grid spacings produce completely different, bigger and intenser precipitating cells in comparison to LES model grid spacings (Figure 6.3) while for the case simulated over the complex terrain, located in the Black Forest (A3), the NWP set does not produce precipitation at all (Figure 6.4).

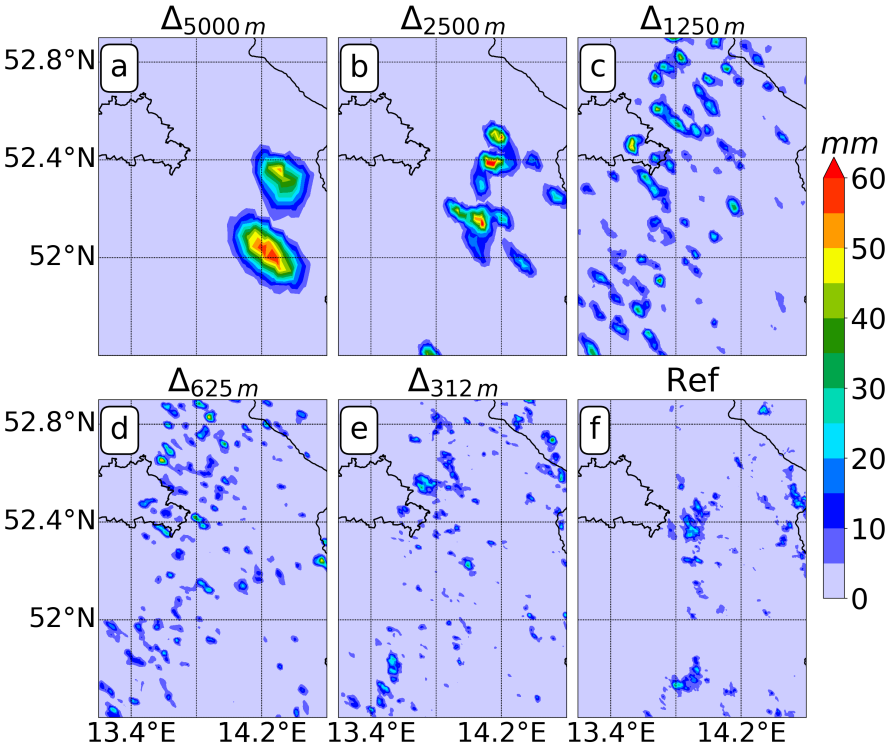

Figure 6.3.: Total accumulated precipitation patterns (colour coded) across the six model grid spacings ($\Delta_{5000\,m}$, $\Delta_{2500\,m}$, $\Delta_{1250\,m}$, $\Delta_{625\,m}$, $\Delta_{312\,m}$ and $\Delta_{156\,m}$) at 2000 UTC over A1, case: 26 July 2012

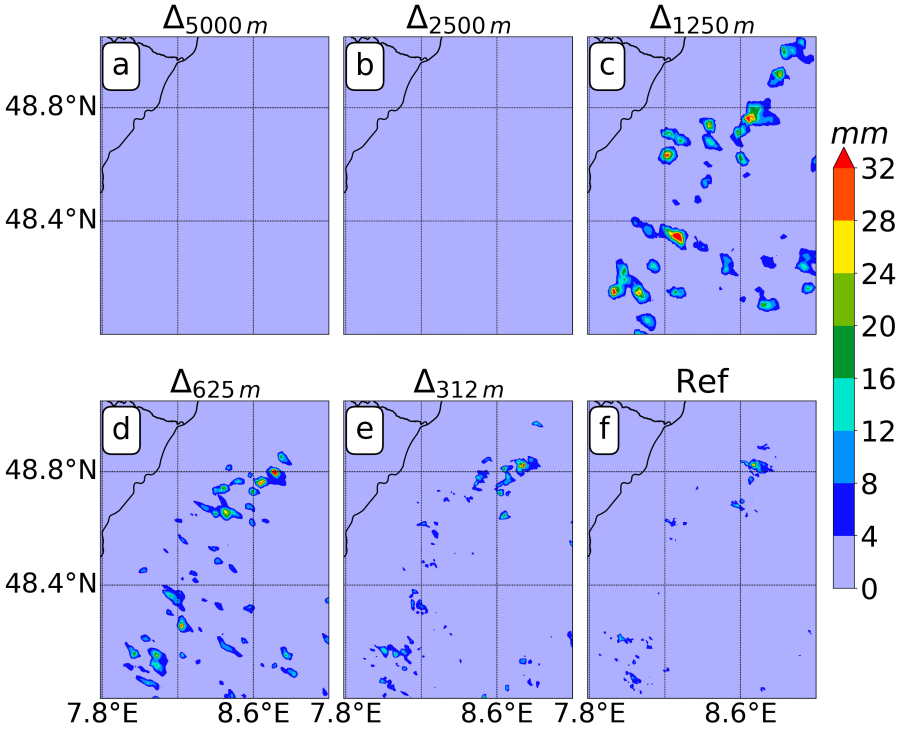

Figure 6.4.: Same as Figure 6.3 but over A3, case: 12 Aug 2015

Thus, a different treatment of turbulence closure can even lead to a no-precipitation situation. The restriction to vertical turbulent exchange and an assumption of the negligible contributions of a horizontal component leads to different forcing of convection. This assumption is strongly violated in complex terrain where 3D effects are important, for example, the advection and the horizontal shear production, act as source terms of TKE (Arnold et al., 2012), make the turbulence parameterization even a more sensitive parameter to choose (Honnert and Masson, 2014; Couvreux et al., 2016; Rotach et al., 2017).
As obvious from Figures 6.3 and 6.4, there are considerable differences between the precipitation patterns at the transition from grid spacing $\Delta_{1250\,m}$ to $\Delta_{2500\,m}$. Although focusing on the sensitivity of convective precipitation to model grid spacing and land-surface resolution, it is worthwhile to know the impact of the different turbulence parameterization schemes (here, NWP and LES) on the precipitation. Therefore, to segregate the impact of model grid spacing and the transition of turbulence parameterizations sensitivity simulations at $\Delta_{1250\,m}$ for the case over A1 (26 July 2012) are performed using the same model setup. However, applying the two turbulence parameterization schemes. Figure 6.5 shows the spatial patterns of precipitation at $\Delta_{1250\,m}$ model grid spacing under two different turbulence parameterizations. $\Delta_{1250\,m}$ -NWP produces intenser and bigger precipitating cells than the smaller and scattered cells of $\Delta_{1250\,m}$ -LES. The results of these sensitivity simulations indicate that the differences between the precipitation patterns in $\Delta_{1250\,m}$ to $\Delta_{2500\,m}$ (Figure 6.3) are a combined effect of the change of grid spacing and the turbulence parameterization alike. In the following, therefore, focus more on the comparison between the simulations from $\Delta_{156\,m}$ to $\Delta_{1250\,m}$.

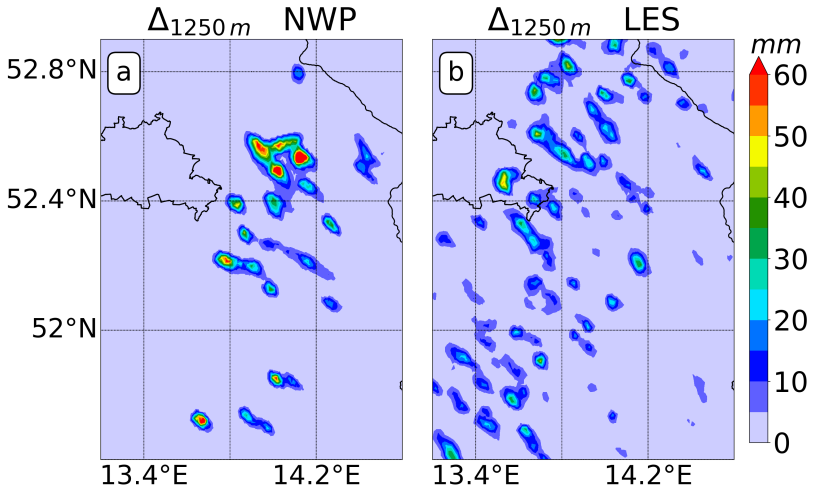

Figure 6.5.: Total accumulated precipitation (colour coded) for $\Delta_{1250\,m}$ in NWP (a) and LES (b) turbulence parameterization schemes at 2000 UTC over A1, case: 26 July 2012.

Diurnal cycle of areal mean accumulated precipitation amount in control runs

The diurnal cycle of areal mean precipitation calculated in the six model grid spacings is investigated. Figure 6.6 is a typical example of the time evolution of the area-averaged accumulated precipitation for a case simulated over A1 (26 July 2012). The precipitation in the reference run starts at 1410 UTC and ends at 1820 UTC resulting in a total of 0.82 mm precipitation. However, the onset of precipitation in $\Delta_{1250\,m}$ is already at 1130 UTC and it ends at 1630 UTC with the mean precipitation of 2.26 mm. That means in $\Delta_{1250\,m}$ the onset of precipitation is nearly two hours earlier and the duration of precipitation is one hour longer than in $\Delta_{156\,m}$. Across the LES model grid spacings, the accumulated mean precipitation amount increases with increasing model grid spacing. Including the diurnal cycles of the precipitation of the other cases and areas (Figure B.9, B.10, B.11, B.12, B.13), a consistent model behaviour exists which says that the onset of areal mean precipitation is earlier in $\Delta_{1250\,m}$ by ≈1-2 hours in comparison to $\Delta_{156\,m}$. It is also shown in Figure 6.6 that the mean precipitation in NWP ($\Delta_{5000\,m}$) is being delayed by almost 1.5 hours as compared to LES ($\Delta_{156\,m}$) model grid spacing. This is found as a consistent behaviour in other cases, where NWP ($\Delta_{5000\,m}$) precipitation occur-

rence is by 1-2 hours later (or even does not occur at all, Figure 6.4) than in LES (Δ_{156m}) (Figure B.9, B.10, B.11, B.12, B.13).

The difference in onset of precipitation between the two turbulence closures is in agreement with the recent simulations done for $\Delta_{x,y}$ = 25 m to 1000 m in Chow et al. (2019).

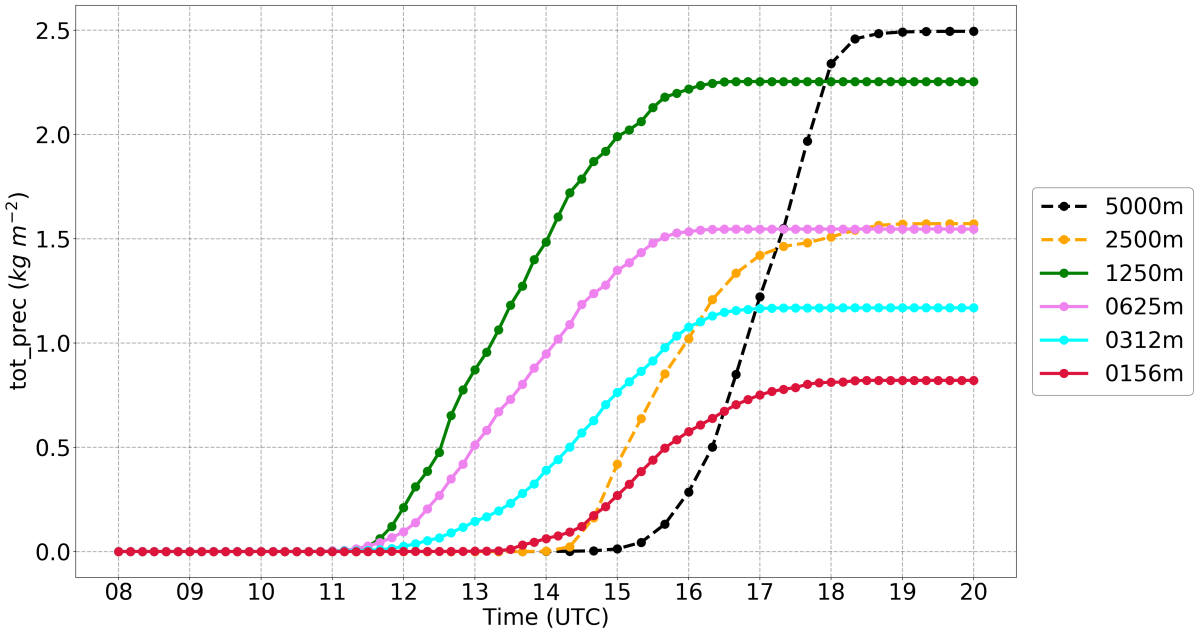

Figure 6.6.: Time series of total accumulated precipitation for NWP (Δ_{5000m}, Δ_{2500m}), dashed-lines, and LES model grid spacings(Δ_{1250m}, Δ_{625m}, Δ_{312m}, Δ_{156m}), solid-lines, over A1, case: 26 July 2012

Spatial pattern of daily accumulated precipitation in land-surface sensitivity runs

To address the impact of land-surface modification on convective precipitation, the numerical simulations have been performed by using the coarser resolution of land-surface properties altogether (LO_5000 m, LO_1250 m) but refined model grid spacing from Δ_{5000m} to Δ_{156m} for all the six cases. See Section 5.5 for details of the simulations strategy. Additionally, the L_5000 m, L_1250 m, O_5000 m, O_1250 m runs have been performed only for the cases over A2 and A3 to understand the relatively dominant sensitivity of convective precipitation to the modification of land surface properties (L) and orography (O). Figure 6.7 is an

example showing the composites of accumulated precipitation at 2000 UTC from the land-surface sensitivity simulations performed over A1 on 26 July 2012. The spatial distribution of the precipitation patterns is similar in the three runs except for the clustered precipitating cell in the east of Berlin, which is relatively bigger in size than the one in the reference run. Similarly, the other simulations with modified land-surface (L) and orography (O) separately from 156 m to 1250 m (L_1250 m, O_1250 m) and 5000 m (L_5000 m, O_5000 m) result into similar precipitation patterns as in the reference runs (Figure B.14, B.15).

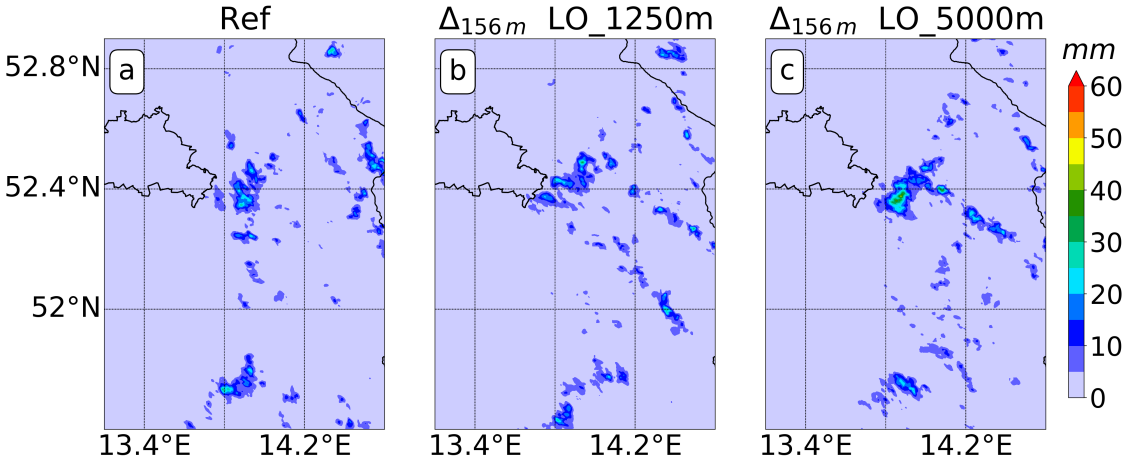

Figure 6.7.: Total accumulated precipitation from reference run ($\Delta_{156\,m}$- control run) (a), $\Delta_{156\,m}$- LO_1250 m run (b) and $\Delta_{156\,m}$-LO_5000 m run (c) at 2000 UTC over A1, case: 26 July 2012.

Diurnal cycle of areal mean accumulated precipitation amount in land-surface sensitivity runs

The impact of the coarsening of land-surface resolution on the diurnal cycle of precipitation is given in Figure 6.8, which shows the time-evolution of areal mean total precipitation calculated in the above sensitivity simulations for the same case over A1 (Figure 6.7). The modulation in land-surface resolution over the scale of 1250 m and 5000 m has almost negligible impact on the onset and duration of precipitation. However, the accumulated mean precipitation amount, in this case, is increasing with coarsening of land-surface resolution. The findings that

the onset and duration of mean precipitation is unaffected by the modification of land-surface resolution also holds for the other cases (Figure B.16, B.17).

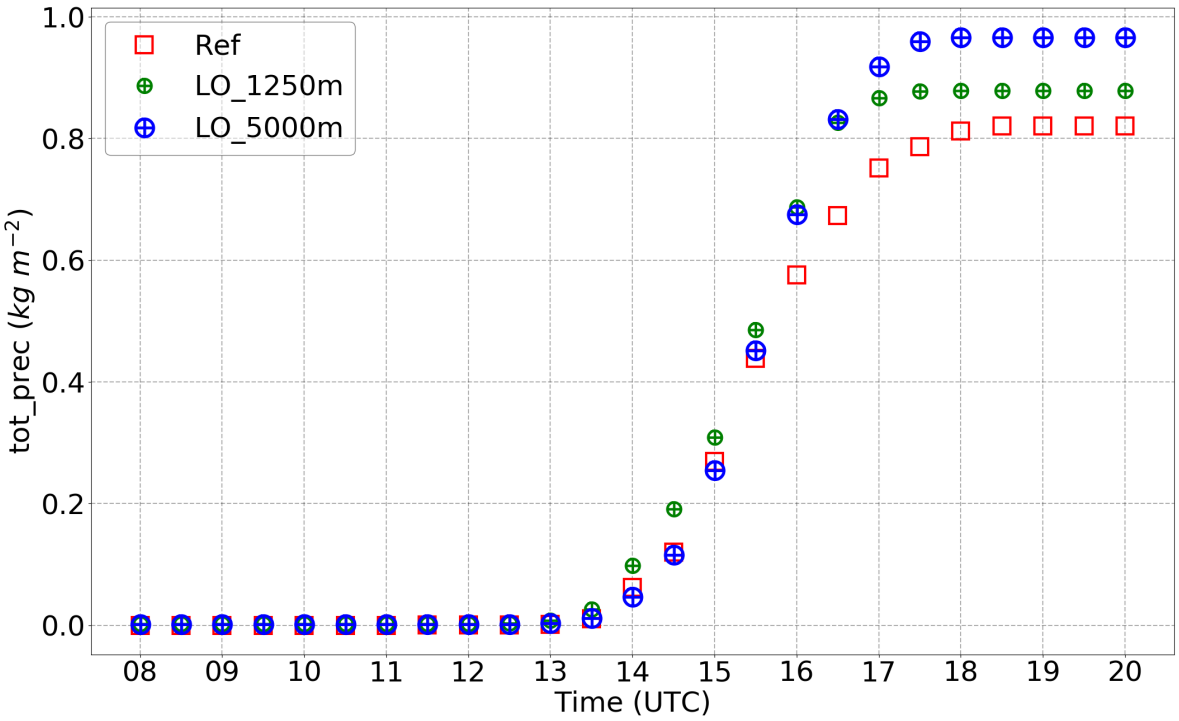

Figure 6.8.: Time series of total accumulated precipitation from reference run (red square markers), Δ_{156m}- LO_1250 m run (green coloured and smaller $\oplus$) and Δ_{156m}- LO_5000 m run (blue coloured and bigger $\oplus$) at 2000 UTC over A1, case: 26 July 2012.

Area-averaged daily accumulated precipitation amount

The overview of the precipitation derived from the simulations with different model grid spacing for all the cases is shown in Figure 6.9a. It shows the Relative Percentage Difference (RPD) of areal mean daily accumulated precipitation with respect to the corresponding reference run (Δ_{156m}- control run of the given case) for the set of LES model grid spacings (Δ_h). The areal mean daily accumulated precipitation amount of the reference runs of the different cases is listed in Table 6.1. In Figure 6.9a, the RPD of areal mean daily accumulated precipitation is consistently decreasing with finer model grid spacing (Δ_{1250m}, Δ_{625m}, Δ_{312m}, Δ_{156m}) except in A2-case: 17 Sept 2017 and A3-case: 29 May 2017 where

Δ_{156m} runs produce slightly higher or similar precipitation as in the other grid spacings. This is mainly caused by more intense precipitating cells in Δ_{156m} compared to Δ_{312m} (Figure B.5, B.8). Positive (negative) RPD values mean that the mean precipitation at the given grid spacing is above (below) the reference run of the individual cases. The variability of the areal mean precipitation in Δ_{1250m} relative to the reference run is in the range of -26 to 400 % with the third quartile (75th percentile), Q3, of 155 % (Figure 6.9a).
Furthermore, the mean precipitation amount caused by land-surface resolution is smoothed down from 156 m to 1250 m results in the RPD ranging from -17% to 37 % with the Q3 of $\approx$ 7% while the range increases to -17 to 49 % and Q3 to 22 %) when the land-surface resolution is smoothed down from 156 m to 5000 m. Therefore, depending upon the cases, the change in model grid spacing (from Δ_{1250m} to Δ_{156m}) leads to a larger variability ($\approx$ 155%) in the areal mean precipitation amount than that caused by the land-surface modification ($\approx$ 7-22%). This

Areas	Cases	Daily accumulated mean precipitation from reference run (Δ_{156m}-control run) (in mm)
A1	26 July 2012	0.82
	17 Sept 2017	1.20
A2	09 June 2018	0.91
	17 Sept 2017	3.08
A3	12 Aug 2015	0.23
	29 May 2017	2.03

Table 6.1.: The areal mean daily accumulated precipitation amount in the reference runs of different cases.

offset in model behaviour gives a hint that there is a lack of convergence in simulated mean precipitation or even the cloud system properties at least for model grid spacing $\geq\Delta_{156m}$. Bryan et al. (2003) has looked into the appropriate model resolution necessary for the simulation of deep moist convection. They analysed the squall lines simulated with grid spacings between 1 km and 125 m. The results

show that there are no systematic trends in the fields like vertical velocity and rainwater as the model resolution is increasing, and also the convergence behaviour of simulated squall line is still missing between 250- and 125-m grid spacings. This section answers the first key question of the thesis, which investigates the relative impact of model grid spacings and land-surface resolution on convective precipitation. The results reveal that the onset of areal mean precipitation is later in Δ_{156m} than that in Δ_{1250m} (Figure 6.6). Also, in LES model grid spacings (Δ_{1250m} to Δ_{156m}) areal mean daily accumulated precipitation amount is highly sensitive to the model grid spacing and shows a stronger variability ($\approx$155 %) (Figure 6.9a) in comparison with the modifications of land-surface resolution, where the variability is significantly smaller ($\approx$7-22 %) (Figure 6.9b). This finding raises further questions:

I. Why the onset and areal mean precipitation amount differ across LES model grid spacings? What are the processes explaining these differences?

II. What are the most relevant factors resulting in the different areal mean precipitation amount?

III. What causes the varying precipitation patterns in LES grid spacings?

The above questions I and II are elaborately discussed in the Section 6.3. To understand the varying precipitation patterns (Question III), the resolved triggering mechanisms by the given LES control runs are investigated in detail in Chapter 7.

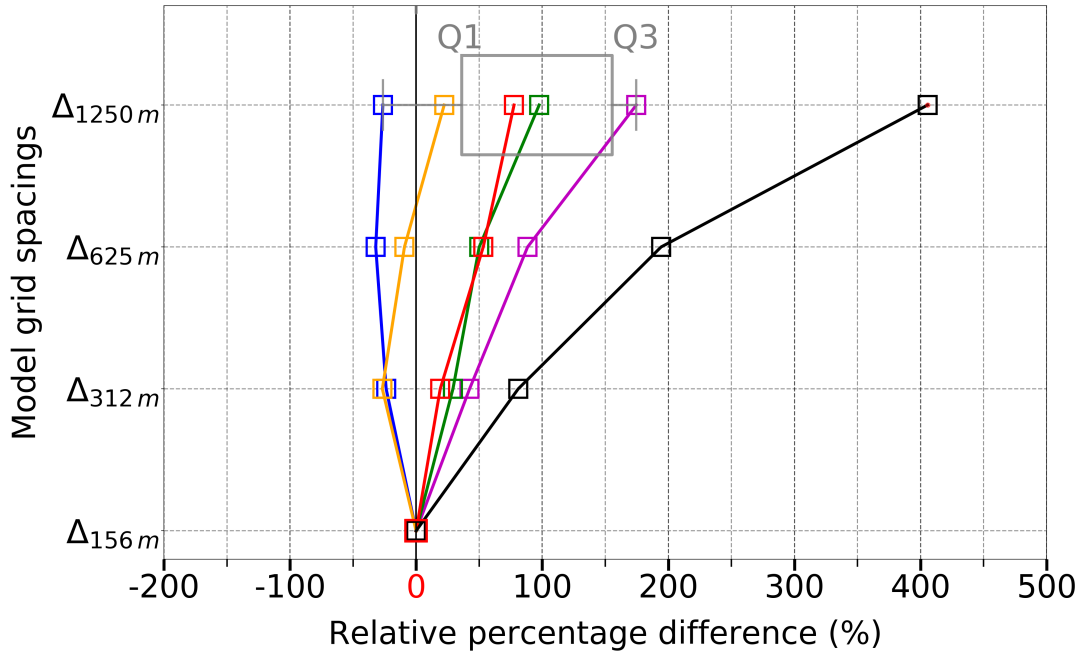

(a)

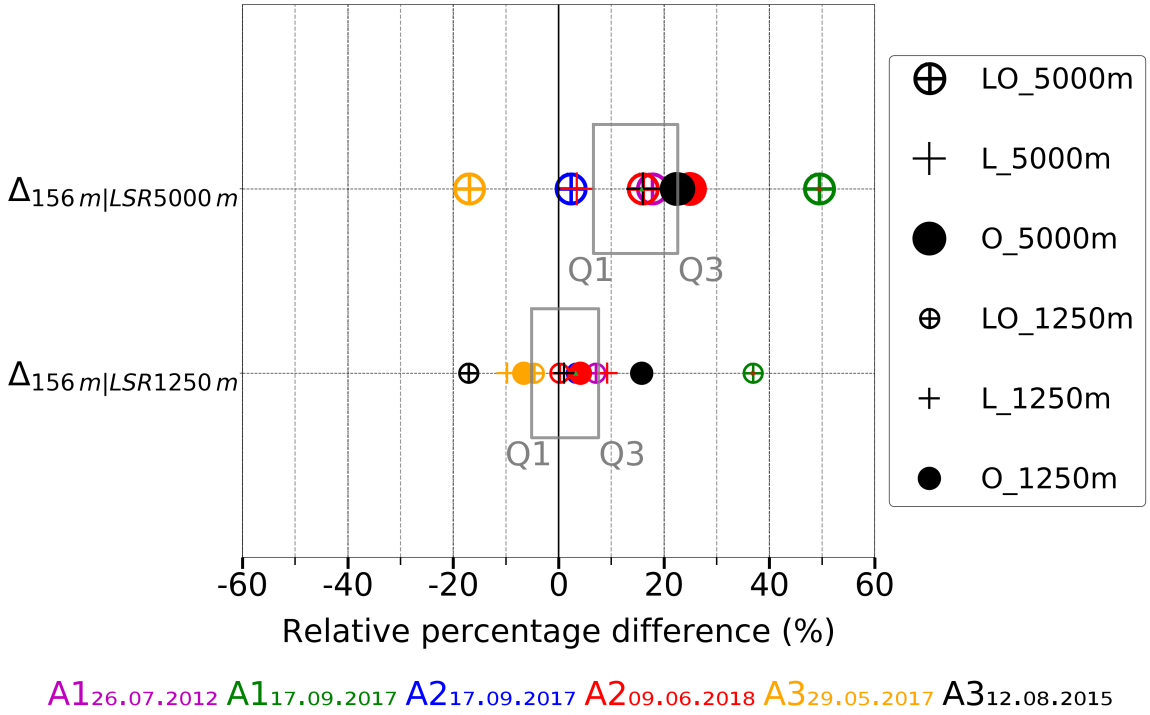

(b)

Figure 6.9.: RPD of areal mean daily total accumulated precipitation amount across LES model grid spacings ($\Delta_{1250\,m}$, $\Delta_{625\,m}$, $\Delta_{312\,m}$, $\Delta_{156\,m}$) of the control runs (□) (a) and in $\Delta_{156\,m}$ of LO_1250 m run (⊕), L_1250 m run (+), O_1250 m run (●), LO_5000 m run (⊕), L_5000 m run (+), and O_5000 m run (○) (b) for the six simulated cases. Q1 and Q3 represent the first (25th) and third quartiles (75th percentiles).

6.3. Possible processes which lead to differences in precipitation: Clouds

This section describes the possible processes resulting in an overall variability of ≈155 % in the mean precipitation amount between the two model grid spacings in LES: Δ_{1250m} and Δ_{156m}. The processes are discussed for the case simulated over A1, dated 26 July 2012, as this day has a considerable variability in the order of ≈175 % in the areal mean precipitation amount between Δ_{1250m}- and Δ_{156m} control runs (Figure 6.9a). Figures 6.10a and 6.10b show the time-height cross section of area-averaged cloud liquid water content and the time series of areal mean precipitation amount in Δ_{156m} and Δ_{1250m}, respectively. The spatially-averaged vertical velocity variance ($\overline{w'^2}$) represents the resolved turbulence activity at a given model grid spacing (Δ_h). The Lifting Condensation Level (LCL) is based on the difference between the 2-m temperature and dew-point temperature, and applying the formula from Iribarne and Godson (2012).
In Δ_{156m}, the resolved vertical velocity variance (turbulence) ($\overline{w'^2}$) within the CBL starts from ≈ 0900 UTC followed by the first cloud formation in the CBL at ≈ 1000 UTC and the precipitation occurrence at 1410 UTC. Moreover, in Δ_{1250m}, the resolved turbulence is detected at 1110 UTC, the first cloud formation at 1000 UTC, and the precipitation at 1140 UTC. That means the resolved CBL convection is earlier in Δ_{156m} in comparison to Δ_{1250m}. Although, both of the grid spacings generate CBL clouds (Figures 6.10a and 6.10b) which trigger at the similar time, the mean precipitation is delayed by 2 hours in Δ_{156m} in comparison to Δ_{1250m}.
In the steps of investigating the questions (I and II) of the Section 6.2, the diurnal cycle of the cloud evolution has been analysed during its three main phases. Based on the cloud evolution in Δ_{156m} (Figure 6.10a) the classified phases are:

a. Environment of CI / CBL processes

b. Cloud evolution

c. Precipitation

a. Environment of CI / CBL processes

Δ_{156m} indicates that considerable resolved turbulence ($\overline{w'^2}$) in the CBL already exists at 1000 UTC (Figure 6.11). This has an impact on the turbulent transport of heat and moisture in the CBL. For example, at 1000 UTC the turbulent transport of heat in the lowest 100 m, i.e. in the surface layer, is mainly handled by the parametrized (subgrid-scale) turbulent sensible heat flux (Figure 6.12). However, above the surface layer the turbulent transport of heat is taken over by the resolved (grid-scale) sensible heat flux. The formulation for the resolved (grid-scale) and parametrized (subgrid-scale) fluxes, respectively are given in Appendix B.2. The effective mixing by resolved convective cells in the CBL results in the development of typical CBL profiles of θ_v and q_v (Figure 6.13a and b). That means the cloud-topped CBL consists of an unstable surface layer and a well-mixed layer above.

In Δ_{1250m}, throughout the CBL there is no considerable resolved convection simulated at 1000 UTC (Figure 6.11), so that the turbulent mixing of heat and moisture must be done by the parametrized turbulent heat fluxes. This is obvious in the sensible heat transport in Δ_{1250m} (Figure 6.12). The contribution by the resolved sensible heat flux is minimal. That means the partitioning of the total turbulent fluxes into resolved and parametrized flux contributions is completely different in Δ_{156m} and Δ_{1250m}. This also has a strong impact on the resulting profiles of θ_v and q_v (Figure 6.13a and b). On the one hand, the near-surface temperature, as well as the humidity, are higher in Δ_{1250m} compared to Δ_{156m}. On the other hand, the resolved convection in Δ_{156m} results in deeper and more homogeneous mixing than in Δ_{1250m} with parametrized turbulence (Figure 6.13b), where the mixed layer is still slightly unstable stratified at 1000 UTC (Figure 6.13a). These differences also have considerable consequences for the pre-convective conditions in the two grid spacings, as demonstrated later in this section. To understand the reasons for the different evolution of the environments for CI and intensification, the areal mean budget terms of heat (θ_v) and moisture (q_v) are calculated. The budget terms evaluate the contribution of each component (for example heat advection, phase change, radiative cooling etc.) in the prognostic equations such as the conservation of heat (θ_v) and moisture (q_v). The detailed budget components and their formulation are discussed in Appendix B. Figure 6.14 shows the vertical profile of the different components of area-averaged heat and moisture budget in

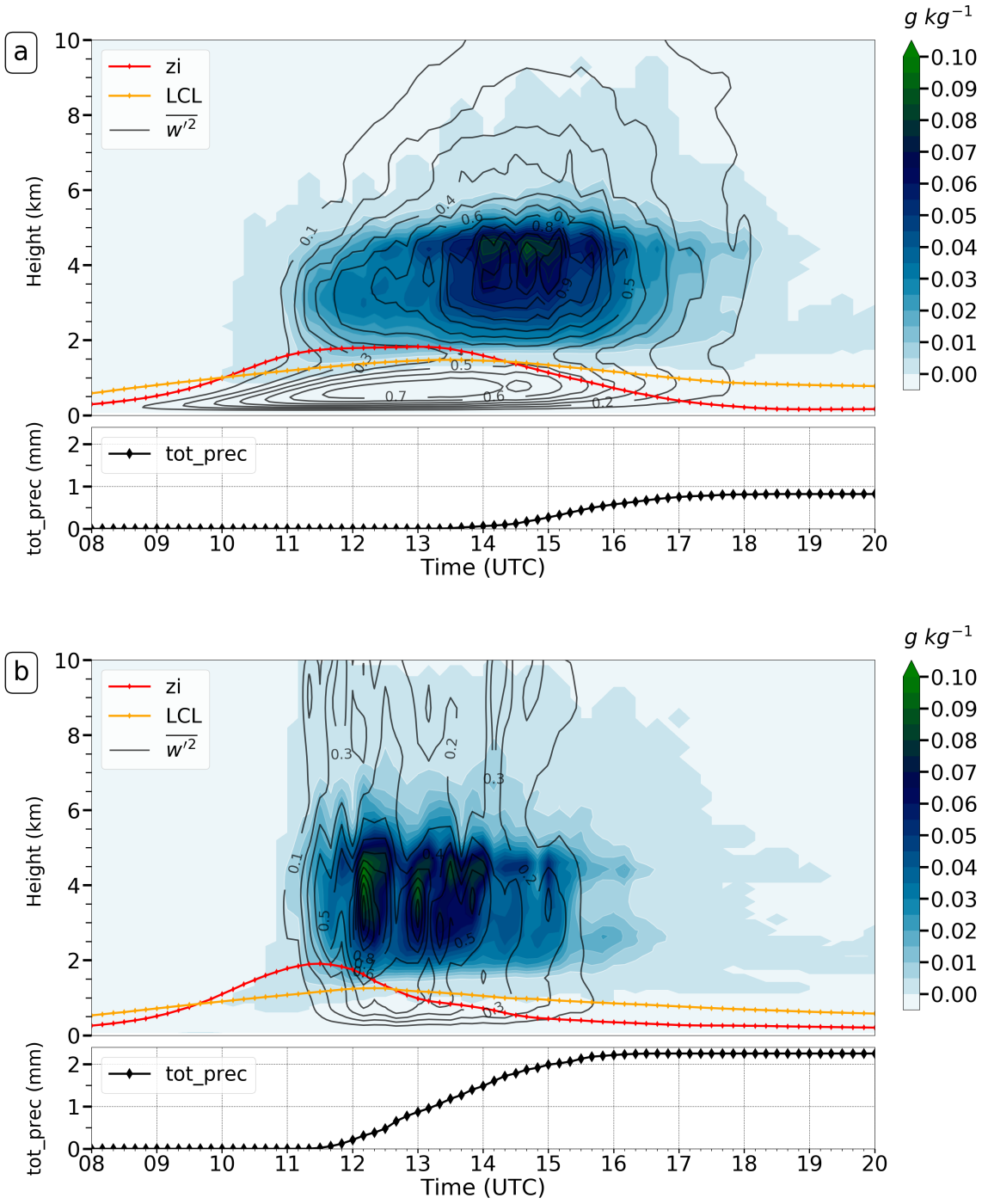

Figure 6.10.: Time-height cross section of cloud liquid water content (colour coded) in Δ_{156m} (a) and Δ_{1250m} (b) -control runs for case over A1, dated 26 July 2012. The red and orange curves are areal mean CBL height (zi) and LCL, respectively. The black isolines indicate the spatially-averaged vertical velocity variance ($\overline{w'^2}$). The black solid line with diamonds in the bottom row indicates accumulated area-averaged precipitation (tot_prec).

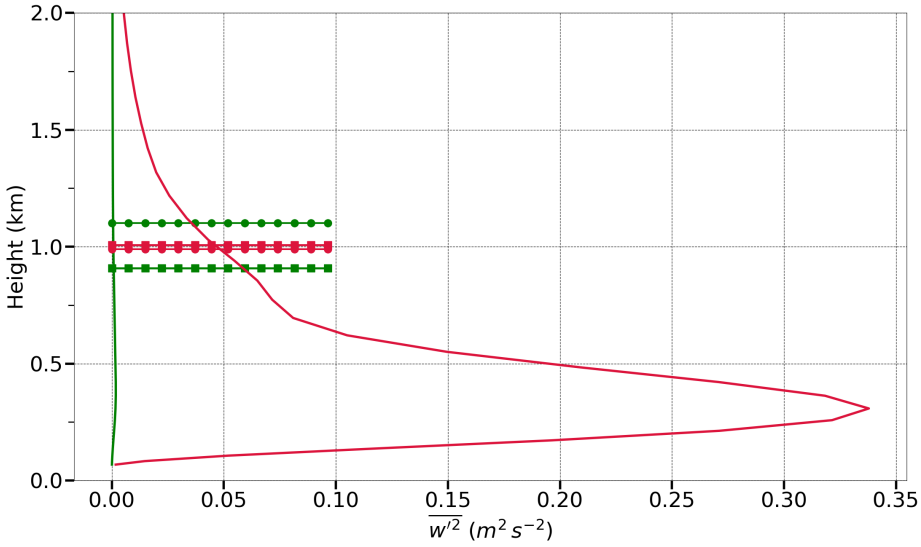

Figure 6.11.: CBL profiles of spatially-averaged vertical velocity variance ($\overline{w'^2}$) at 1000 UTC in Δ_{156m} (red) and Δ_{1250m} (green) of case over A1, dated 26 July 2012. The horizontal lines with square and circle markers denote LCL and areal mean CBL height (zi), respectively.

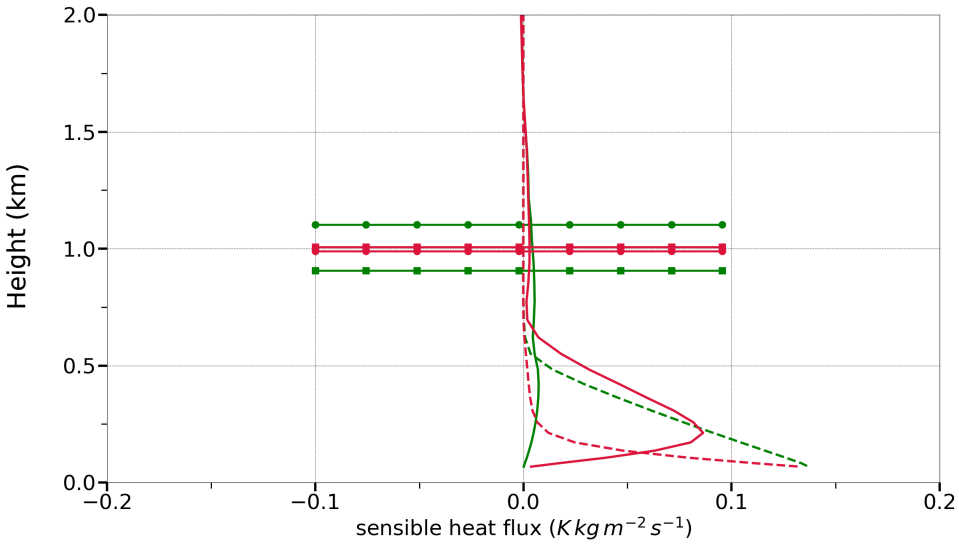

Figure 6.12.: Vertical profiles of areal mean mass-weighted grid-scale (solid line) and subgrid-scale sensible heat fluxes (dashed line) at 1000 UTC in Δ_{156m} (red) and Δ_{1250m} (green) for case simulated over A1, dated 26 July 2012. The horizontal lines with circle and square markers denote the areal mean CBL height (zi) and LCL, respectively.

the CBL at 1000 UTC for Δ_{156m}. The SUM_{θ_v} (SUM_{qv}) represents the net heating (moistening) rate. The $MICR_{\theta_v}$ ($MICR_{qv}$) represents the contribution of micro-

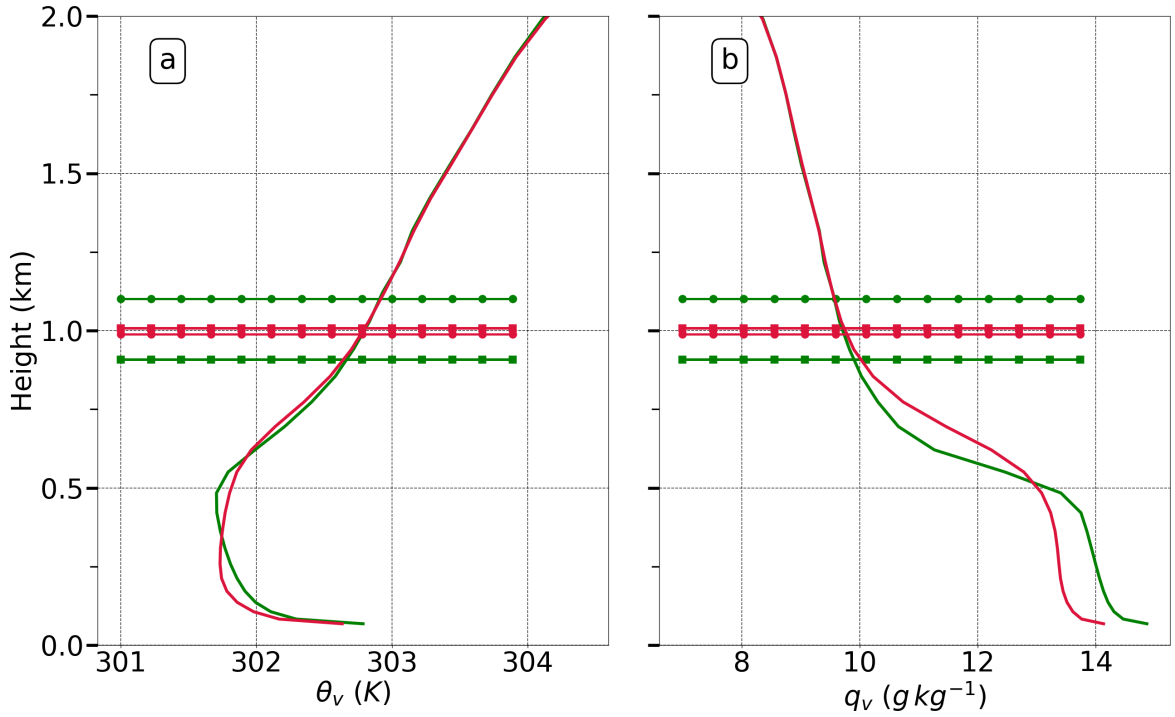

Figure 6.13.: Vertical profiles of areal mean virtual potential temperature (θ_v) (a) and specific humidity (q_v) (b) in Δ_{1250m} (green curve) and Δ_{156m} (red curve) at 1000 UTC for case simulated over A1, dated 26 July 2012. The horizontal lines with circle and square markers denote the areal mean CBL height (zi) and LCL, respectively.

physics to the net temperature (moisture) tendency, in other words, it is the net body source terms associated with the phase changes. The $TURB_{\theta_v}$ ($TURB_{qv}$), represents the divergence of turbulent heat (moisture) flux, which describes the contribution of the parametrized turbulence to the net heating (moistening) rate. The ADV_{θ_v} (ADV_{qv}) shows the advection of temperature (moisture) by the mean wind. The other component is the net radiation RAD_{θ_v} (shown here as the sum of short-wave cooling, $RADSW_{\theta_v}$, and long-wave warming, $RADLW_{\theta_v}$) tendency terms.

In Δ_{156m} at 1000 UTC, the profile of the net temperature tendency, SUM_{θ_v}, can be separated into two distinct layers (Figure 6.14a). A nearly constant net heating of 1 $K\,h^{-1}$ can be found in the lowest 450 m while net cooling of up to 0.5 $K\,h^{-1}$ occurs between approximately 600 and 1000 m. This SUM_{θ_v} profile in the CBL mainly results from three heat budget components: turbulent flux divergence, $TURB_{\theta_v}$, radiation flux divergence, RAD_{θ_v}, and advection of heat, ADV_{θ_v}.

The $TURB_{\theta_v}$ contributes to the net heating in the lowest 250 m only, reaching up to 4.5 $K\,h^{-1}$ close to the ground. The contribution by RAD_{θ_v} to net heating is mainly confined to the lowest 200 m. The ADV_{θ_v} contributes to the net heating in three different ways: cooling in the lowest 250 m, warming between 250 m and 600 m, and cooling between 600 m and 1000 m.
Concerning the net moisture budget, two layers can be distinguished, a layer with net drying of up to -0.5 $g\,kg^{-1}\,h^{-1}$ below 500 m, while moistening of up to 2.3 $g\,kg^{-1}\,h^{-1}$ occurs between 500 m and 1000 m (Figure 6.14b). Two processes contribute to this net moisture tendency, turbulent transport of moisture, $TURB_{q_v}$, causes moistening in the lowest 250 m while ADV_{q_v} leads to drying (up to 3 $g\,kg^{-1}\,h^{-1}$) below 500 m and the moistening above.
It is clearly seen that $TURB_{\theta_v}$ ($TURB_{q_v}$) and ADV_{θ_v} (ADV_{q_v}) are the two dominant components contributing to the SUM_{θ_v} (SUM_{q_v}). Further, the role of the areal mean ADV_{θ_v} term is investigated in more detail for both the temperature and moisture budget. ADV_{θ_v} is the sum of horizontal ($HADV_{\theta_v}$) and vertical advection ($ZADV_{\theta_v}$). $ZADV_{\theta_v}$ can be decomposed into an areal mean flux and mean grid-scale turbulent (resolved) flux (for details of their formulations see Appendix B). To determine the contribution of this areal mean grid-scale sensible heat flux convergence ($-\frac{\partial \overline{w'\theta_v'}}{\partial z}$) to the ADV_{θ_v}, the amount was calculated using the model output fields. Figure 6.15 shows the areal mean heat advection, ADV_{θ_v}, and the convergence of the vertical grid-scale sensible heat flux for $\Delta_{156\,m}$ at 1000 UTC. As evident, the convergence of the vertical grid-scale sensible heat flux corresponds mainly to the profile of the mean advection of heat. The same finding holds for the convergence of the vertical grid scale latent heat flux and mean advection of moisture (not shown). That means the resolved convective cells transport heat and moisture from the lower layers (below 250 m) to upper layers (Figure 6.14a,b), resulting in the well-mixed layer shown in Figure 6.13a and b. Two other things are worth to be mentioned, too. First, the layer with negative net temperature tendency and positive net moisture tendency between 600 and 1000 m indicates the growth section of the CBL (Figure 6.14a,b). Second, as a consequence of this CBL growth, the areal mean CBL top reaches the areal mean LCL at around 1000 UTC so that the CBL clouds could develop in the investigation area.
The vertical profiles of area-averaged heat and moisture budget terms in $\Delta_{1250\,m}$ at 1000 UTC are shown in Figure 6.16. The overall behaviour of the net temperature

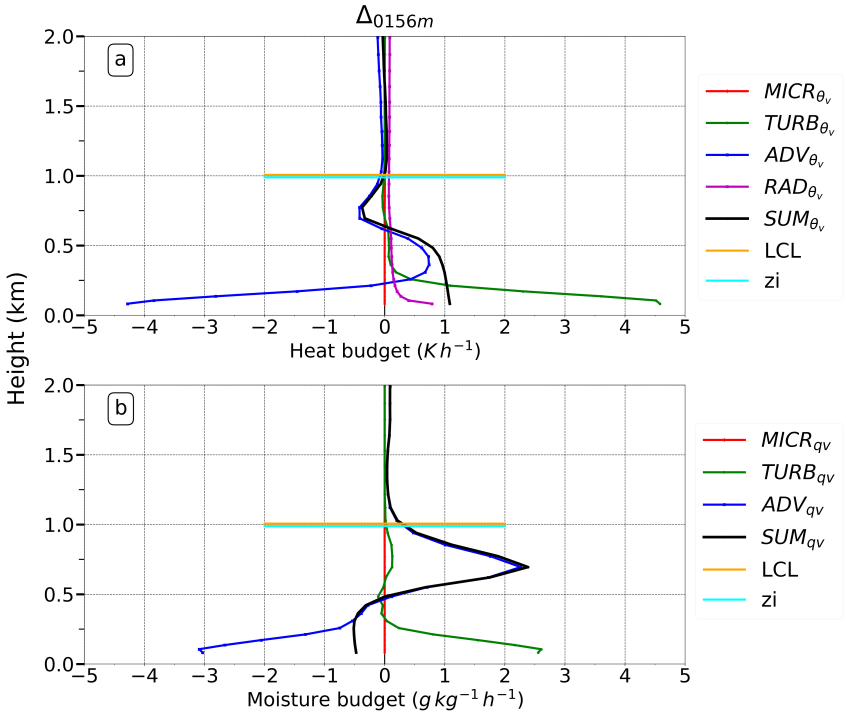

Figure 6.14.: Vertical profile of areal mean heat (a) and moisture (b) budget terms within the CBL in Δ_{156m} at 1000 UTC for case over A1, dated 26 July 2012. The horizontal line in orange and cyan color shows the LCL and mean CBL height (zi), respectively.

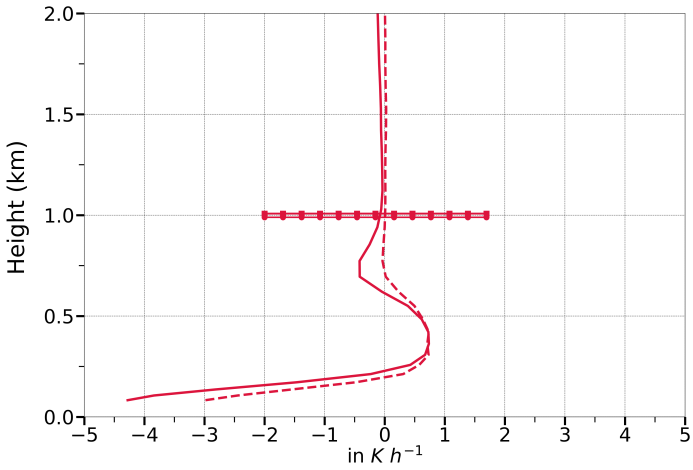

Figure 6.15.: Vertical profile of areal mean total heat advection (solid) and grid scale vertical sensible heat flux convergence (dashed) at 1000 UTC in Δ_{156m} of case over A1, dated 26 July 2012. The horizontal lines with circle and square markers denote the areal mean CBL height (zi) and LCL, respectively.

and moisture tendency is similar to that in Δ_{156m}. The contribution by radiative heating to the net temperature tendency is again mainly restricted to the lowest

200 m. In contrast to Δ_{156m} however, $TURB_{\theta_v}$ and $TURB_{q_v}$ dominate the temperature and moisture tendencies, respectively. That means parametrized turbulence is responsible for mixing processes in the developing CBL and grid-scale flux convergence is of minor relevance. This is also documented in Figure 6.17, where $\frac{\partial \overline{w'\theta_v'}}{\partial z}$ and ADV_{θ_v} are compared. Finally, in Δ_{1250m} the mean CBL depth exceeds the areal mean LCL so that boundary layer clouds could develop at this time. The CBL clouds, which occur in Δ_{156m} and Δ_{1250m} at around 1000 UTC developed differently in the following hours (Figure 6.10a and 6.10b). The reasons for that are investigated in the next section.

As outlined in the previous discussion, the partitioning of total turbulent heat and moisture fluxes into resolved and parameterized fluxes results in warmer and moister conditions in the lowest 500 m in Δ_{1250m} than Δ_{156m} (Figure 6.13). This affects the potential energy of the air parcels. Figure 6.18 shows the time evolution of area-averaged Convective Available Potential Energy of mean surface layer parcel (MLCAPE) and Convective Inhibition of mean surface layer parcel (MLCIN) for the same case as before. The MLCAPE and MLCIN use the thermodynamical properties (mean temperature and humidity) of the representative shallow surface layer (50 hPa $\approx$ 500 m). Δ_{1250m} calculates the maximum areal mean MLCAPE in the order of $\approx$1350 $J\,kg^{-1}$ at 1010 UTC and the minimum areal mean MLCIN in the order of $\approx$1 $J\,kg^{-1}$ at 1110 UTC. In Δ_{1250m} the MLCAPE removal occurs as soon as the air parcels overcome the associated MLCIN. Furthermore, Δ_{156m} calculates the maximum areal mean MLCAPE of $\approx$1000 $J\,kg^{-1}$ at 0950 UTC and the minimum MLCIN in the order of $\approx$2 $J\,kg^{-1}$ at 1300 UTC.

Higher MLCAPE ($\approx$1350 $J\,kg^{-1}$) in Δ_{1250m} together with similar MLCIN ($\approx$1 $J\,kg^{-1}$) anticipates a higher potential to trigger deep convective systems than in Δ_{156m} with relatively lower MLCAPE ($\approx$1000 $J\,kg^{-1}$). This could be one factor explaining higher amount of precipitation in Δ_{1250m} than in Δ_{156m} (Emanuel, 1994).

Interestingly, the MLCAPE removal in Δ_{156m} already starts at 0950 UTC while the MLCIN is yet not overcome and before the precipitation could cause a reduction of MLCAPE (first precipitation occurs later at 1410 UTC). The MLCAPE removal can be explained by analysing the MLCAPE behaviour at two times, (i) when peaks to the maximum value $\approx$1000 $J\,kg^{-1}$ (at 0950 UTC) and (ii) at 1200 UTC when it is reduced down to $\approx$705 $J\,kg^{-1}$. Figure 6.19 shows the vertical

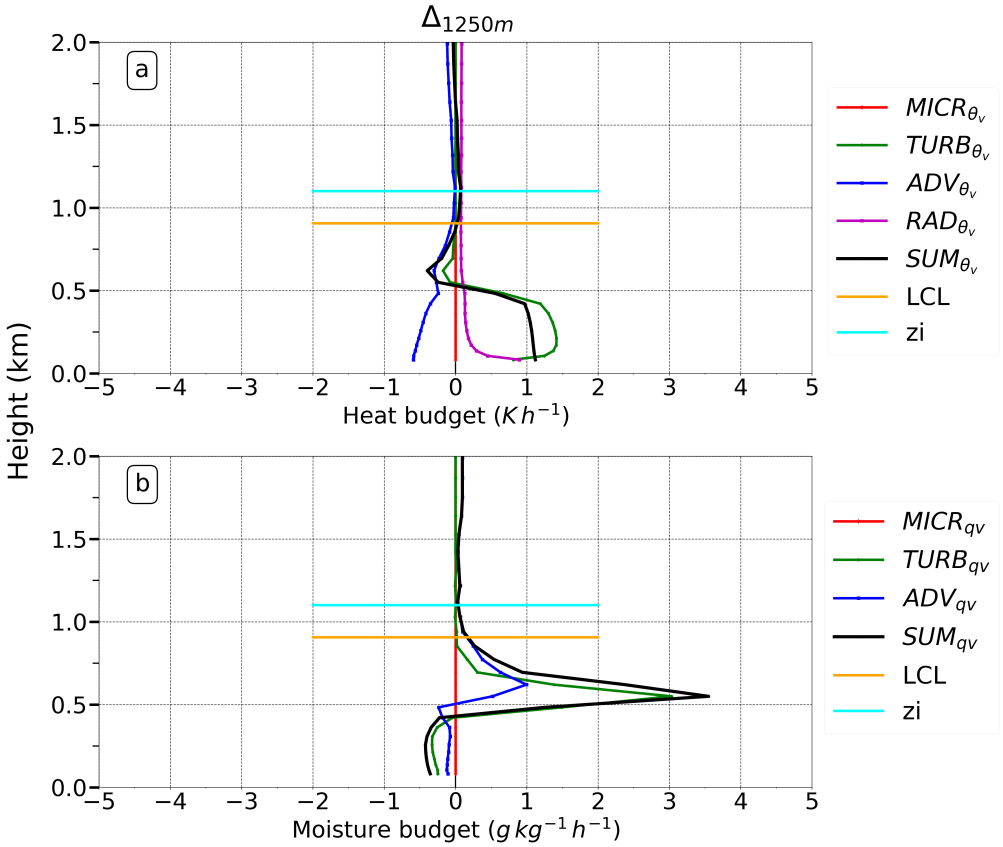

Figure 6.16.: Same as Figure 6.14 but in Δ_{1250m}

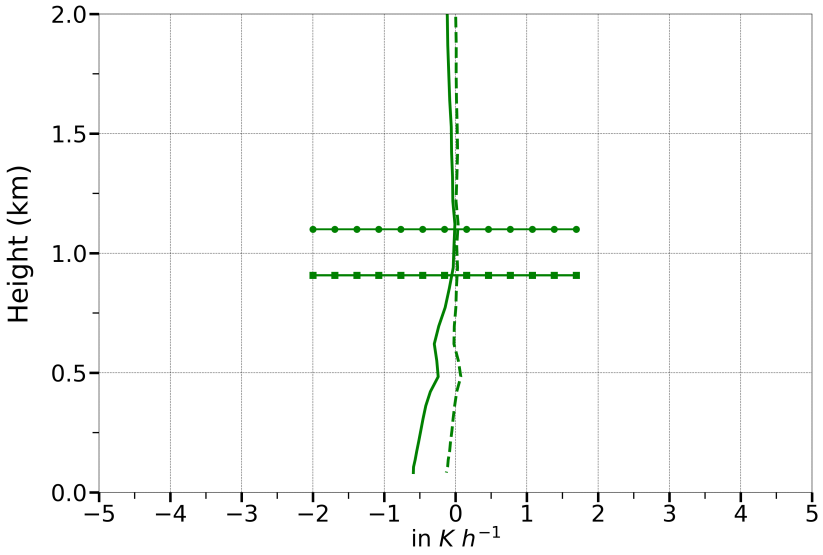

Figure 6.17.: Same as Figure 6.15 but in Δ_{1250m}

profiles of specific humidity (q_v) within the CBL at 0950 UTC and 1200 UTC. At 1200 UTC the lowest ≈500 m of the CBL is drier than at 0950 UTC which

attributes to a drop in dew-point temperature. This breaches the resultant Level of Free Convection (LFC) and the rise in the LFC results into a lower MLCAPE at 1200 UTC. That means the strong the CBL growth with deeper mixing of moisture between 0950 UTC and 1200 UTC is the major factor for the removal of MLCAPE already before the precipitation occurrence.

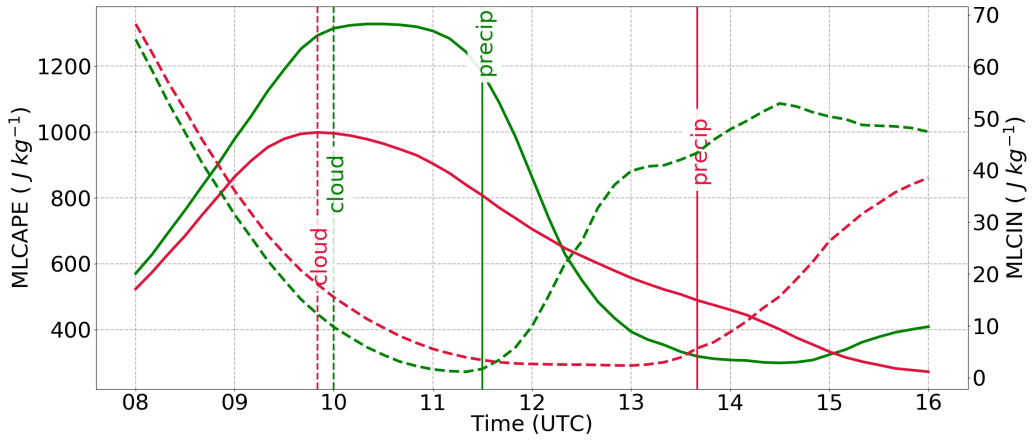

Figure 6.18.: Time-series of areal mean MLCAPE for Δ_{1250m} (solid green) and Δ_{156m} (solid red) and MLCIN for Δ_{1250m} (dashed green) and Δ_{156m} (dashed red) for case simulated over A1, dated 26 July 2012. The vertical dashed and solid lines show the time of formation of first cloud and the first occurrence of precipitation in the domain, respectively.

b. Cloud evolution

Δ_{156m} and Δ_{1250m} both result in cloud-topped CBL (Figure 6.10). However, e.g. until 1200 UTC clouds grow deeper in Δ_{1250m} ($\approx$8000 m) in comparison to Δ_{156m} ($\approx$6100 m). This raises the question, which processes are responsible for this differences in cloud development. One reason could be the higher potential energy in terms of favourably higher MLCAPE and lower MLCIN values in Δ_{1250m} than that in Δ_{156m}, as discussed in the previous section. Additional insights could be gained by investigating the cloud properties and heat and moisture budgets for the period when CBL clouds develop into deep convection. The diurnal cycle of the column integrated cloud liquid water content (tqc) and water vapour (tqv) is

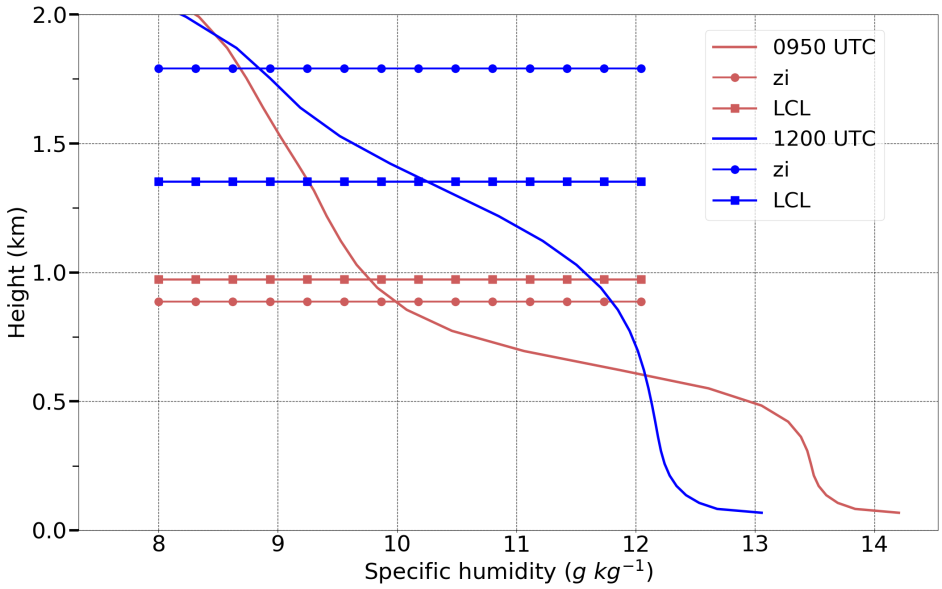

Figure 6.19.: Vertical profiles of areal mean specific humidity in Δ_{156m} at 0950 UTC (red) and 1200 UTC (blue) for case simulated over A1, dated 26 July 2012. The horizontal lines with circle and square markers denote the areal mean CBL height (zi) and LCL, respectively.

shown in Figure 6.20. Δ_{1250m} has the maxima of tqc in the order of $\approx$0.25 $kg\,m^{-2}$ at 1210 UTC in conjunction with a reduction in tqv which means that the most of the water vapour (q_v) at this hour has been converted to cloud liquid water (q_c). This can be also seen with the cross-section of qc at around 1210 UTC in the Figure 6.10b. Δ_{156m} simulates the maxima of tqc in the order of $\approx$0.17 $kg\,m^{-2}$ between 1400 and 1500 UTC with only a slightly reduce increase of the mean tqv. That means only some part of the water vapour q_v has been transformed in cloud liquid water (q_c). With this, Δ_{1250m} calculates higher tqc than Δ_{156m} at around 1200 UTC which is also evident in the time-height cross section of cloud liquid water (Figure 6.10a and 6.10b).

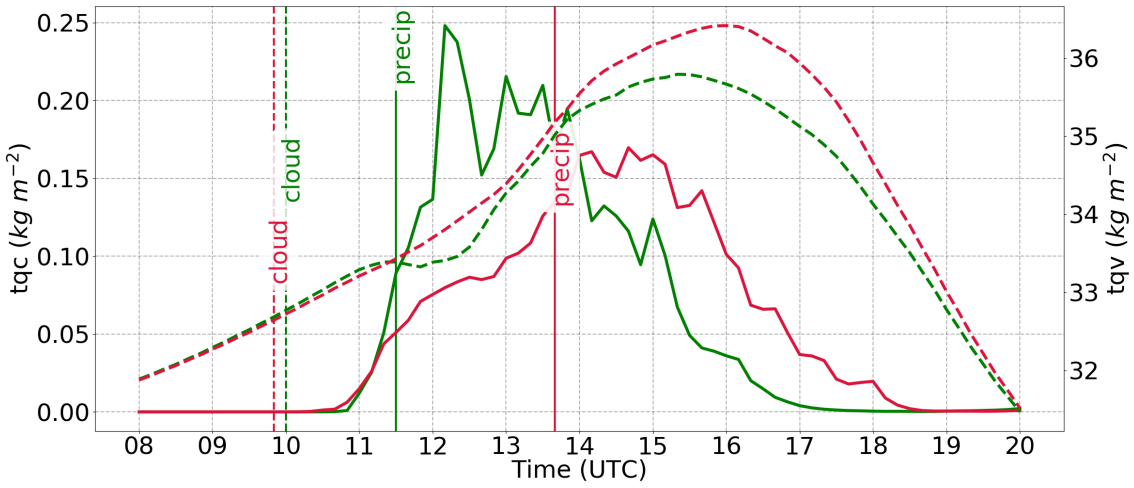

Figure 6.20.: Time-series of areal mean total column integrated cloud liquid water (tqc) (solid line) and total column integrated water vapour (tqv) (dashed line) in Δ_{156m} (red) and Δ_{1250m} (green) for case simulated over A1, dated 26 July 2012. The vertical dashed and solid lines show the time of formation of first cloud and the first occurrence of precipitation in the domain, respectively.

Figures 6.21 and 6.23 show the vertical profiles of the components of area-averaged heat (a) and moisture (b) budget in the CBL and free troposphere at 1200 UTC for Δ_{1250m} and Δ_{156m}, respectively. This time was selected because Δ_{156m} shows no precipitation whereas Δ_{1250m} simulates some precipitation (Figure 6.10a and 6.10b). This makes it a suitable hour for analysing the processes causing differences in the cloud evolution and the precipitation onset.

In Δ_{1250m}, the SUM_{θ_v} profile can be separated mainly into four layers: cooling in the lowest 100 m, warming between 100 m and cloud base, which corresponds with the LCL, warming from cloud base up to approximately 3 km (Figure 6.21a). In the layer between 3 km and 8 km, the SUM_{θ_v} is small. To this SUM_{θ_v}, the $TURB_{\theta_v}$ contributes only in the subcloud layer by heating, decreasing nearly linearly from about +1.9 Kh^{-1} at the surface to 0 Kh^{-1} at the cloud base. Appreciable heating by radiative processes (RAD_{θ_v}) of up to 0.7 Kh^{-1} is restricted to the lowest 100 m. The most prominent contributions to the heat budget are advective and microphysical processes. In the subcloud layer, $MICR_{\theta_v}$ causes cooling (approximately -0.6 Kh^{-1}), which is due to evaporation of rain, and heating by condensation from the cloud base to cloud top at about 8 km. Condensational heating

is highest with values of about 1.5 $K\,h^{-1}$ in the lower part of the cloud layer. The contribution by ADV_{θ_v} to the SUM_{θ_v} can be separated into three layers: cooling of up to -2.9 $K\,h^{-1}$ in the lowest 150 m, heating between 150 m and cloud base and cooling from the cloud base to the cloud top. Once again separating the advection term into the convergence of the grid-scale vertical sensible heat flux (-$\frac{\partial \overline{w'\theta_v'}}{\partial z}$) and the remaining part of ADV_{θ_v} leads to more insight into the active advection processes. The result is shown in Figure 6.22. In the CBL, the -$\frac{\partial \overline{w'\theta_v'}}{\partial z}$ profile nearly equals ADV_{θ_v} profile. That means in Δ_{1250m} at 1200 UTC, convection is large enough to be resolved so that the grid-scale vertical sensible heat fluxes transport heat from the surface layer to upper parts of the CBL. Note this roughly corresponds to the conditions of Δ_{156m} two hours earlier (Figure 6.15). In the cloud layer, however, the contribution of -$\frac{\partial \overline{w'\theta_v'}}{\partial z}$ to ADV_{θ_v}, apart from the lower 500 m of the cloud layer, is small. That means horizontal advection is responsible for cooling in most parts of the cloud layer and by this is compensating the condensational heating. The different contribution by vertical and horizontal heat exchange in the CBL and free troposphere can be understood by this: in the CBL, the gradients of temperature are strongest in the vertical which makes $ZADV_{\theta_v}$ respectively -$\frac{\partial \overline{w'\theta_v'}}{\partial z}$ the decisive factor for the heat exchange. In the free troposphere, horizontal temperature differences could be considerable, too, as temperature differences exist between clouds and their environment. The moisture budget of Δ_{1250m} is shown in Figure 6.21b. Concerning the net moisture tendency, two main layers exist: drying in the subcloud layer and moistening above – interrupted by a shallow layer with drying just on top of the CBL. Moistening by the $TURB_{q_v}$ is restricted to the lowest 100 m. In the subcloud layer, the evaporation of rain contributes to a slight increase of moisture (approximately +0.1 to +0.2 $g\,kg^{-1}\,h^{-1}$). In contrast, in the cloud layer, condensation contributes to a reduction of moisture, with maximum values of -0.5 $g\,kg^{-1}\,h^{-1}$ in the lower part of the cloud layer. Finally, ADV_{q_v} dominates the net moisture tendency profile. Similar to the heat budget, investigating the convergence of the grid-scale vertical latent heat transport with ADV_{q_v}, shows that -$\frac{\partial \overline{w'q_v'}}{\partial z}$ corresponds to ADV_{q_v} (Figure B.18). That means grid scale vertical latent heat fluxes mainly transport moisture from the CBL into the lower cloud layer. Additionally, -$\frac{\partial \overline{w'q_v'}}{\partial z}$ moistens the upper part of the cloud layer, too, which is possible because the mean humidity profile shows a decrease with height.

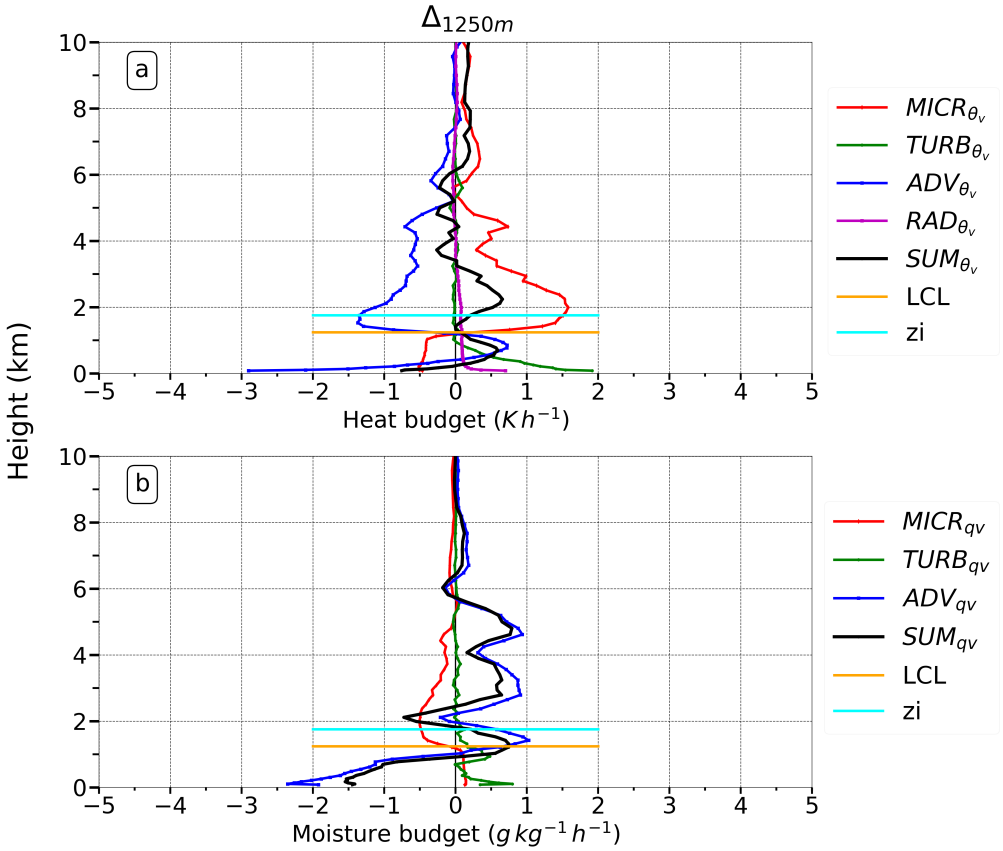

Figure 6.21.: Same as Figure 6.16 but for CBL and free troposphere and at 1200 UTC.

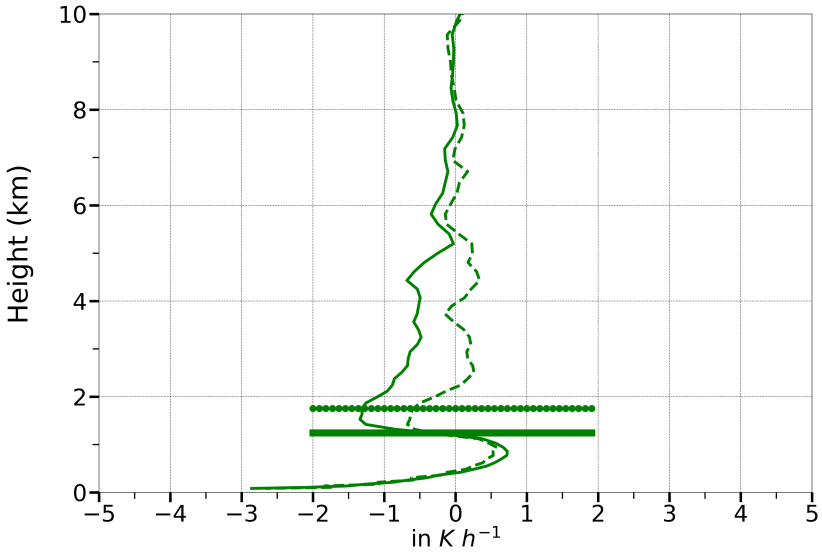

Figure 6.22.: Same as Figure 6.17 but for CBL and free troposphere and at 1200 UTC.

Unlike the Δ_{1250m}, the Δ_{156m} results into a net heating layer in the subcloud layer, caused by the same set of the processes of the heat budget which were already

active at 1000 UTC (Figure 6.14a) i.e. $TURB_{\theta_v}$, RAD_{θ_v}, and ADV_{θ_v}. The cooling by ADV_{θ_v} in the lowest 200 m of the CBL and warming up to the cloud base is again due to the resolved convection ($-\frac{\partial \overline{w'\theta_v'}}{\partial z}$) (Figure 6.24). The moisture budget is also still very similar to the one at 1000 UTC (Figure 6.14b), $TURB_{q_v}$ causes moistening of the lowest 200 m of the CBL and resolved convection ($-\frac{\partial \overline{w'q_v'}}{\partial z}$) transports the moisture into the upper part of the CBL (subcloud and cloud layer) (Figure 6.23b, B.19). Between 1000 UTC and 1200 UTC, the CBL clouds grew already deep into the free troposphere reaching up to $\approx$ 6100 (Figure 6.10a). In the cloud layer, the budget terms are as follows: the net heating (0.4 $K\,h^{-1}$) is limited until $\approx$3000 m only. This heating has a positive contribution from $MICR_{\theta_v}$ which is partly compensated by a simultaneous advective cooling from ADV_{θ_v}. There is simultaneous moisture consumption in this layer indicating cloud formation in the lower half of the cloud layer. On top of the net heating layer, there exists a net cooling layer (-0.5 $K\,h^{-1}$) where $MICR_{\theta_v}$ shows the dominant contribution. This indicates the existence of evaporative cooling and it results into a simultaneous release of moisture in this layer (Figure 6.23b). Consequently, there are some major differences between the heat and moisture budget of Δ_{156m} and Δ_{1250m} at 1200 UTC (Figures 6.23 and 6.21). While cloud formation ($MICR_{\theta_v}$) in Δ_{1250m} reaches from the cloud base up to the cloud top in 8000 m, in Δ_{156m} $MICR_{\theta_v}$ contributes to cloud formation in the lower half of the cloud layer (3000 m) while contributing to cloud dissolution in the upper part of the cloud layer (3000 to 5500 m).

To further understand the clouds behaviour in this evaporative cooling layer between 3000 and 5500 m, the spatial distribution of $MICR_{\theta_v}$ at a height of $\approx$4000 m is shown for Δ_{1250m} and Δ_{156m} in Figure 6.25. It shows a zoomed view of typical clouds for the two grid spacings. Positive $MICR_{\theta_v}$ indicates Latent Heat Release (LHR) at the cloud core while negative $MICR_{\theta_v}$ is an indication of associated cooling. It is apparent that Δ_{1250m} produces bigger clouds whereas Δ_{156m} simulates more number of small clouds. Though the heating due to $MICR_{\theta_v}$ in the cloud core is comparable in both of the grid spacings, the clouds in Δ_{156m} show significantly stronger cooling at the cloud edge and shell region in comparison to Δ_{1250m}. The strong evaporative cooling in Δ_{156m} between 3000 and 5500 m causes the dissolution of clouds so that on average the clouds do not grow that deep at that time (Figure 6.10a). The possible cause behind the occurrence of this cooling

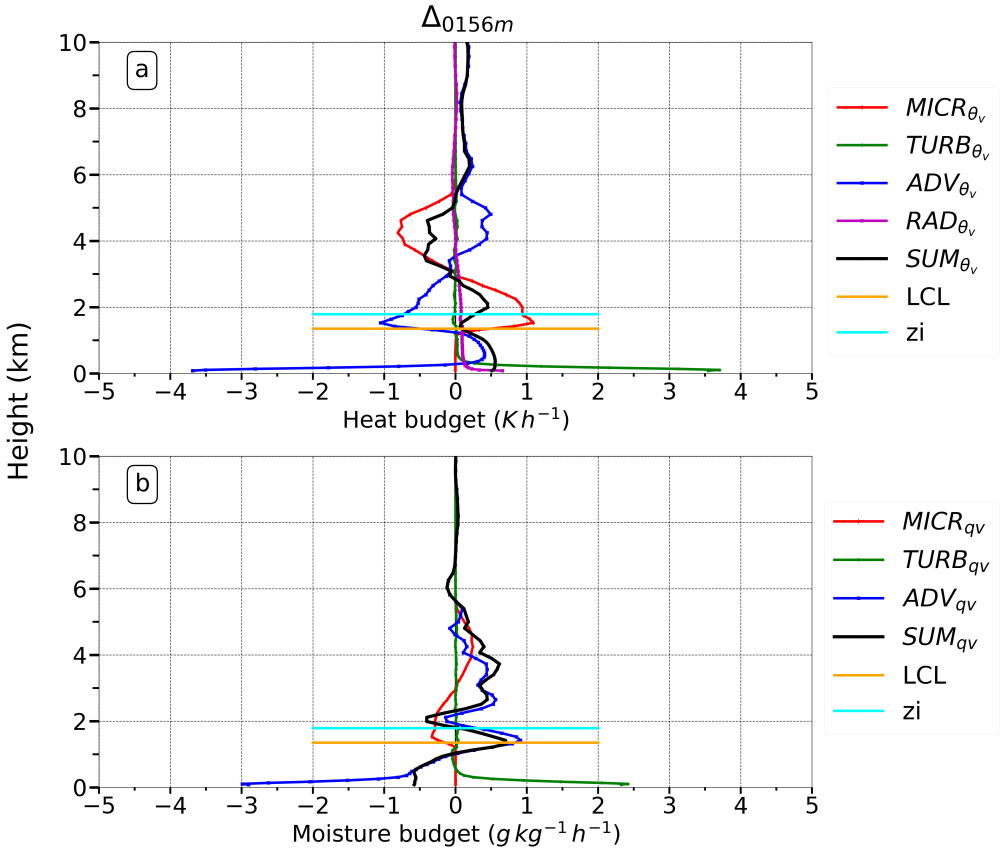

Figure 6.23.: Same as Figure 6.14 but for CBL and free troposphere and at 1200 UTC.

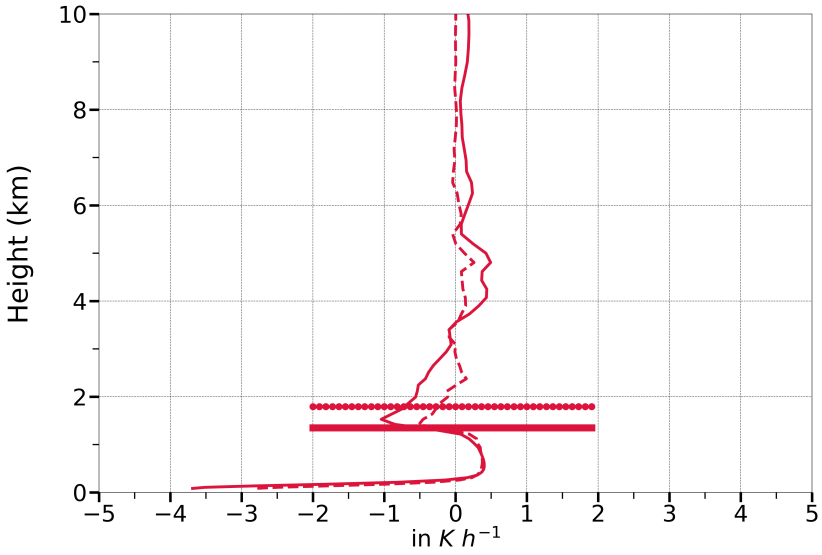

Figure 6.24.: Same as Figure 6.15 but for CBL and free troposphere and at 1200 UTC.

layer is explained using the size distribution of clouds calculated for the cloud cover simulated in Δ_{1250m} and Δ_{156m}. Figure 6.26a and b are snapshots showing

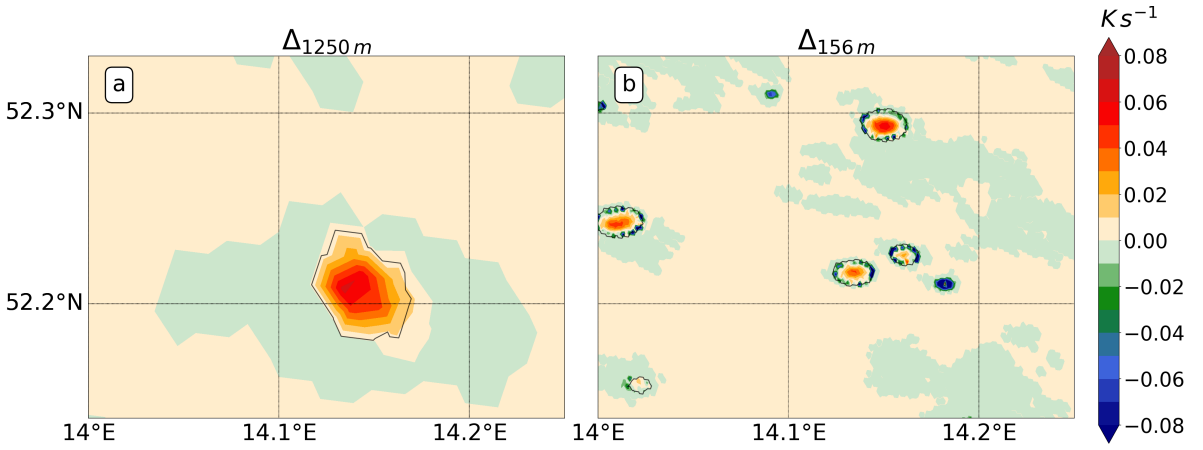

Figure 6.25.: Spatial distribution of temperature microphysics tendency ($MICR_{\theta_v}$) (colour coded) in $\Delta_{1250\,m}$ (a) and $\Delta_{156\,m}$ (b) at $\approx$ 4000 m height at 1200 UTC for case over A1, dated 26 July 2012. The black contours are the isolines for cloud liquid water content of 0.1 $g\,kg^{-1}$ at that level.

vertical cross section of equivalent diameter of the simulated cloud cover and the numbers of clouds formed at 1200 UTC in $\Delta_{1250\,m}$ and $\Delta_{156\,m}$, respectively. Equivalent diameter equals to the diameter of a circle whose surface area is equal to the respective contour area. As evident, $\Delta_{156\,m}$ grid spacing produces more number of smaller and shallow clouds than the bigger and deeper clouds of $\Delta_{1250\,m}$. Morton et al. (1956) and Turner (1963) have given a quantitative description of entrainment which is based on a laboratory water tank experiments of thermal plumes, describing the relation between mass flux (M), entrainment rate (ε) and the radius of the rising plume (R) (Eq. 6.2).

$$\frac{1}{M}\frac{\partial M}{\partial z} = \varepsilon \simeq \frac{0.2}{R}. \tag{6.2}$$

It says that the entrainment rate is approximately inversely proportional to the radius of the rising plume. That means the smaller the plume, the higher the entrainment rate. Therefore, the smaller clouds in $\Delta_{156\,m}$ are easily get detrained by the dry environmental air, which results in the dissolution of deep clouds in $\Delta_{156\,m}$ in the early stage. The entrainment causes evaporative cooling, which further reduces the buoyancy of the convective parcels. The evaporation between 3000 and 5500 m results in a moisture increase in that layer (Figure 6.23b). Moreover, the addition of moisture to the environment reduces the efficiency/extent of cloud dissolution by lateral entrainment processes. There is considerable dependence on

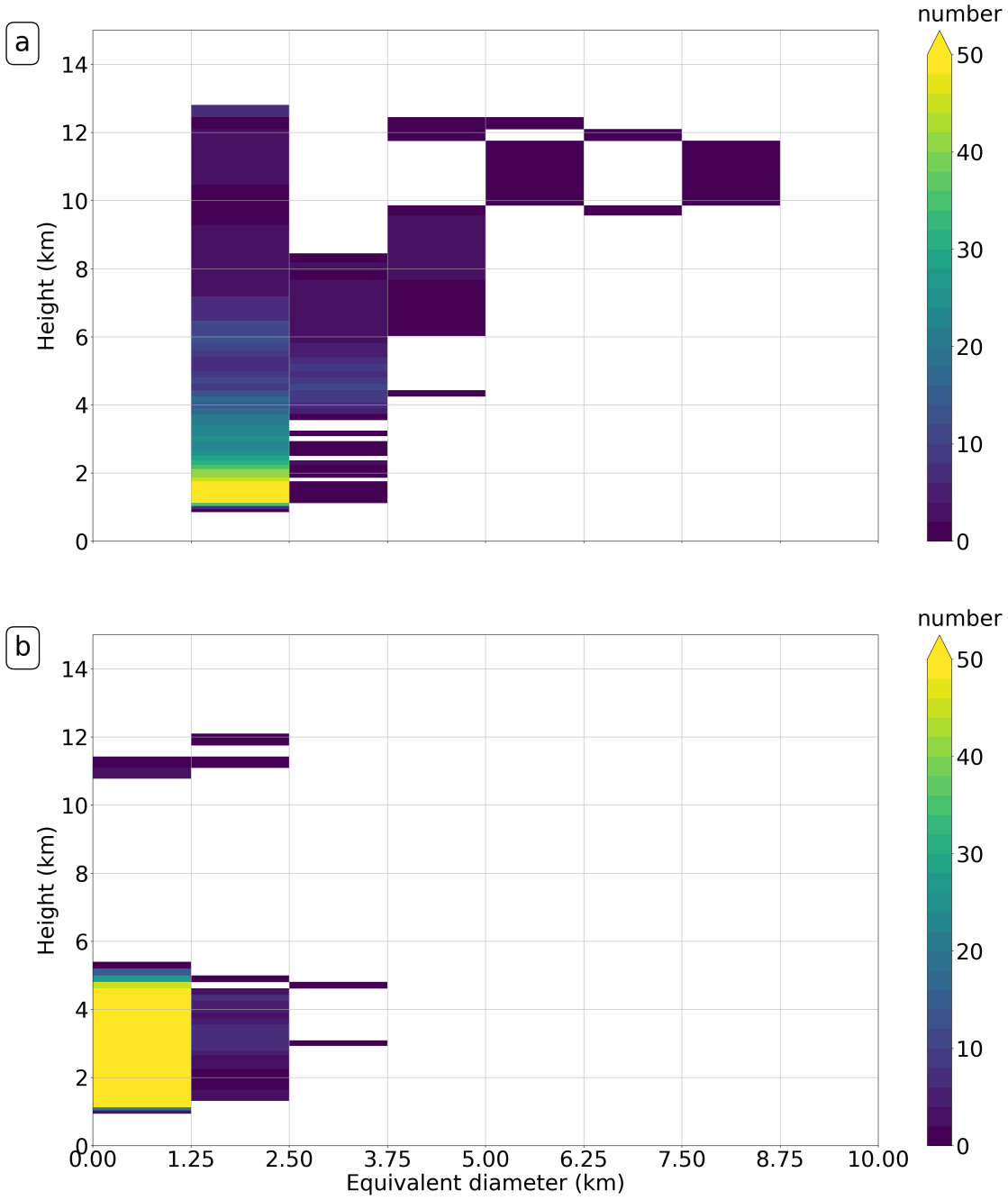

Figure 6.26.: Vertical distribution of equivalent diameter of clouds and number of clouds (colour coded) in Δ_{1250m} (a) and Δ_{156m} (b), respectively at 1200 UTC for case over A1, dated 26 July 2012.

the development of deep convection on the water vapour content in the middle troposphere (Metzger et al., 2014). The evaporative cooling in the small-sized clouds is a prominent phenomenon analysed in Δ_{156m} grid spacings also in the other case

(A2, case: 09 June 2018), resulting in the formation of detached shallow-cumulus clouds (Figure B.20, B.21).

In addition to the latent heating and the evaporative cooling, the mean updraught and downdraught speed inside the clouds and its environment provide macro-physical characteristics of clouds. Figure 6.27 shows the vertical profiles of areal mean $MICR_{\theta_v}$, mean updraught in the cloudy regions (defined by $q_c > 0$), mean downdraught speed in the cloud- edge and shell regions, and the normalised grid fraction of cloudy region for Δ_{1250m} and Δ_{156m} at 1200 UTC. The shell region is taken as the cloudy and non-cloudy regions having vertical velocity $w <$ -0.5 ms^{-1}.

As discussed in Section 6.3, at 1200 UTC the clouds are precipitating in Δ_{1250m} but not in Δ_{156m}. In Δ_{156m}, on average heating due to $MICR_{\theta_v}$ occurs from the cloud base up to approximately 3000 m and evaporative cooling from 3000 to 5500 m (Figure 6.27a). Grid fraction with clouds is highest just above the cloud base (5 %) decreasing nearly continuously up to the cloud top (Figure 6.27d). In the cloud layer, the mean updraught speed increases from the cloud base up to 4.25 km (Figure 6.27b), which corresponds with the level where evaporative cooling is strongest (Figure 6.27a). The mean downdraught speed also reaches maximum values in the upper part of the cloud (-1.2 ms^{-1}, Figure 6.27c) i.e. where the evaporative cooling is strongest Figure 6.27a). A typical feature in Δ_{156m} at 4 km, i.e. the level with the lowest $MICR_{\theta_v}$ value, during the period when the cloud fraction grows, is that the donwdraughts occupy a greater area than the updraughts (Figure 6.28).

In Δ_{1250m}, the cloud fraction is approximately 6 % just above the cloud base (Figure 6.27d). A secondary maximum of 3.5 % can be found at about 4500 m. At about 5500 m, the cloud fraction decreases, reaching a value of about 1%. This part of the cloud layer with higher cloud fraction, i.e. between the cloud base and 5.5 km, corresponds with heating due to LHR Figure 6.27a). Concerning up- and downdraught speeds, the values are rather homogeneously distributed over the cloud layer (Figure 6.27b,c) and the grid fraction clouds with up- and downdraughts at 4 km, at least during the growing phase of cloud fraction (1100 to 1200 UTC), is quite similar (2 %) (Figure 6.28).

To summarise the main differences between Δ_{156m} and in Δ_{1250m} at 1200 UTC: in Δ_{156m} the profile of the downdraught speed exhibits considerable differences,

being stronger in the layer where evaporative cooling exists (around 4 km) than in the layers with condensational heating, while in Δ_{1250m}, the downdraught speed is more similar in the whole cloud layer. Additionally, in Δ_{156m} at 4 km the grid fraction with donwdraughts exhibits the one with updraughts while Δ_{1250m} it is nearly the same. That means the layer with evaporative cooling has a considerable impact on the macro-physical properties of the clouds. Therefore, the evaporative

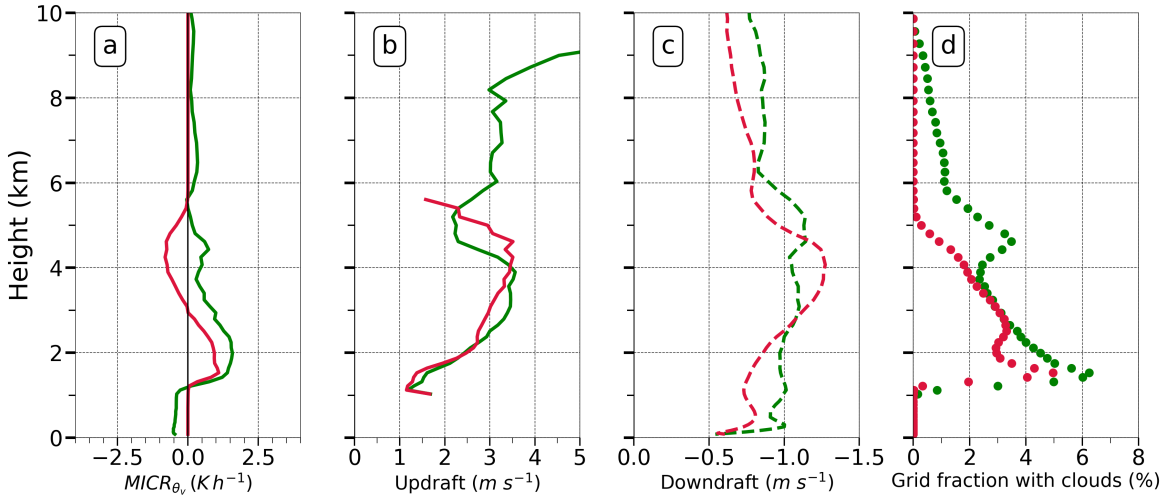

Figure 6.27.: Vertical profile of area mean temperature microphysics tendency, $MICR_{\theta_v}$ (a), updraught speed in cloudy region (b), downdraught speed in the cloud-edge and shell area (c), and grid fraction with clouds (d) in Δ_{156m} (red) and Δ_{1250m} (green) at 1200 UTC of case over A1, dated 26 July 2012.

cooling results in the dissolution of clouds in this layer which inhibit the growth of clouds, and this explains why there is no precipitation in Δ_{156m} at 1200 UTC.

c. Precipitation

As obvious from Figure 6.10a, first precipitation occurs in Δ_{156m} at about 1350 UTC. Therefore, the main question arises what happens between 1200 UTC and 1400 UTC allowing the clouds to grow deeper and to precipitate. This is demonstrated in Figure 6.29. In the CBL and the cloud layer turbulence ($\overline{w'^2}$) becomes stronger and reaches higher up, i.e. the 0.2 $m^2\,s^{-2}$ isolines increased from about 5 km at 1200 UTC to 8 km at 1400 UTC. Simultaneously, latent heat release in

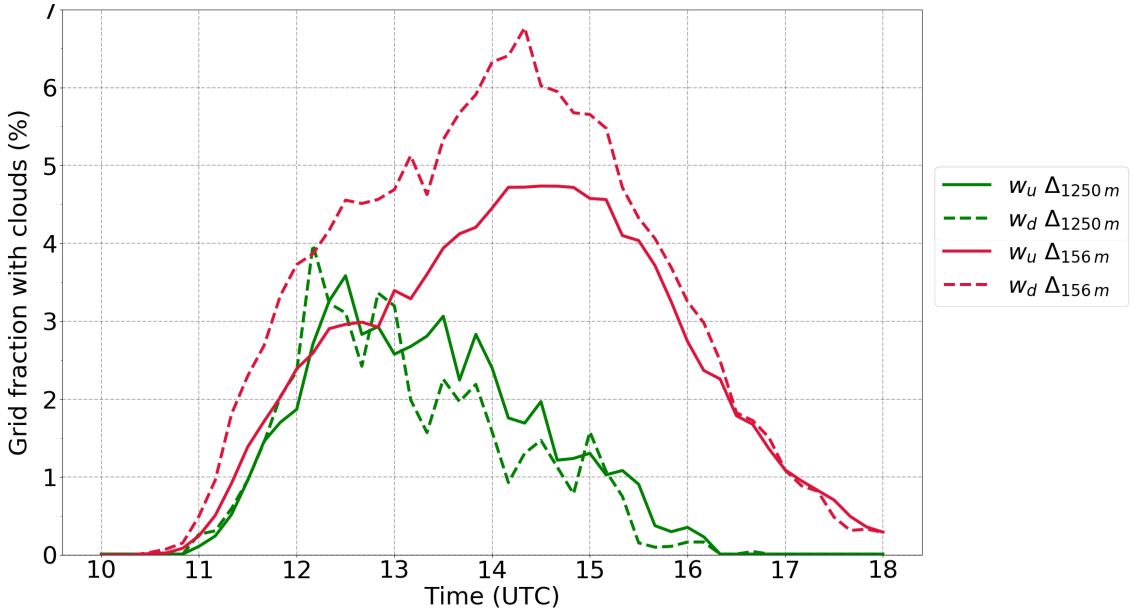

Figure 6.28.: Time series of mean updraught (solid) and downdraught (dashed) grid fraction at ≈ 4000 m for cloudy region in Δ_{1250m} (green) and Δ_{156m} (red) of case over A1, dated 26 July 2012.

the lower part of the cloud layer (approximately 1.8 km – 3 km) intensified reaching values of $MICR_{\theta_v}$= 1.5 $K\,h^{-1}$ when the first precipitation occurred. Shortly after that, i.e. at about 1430 UTC, the evaporative cooling in the layer around 5 km nearly diminishes. In parallel to the changing of the microphysical cloud processes, the macro-physical cloud conditions also changed. The clouds became broader and deeper. For example, at 1400 UTC clouds with an equivalent diameter of ≈8.75 km can be found reaching up to 5.5 km while few clouds tops reached up to the tropopause (Figure 6.31). This cloud growth between 1200 UTC (Figure 6.32a) and 1400 UTC (Figure 6.32b) is attributed with cloud aggregation. The cloud aggregation can be seen in the spatial distribution of low-level cloud cover at 1400 UTC (Figure 6.32b) where the aggregated clouds form mainly in the east and northeast of Berlin. Further, the height vs longitude diagram after averaging the cloud liquid water content over the latitude from 51.6° N to 52.9° N at 1400 UTC (Figure 6.33) clearly shows that the aggregated clouds extend till 5 to 6 km. Between 1200 to 1400 UTC, there is an increase of the areal mean relative humidity in the free troposphere up to 5.5 km (e.g. about 18 % at around 4 km) (Figure 6.30). It indicates that the dissolution of clouds moistens the free troposphere, which makes the atmosphere less dry. In the subsequent 3 hours,

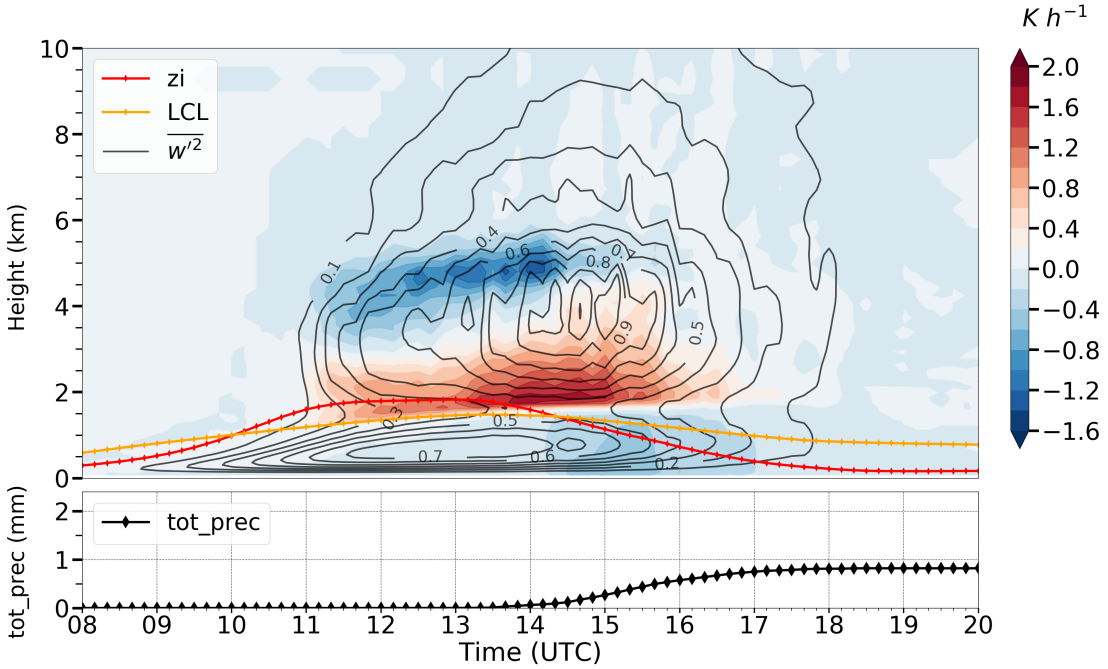

Figure 6.29.: Time height cross-section of temperature microphysics tendency $MICR_{\theta_v}$ (colour coded) in $\Delta_{156\,m}$-control run for case over A1, dated 26 July 2012. The red and orange curves are areal mean CBL height and LCL, respectively. The black contours are area-averaged vertical wind variance ($\overline{w'^2}$).

convective precipitation occurred (clustered precipitation patterns in Figures 6.3 and 6.32c) with evaporative cooling in the subcloud layer due to evaporation of precipitation (Figure 6.29). Until 1600 UTC, MLCAPE degraded considerably (Figure 6.18) and cloud liquid water (tqc) was removed completely from the atmosphere (Figure 6.20) so that the convective activity stopped (Figure 6.29).

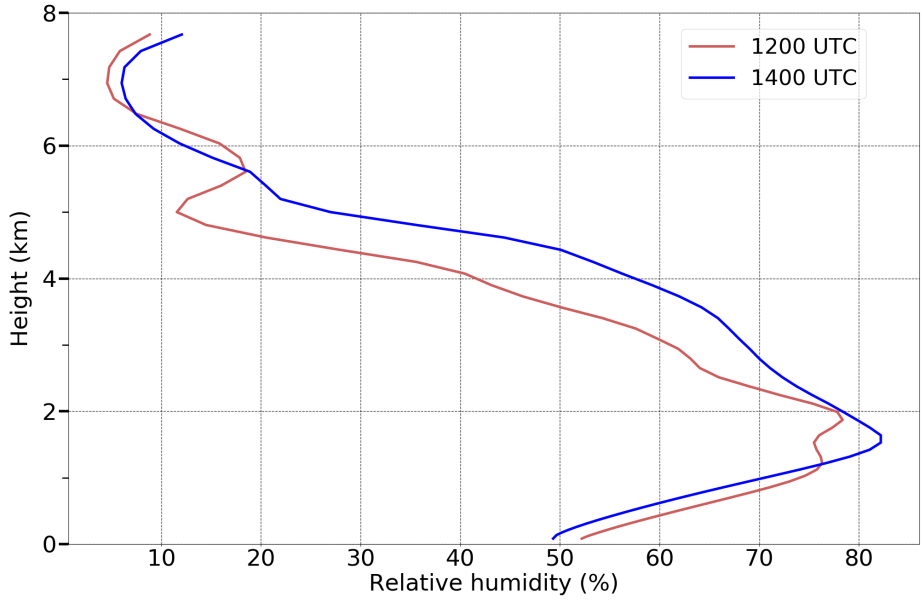

Figure 6.30.: Vertical profiles of mean relative humidity in Δ_{156m} at 1200 UTC (red) and 1400 UTC (blue) for case simulated over A1, dated 26 July 2012.

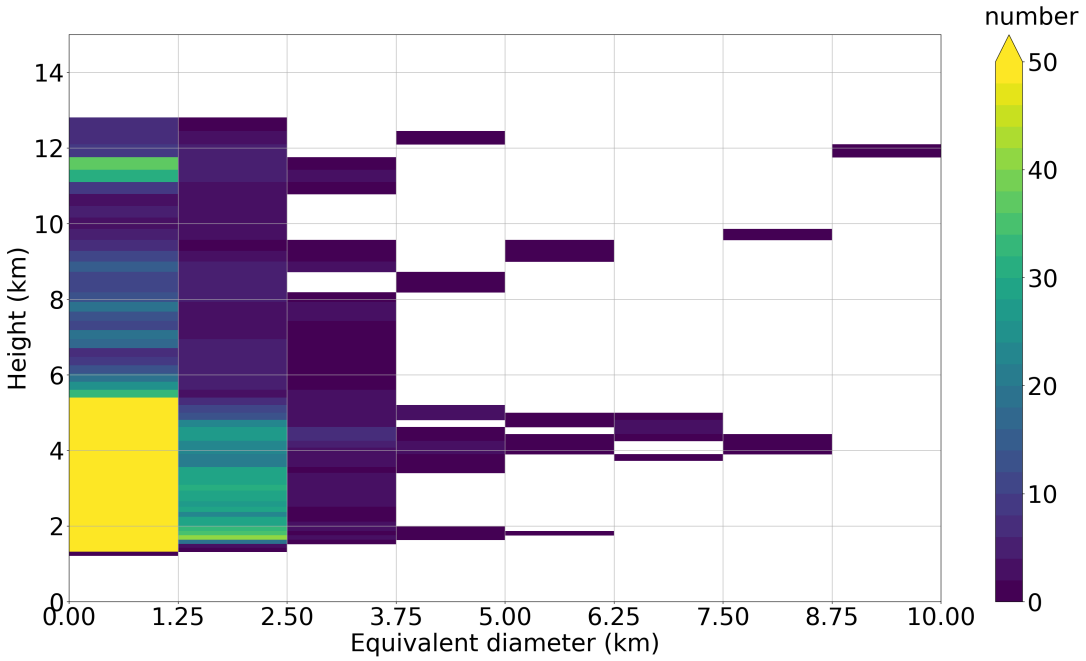

Figure 6.31.: Vertical cross section of cloud size distribution in Δ_{156m} at 1400 UTC for case over A1, dated 26 July 2012.

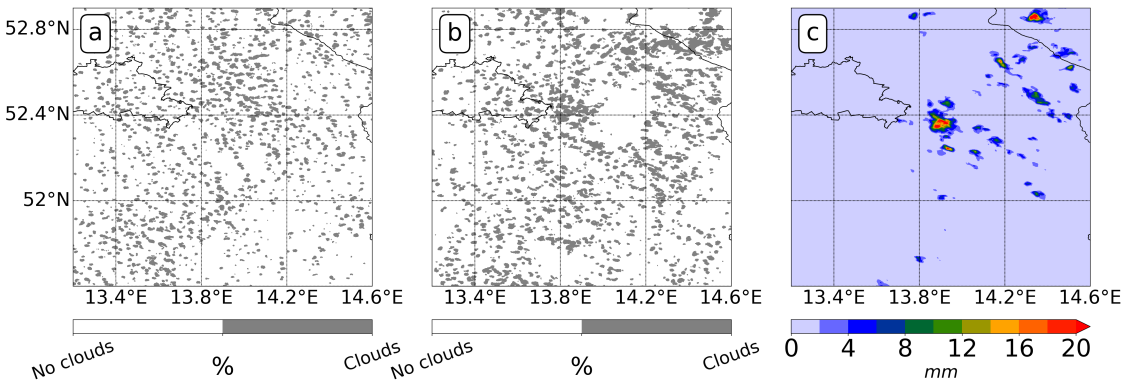

Figure 6.32.: Low-level cloud cover at 1200 UTC (a), at 1400 UTC (b), and total accumulated precipitation until 1500 UTC (c) in Δ_{156m} of case over A1, dated 26 July 2012.

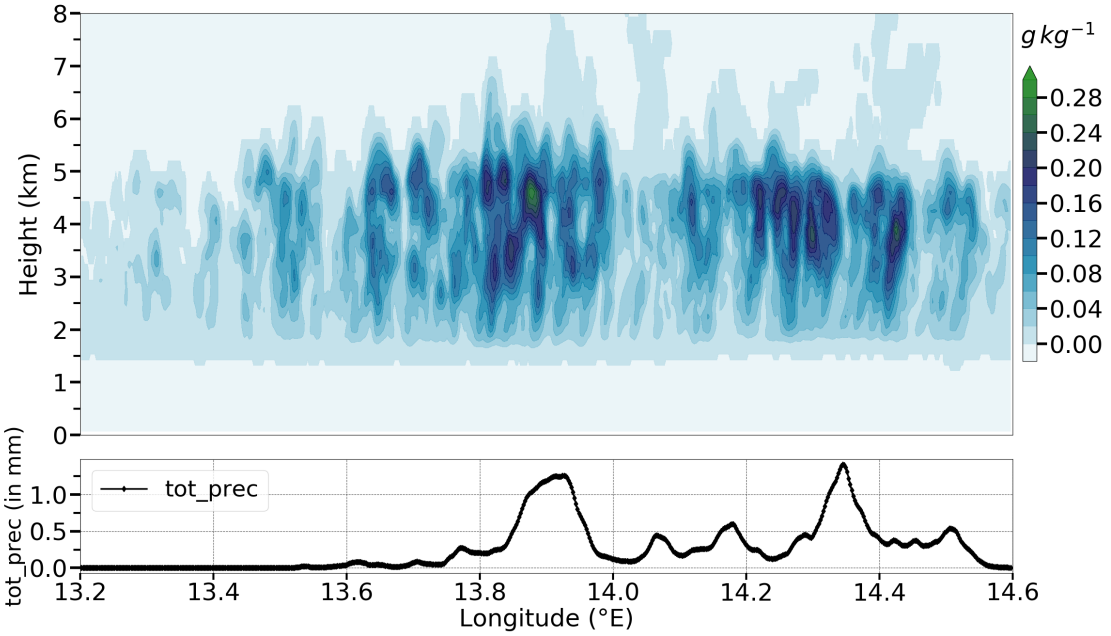

Figure 6.33.: Latitudinally averaged time-longitude diagram of cloud liquid water content at 1400 UTC in the first row and total accumulated precipitation at 1500 UTC in the second row in Δ_{156m} of case over A1, dated 26 July 2012.

Lesson drawn

The first take-home message here is that the areal mean daily accumulated precipitation amount in LES model grid spacings (Δ_{1250m} to Δ_{156m}) is more sensitive to the model grid spacing and shows a stronger variability ($\approx$155 %) in comparison to the land-surface resolution ($\approx$7-22 %). Across the LES grid spacings, on most of the investigated days the areal mean precipitation amount decreases with increasing grid spacing. Additionally, precipitation onset is delayed by 1 or 2 hours for the higher grid spacing runs. This is associated with the fact that in the simulations with finer horizontal grid spacing, first smaller clouds develop which show intensive evaporative cooling at their shell and edges. This restricts the cloud growth and therefore suppresses precipitation. Later on, cloud aggregation is an important process to allow these clouds to grow deeper and to precipitate.

7. Identified triggering mechanisms

This chapter describes the triggering processes of convection depending on land surface identified in the above-mentioned case studies. The basic ingredients of the triggering of convection or CI are atmospheric instability, sufficient moisture supply and wind convergence (Doswell III, 1987; Chen and Avissar, 1994; Kalthoff et al., 2011; Barthlott and Kalthoff, 2011; Adler et al., 2011). The surface layer which in direct contact with the Earth's surface is influenced by the surface sensible and latent heat fluxes. The turbulent heat flux further transports heat into the CBL and causes differential heating in the atmospheric layer when the surface is heterogeneous. As a result, the evolution of the CBL itself experiences a diurnal cycle. According to Segal and Arritt (1992), the daytime spatial heterogeneity in surface sensible heat flux can lead to thermally-induced circulations. The spatial distribution of surface sensible heat flux depends on different factors like landforms, land use variation, soil moisture heterogeneity and cloud cover. That means the surface sensible heat flux is one measure to quantify the land-surface heterogeneity. Additionally, the triggering mechanisms could be different depending upon the scale of land-surface heterogeneity and the synoptic situation.

Here, the land-surface heterogeneity has been broadly categorised into land-surface properties and orography. The first investigation area, A1, could show the formation of moist convection due to variation in land-surface properties, for example, vegetation, soil type, land use (including water, sealed surface). The inhomogeneities in land-surface properties cause differential surface fluxes and form pressure gradients which trigger mesoscale circulations. Another key factor in this regard is the orography. For areas A2 and A3, additional to the land-surface properties, orography becomes gradually more important.

In general, the triggering mechanisms over the heterogeneous regions could be based on dynamically as well as thermally-driven circulations. Under fair weather conditions, the thermally-driven circulation over heterogeneous terrain (e.g. at crestlines and adjacent land surfaces) poses a reversal of wind direction twice

every day (Whiteman, 2000). Subsequently, the temperature difference results in the density variation of air masses, which induces a horizontal pressure gradient and initiates the circulation. The air mass close to the surface flows from areas of higher pressure to the areas of low pressure. Conceptually, the upper branch of the current circulation runs in the opposite direction. Therefore, baroclinicity tends to generate mesoscale wind systems. Some examples of these circulations are lake breezes, slope-wind systems and valley-wind systems. Triggering processes which are based on differential heating and the local wind circulations are called as primary triggering mechanism.

Further, the above factors precondition the atmosphere for the generation of moist convection which then can result in precipitation. The precipitation itself is a decisive factor which controls the formation of new convective cells. The triggering of new cells depends upon the transient primary triggering mechanisms. Therefore such processes are called secondary triggering mechanisms. For example, the triggering through gust fronts and the outflow boundaries of existing or decayed precipitation systems could generate new convective cells. The evaporation of rain causes a cooling effect in the surface layer accompanied by a strong downdraught. This evaporatively cooled region of downdraught air is called a cold pool. This cold and dense air then spreads laterally at the surfaces and tends to lift the surrounding warm and light air. This process is called mechanical lifting (Torri et al., 2015). The lifting can also occur due to the convergence of gust fronts of the cold pools and the environment wind. Due to mechanical lifting, a cold-pool system is very likely to generate a small convective cell at the cold pool edge. The details of the genesis and formation of new convective cells due to cold pools will be discussed in Section 7.2.1. Moreover, the high-resolution simulations allow us to understand the small features embedded into cold-pool evolution for example associated gust fronts, generation of new convective cells.

Another way of categorising the triggering is through the underlying sources of heterogeneity itself. These sources of triggering can be represented under two categories, namely static and dynamic. Effects under static heterogeneity comprise the phenomenon generated due to surface properties variation, for example, lake-breeze, Urban Heat Island (UHI) effect and orographically-induced circulations (Kang and Bryan, 2011; Rieck et al., 2014). In contrast the dynamic het-

erogeneity pertains the processes which are triggered due to the modulation from cloud radiative effects or cold pools (Marsham et al., 2007; Rieck et al., 2015).

7.1. Primary triggering

The primary triggering mechanism can be broadly divided into two categories. The first category involves those locally induced processes which are caused by inhomogeneities in land-surface properties or due to the spatial pattern of Bowen ratio (the ratio of surface- sensible heat flux and latent heat flux) generated by heterogeneous soil type, soil moisture and vegetation, for example, thermally-induced circulations. The second category consists of orographically induced circulations, for example, slope winds, valley winds. The above processes occur independently or in a way that they are superposed.

7.1.1. Thermally-driven circulation

Theoretical background

Bowen ratio gives the partitioning of the available energy into surface- sensible heat flux and latent heat flux. The spatial pattern of Bowen ratio modulates the CBL state, which impacts the conditions resulting in locally induced convective systems, for example, lake breeze (Section 7.1.1a) and UHI (Section 7.1.1b). A lake breeze can be used as an example to explain the fundamentals of a thermally-driven circulation system. Generally, lake breeze (sea breeze) can be seen as the onshore/offshore winds occurring during daytime and observed over the lake/sea. As the name suggests, the wind blowing from the lake (land) in the daytime (nighttime) and blowing towards land (lake) is called lake (land) breeze. It is caused by the surface temperature difference of the lake and the adjacent land. This creates a pressure gradient at lower levels in the atmosphere, which results in the lake-breeze near the Earth's surface (Atkinson, 1981). The definition of lake/sea-breeze circulation is based on Bjerknes' circulation theorem (Bjerknes et al., 1898; Thorpe et al., 2003) which is an expression obtained by taking the line integral of Newton's second law for a closed curve in the fluid. This gives a relation between

the *relative* circulation C (a measure of the rotation of the fluid) and the enclosed area projected on the equatorial plane A_e.

$$\frac{DC}{Dt} = -\oint \frac{dp}{\rho} - 2\Omega \frac{DA_e}{Dt} \tag{7.1}$$

In equation 7.1, the term on the left hand side denotes the rate of change of relative circulation, the first term on the right hand side is called solenoidal term. The solenoid term originates from the intersection of isobaric and isothermal surfaces due to the density variation, which results in a rotational acceleration (or solenoid). The second term denotes the inertial effect. Ω is the angular speed of the Earth's rotation. Using Stoke's theorem the equation 7.1 can be expanded as:

$$\frac{DC}{Dt} = -\int_A (\nabla\alpha \times \nabla p) \cdot \mathrm{d}\vec{A}, \tag{7.2}$$

$$\frac{DC}{Dt} = -\int_A |\nabla\alpha \| \nabla p| | \sin(\beta)\, \mathrm{d}A, \tag{7.3}$$

where α and p are the specific volume ($\alpha = \frac{1}{\rho}$) and pressure, respectively. β denotes the angle between the gradients of α and p.

According to this theorem, the rate of change of *relative* circulation (C) of a closed chain of fluid particles is determined by two effects: a) the solenoid effect, in which the solenoids tend to modulate the circulation. This can be quantified using the total number of solenoids falling into the closed curve. This equals to the flux of the vector product of the gradients of each quantity (α and p in equation 7.2) through a surface area bounded by the curve. b) the inertial effect which tends to decrease the relative circulation by a quantity proportional to the rate of change of the enclosed area (A_e), which is projected on an equatorial plane.

For a barotropic fluid in which the density is a function only of pressure, the solenoidal term is zero. That means the *absolute* circulation following the motion is conserved in barotropic fluid and therefore, the *relative* circulation for a closed chain of fluid particles will be modulated only by the enclosed horizontal area or the average latitude changes. But unlike the barotropic fluid, the density of the baroclinic fluid is a function of both temperature and pressure and therefore possesses a distinct air mass region, hence density gradients. Therefore, the

expression for Bjerknes' theorem for baroclinic flow represents the generation of pressure-density based solenoid circulation, which further explains the development of a thermally driven lake-breeze circulation. Using the ideal gas law, the solenoidal term in equation 7.1 can be expressed as:

$$\frac{DC_a}{Dt} = -\oint RT\, d\ln p \tag{7.4}$$

$$\frac{DC_a}{Dt} = Rd\ln\left(\frac{p_0}{p_1}\right)(\overline{T_2} - \overline{T_1}) \tag{7.5}$$

where C_a is the absolute circulation, $\overline{T_1}$ and $\overline{T_2}$ represent the mean temperature over the lake and land-surface respectively. During daytime, $\overline{T_2}$ is greater than $\overline{T_1}$ which therefore leads to $\frac{DC_a}{Dt} > 0$. This resultant circulation, in general, explains the mechanism behind a thermally-driven circulation.

The structure, evolution and life-cycle of sea and lake breezes are thoroughly studied and also reviewed both using observations (Atkinson, 1981; Simpson, 1994; Steyn, 1998) and the numerical studies (Miller et al., 2003; Antonelli and Rotunno, 2007; Porson et al., 2007; Crosman and Horel, 2010). The recurrent and ubiquitous nature of these thermally-driven systems makes them a crucial system or mechanism for triggering of convection. Moreover, the same theoretical consideration is basically valid for the other thermally-driven circulations caused by differences in land-surface properties like UHI. UHI effect directly affects the mankind by generating high temperature in the urban/city areas in comparison to the rural or countryside areas, which influences the regional weather, increase the pollution level and affect the well being of inhabitants. It is the result of the reduction in vegetated areas, thus evaporation, or varying land use, by replacing green areas with roads, building and other human-made structures which absorb the short wave radiation more and reflect less because of their low albedo, and therefore, cause surface temperature to rise (Oke, 1987; Golden, 2004; Nakayama and Fujita, 2010).

a. Lake breeze in ICON-LEM

Lake-breeze systems are captured in all the LES grid spacings for the case over A1, dated 26 July 2012. The lake breeze is one of the triggering mechanisms that contributed to the formation of the convective precipitation over this area. In

this example, the convection is developed adjacent to Scharmützelsee, which is a lake located in Brandenburg, Germany. This lake is about 10 km long and 1.5 km wide surrounded by agriculture areas in the west and east, and with forest in the north and south. This convection is triggered and reproduced by all LES resolutions, but the clouds do not precipitate in the $\Delta_{156\,m}$. $\Delta_{625\,m}$ is used to investigate

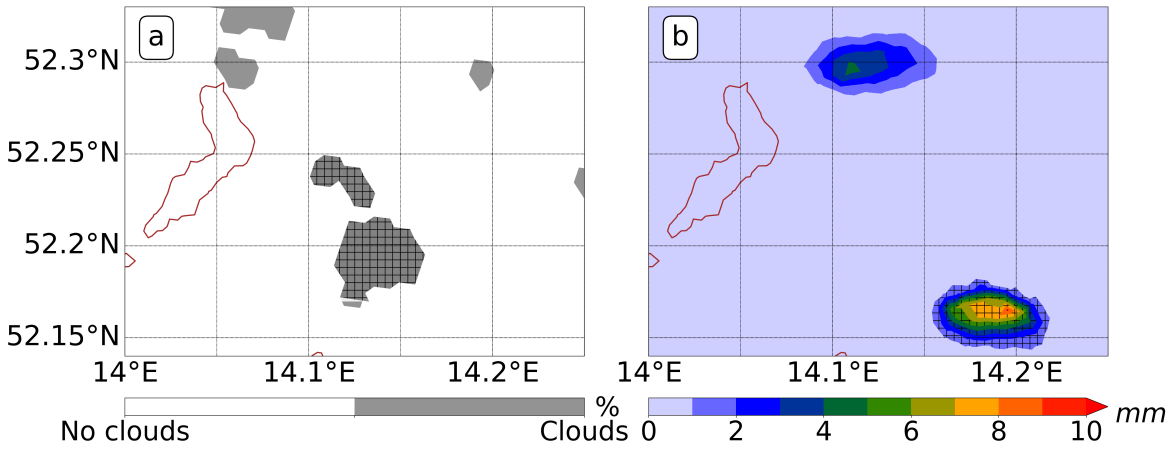

Figure 7.1.: Cloud cover at 1100 UTC (a) and the accumulated precipitation until 1200 UTC (b) in $\Delta_{625\,m}$ of case over A1, dated 26 July 2012. The brown contours encircle the areas with lakes.

the triggering processes over flat terrain, i.e. the process chain from initiation of convection via cloud formation and precipitation. In $\Delta_{625\,m}$, the first cloud is formed at 1020 UTC in this region and the precipitation occurred at 1140 UTC. Figure 7.1 shows the cloud cover at 1100 UTC and the resulting accumulated precipitation until 1200 UTC. With the north-northwesterly large scale wind, these clouds precipitate further to the southeast of Scharmützelsee.

Furthermore, the source region of the triggered cloud and its embedded convective structure is identified using the backward trajectory. For this purpose, the backward trajectories are calculated using LAGRANTO (for details about LAGRANTO see Section 5.6) over a 50 km x 60 km box i.e. 13.85° E, 52° N; 14.30° E, 52° N; 13.85° E, 52.5° N; 14.30° E, 52.5° N starting from the cloud base at 1100 UTC (Figure 7.2). The selection criteria applied to the pre-calculated trajectories gives a subset of the trajectory lines originating from the cloud base.

Figure 7.2 shows in the 3-D view of first part of the process chain. The specific humidity is traced back along the trajectories, which provides further insights into the physical properties of the air parcels. It shows that most of the air parcel seeded into the clouds originated from near-surface over this period. The moist parcels originated above the lake, travel near-surface towards the eastern area of Scharmützelsee and then rise vertically, into the cloud base. Now, the surface con-

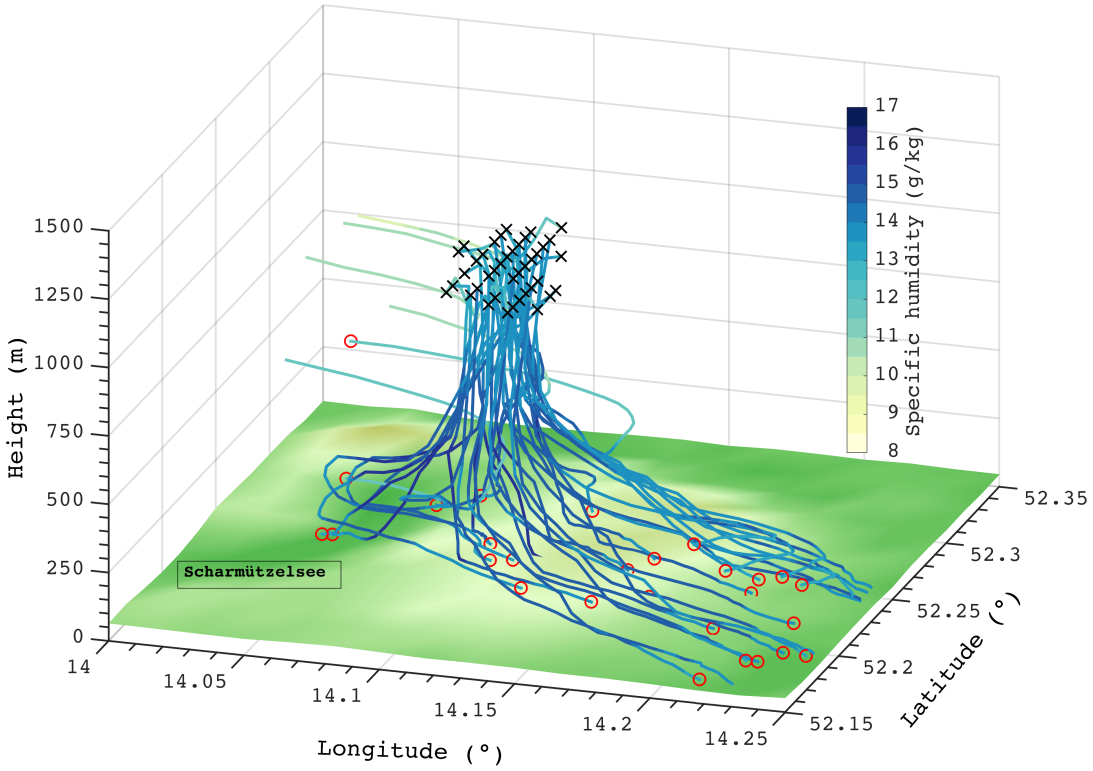

Figure 7.2.: Backward Lagrangian trajectories using LAGRANTO in $\Delta_{625\,m}$ of case over A1, dated 26 July 2012. The black crosses denote the starting points at the cloud base at 1100 UTC and the red circles denote the end points of trajectory integration until 0600 UTC. The colours along the trajectories indicate specific humidity ($g\,kg^{-1}$) and the colour in the xy plane denotes orography.

dition of the area where the parcels converge and rise are investigated. Figure 7.3a shows the surface sensible heat flux in background colour and the trajectory points which are projected in space (circles) and coloured with the specific humidity both

at 1000 UTC. The visual inspection shows on one hand that the moist air parcels are positioned at the transition area of surface sensible heat fluxes before they start to rise. Few of the relatively dry parcels, as they are aloft to ≈300 m, from the northwest also converge over this area. On the other hand, the areas with enhanced surface sensible heat flux develop in the east of the bow-shaped Scharmützelsee. That means the region with differential sensible heat flux leads to the triggering of convection. To identify the possible factors causing the high sensible heat flux, the areal mean Standardized Multiple Regression Coefficient (SMRC) (Siegel, 2016) is calculated for surface- sensible heat flux (H) and latent heat flux (E). For example the formulation for H is:

$$\mathrm{SMRC}_H = b_k * \frac{\sigma_k}{\sigma_H}, \tag{7.6}$$

where k represents the explanatory variable like Soil Moisture Index (SMI), TAI, orography, net radiation, and horizontal wind at 10 m. b_k is the coefficient estimate of H, and σ_k and σ_H are the standard deviation of the explanatory variable and the outcome variable (H), respectively. These variables are selected because they are assumed to be the most relevant parameters determining the partitioning of energy exchange at the Earth's surface into the surface- sensible and latent heat flux, respectively.

The SMRC estimates how much increase in the explanatory variable affects its relative importance or position within the group for the determination of the outcome variable (H, E). The high value of SMRC for an explanatory variable shows its more significant contribution to the determination of the outcome variable and vice versa. Investigating the period before the first clouds were generated, which is before 1020 UTC, the sensible heat flux shows the strongest positive correlation of $SMRC_H \simeq +0.6$ to $+0.7$ with the horizontal wind speed (Figure 7.4a). A much lower, but also a positive correlation of H exists with the net radiation ($SMRC_H \simeq +0.17$) whereas H is only weakly negatively correlated with SMI and TAI, and nearly no correlation exists with orography. Moreover, before cloud formation occurs the latent heat flux, E, has strong correlation of $SMRC_E \simeq +0.65$ is with TAI (Figure 7.4b). A less, but still positive correlation of E exists with 10 m wind speed ($SMRC_E \simeq +0.3$), followed by even a weaker dependence of E on radiation and SMI. Finally, the dependence of E on orography is smallest. The results indicate that in this case, H is not highest where the net radiation, i.e. the avail-

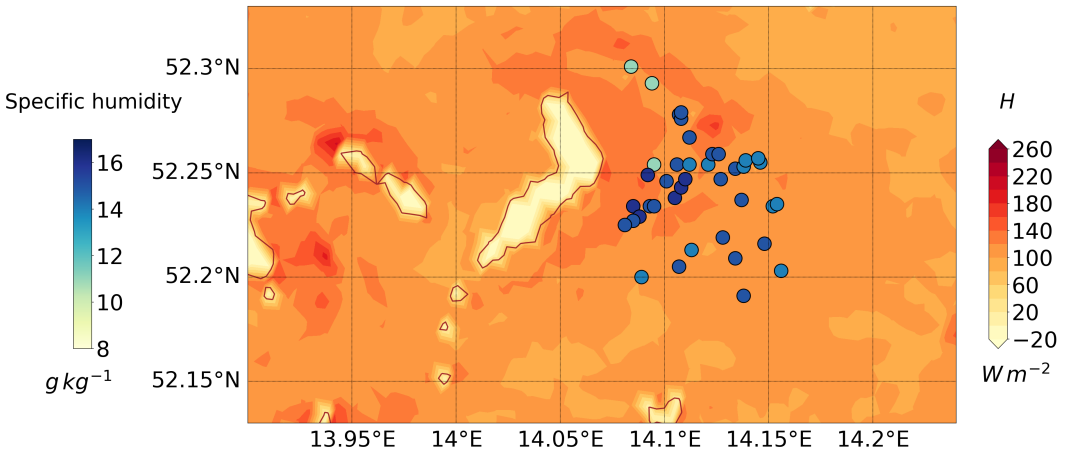

(a)

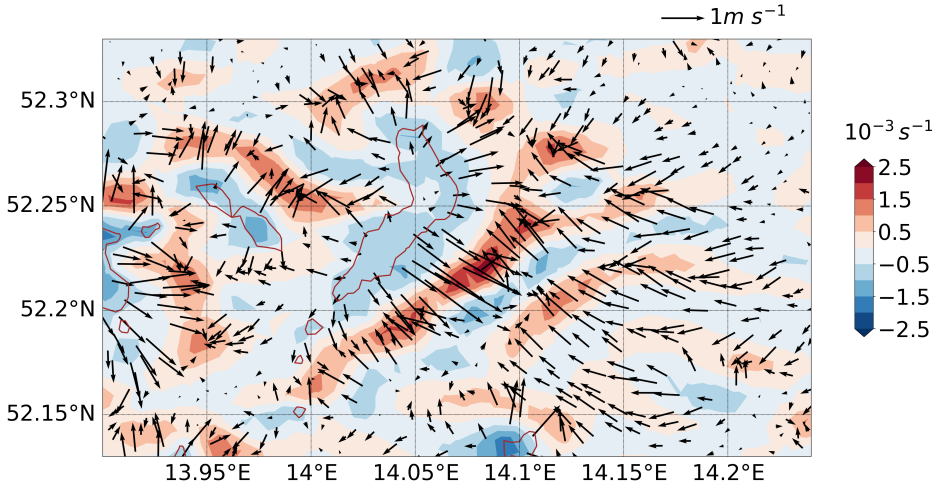

(b)

Figure 7.3.: Surface sensible heat flux (colour shaded) and the trajectory points (circles with specific humidity in the colour shade) (a), wind convergence (colour shaded) and wind vectors (b) at 10 m at 1000 UTC, in $\Delta_{625\,m}$ of case over A1, dated 26 July 2012. The brown contours encircle the areas with lakes.

able energy for transformation into the turbulent fluxes is highest. Instead, the near-surface wind speed – a relevant factor in determining the vertical turbulent diffusion - is the dominant factor to H. It suggests that the main mechanism supporting the higher sensible heat flux is through the lake-breeze circulation system, which is visible in Figure 7.3b. Triggering then occurs along the sea breeze front, where considerable wind convergence with lifting is generated. This region is also

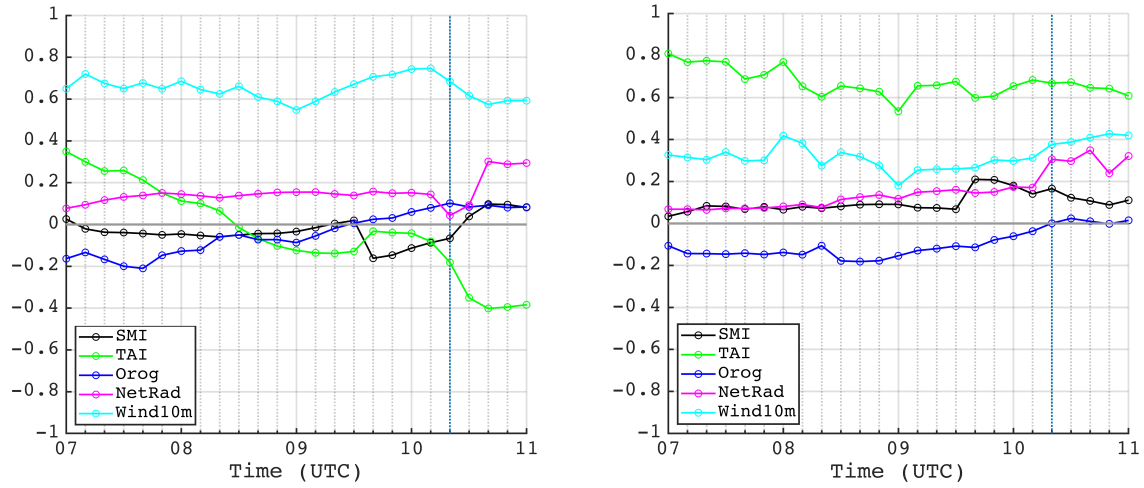

Figure 7.4.: The areal mean SMRC for SMI in black, TAI in green, orography (Orog) in blue, net radiation (NetRad) in pink, and horizontal wind at 10 m (Wind10m) in cyan with respect to H (a) and E (b), respectively for $\Delta_{625\,m}$ of case over A1, dated 26 July 2012. The vertical dotted line shows the onset time of first cloud in this investigation region.

corresponding with the origin of most of the trajectory points (Figure 7.3a) which anticipates the formation of the secondary circulation system.

b. UHI effect

The impact of a city on triggering of convection with subsequent precipitation also showed up in area A1 on 26 July 2012. This effect is identified over the city named Fürstenwalde located in the north east of Germany (Figure 7.5). The city covers an area of approximately 12 km^2, i.e. the diameter of the city is roughly 4 km. In the north, the city is surrounded by more agricultural-used land while in the west, south and east, forested areas dominate. The cloud of interest formed at 1110 UTC over the southern part of Fürstenwalde and moved with the ambient north-northwesterly wind further to the southeast. The cloud cover at 1130 UTC and the resulting accumulated precipitating system at 1230 UTC in $\Delta_{625\,m}$ in Figure 7.5 a and b, respectively. At 1130 UTC, the diameter of the cloud was about 4 km, and the cloud top reached up to 3.5 km and grew to 5.5 km before the precipitation started. At 1230 UTC, the precipitation in the centre of the cloud reached up to 5 mm.

In order to identify the triggering of this cloud system the backward trajectories are calculated over a box of 13.85° E, 52.2° N; 14.25° E, 52.2° N; 13.85° E, 52.5° N; 14.25° E, 52.5° N extent. Similar to the above example of the lake-breeze system, Figure 7.6 shows the 3-D view of the resulting convective system. The trajectories start from the grid points of the cloud base, ≈1000 m, at 1130 UTC and then integrated backwards until 0700 UTC. It shows that most of the air parcel seeded into the clouds originated from the near-surface region over this period, and converge over the western premises of the city (Figure 7.7b). The surface sensible heat flux at 1030 UTC, i.e. 40 min before the cloud forms, together with the projected trajectory points, are shown in Figure 7.7a. Because of the sealed surfaces in the city area, the surface sensible heat flux reached values of up to 220 $W\,m^{-2}$ while in the surrounding, the fluxes are much less ($H \simeq 100\,W\,m^{-2}$). In the south of the city, the northern tip of the Scharmützelsee with its characterised low sensible heat fluxes ($H \simeq -20\,W\,m^{-2}$) over the water body and enhanced sensible heat fluxes east of the lake are visible again. The spatial distribution of the latent heat flux is vice versa (not shown), i.e. evaporation is lower over the city and higher over the surrounding areas. At 1030 UTC, according to the trajectory points, the air parcels already reached the border of the city or the city centre itself. Afterwards, they are lifted to the cloud base (Figure 7.6). To investigate the main dependencies of the

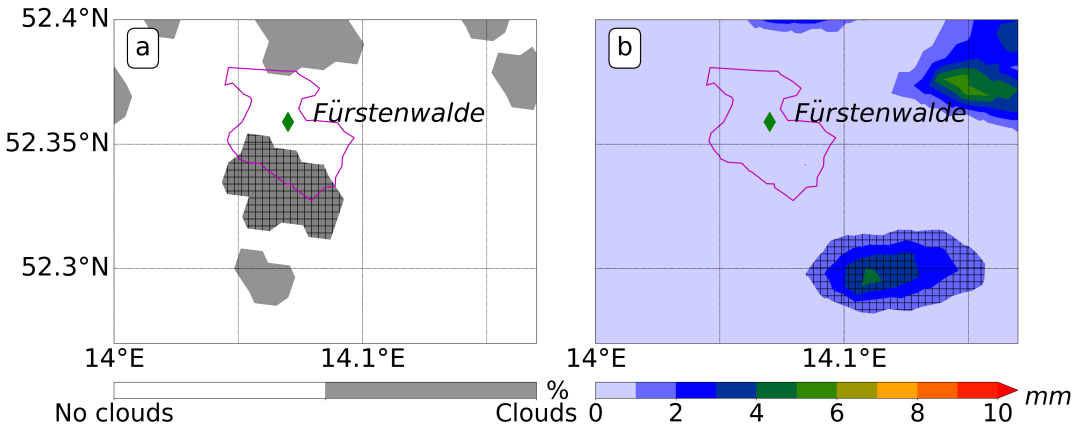

Figure 7.5.: Cloud cover at 1100 UTC (a) and the precipitating cell at 1200 UTC (b) in $\Delta_{625\,m}$ of case over A1, dated 26 July 2012. The magenta coloured solid lines enclose the area of Fürstenwalde. The investigated cloud is indicated by crossed lines.

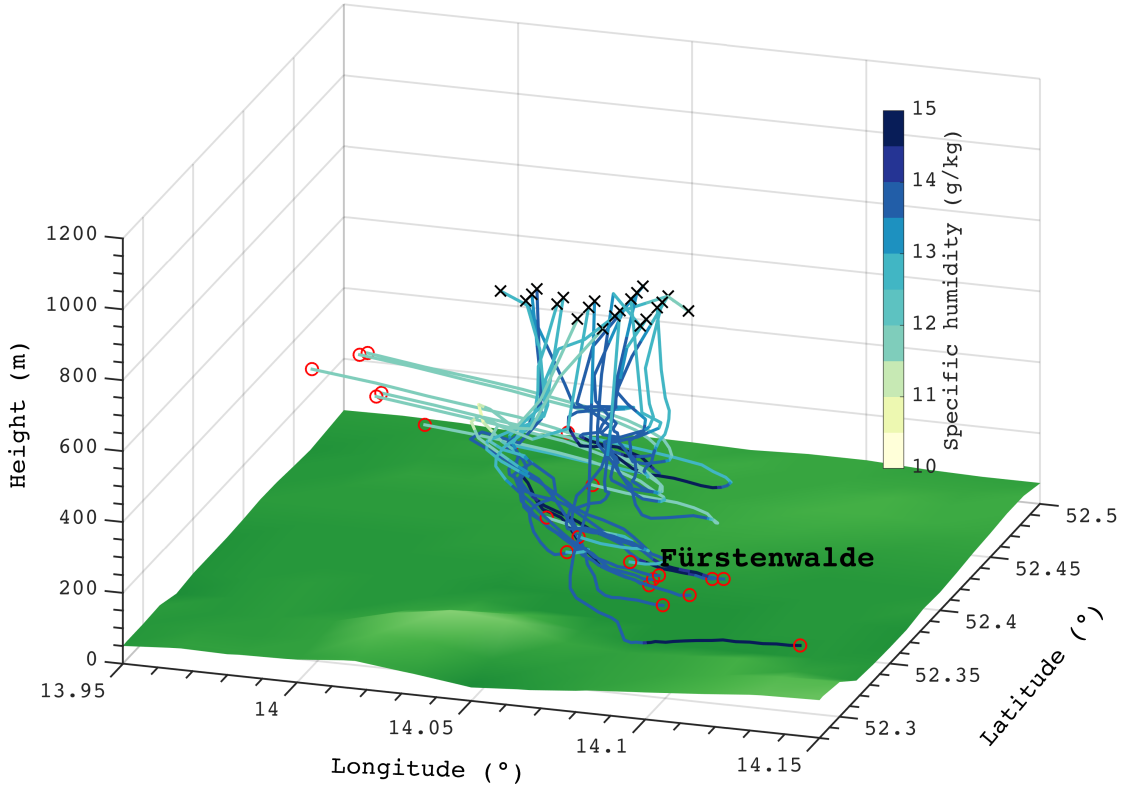

Figure 7.6.: Backward Lagrangian trajectories using LAGRANTO in Δ_{625m} of case over A1, dated 26 July 2012. The black crosses denote the starting points at the cloud base at 1130 UTC and the red circles denote the end points of trajectory integration until 0700 UTC. The colours along the trajectories indicate specific humidity ($g\,kg^{-1}$) and the colour in the xy plane denotes orography.

surface sensible and latent heat fluxes, the corresponding SMRCs are calculated again (Equation 7.6). In the period before the cloud formation, i.e. at 1110 UTC, the TAI and the horizontal wind speed at 10 m show considerably stronger influence on H in comparison to the net radiation, orography and SMI (Figure 7.8a). As expected H shows a considerable negative correlation ($\simeq$ -0.5) with TAI and a positive correlation ($\simeq$ +0.3 to 0.4) with wind speed at 10 m while H is only weakly correlated with the other variables ($\simeq$ +0.1). Moreover, E shows a strong positive correlation with TAI and 10 m wind speed in the order of $\simeq$ +0.7 and $\simeq$ +0.4, respectively, while E is weakly correlated with the other factors during this period (Figure 7.8b). That means the reduction in vegetation or plant cover (TAI) in the city results into higher H, i.e. more warming of surface in comparison to the surrounding. This differential heating creates a horizontal pressure gradient and

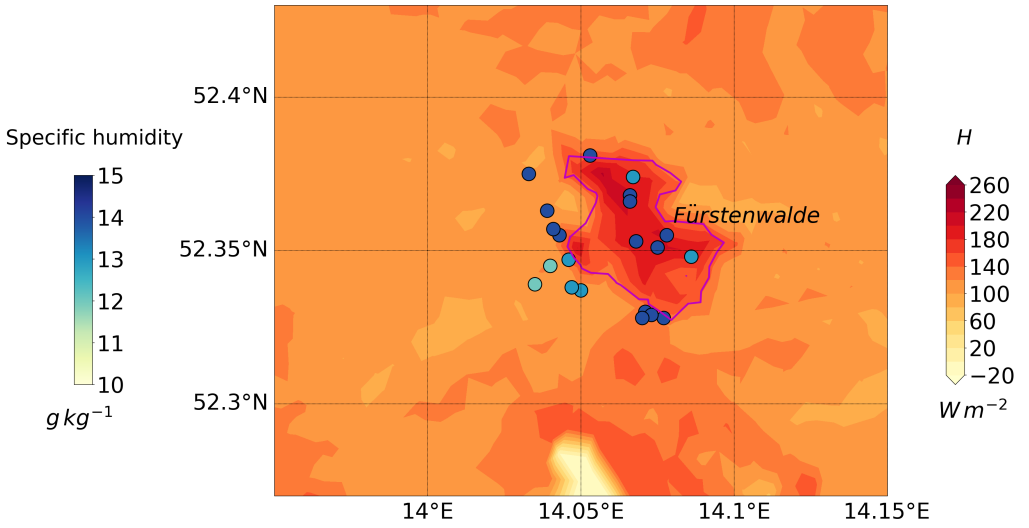

(a)

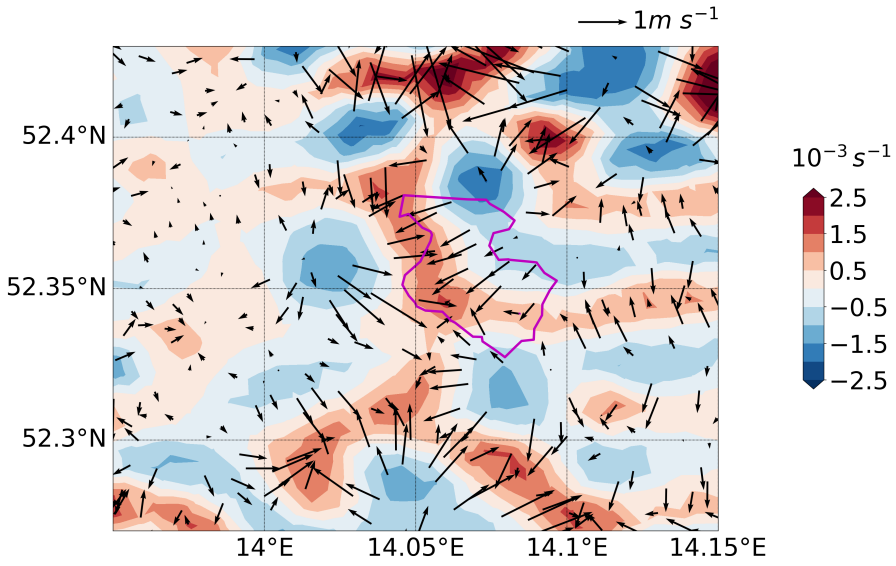

(b)

Figure 7.7.: Surface sensible heat flux (colour shaded) and the trajectory points (circles with specific humidity in the colour shade) (a), wind convergence (colour shaded) and wind vectors (b) at 10 m (b) at 1030 UTC, in $\Delta_{625\,m}$ of case over A1, dated 26 July 2012. The magenta coloured solid lines enclose the area of Fürstenwalde. The negative sensible heat flux $\simeq -20\,W\,m^{-2}$ indicates the Scharmützelsee.

the moist parcels coming from the surrounding converge over the areas of high sensible heat flux (Figure 7.7a) and trigger the convection. Another example of triggering process based on the soil type heterogeneity is identified over A3 for the case dated 12 Aug 2015 (Figures B.23, B.24, B.25).

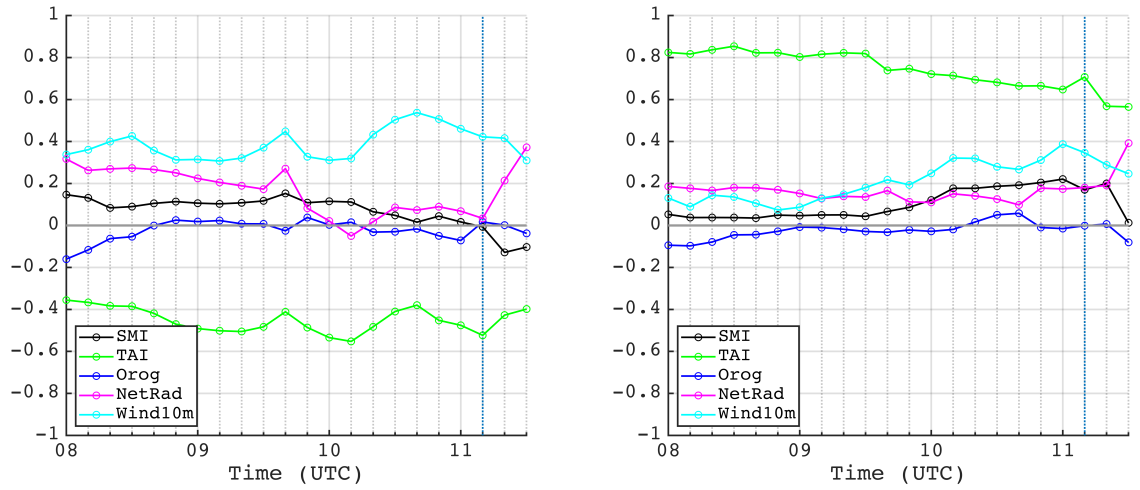

Figure 7.8.: The areal mean SMRC for SMI in black, TAI in green, orography (Orog) in blue, net radiation (NetRad) in pink, and horizontal wind at 10 m (Wind10m) in cyan with respect to H (a) and E (b), respectively for $\Delta_{625\,m}$ of case over A1, dated 26 July 2012. The vertical dotted line shows the onset of first cloud in the investigation region.

The above section describes the identified land surface-based triggering mechanisms using an example of one of the grid spacings ($\Delta_{625\,m}$) of the control runs (for details of the simulation setup see Section 5.5). Triggering of the two precipitating cells was observed in all the LES grid spacings of control runs ($\Delta_{156\,m}$ to $\Delta_{625\,m}$), although the cells were slightly different in shape. The question is, however, how does the modulation in land-surface resolution impact the triggering of these processes. To investigate this, an overview comparison of the lake breeze and UHI generated clouds is provided for the land-surface sensitivity experiments i.e., LO_1250 m (Figure 7.9d-f) and LO_5000 m (Figure 7.9g-i) with respect to control run ($\Delta_{625\,m}$, Figure 7.9a-c). With respect to the sensible heat flux patterns, the results show that the lakes and the city are still resolved in the LO_1250 m simulations - at least their substantial parts (Figure 7.9d-f) - but not in LO_5000 m run (Figure 7.9g-i). This is, because the spatial heterogeneity of these land-surface structures (water bodies, city) range in between 4-5 km, for which on one hand the land-surface resolution of 1250 m is sufficient, and on the other hand at this spatial heterogeneity scale thermally induced circulations often tend to be generated (Shuttleworth, 1991). However, as the land-surface resolution 5000 m does not resolve these patterns anymore, secondary-circulations systems are miss-

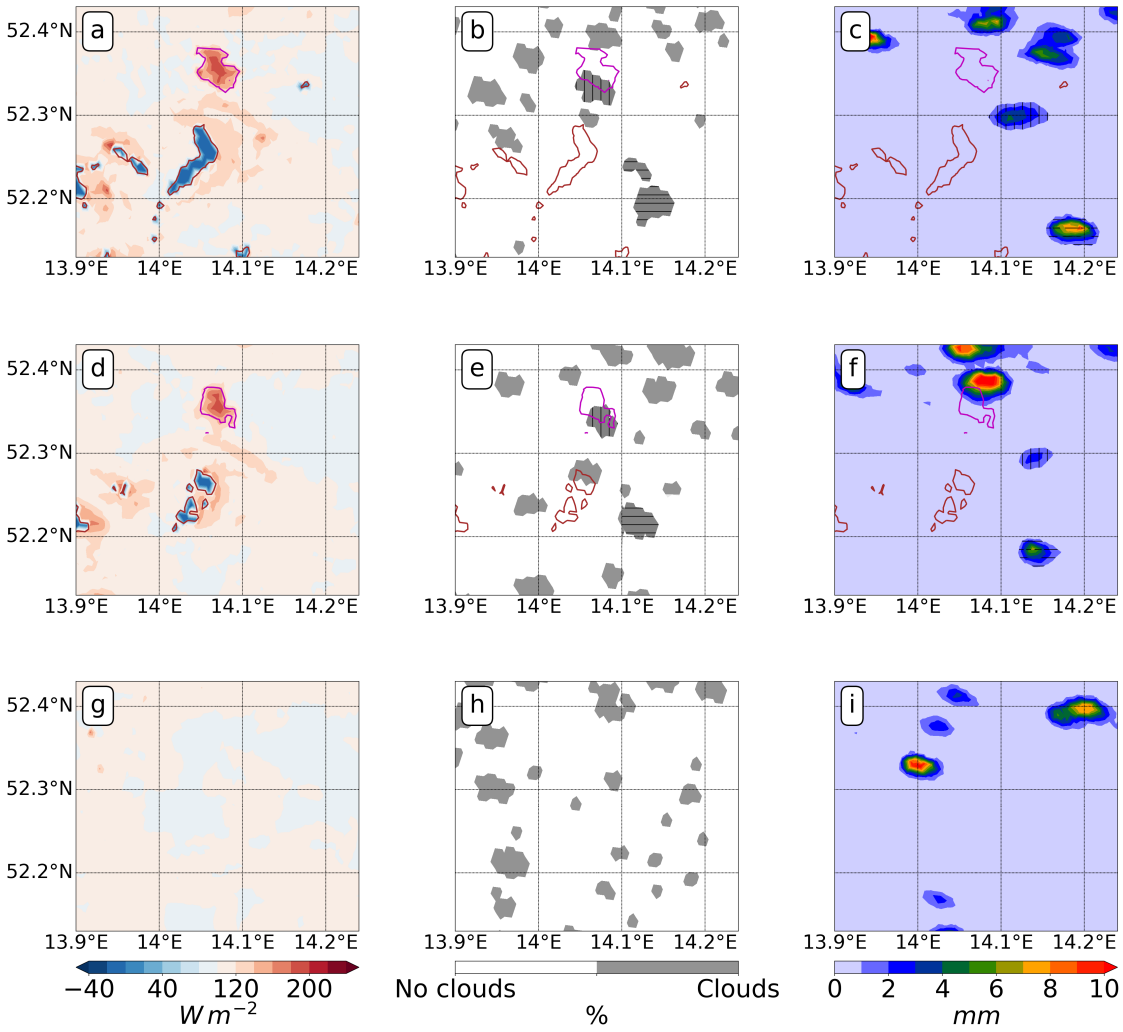

Figure 7.9.: Spatial patterns of surface sensible heat flux at 1000 UTC, low-level clouds 1130 UTC, and accumulated total precipitation at until 1230 UTC in $\Delta_{625\,m}$ of the control run (a-c), LO_1250 m (d-f), and LO_5000 m (g-i) of case over A1, dated 26 July 2012. The clouds and precipitating cells marked with horizontal and vertical bars denote the respective cloud and the resulting precipitation through the lake-breeze circulation and UHI effect, respectively. The brown solid lines enclose the areas with lakes.

ing in the LO_5000 m simulations as well as the corresponding precipitating cells (Figure 7.9g-i). Nevertheless, precipitating cells of similar size and intensity are generated in other areas i.e. other triggering processes are active because the environmental conditions are favourable in the investigation area. This, in turn, agrees with the finding that the areal mean precipitation of LO_5000 does not differ that much from the corresponding control run ($\Delta_{625\,m}$) (Section 6.2).

7.1.2. Orographically-induced circulation

Theoretical background

Orography may generate the dynamically-driven clouds through orographic lifting, which is needed to overcome the CIN and release the CAPE. This process depends upon the shape and size of the obstacle (mountains) and the background wind. Moreover, the thermally driven daytime upslope and up-valley winds in the lowest atmospheric layers can occur. The genesis of these processes are well studied and identified (Steinacker, 1984; Atkinson, 1981; Markowski and Richardson, 2011; Zardi and Whiteman, 2013). The prerequisites are calm and cloud-free conditions so that the daytime absorption of radiation by the sloping surface creates warming of air close to the surface (Whiteman, 2000). By that, the air near the sloping surface becomes warmer than the air in the free atmosphere at the corresponding height above sea level. Based on the hydrostatic principle, a horizontal pressure gradient will be induced. This generates a low-level horizontal pressure gradient, under which upslope wind occurs. Further, valley winds are thermally-induced circulations. They are primarily driven by pressure gradients, induced due to along-valley temperature differences Whiteman (1990). These differences can be explained by the so-called geometric or Topographic Amplification Factor (TAF) (e.g., Steinacker (1984); McKee and O'Neal (1989); Whiteman (2000)). The volume of the air in a box above a valley atmosphere is less than over flat terrain. That means during the daytime, the same surface turbulent heat and moisture fluxes would result in a greater increase of heat and moisture in the air over the valley than over the adjacent foreland and results in up-valley wind systems.

The following section discusses typical examples of thermally-driven circulation systems which are orography based and superposed with others. Unlike for the flat terrain cases where $\Delta_{625\,m}$ is sufficient to show the land-surface properties based circulations, the $\Delta_{156\,m}$ results are shown for the examples of orography-based triggering processes as it comprehensibly represents the fine orographic based circulations.

Superposition of slope- and soil-type heterogeneity-based circulation

An example of such an orographically-induced circulation which trigged convection identified in a case simulated over the orographic area A2 dated 09 June 2018 is discussed (details of the case is discussed in Section 3.2). On this day, the convection formed over the Harz mountain range. The day has east-southeasterly large-scale wind, and the first cloud was formed at 0920 UTC. over the mountain ridge. Figure 7.10 shows the orography, soil type, cloud cover at 1010 UTC and the resulting accumulated precipitation of the system until 1200 UTC. The orography indicates that the highest peaks are situated in the western part of the Harz mountain, like its highest peak, the Brocken (1141 m) (Figure 7.10a). The dom-

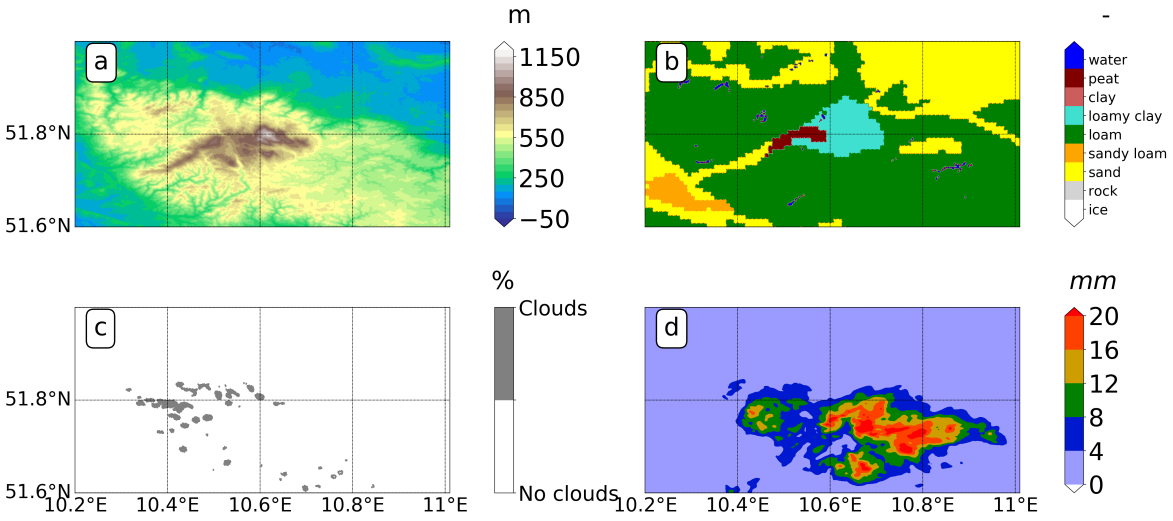

Figure 7.10.: Orography (a), soil type (b), low-level cloud cover at 1010 UTC (c) and the resulting accumulated precipitation at 1200 UTC (d) in Δ_{156m} of case over A2, dated 09 June 2018.

inating soil type in the Harz is loam (Figure 7.10b). However, in the eastern part of the peaks is loamy clay, while a stripe of peat stretches to the west. In the flat areas around the Harz mountain range, sand and sandy loam is the dominating soil type. At 1010 UTC, convective clouds are mainly present over the highest peaks of the Harz mountain (Figure 7.10c). Further, Figure 7.10d shows that this is the

region where precipitation occurred in the subsequent 2 hours. The precipitation pattern covers most of the area of the Harz mountain ridge.
The conditions, which led to the simulated precipitation are as follows: the sensible heat flux distribution at 0830 UTC shows higher values over the Harz than over the surrounding flat land (Figure 7.11a). Maximum values of up to 280 $W\,m^{-2}$ can be found over the spot with peat in the west of the Brocken. Analysis of the dependence of the turbulent fluxes on the aforementioned parameters indicates that H is considerably correlated with orography ($\simeq$ +0.40) and SMI ($\simeq$ -0.38), which is also reciprocated with a considerable correlation of E with orography ($\simeq$ -0.42), SMI ($\simeq$ +0.40), and TAI ($\simeq$ +0.38) (Figure 7.13). That means the orography together with the soil type results in the simulated surface heat flux pattern with its maximum over the area of mountain crest where loamy clay and peat can be found. The corresponding development of lower pressure in this area then led the parcels to converge and to trigger clouds.
As evident from the near-surface wind field (Figure 7.11b), up-slope winds on the slopes of the Harz have developed already at 0830 UTC as well as up-valley winds in some of the valleys which extend from the foreland to the inner centre of the Harz, like the one in the southwest.
Figure 7.12 shows the backward trajectories of the parcels with a starting position at cloud base ($\approx$ 1700 m) at 1110 UTC and then integrated backwards until 0700 UTC. The 3-D view of the backward trajectories of the investigated convective system shows that the air parcels originate from near-surface positions of the surrounding flat forelands of the Harz in the north and south. As transported upwards along the slopes of the Harz by upslope winds, they reach the top of the Harz, as evident from the position of the trajectories at 0830 UTC. Additionally, one branch of trajectories comes along the valley in that is positioned in the the southwest slope of the Harz (Figure 7.11a) and finally feeds the convective cloud. At that time, all trajectories are concentrated within an area with a diameter of about 15 km (Figure 7.11a).

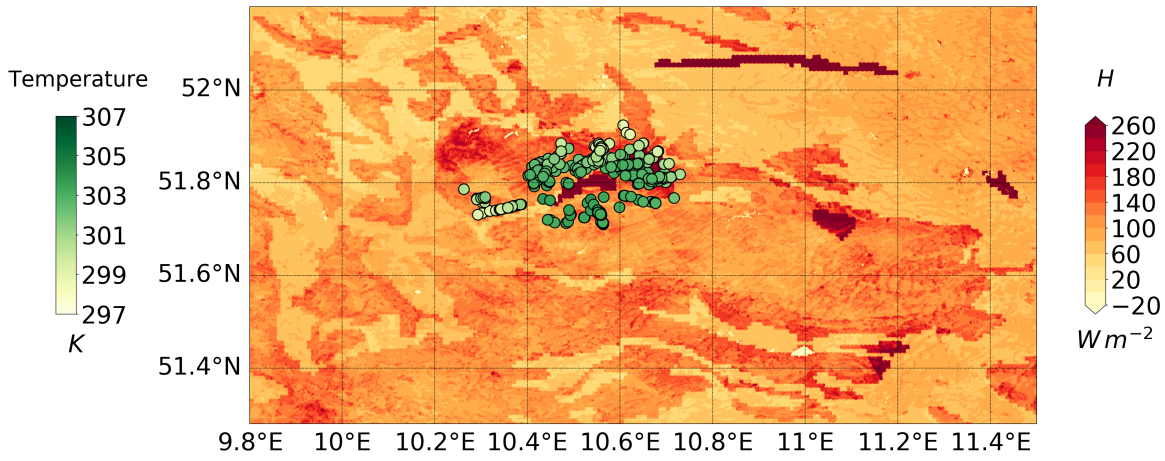

(a)

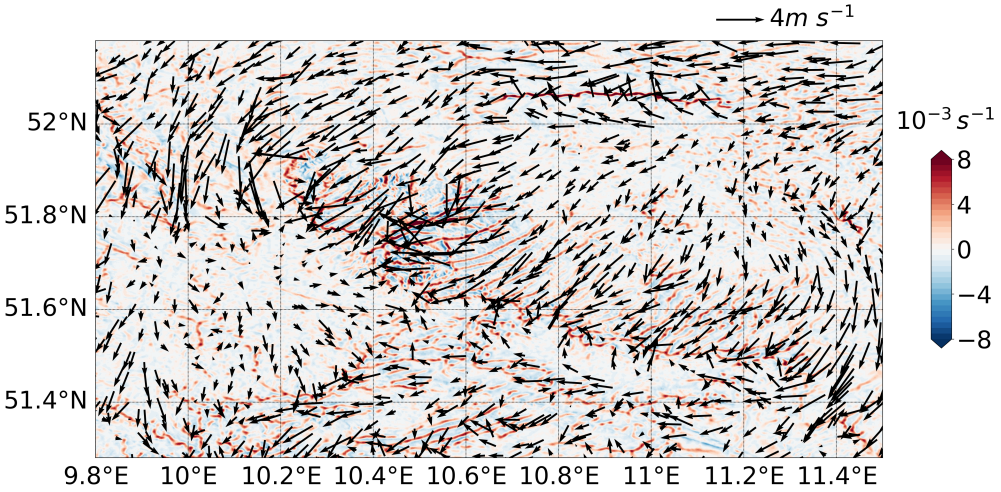

(b)

Figure 7.11.: Surface sensible heat flux (colour shaded) and the trajectory points (circles with air temperature in the colour shade) (a), wind convergence (colour shaded) and wind vectors at 10 m (b) at 0830 UTC, in Δ_{156m} of case over A2, dated 09 June 2018.

7.2. Secondary triggering

7.2.1. Cold pools

As the name suggests, cold pools are the evaporatively-cooled regions of downdraught air. They typically form in the boundary layer as a result of convective precipitating systems. The evaporating rain and hydrometer loading creates the density anomaly (Torri et al., 2015). In this way, the lateral expansion of this cold and dry

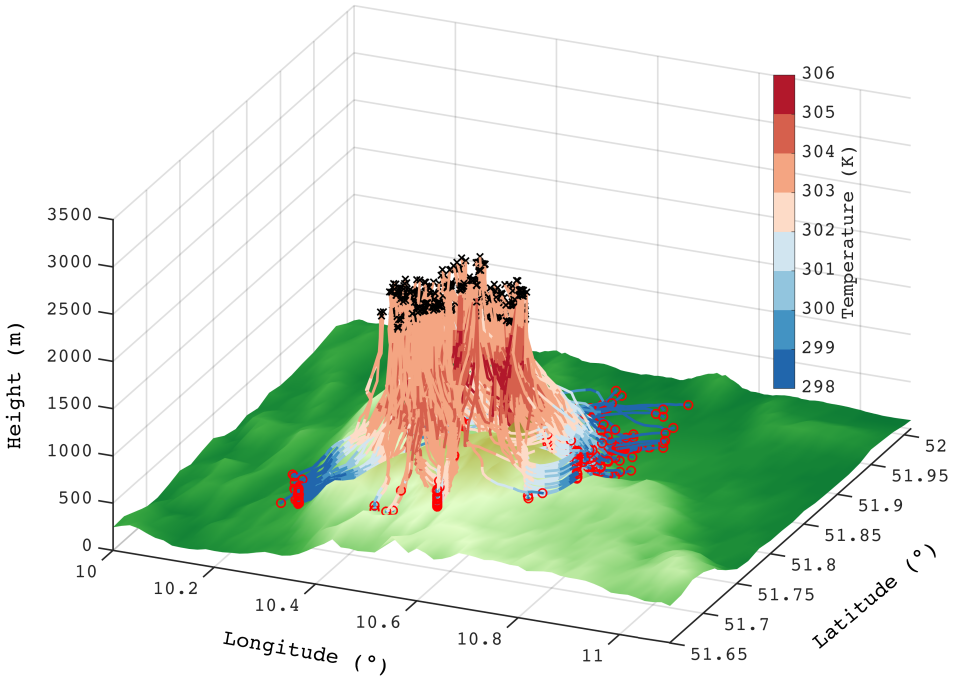

Figure 7.12.: Backward Lagrangian trajectories using LAGRANTO in Δ_{156m} of case over A2, dated 09 June 2018. The black crosses denote the starting points at the cloud base at 1010 UTC and the red circles denote the end points of trajectory integration until 0700 UTC. The colours along the trajectories indicate the air temperature (K) and the colour in the xy plane denotes orography.

region is governed by the density current dynamics (Charba, 1974). This cold air creates a region of enhanced surface pressure which further generates a horizontal pressure gradient force that drives the outward flow of cold pools and thus forms an outflow boundary called as gust front. Therefore, the ideal parameter for the identification of these density currents (cold pool) is the density or virtual potential temperature (Emanuel, 1994). This is also a prognostic variable used in ICON and a model output field, which is defined as:

$$\theta_v = \theta[1 + (\frac{R_v}{R_d} - 1)q_v - \sum_{k \neq v,d} q_k] \tag{7.7}$$

where θ_v is the virtual potential temperature, θ is potential temperature, R_d and R_v are the gas constant of dry air and water vapour, having values 287.04 $J\,kg^{-1}\,K^{-1}$ and 461.5 $J\,kg^{-1}\,K^{-1}$, respectively. q_v and q_k are the specific humidities of water vapour and condensate water species, respectively. Cold pools play a crucial role

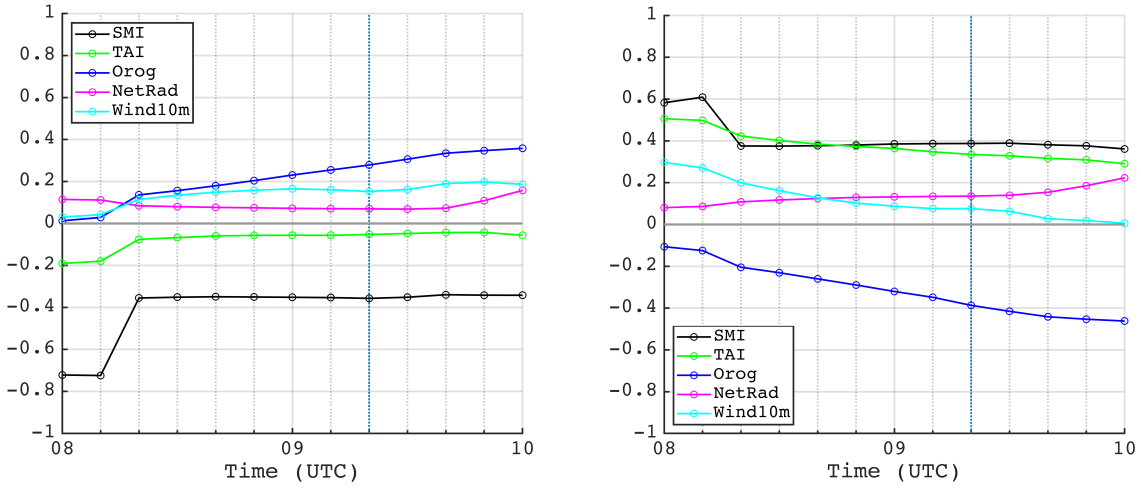

Figure 7.13.: The areal mean SMRC for SMI in black, TAI in green, orography (Orog) in blue, net radiation (NetRad) in pink, and horizontal wind at 10 m (Wind10m) in cyan with respect to H (a) and E (b), respectively for $\Delta_{625\,m}$ of case over A2, dated 09 June 2018. The vertical dotted line shows the onset time of first cloud in this investigation region.

in the convective organisation of clouds and therefore, modulating the coupling between the CBL and free troposphere.

Moreover, cold pools aid the formation of deeper, wider and more buoyant clouds in association with higher precipitation rates, which further lead to the creation of stronger cold pools (Böing et al., 2012). According to Weisman and Rotunno (2004), cold pools also play a crucial role in the maintenance of long-lived squall lines. They presented the analysis of the simplified two-dimensional vorticity - stream function model, which confirms the role of shear in the modulation of flow around the cold pools. This study proposed that the buoyancy gradient at the cold pool edge generates the horizontal vorticity at the gust front, which can easily interact with the vorticity generated by the environmental wind shear and result into vertical updraughts. (Rotunno et al., 1988; Weisman and Rotunno, 2004). This sort of lifting is called as mechanical forcing, where the near-surface ambient air is lifted by the dense cold pool air mass, and thus initiates new convection. The second mechanism through which cold pools can initiation new convection is thermodynamic forcing. Necessarily, cold pools can trigger convection also in an environment of low vertical wind shear. The decaying cold pool could leave moisture behind via its precipitating downdraught, and this accumulated moisture

may also provide enough buoyancy so that a small forcing could also trigger a new convection (Tompkins, 2001). This process is termed as thermodynamic forcing. Thermodynamic forcing creates the region of favourable convection initiation, and the mechanical forcing is needed in order to lift the parcels so that it can overcome the CIN and reach the LFC (Torri et al., 2015; Jeevanjee and Romps, 2015).
Though the cold pools are itself the structures developed after the precipitating system, cold pools can also trigger new convection through other different kinds of forcings, for example, by intersecting cold pools itself. Therefore, cold pools result in "primary-generation" precipitation initiating "secondary-generation" shallow to deep clouds or resulting in the organisation of clouds. The convective initiation can occur preferably at the region of localised differences in the turbulent fluxes, low-level diabatic heating and moisture transport. This develops a pressure gradient over the area and therefore locally enhanced low-level wind convergence. According to Atkins et al. (1998) and Bluestein et al. (1990), the local deepening of a moist layer tends to occur at the intersection point of a dryline and an outflow boundary (cold pool). The outflow carries the gust front at its leading edge which lifts the air parcels ahead of it to the LCL and acts as a primer element for the formation of deep convection.

Main characteristics of cold pools

As discussed in Section 6.3, after self-aggregation of shallow cumulus clouds, precipitation occurred in Δ_{156m} in the east of Berlin and eventually resulted in cold pool formation. Following the general characteristics of cold pools as described in Torri et al. (2015); Drager and van den Heever (2017), Figure 7.14 shows the spatial pattern of θ_v anomaly, q_v anomaly, and vertical velocity at $\approx$1 km, giving an example of the cold pool formation in Δ_{156m} for case simulated over A1, dated 26 July 2012. The characteristics are:

- The innermost region is colder (by $\approx$1K), negatively buoyant and drier than the average (or boundary layer air) (Figure 7.14a,b).

- Cold pool edges characteristically pose negative temperature anomaly and enhanced water vapour than the average (Figure 7.14a,b).

- Additionally, the cold pools are associated with gusty winds (Figure 7.14c), so that the horizontal outflow bounded with the gust front would propagate

with a speed which would be proportional to the density difference, therefore buoyancy, between the cold pool and the environment air.

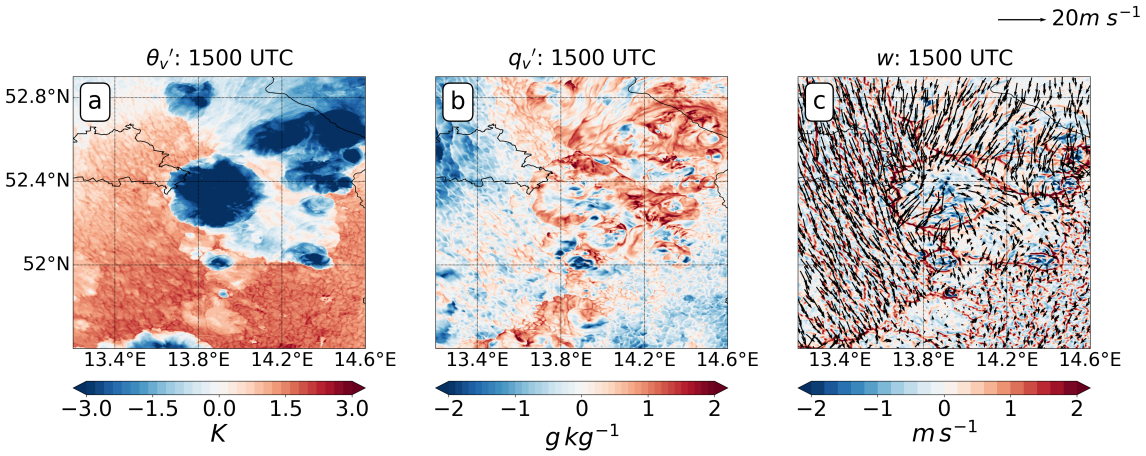

Figure 7.14.: Spatial pattern of virtual potential temperature anomaly $\theta_v{}'$ at 10 m (a), specific humidity anomaly $q_v{}'$ at 10 m, and vertical velocity at ≈1 km (c) at 1500 UTC in Δ_{156m} of case over A1, dated 26 July 2012.

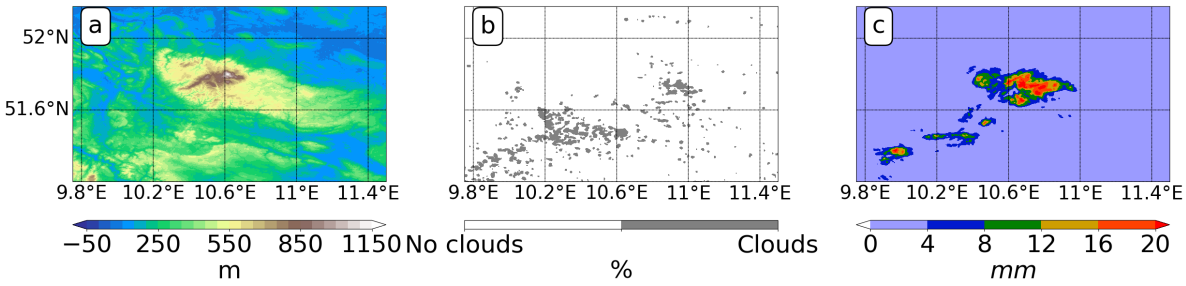

Figure 7.15.: Orography (a), cloud cover at 1250 UTC (b) and the resulting accumulated precipitation at 1500 UTC (c) in Δ_{156m} of case over A2, dated 09 June 2018.

Superposition of orographically-induced wind and cold-pool outflow

In this section, an example of convective precipitation generated through low-level wind convergence is discussed for Δ_{156m} of case A2, dated 09 June 2018.

The convection developed in the southwest of Harz mountains (Figure 7.15). This convective precipitation is in continuation with the above discussed up-slope wind example (Section 7.1.2). The diurnal cycle of the accumulated mean precipitation of this day shows two periods with precipitation events (Figure B.10). The precipitation during the first period (1100 to 1400 UTC) is the result of clouds formed over the Harz mountains due to primary triggering processes (Section 7.1.2). This is followed by precipitation in the second period (1500 to 1800 UTC). It is the result of clouds triggered in the southwest of Harz due to the superposition of primary and secondary triggering mechanisms. This region comprises of moderately elevated areas with some valleys (Figure 7.15a). The clouds are formed at 1200 UTC (Figure 7.15b). With ambient east-southeasterly wind, these clouds precipitated out around 1320 UTC near the southeastern tips of the valleys of this region (Figure 7.15c) and resulted in precipitating cells with a maximum precipitation core of ≈22 mm. To understand the triggering mechanisms of these clouds, the low-level wind field and wind convergence are shown in Figure 7.16. There are three branches of wind causing wind converging in the southwest of the Harz mountain. The first branch is the flow deflected by the Harz mountain itself, coming from southeast. To determine why the flow on this day goes around instead of over the mountain can be explained by the Froude number $Fr = U/Nh_0$ (Smith, 1989), where U is the horizontal wind speed, h_0 the height of the obstacle and the Brunt-Vaisala frequency $N = \sqrt{\frac{g}{\theta_v}\frac{\partial \theta_v}{\partial z}}$. A Froude number of Fr > 1 indicates that the flow has enough kinetic energy to surmount the mountain, while Fr < 1 shows blocking of the flow so that the flow goes around the mountain. The mean Fr for the layer (≈240 m a.g.l.) at 1000 UTC is ≈ 0.41. This explains why the flow goes around the Harz in the lowest layers rather over the mountains, and this deflected southeasterly wind forms the first branch of the low-level wind convergence (Figure 7.16). Most likely, the deep convective cell over the Harz also supports a deflection of the approaching southeasterly wind. The second branch consists of the valley winds generated in the valleys located in the west of Harz mountains. These valley winds are further assisted by the wind flowing around the Harz in the north and turning into a northwesterly wind at the western tip of the Harz (Figure 7.16). Lastly, the third branch generating the wind convergence is the cold pool outflow. The deep convective cells which formed over Harz mountains subsequently resulted into cold-pool formation. The gust front associated with

the cold pool assisted the wind convergence in the region southwest of the Harz mountain, which ultimately triggers the cloud formations. The contribution of the three flows contributing to the wind convergence can also be seen evidently in the backward trajectories calculated for these clouds. The backward trajectories are

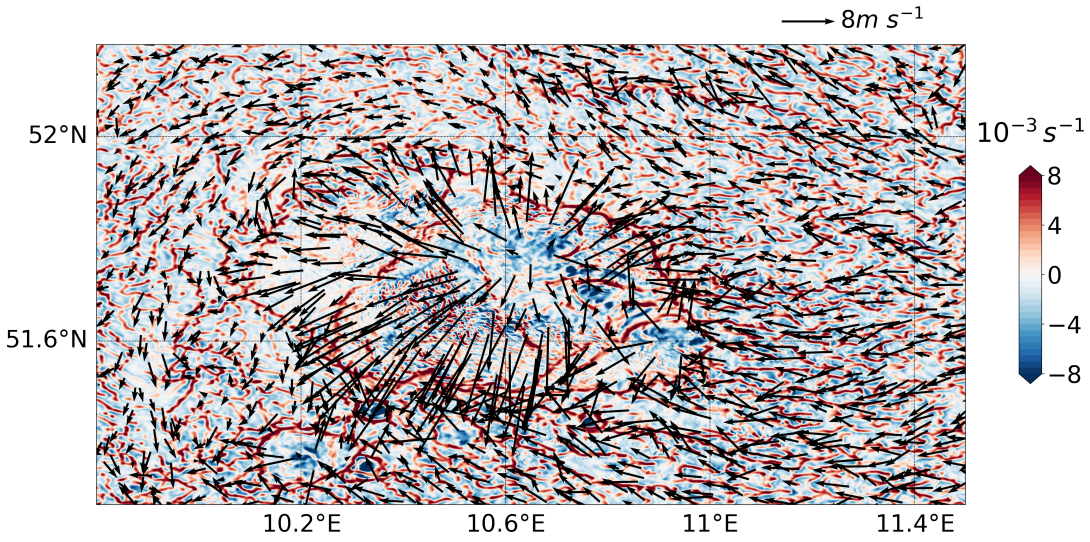

Figure 7.16.: Wind convergence (colour shaded) and wind vectors at ≈200 m at 1230 UTC, in Δ_{156m} of case over A2, dated 09 June 2018.

initiated from cloud base at 1250 UTC and integrated backwards until 0900 UTC (Figure 7.17). The trajectory lines follow the southeasterly wind flowing around the Harz, the northerly valley winds, and the cold air parcels originated from the ridges of Harz mountain.

The three branches can be further investigated through the positioning of these trajectory points relative to the surface sensible heat distribution (Figure 7.18). At 0900 UTC the first set of warm air parcels along the southern flank of Harz can be seen which constitutes the deflected east-southeasterly wind in this region (Figures 7.16 and 7.18a). The second set is the trajectory points located along the northwest - southeast oriented valley axis and which are colder and denser, travelling in the southeast direction (Figures 7.16 and 7.18a). As a result of precipitation occurrence over the ridge of Harz, the cold pool forms and at 1200 UTC the cold and moist parcels originated from the cold pool itself assisted the convergence line

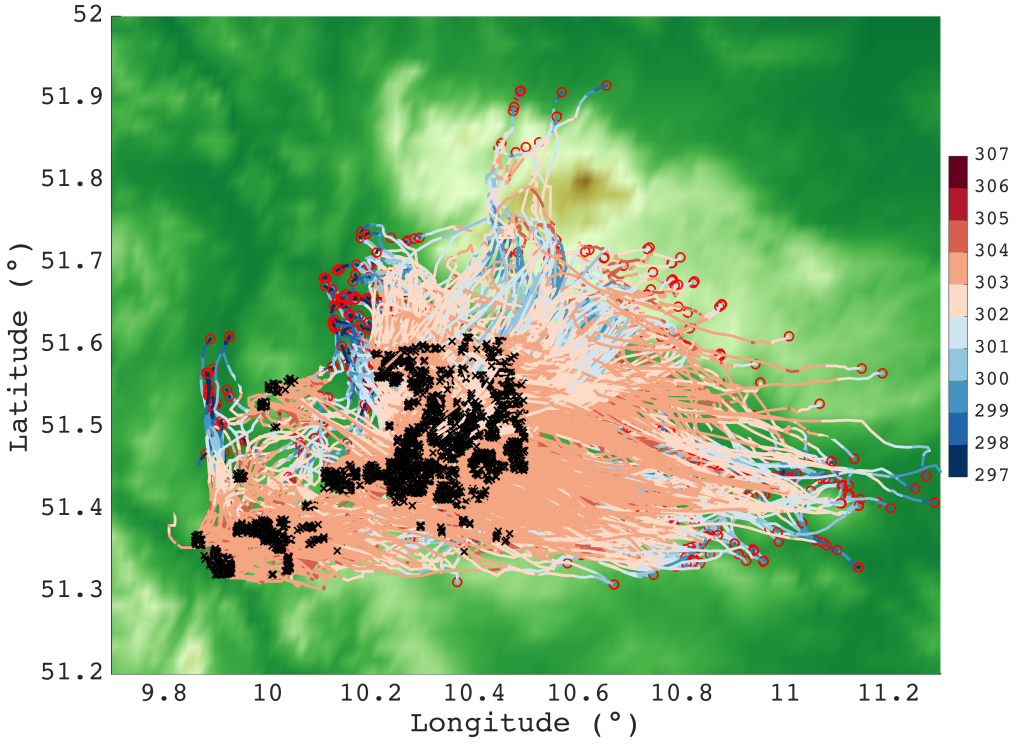

Figure 7.17.: Backward Lagrangian trajectories using LAGRANTO in Δ_{156m} of case over A2, dated 09 June 2018. The black crosses denote the starting points at the cloud base at 1250 UTC and the red circles denote the end points of trajectory integration until 0900 UTC. The colours along the trajectories indicate the air temperature (K) and the colour in the xy plane denotes orography.

in the southwest of Harz (Figures 7.18a and 7.18b). The low-level wind convergence zones originate from three different sources attributed to the triggering of these clouds. The wind flow over this region is summarised in Figure 7.19. At 0900 UTC the ambient east-southeasterly and the northwesterly up-valley wind already exist with an average wind speed of 3 and 4 ms^{-1}, respectively. At 1200 UTC, the strong northeasterly wind (>8 ms^{-1}) originated from the cold-pool outflow, the northwesterly wind which indicates the up-valley wind, and the ambient east-southeasterly wind exist. This superposition of lee-side wind convergence and cold-pool outflow in the southwest of Harz resulted in cloud formation over this region. These thermally-induced and orography-based triggering mechanisms over A2 and A3 are identified in all of the LES grid spacings. But they show slight differences in the location of triggering of clouds depending upon the underlying land-surface resolution. As such, the dominating triggering factors over A2 like the soil type inhomogeneity, the valleys are almost resolved at 5000 m and

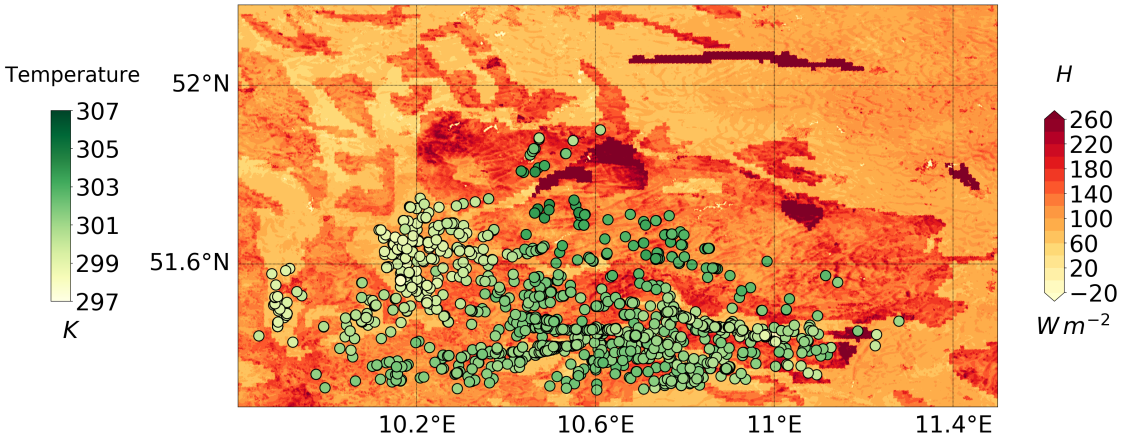

(a)

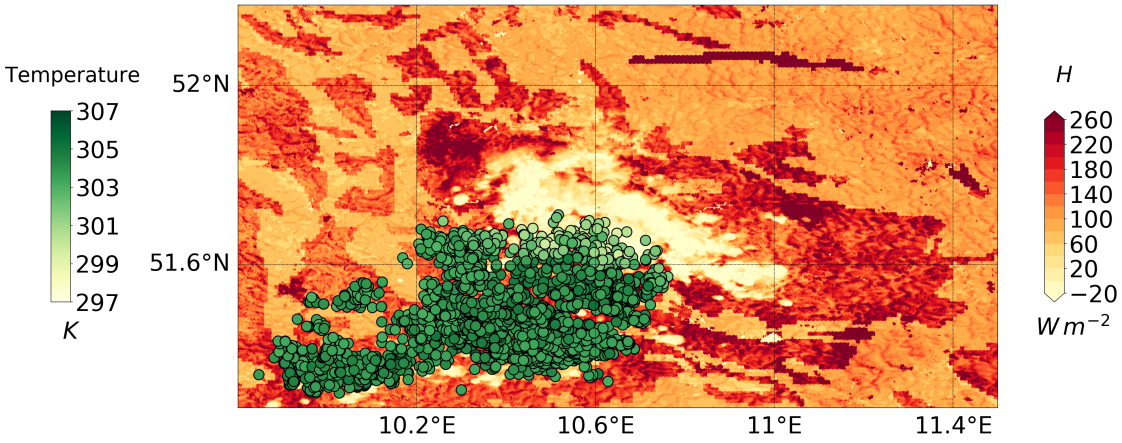

(b)

Figure 7.18.: Surface sensible heat flux (colour shaded) and the trajectory points (circles with air temperature in the colour shade) at 0900 UTC (a) and 1200 UTC (b) in Δ_{156m} of case over A2, dated 09 June 2018.

1250 m. Therefore, the modification in the land-surface resolution over this scale has a small effect on the triggering mechanisms (not shown) and the precipitation patterns (Figure B.14). In particular, the coarsening of land-surface resolution from 156 m to 1250 m results in a relative precipitation difference of 10 % and up to 25 % with 5000 m (Figure 6.9b). However, the resulting precipitation varies up to 75 % across the given LES grid spacings (Figure 6.9a) (lower for Δ_{156m} and higher for Δ_{1250m}) as the clouds are smaller in size and therefore, exposed to stronger evaporative cooling (Section 6.3).

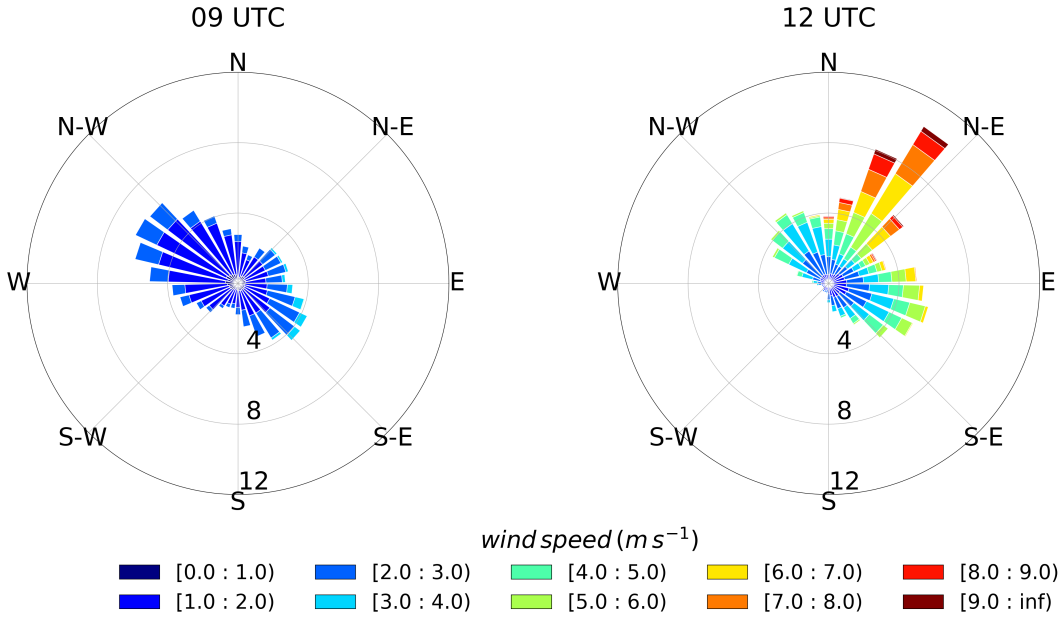

Figure 7.19.: Wind rose diagram for wind speed and direction over a region of convergence zone in the south west of Harz in $\Delta_{156\,m}$ of case over A2, dated 09 June 2018.

Lesson drawn

The above-mentioned thermally-induced and orography-based triggering mechanisms over different areas are identified in all of the LES grid spacings. Differences depend on whether the relevant land-surface heterogeneities are resolved by the model grid spacing or not. Therefore, the land-surface resolution determines if precipitation is triggered and how the precipitation patterns look like. One very process of precipitation initiation is associated with the superposition of different trigger mechanisms, as described in the example for the Harz mountain, where orographically-generated convergence and a cold-pool outflow are responsible for convective precipitation.

8. Summary and conclusions

ICON provides an advanced tool to study its modelling skills concerning convective precipitation in the LEM mode. This investigation is done within the framework of the HD(CP)^2 project. More specifically, as part of the synthesis module (S4: land surface heterogeneity) of HD(CP)^2 . The focus of this study is to investigate the impact of model grid spacing and land-surface resolution on clouds and precipitation using ICON-LEM simulations and to determine the processes which result into the differences across model grid spacing (Δ_h). It furthermore explores the capability of ICON - in dependence of grid spacing and land-surface resolution - to simulate those processes, which are responsible for the triggering of convective precipitations. At first, the geographical areas with a hierarchy of orography and associated deep convection Germany-wide are selected. These three regions are i) the flat terrain near Berlin (A1), ii) the isolated mountain range in the central part of Germany, called as Harz mountains (A2), and iii) the complex terrain, the Black Forest mountains (A3). Six suitable days with low synoptic forcing, two for each area, are selected. After selecting the areas and suitable cases, the ICON-LEM simulations are designed with six model grid spacings in a nested setup: $\Delta_{5000\,m}$, $\Delta_{2500\,m}$, $\Delta_{1250\,m}$, $\Delta_{625\,m}$, $\Delta_{312\,m}$ and $\Delta_{156\,m}$ with the same model configuration. $\Delta_{5000\,m}$ and $\Delta_{2500\,m}$ use NWP turbulence and diagnostic cloud cover schemes, whereas $\Delta_{1250\,m}$ to $\Delta_{156\,m}$ use LES turbulence and grid-scale cloud cover schemes. Those simulations along the line from $\Delta_{5000\,m}$ to $\Delta_{156\,m}$, where the model grid spacing and land-surface resolution changes simultaneously are designated as control runs. The control run $\Delta_{156\,m}$ is named reference run, and all results are compared with respect to this simulation. Moreover, the land-surface sensitivity experiments at a scale of 1250 m and 5000 m (L_$<res>$, O_$<res>$ and LO_$<res>$) have been performed in order to understand the relative impact of model grid spacing (Δ_h) and land-surface resolution on convective precipitation. That gives in total six sets of control runs and 30 sets of land-surface sensitivity experiments.

In the first step, the variability of the land-surface heterogeneity of the areas across the given grid spacings is quantitatively described. For that, the areas have

been classified using the area-mean Coefficient of Variation (CV) of orography, soil type and TAI resolved across the selected range of model grid spacings for all areas (A1, A2 and A3). The results show that TAI values have the strongest variability than orography and soil type. That means TAI could pertain a considerable impact on the spatio-temporal behaviour of the locally-induced precipitation.
Concerning the first science question, i.e. the impact of model grid spacing and land-surface resolution on clouds and precipitation, the results are based on area-mean values calculated for the three geographical regions with different degree of orographic complexity. The results show that the areal average of accumulated precipitation for most of the cases decreases systematically across the LES grid spacings from $\Delta_{1250\,m}$ to $\Delta_{156\,m}$. More specifically, the differences of the areal mean precipitation between the control runs ($\Delta_{1250\,m}$, $\Delta_{625\,m}$, $\Delta_{312\,m}$) and the reference run normalised by the reference run can be quite considerable, i.e. the values are in the range of -26 to 400 % with the 75th percentile of 155 %. It is also found that the precipitating cells in $\Delta_{1250\,m}$ are typically intenser in comparison to the other finer LES model grid spacings. Additionally, the onset time of precipitation can differ by 1 to 2 hours (normally precipitation starts earlier in $\Delta_{1250\,m}$ than $\Delta_{156\,m}$). This is a consistent model behaviour found in the precipitation patterns simulated for all cases.
The differences in the areal mean precipitation due to the modifications of respective land-surface resolutions are considerably small. The relative differences range from about -17 to 37 % with the 75th percentile of 7 % with the land-surface resolution of 1250 m and increases to a range of -17 to 49 % and the 75th percentile of 22 % with the land-surface resolution of 5000 m. These ranges hold for all type of sensitivity experiments (L_$<$ *res* $>$, O_$<$ *res* $>$ and LO_$<$ *res* $>$). Comparison of the sensitivity runs with reference run also shows that the onset of convection nearly occurs at the same time, the precipitation patterns are in the same regions, and the intensity of the precipitation cells is very similar.
The comparison of precipitation between NWP runs ($\Delta_{2500\,m}$ and $\Delta_{5000\,m}$) with the other LES control runs ($\Delta_{156\,m}$ to $\Delta_{1250\,m}$) shows that both considerably higher (A1 and A2) or lower (A3) values can occur. For one case in A3, $\Delta_{2500\,m}$ and $\Delta_{5000\,m}$ runs do not generate precipitation, although precipitation exists in the LES runs. To investigate whether this is due to model grid spacing or turbulence scheme, both NWP and LES turbulence closures were applied in an additional $\Delta_{1250\,m}$

run. The comparison shows that already the transition from LES to NWP turbulence parameterization leads to considerably different precipitation behaviour and amount. That means the differences between the step from LES ($\Delta_{1250\,m}$) to NWP ($\Delta_{2500\,m}$) simulations is caused by both the parameterization scheme and model grid spacing.

The above findings pose the question of responsible factors and processes, causing such large differences in precipitation across the model grid spacings (Δ_h). To investigate and answer this follow-up question (second science question), one case from A1 was selected, which indicates quite substantial differences in precipitation between the LES control runs $\Delta_{156\,m}$ and $\Delta_{1250\,m}$. Consistent impacts of model grid spacing (Δ_h) on the onset of CBL- convection and cloud evolution are found.

Additional insight in the cloud evolution and precipitation of $\Delta_{156\,m}$ and $\Delta_{1250\,m}$, which show a similar onset time of CBL clouds but the earlier onset of precipitation in $\Delta_{1250\,m}$ (at 1200 UTC) than in $\Delta_{156\,m}$ (at 1400 UTC), is gained by analysing the macro-physical cloud properties in combination with the heat and moisture budget. It is found that the model grid spacing directly impacts the macro-physical cloud properties. For example, at the beginning of cloud formation, a higher number of small and more scattered clouds are produced in $\Delta_{156\,m}$ than $\Delta_{1250\,m}$. In the subsequent hours, these CBL-based clouds grew deeper into the free troposphere in both of the grid spacings. However, while the thicker clouds in $\Delta_{1250\,m}$ reached levels of 8 km and started to precipitate already at 1200 UTC, in $\Delta_{156\,m}$ the cloud tops remained much lower (approximately 6 km). According to the areal mean budget calculations, in $\Delta_{156\,m}$ in the layer between 3 to 5.5 km the microphysics term indicates a temperature decrease due to evaporative cooling. A horizontal cross-section of the microphysics term at 4 km shows that the areal average evaporative cooling is mainly generated by strong cooling at the edge and shell regions of the clouds. This eventually results in the dissolution of most of the clouds, particular because this layer of the atmosphere is still quite dry. At midday, the dissolution of clouds even suppresses the precipitation in $\Delta_{156\,m}$ but simultaneously enhances the moisture in the corresponding layers where evaporation occurs. Later on, cloud aggregation is an important factor with respect to the onset of precipitation: as soon as small clouds aggregate, the evaporative cooling, which caused the dissolution of clouds by entrainment, reduced considerably

and the clouds could grow deeper into the atmosphere. Subsequently, the cloud clusters result in precipitation, too.

Next, the spatial distribution of precipitation is analysed. This investigation can be seen in conjunction with the third objective of the thesis, i.e. the triggering mechanisms in relation to grid spacing and land-surface resolution. Overall, it is found that the precipitating patterns of the control runs (from $\Delta_{156\,m}$ to $\Delta_{1250\,m}$) are quite similar. This finding also holds for the precipitation patterns between the reference and the corresponding land-surface sensitivity experiments, as long as the land-surface resolution is $\leq$ 1250 m because most of the land-surface patterns are still resolved. However, for land-surface resolutions of 5000 m, the precipitation patterns could be quite different.

Some of the precipitation patterns found in the aforementioned simulations and the responsible triggering mechanisms are then investigated in more detail. The identified triggering mechanisms are classified into two categories, the thermal and dynamic triggering mechanisms which can also be decomposed into primary and secondary triggering, based on the origin of the respective triggering. In the first category, the typical thermal or primary triggering algorithm is due to thermally-induced circulations, generated by land-surface heterogeneity or orography. The examples presented show the corresponding thermally-induced triggering mechanisms, like lake-breeze circulations and UHI, especially active over the flat terrain.

Further, the thermally-induced circulations have been effective together with the orographically-induced circulations. The superposition of two of the triggering processes seems more effective among the identified example, e.g. superposition of upslope-, up-valley winds and soil-type inhomogeneity-based circulations over the Harz mountains. This led to intensive precipitation over the mountain ridge, which eventually formed the cold pools. This further led to the example of the secondary triggering process on this day.

The other category comprises of typical dynamic and secondary-triggering mechanism, for example, triggering from cold pools. In the given example, the triggering is most effective when orographically-induced lee-wind convergence superimposes the convergence zones of the cold-pool outflow. It is shown that the secondary triggering does not occur when one of these preconditions are missing.

The overall comparison of triggering processes in the control runs together with the land-surface sensitivity experiments show that the model grid spacing of $\sim \Delta_{1250m}$ and finer led to a similar set of triggering mechanisms. However, convection which is triggered under high land-surface resolution does not occur when the land-surface resolution is too coarse (e.g. 5000 m) to resolve those land-surface inhomogeneities, which are responsible for the generation of thermally-induced circulations and the subsequent initiation of convection. Therefore, considerable differences can be seen between the triggering processes at land-surface resolutions of 156 m and 5000 m. Additionally, as proved for Δ_{156m} and Δ_{1250m} the processes which are responsible for further development of clouds, like evaporative cooling, could be different and thus be responsible for differences in the precipitation patterns. These differences are reciprocated to the range of variability in the areal mean precipitation which is in the order of ≈ 22 % in total when the land-surface resolution is modified from 156 m to 5000 m.

Acknowledgement

I would like to sincerely thank my supervisor Prof. Christoph Kottmeier for his support and mentoring. I am also very thankful to Prof. Dr. Corinna Hoose for co-supervising this thesis.

I am especially grateful to Dr. Norbert Kalthoff for the outstanding support, mentoring and constructive discussions, for being patient and always taking time to help me throughout this research and also for the opportunity to participate in field campaigns.

I am also thankful to my project colleague and the officemate Dr. Leonhard Gantner for the valuable suggestions and implementing the budget terms in ICON, which has been thoroughly used in this study. Many thanks to PD Dr. Michael Kunz for providing the lightning data. I am also thankful to Dr. Michael Sprenger from ETH Zürich for his assistance in adapting LAGRANTO as per ICON model.

I am very grateful to my working group colleagues and friends for their support and creating a healthy environment at work. Many thanks to Dr. Olga Kiseleva for sharing the office with me, exciting discussions and creating a bright and pleasant atmosphere. I am especially thankful to my coffee mates Lukas Muser and Philipp Gasch for taking care of my supper and the coffee breaks. I am very grateful to Gabi Klinck for her quick and constant support with the technical problems. I wish to thank Dr. Ulrich Corsmeier, Rosalba Gräbner and Doris Stenschke for their help in the administrative things.

This work was funded by the BMBF in Germany as part of the research program 'High Definition Clouds and Precipitation for Climate Prediction— $HD(CP)^2$' (Förderkennzeichen (FKZ): 01LK1506E). I highly appreciate the support of my project colleagues especially Stefan Poll from University of Bonn, Dr. Daniel Klocke and Dr. Günther Zängl from DWD, and Dr. Anurag Dipankar with solving ICON related problems. I wish to thank Prof. Dr. Bjorn Stevens from MPI-M for his helpful discussions during the project meetings.

Finally, I am very grateful to my family and many friends in India, especially my parents for their patience and support, and particularly my little siblings for always cheering me up during my time in Germany.

A. Acronyms

ASTER Advanced Spaceborne Thermal Emission and Reflection Radiometer

BLIDS Siemens lightning information service

BMBF Federal Ministry of Education and Research

CAPE Convective Available Potential Energy

CBL Convective Boundary Layer

CI Convection Initiation

CIN Convective Inhibition

COPS Convective and Orographically-induced Precipitation Study

COSMO COnsortium for small-scale MOdelling

CPMs Convection-Permitting Models

CSIP Convective Storm Initiation Project

CV Coefficient of Variation

DC Deep Convection

DRM Dynamic Reconstruction Model

DWD Deutscher Wetterdienst

ECMWF European Centre for Medium-Range Weather Forecasts

ECMWF-IFS ECMWF-Integrated Forecasting System

ERA ECMWF Re-Analysis

ESA European Space Agency

EUCLID European Cooperation for Lightning Detection

EXTPAR External Parameter for Numerical Weather Prediction and Climate Application

FKZ Förderkennzeichen

HYSPLIT Hybrid Single Particle Lagrangian Integrated Trajectory model

HWSD Harmonized World Soil Database

ICON ICOsahedral Nonhydrostatic

ICON-EU ICON-Europe

ICON-LEM ICOsahedral Nonhydrostatic - Large Eddy Model

IHOP International H2O Project

LAGRANTO LAGrangian ANalysis TOol

LAI Leaf Area Index

LAM Limited Area Mode

LCL Lifting Condensation Level

LEM Large Eddy Model

LES Large Eddy Simulation

LFC Level of Free Convection

LHR Latent Heat Release

LSMs Large-Scale Models

MetUM UK Met Office Unified Model

METI Ministry of Economy, Trade, and Industry of Japan

MLCAPE Convective Available Potential Energy of mean surface layer parcel

MLCIN Convective Inhibition of mean surface layer parcel

MPI-M Max-Planck-Institute for Meteorology

MTSAT-1R Japanese geostationary meteorological satellite

NASA National Aeronautics and Space Administration, United States

NICAM Nonhydrostatic icosahedral atmospheric model

NWP Numerical Weather Prediction

PDF Probability Density Function

RADOLAN Radar Online Adjustment

RBF Radial Basis Function

RPD Relative Percentage Difference

RRTM Rapid Radiation Transfer Model

SMI Soil Moisture Index

SMRC Standardized Multiple Regression Coefficient

TAF Topographic Amplification Factor

TAI Transpiration Area Index

TERRA-ML TERRA - Multi Layer

TKE Turbulent Kinetic Energy

UHI Urban Heat Island

UTC Coordinated Universal Time

WRF Weather Research and Forecasting

B. Figures

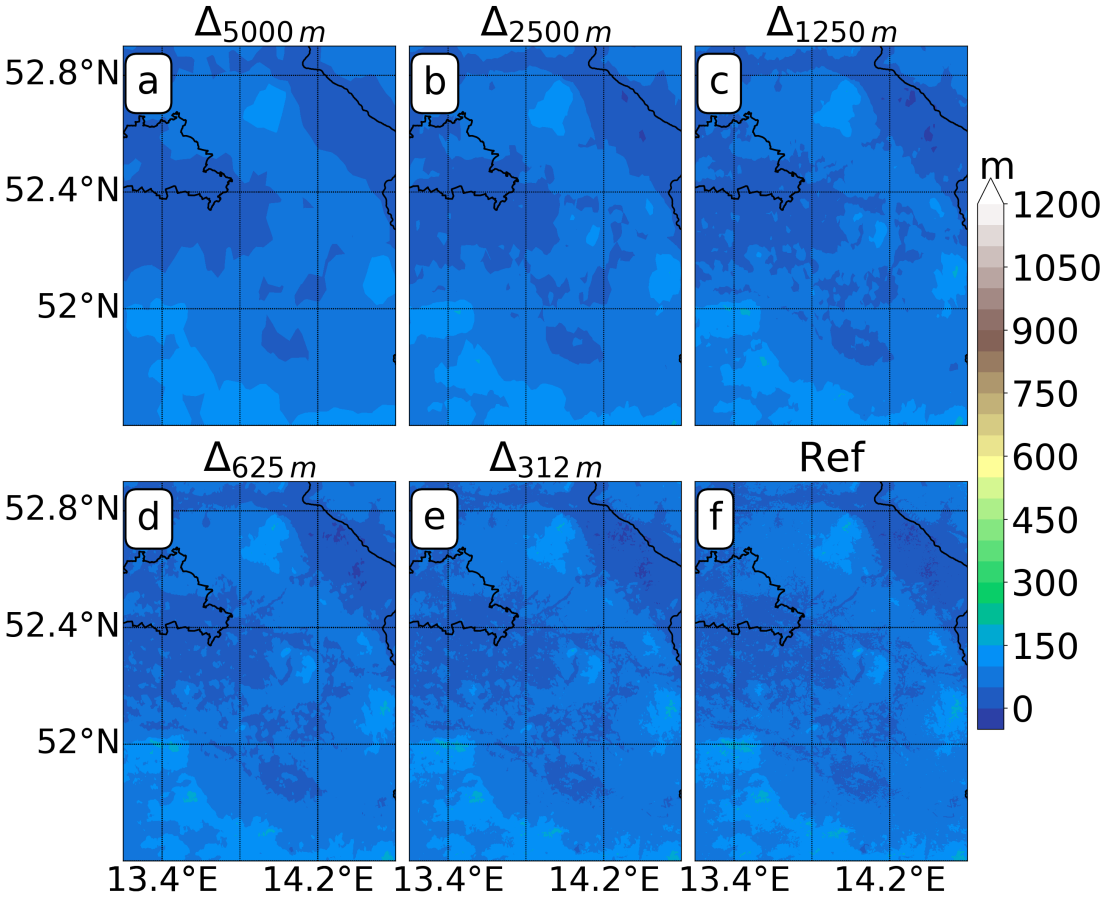

(a) Orography over A1

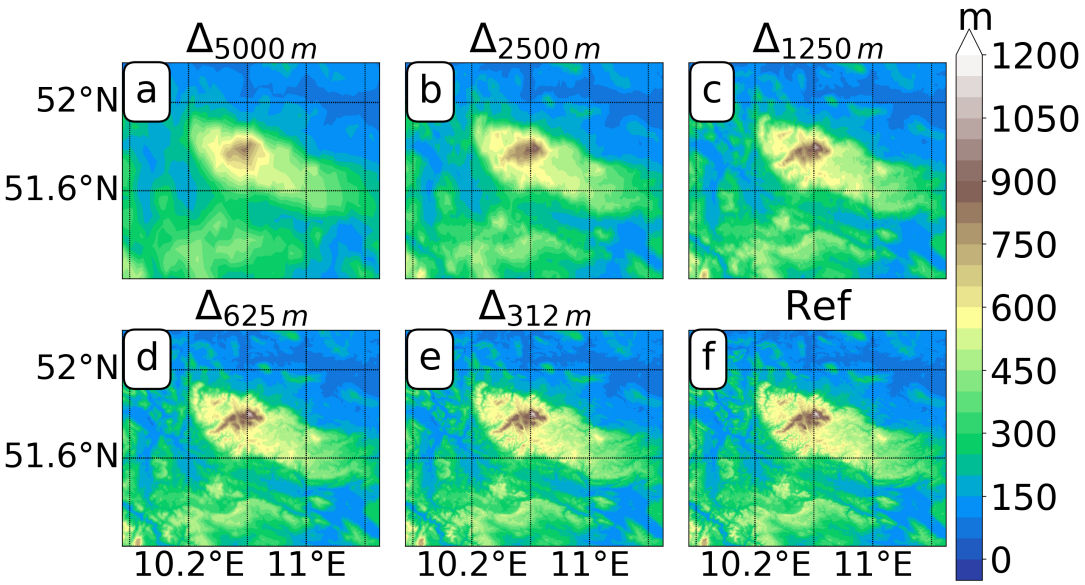

(b) Orography over A2

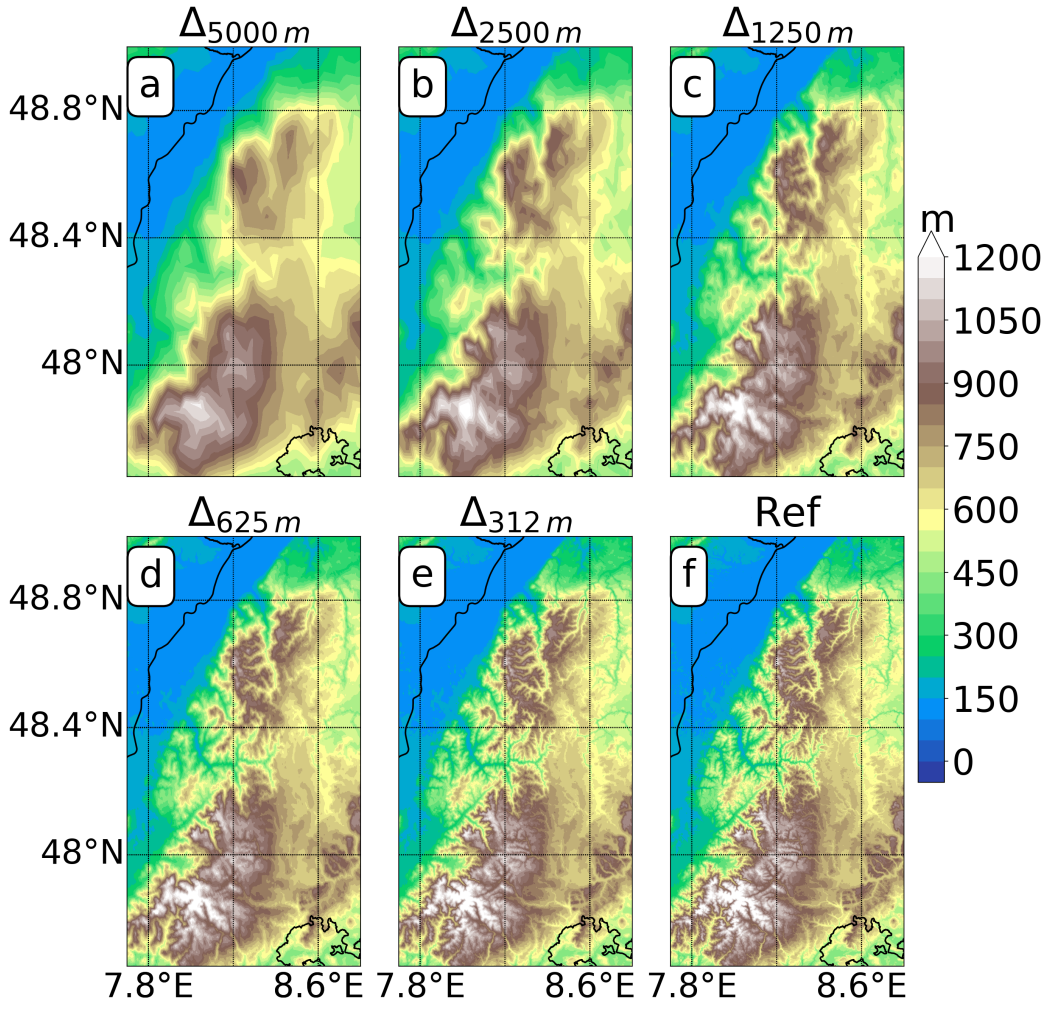

(c) Orography over A3

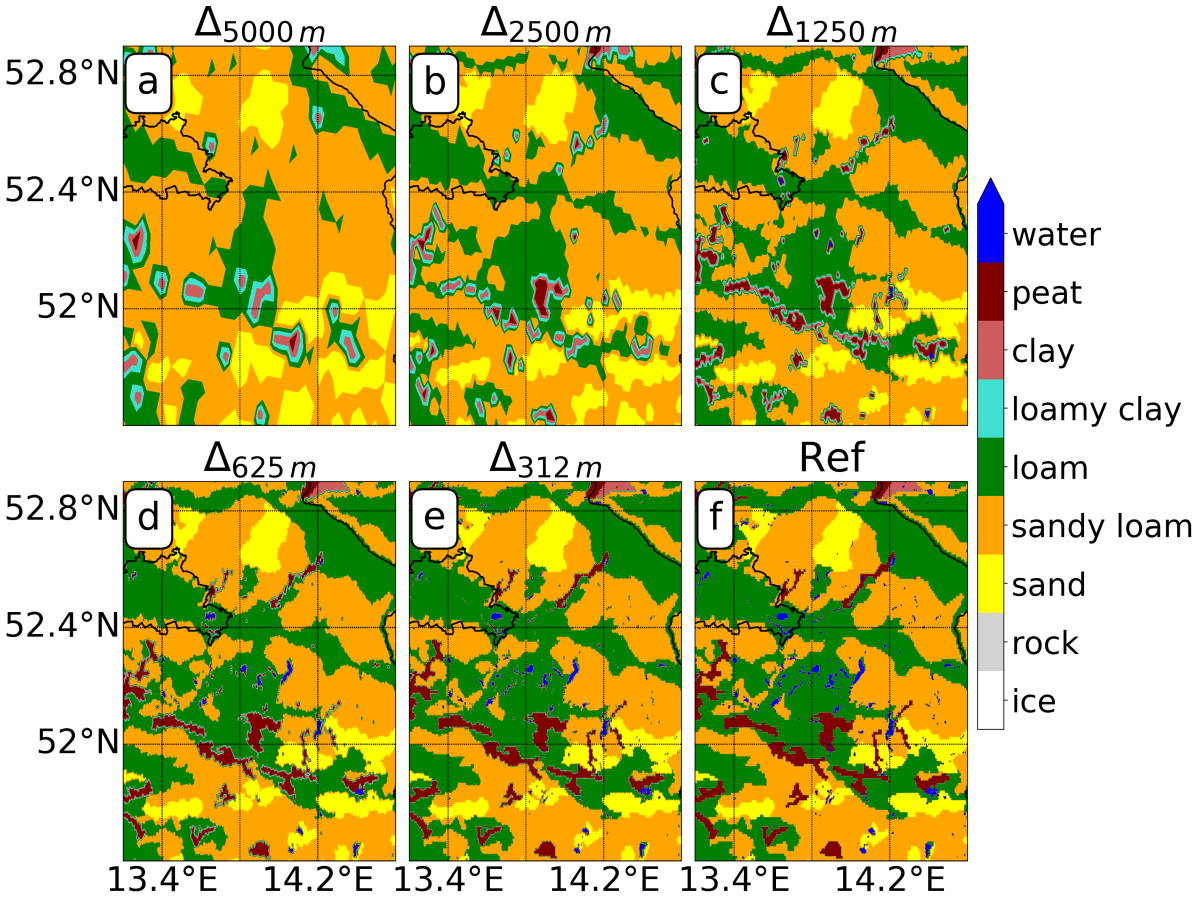

(d) Soiltype over A1

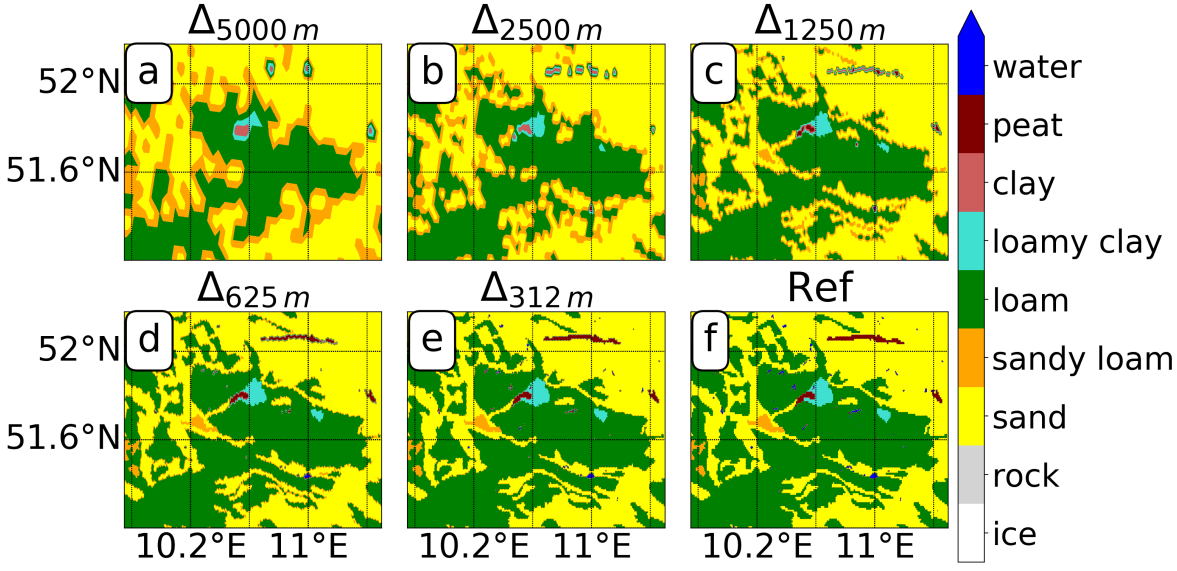

(e) Soiltype over A2

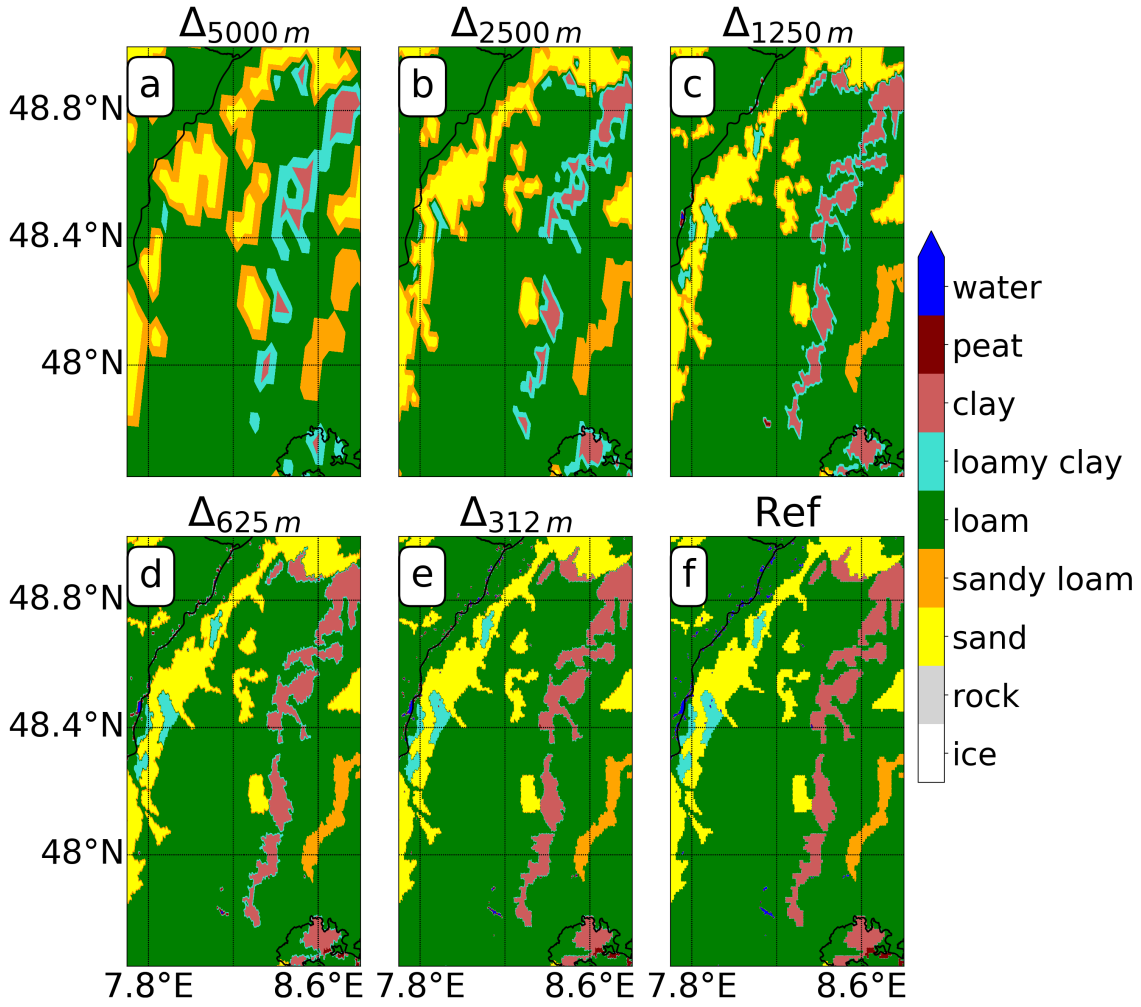

(f) Soiltype over A3

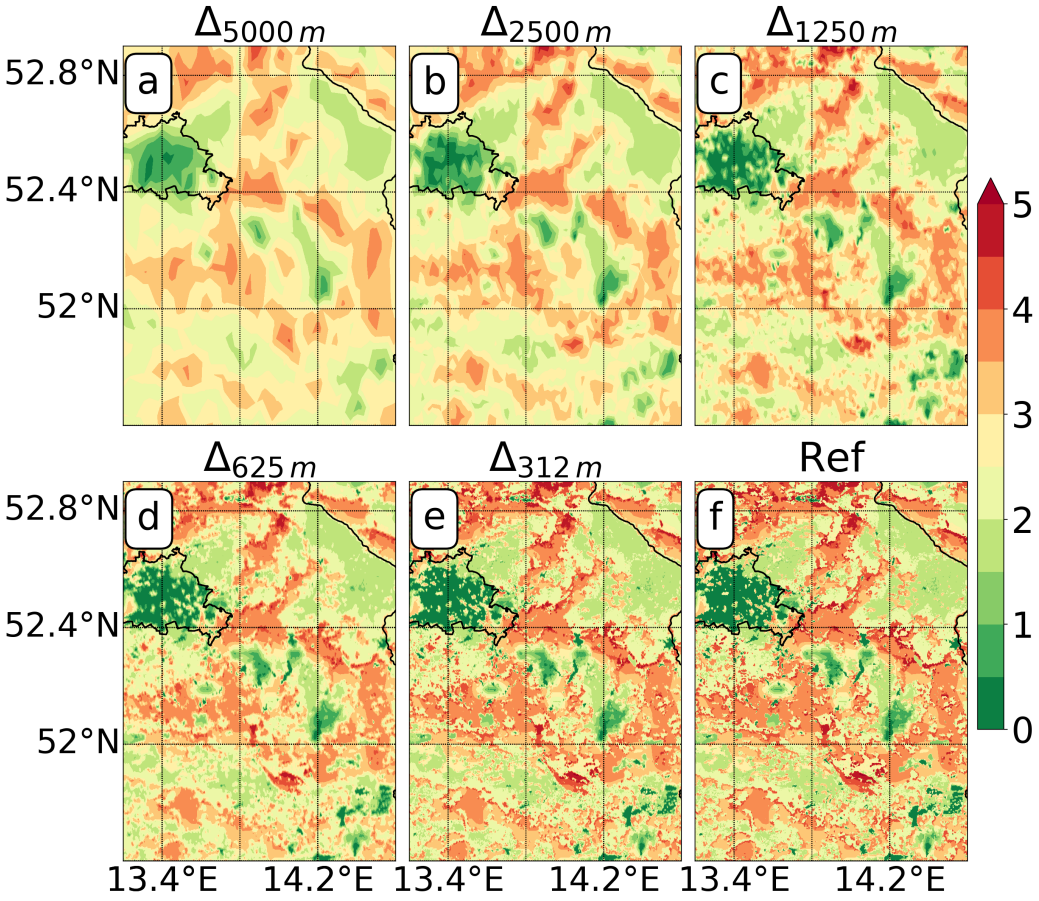

(g) TAI over A1

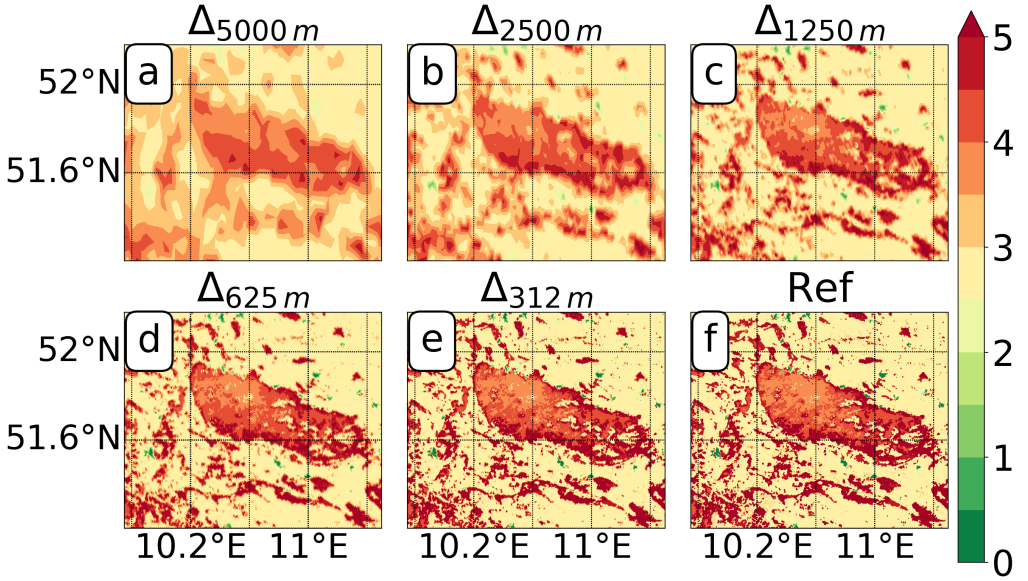

(h) TAI over A2

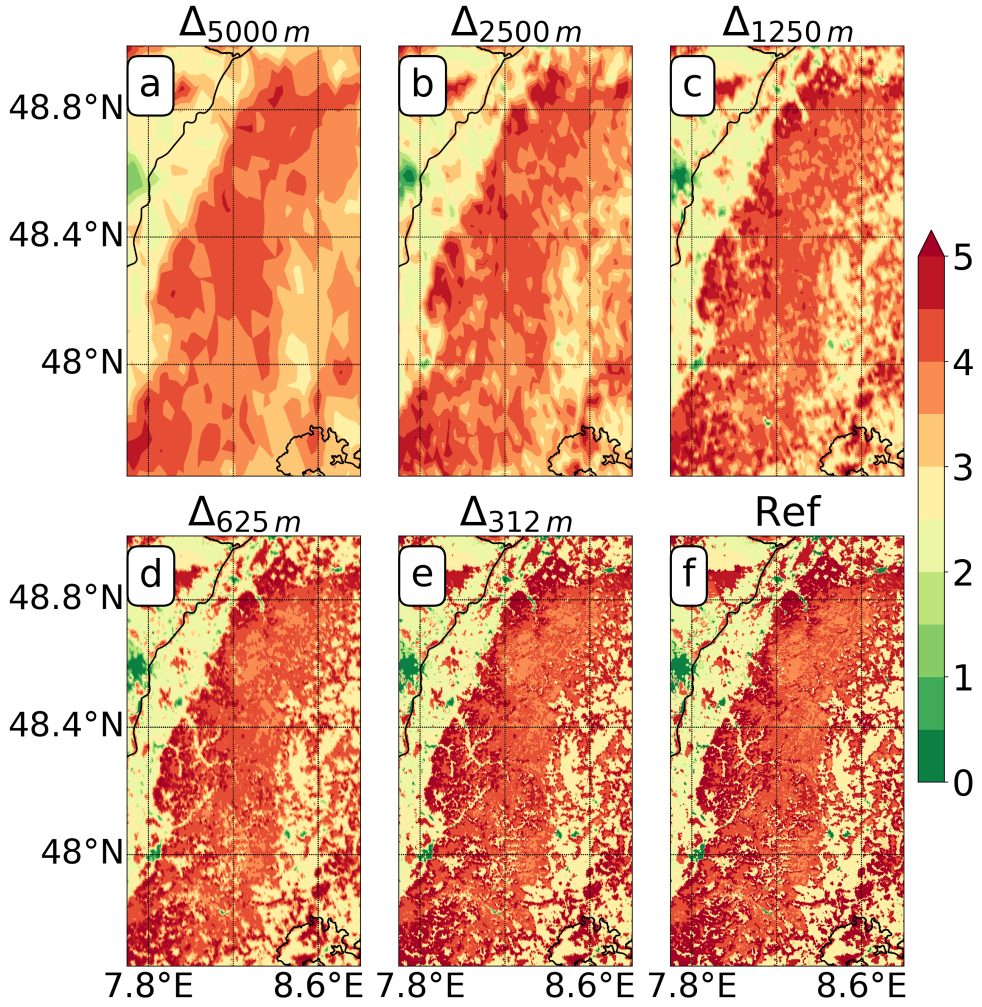

(i) TAI over A3

Figure B.1.: Composites of modelled orography (a-c), soil type (d-f) and TAI (g-i) across the chosen model grid sapcings ($\Delta_{5000\,m}$, $\Delta_{2500\,m}$, $\Delta_{1250\,m}$, $\Delta_{625\,m}$, $\Delta_{312\,m}$, $\Delta_{156\,m}$) over flat terrain (A1), isolated mountain range (A2) and complex terrain (A3).

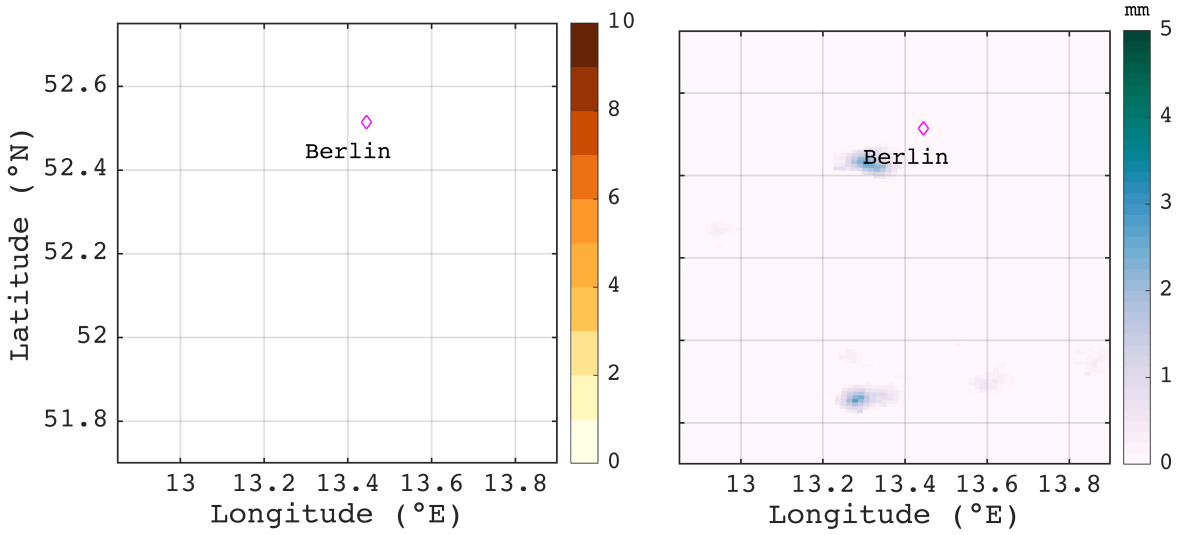

(a) (b)

Figure B.2.: Horizontal distribution of lightning density (a) and observed (RADOLAN RW) daily accumulated precipitation (b) over A1 on 17 Sept 2017.

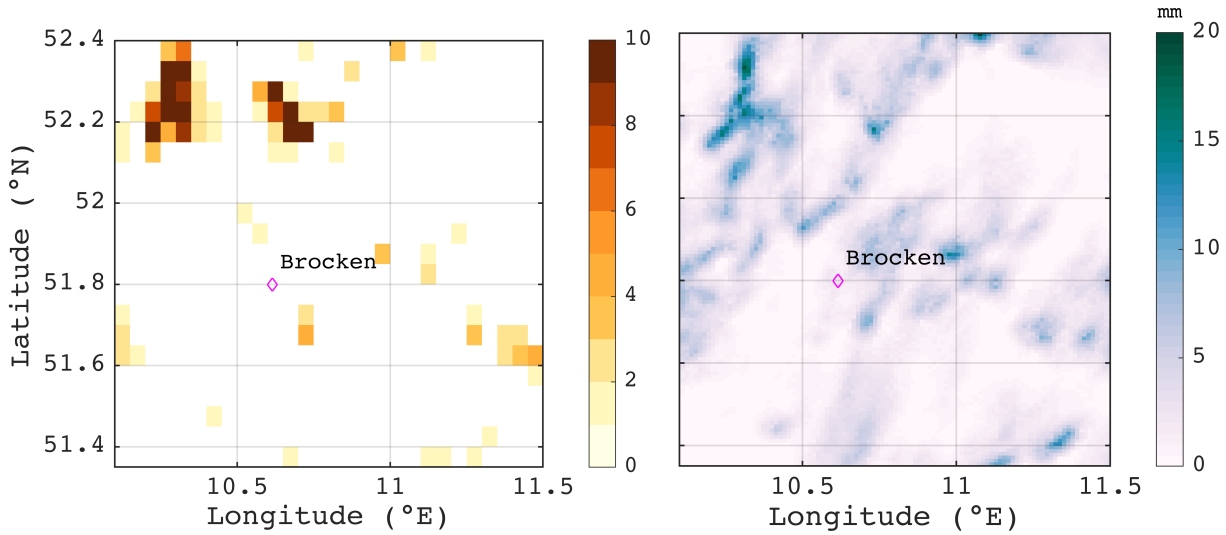

(a) (b)

Figure B.3.: Same as Figure B.2 but over A2 on 17 Sept 2017.

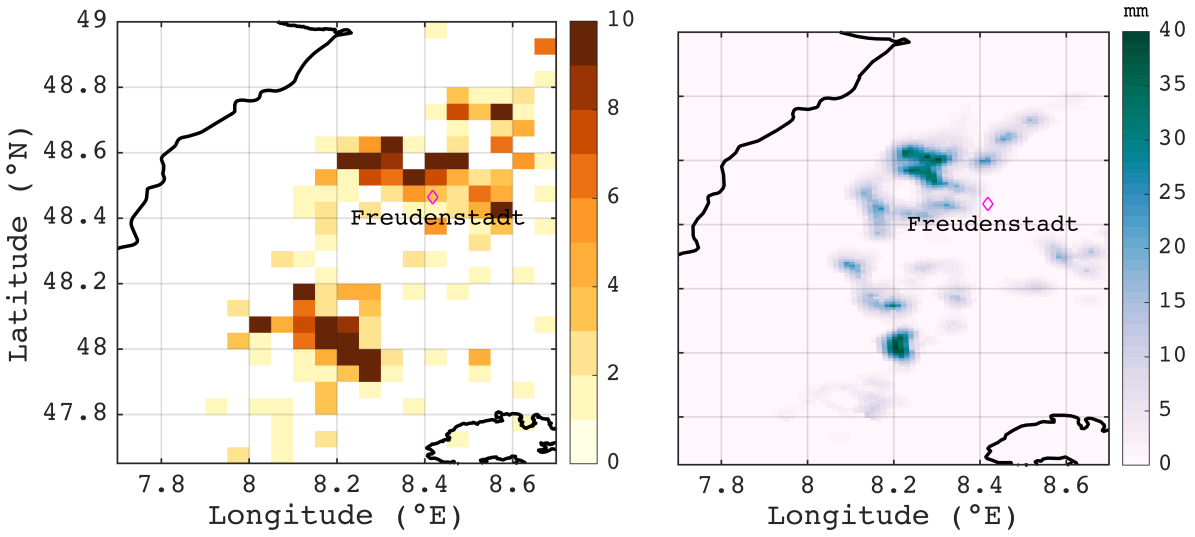

Figure B.4.: Same as Figure B.2 but over A3 on 29 May 2017.

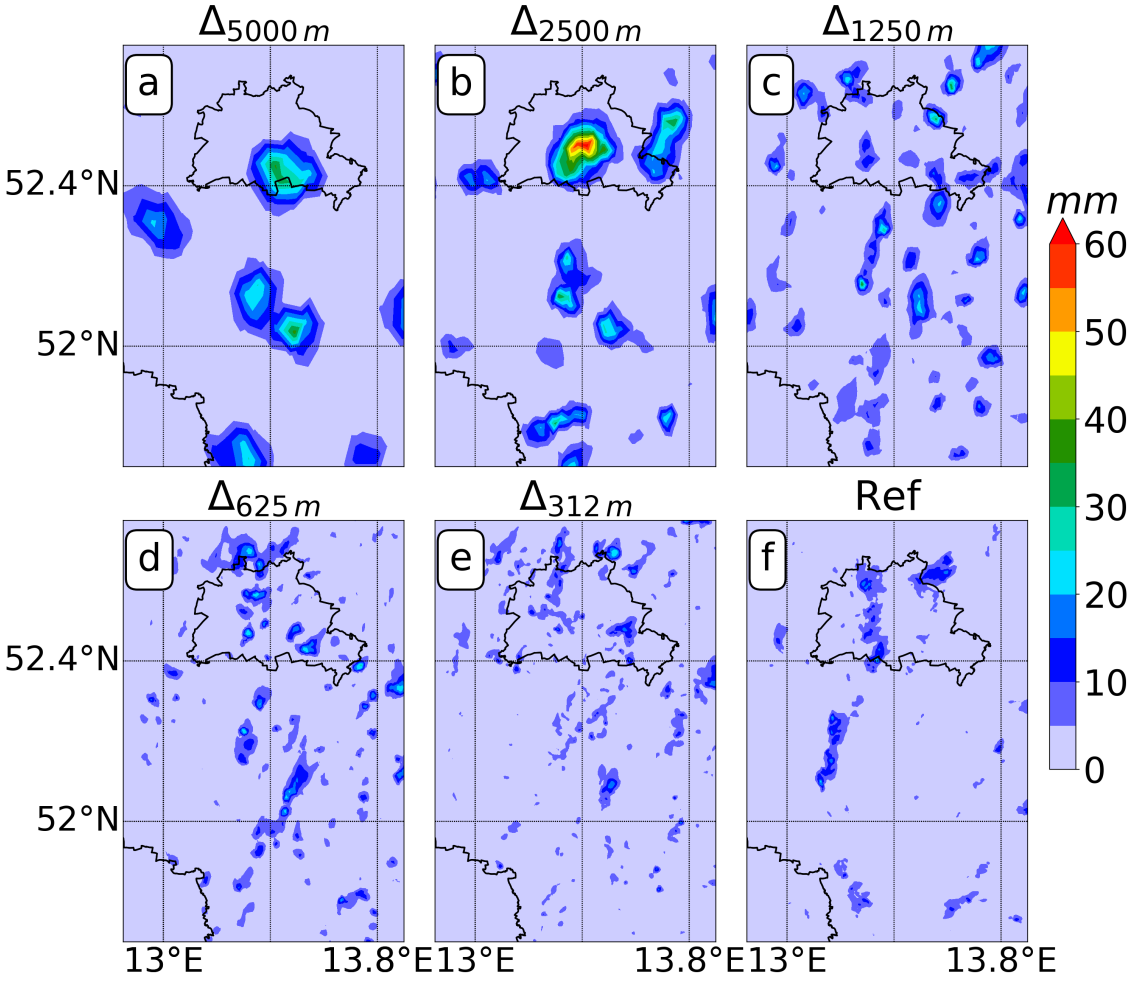

Figure B.5.: Total accumulated precipitation at 2000 UTC over A1, case: 17 Sept 2017.

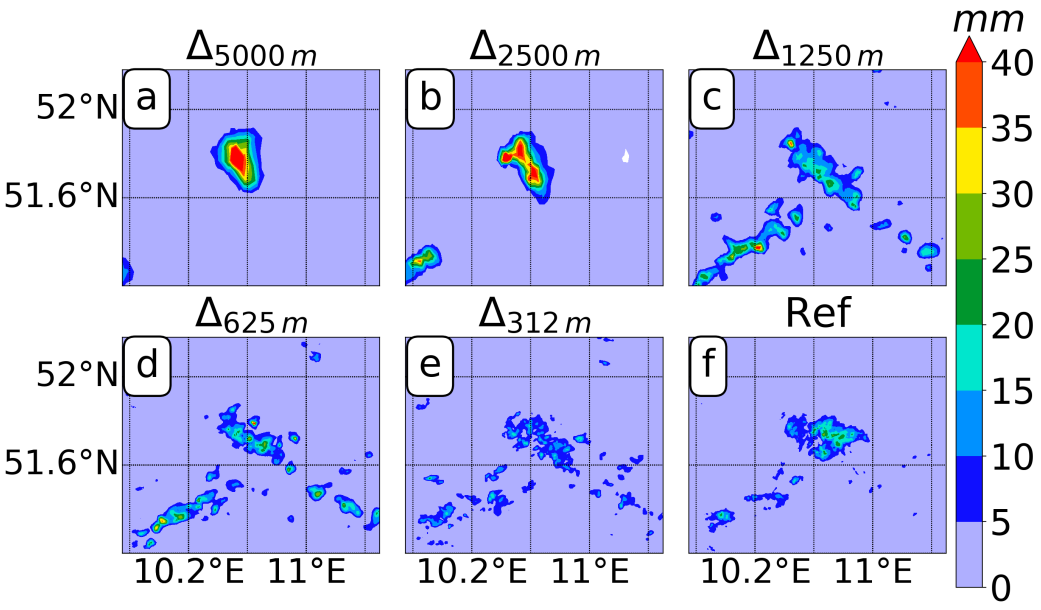

Figure B.6.: Total accumulated precipitation at 2000 UTC over A2, case: 09 June 2018.

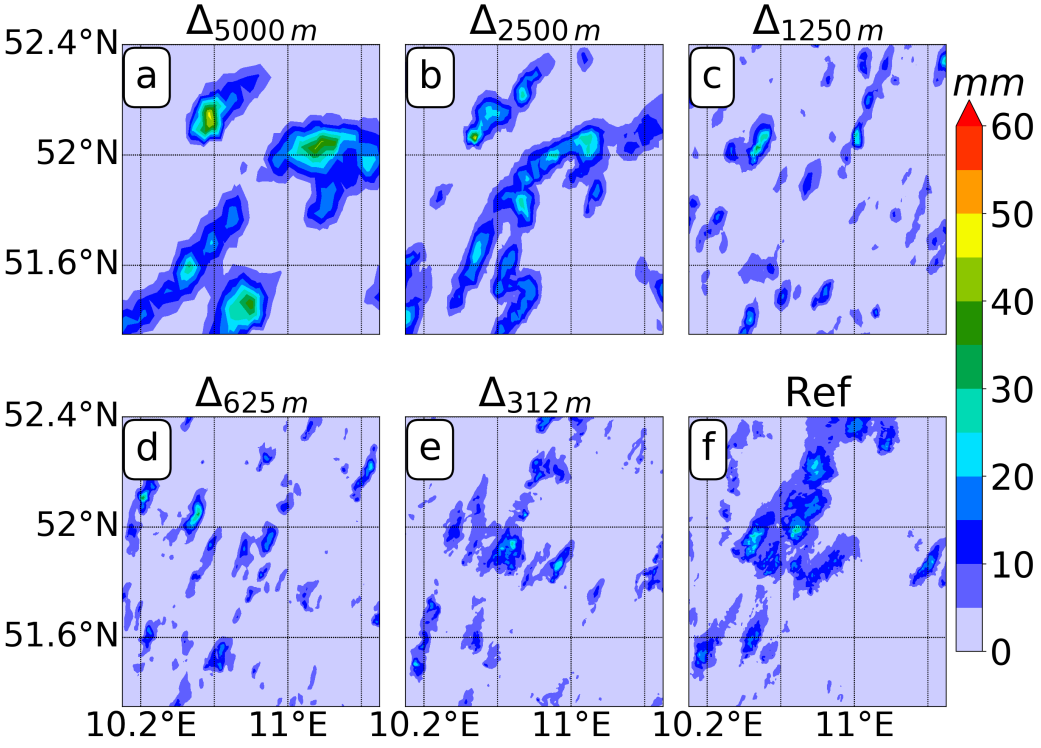

Figure B.7.: Total accumulated precipitation at 2000 UTC over A2, case:17 Sept 2017.

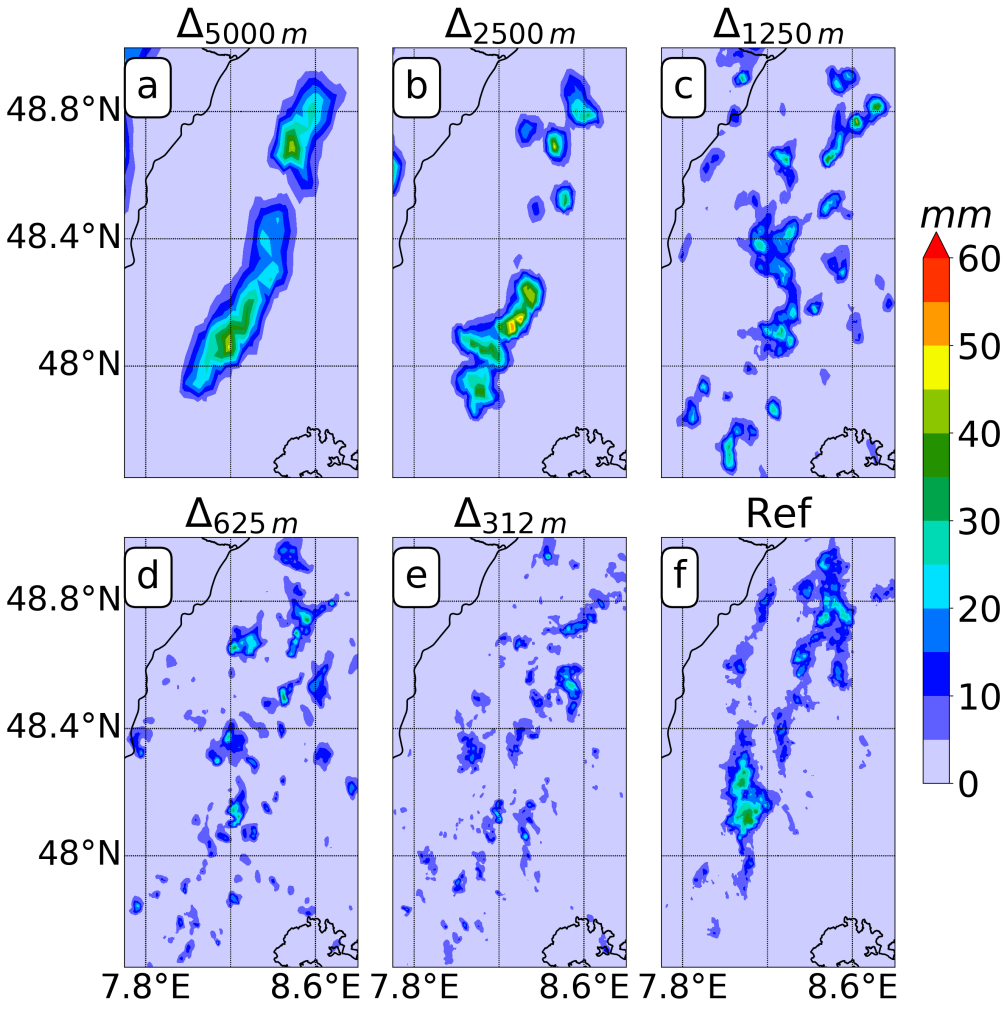

Figure B.8.: Total accumulated precipitation at 2000 UTC over A3, case: 29 May 2017.

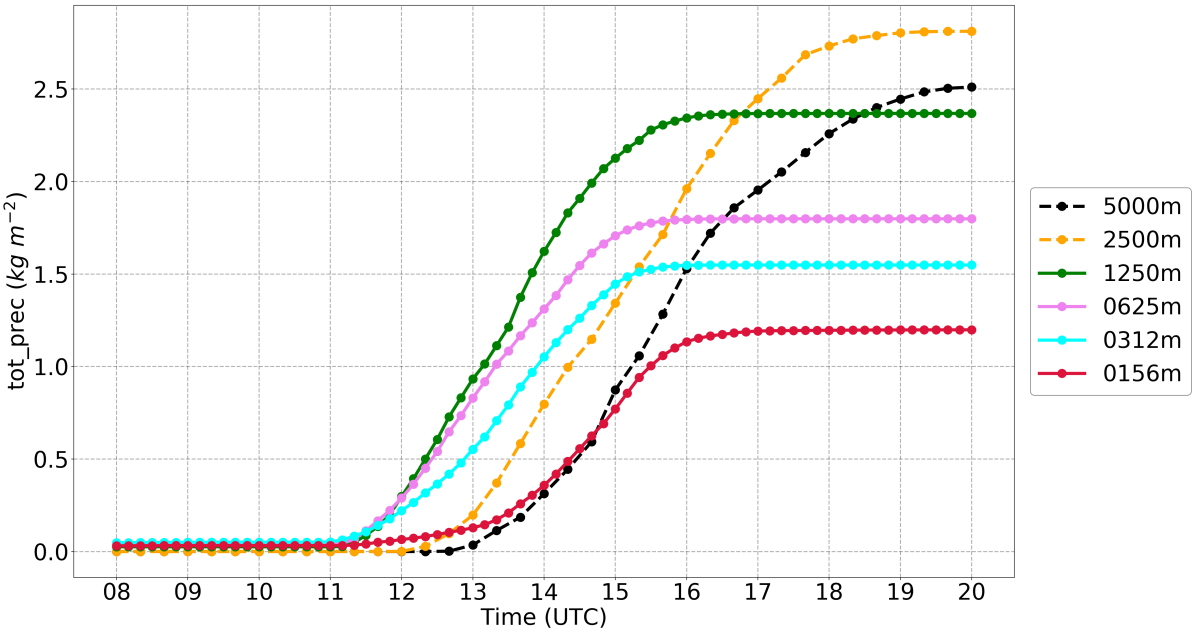

Figure B.9.: Time series of total accumulated precipitation for NWP (Δ_{5000m}, Δ_{2500m}), dashed lines, and LES model grid spacings(Δ_{1250m}, Δ_{625m}, Δ_{312m}, Δ_{156m}), solid lines, over A1, case: 17 Sept 2017.

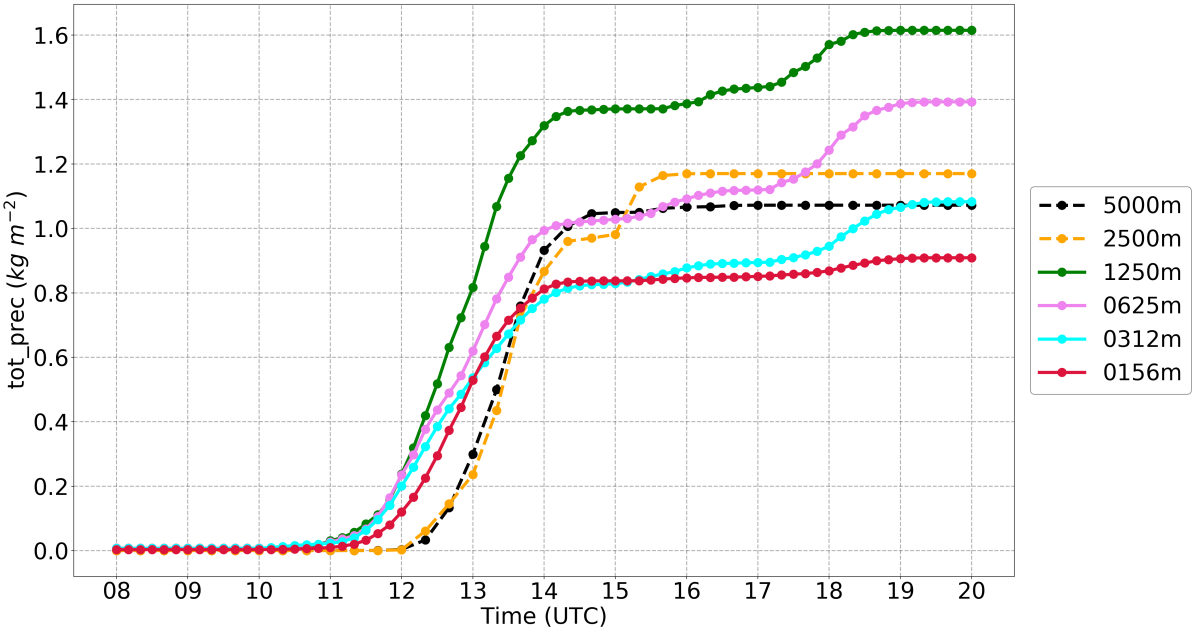

Figure B.10.: Time series of total accumulated precipitation for NWP (Δ_{5000m}, Δ_{2500m}), dashed lines, and LES model grid spacings(Δ_{1250m}, Δ_{625m}, Δ_{312m}, Δ_{156m}), solid lines, over A2, case: 09 June 2018.

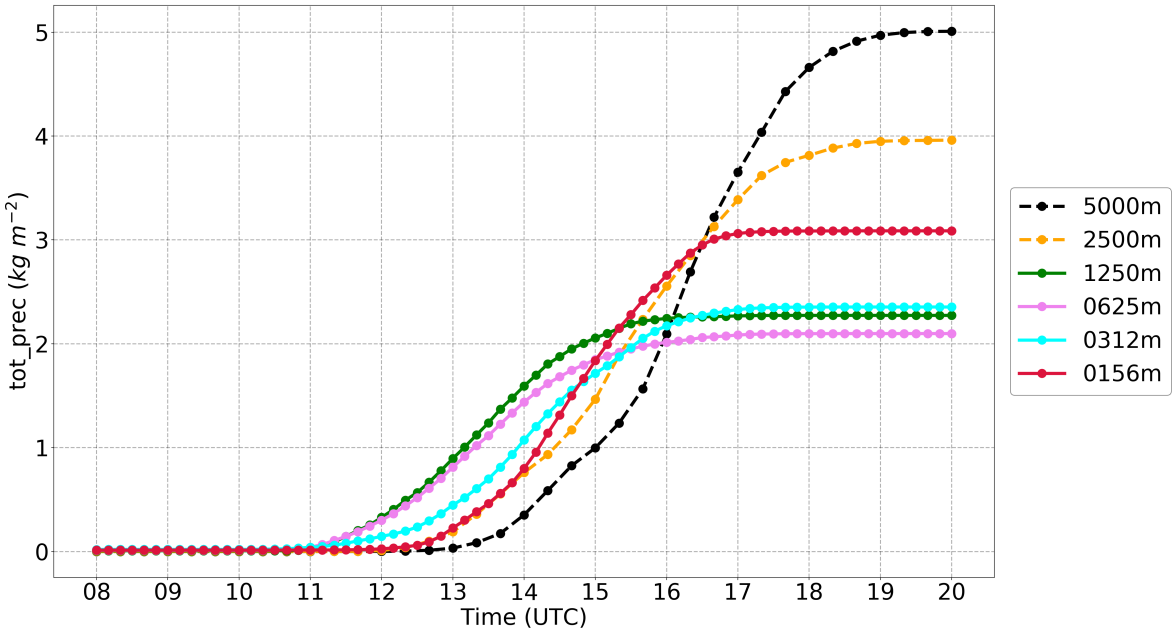

Figure B.11.: Time series of total accumulated precipitation for NWP (Δ_{5000m}, Δ_{2500m}), dashed lines, and LES model grid spacings(Δ_{1250m}, Δ_{625m}, Δ_{312m}, Δ_{156m}), solid lines, over A2, case: 17 Sept 2017.

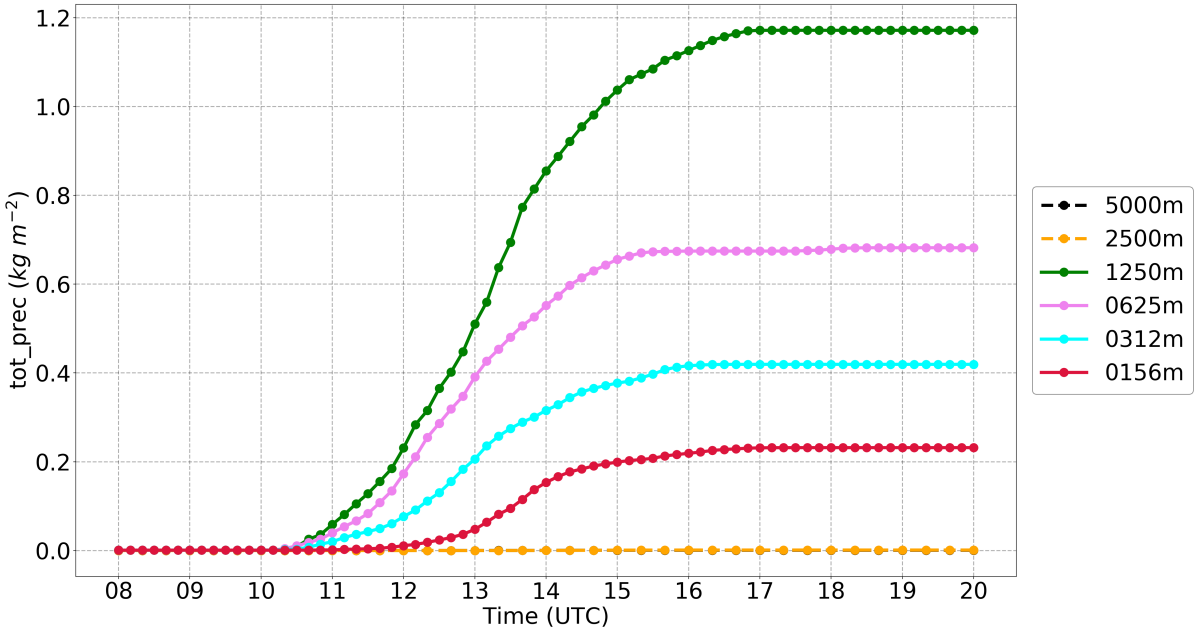

Figure B.12.: Time series of total accumulated precipitation for NWP (Δ_{5000m}, Δ_{2500m}), dashed lines, and LES model grid spacings(Δ_{1250m}, Δ_{625m}, Δ_{312m}, Δ_{156m}), solid lines, over A3, case: 12 Aug 2015.

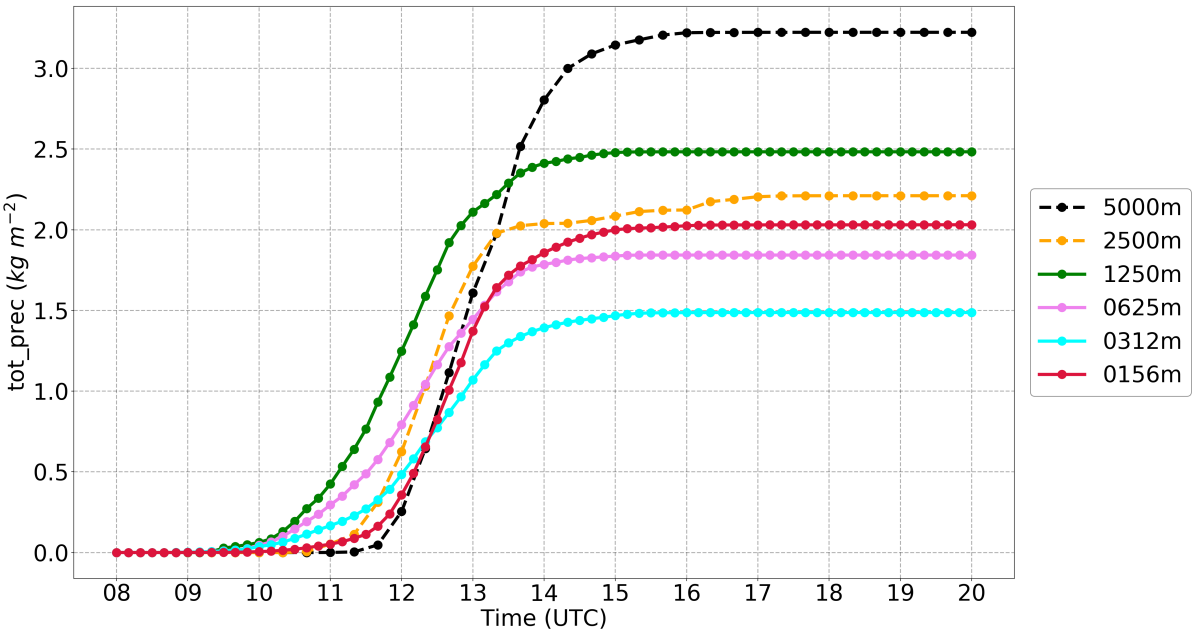

Figure B.13.: Time series of total accumulated precipitation for NWP (Δ_{5000m}, Δ_{2500m}), dashed lines, and LES model grid spacings(Δ_{1250m}, Δ_{625m}, Δ_{312m}, Δ_{156m}), solid lines, over A3, case: 29 May 2017.

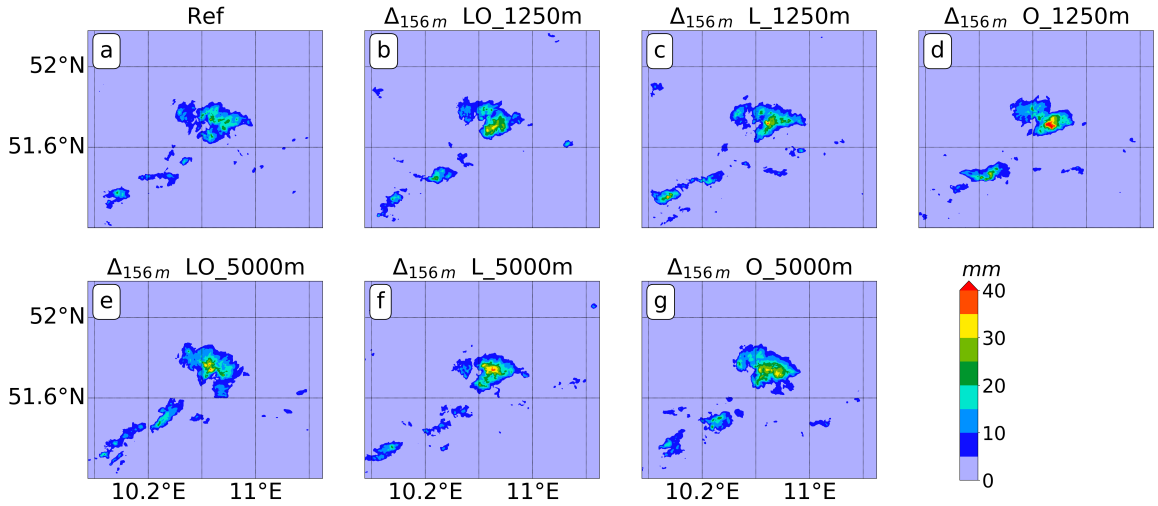

Figure B.14.: Total accumulated precipitation from Δ_{156m}- control run (a), Δ_{156m}-LO_1250 m run (b), Δ_{156m}- L_1250 m run (c), Δ_{156m}- O_1250 m run (d), Δ_{156m}-LO_5000 m run (e), Δ_{156m}-L_5000 m run (f), and Δ_{156m}-O_5000 m run (g) at 2000 UTC over A2, case: 09 June 2018.

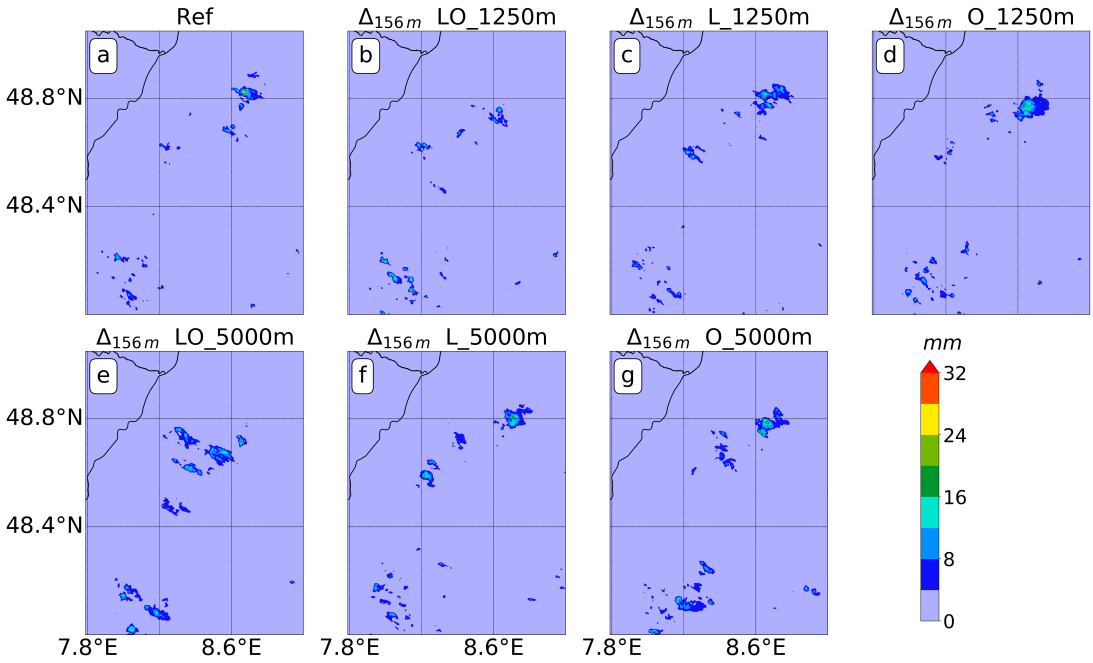

Figure B.15.: Total accumulated precipitation from Δ_{156m}- control run (a), Δ_{156m}-LO_1250 m run (b), Δ_{156m}- L_1250 m run (c), Δ_{156m}- O_1250 m run (d), Δ_{156m}-LO_5000 m run (e), Δ_{156m}-L_5000 m run (f), and Δ_{156m}-O_5000 m run (g) at 2000 UTC over A3, case: 12 Aug 2012.

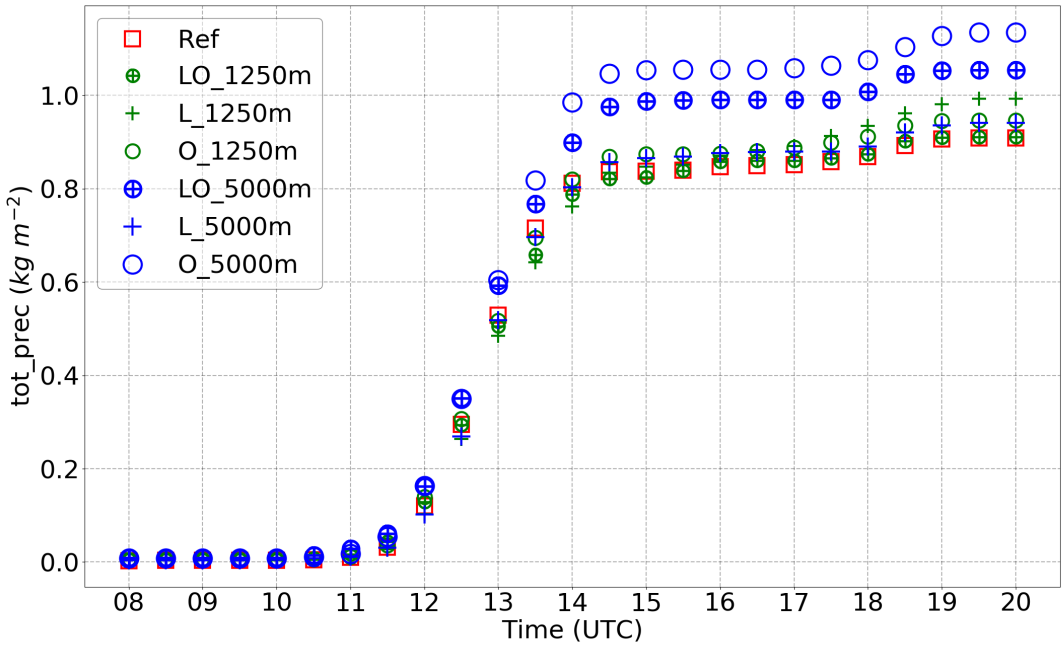

Figure B.16.: Time series of total accumulated precipitation from Δ_{156m}- control run (□), Δ_{156m}- LO_1250 m run (⊕), Δ_{156m}- L_1250 m run (+), Δ_{156m}- O_1250 m run (○), Δ_{156m}-LO_5000 m run (⊕), Δ_{156m}-L_5000 m run (+), and Δ_{156m}-O_5000 m run (○) over A2, case: 09 June 2018.

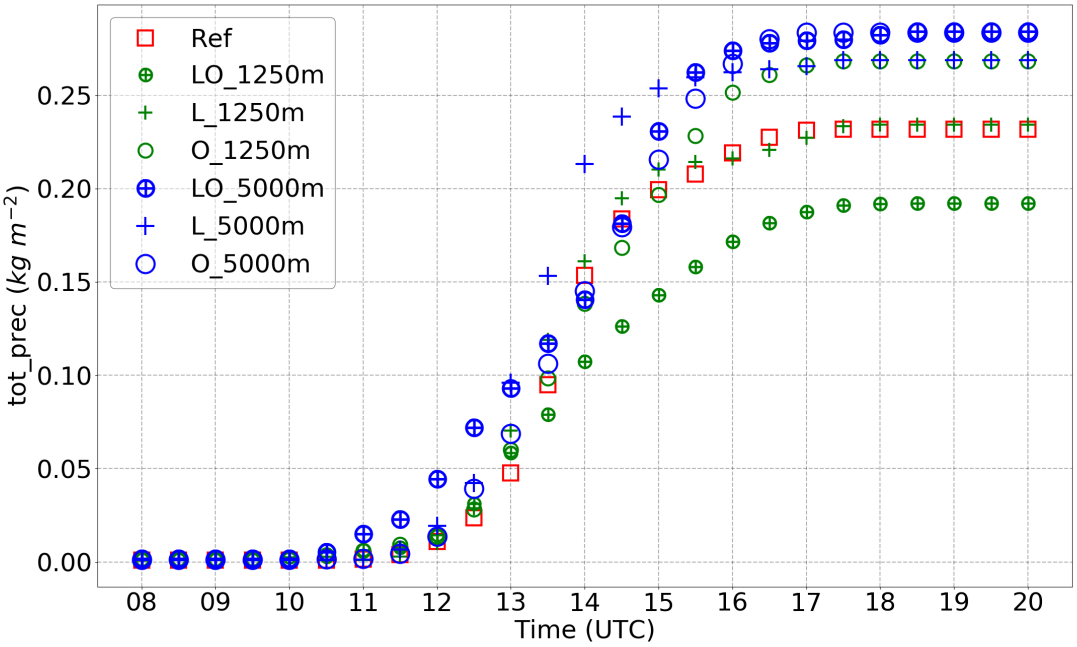

Figure B.17.: Same as Figure B.16 but over A3, case: 12 Aug 2015.

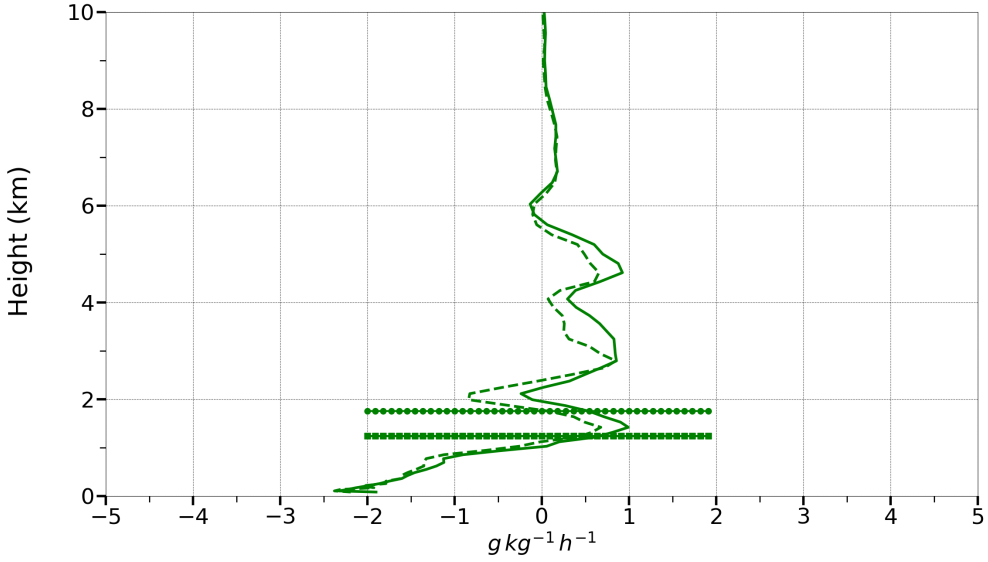

Figure B.18.: Vertical profile of total moisture advection (solid) and grid-scale latent heat flux convergence (dashed) at 1200 UTC in $\Delta_{1250\,m}$ of case over A1, dated 26 July 2012. The horizontal lines with circle and square markers denote the areal mean CBL height (zi) and LCL, respectively.

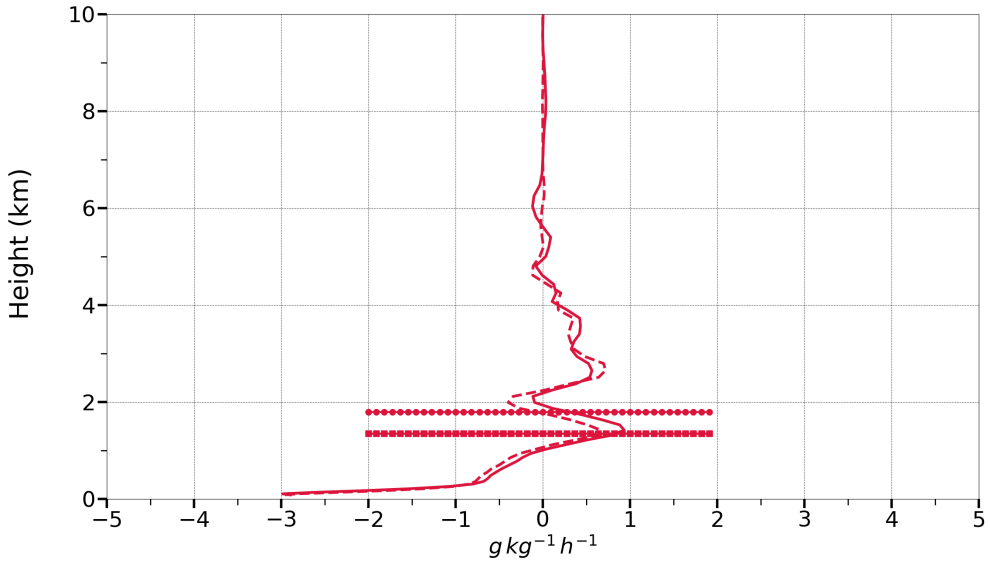

Figure B.19.: Same as figure B.18 but for Δ_{156m}.

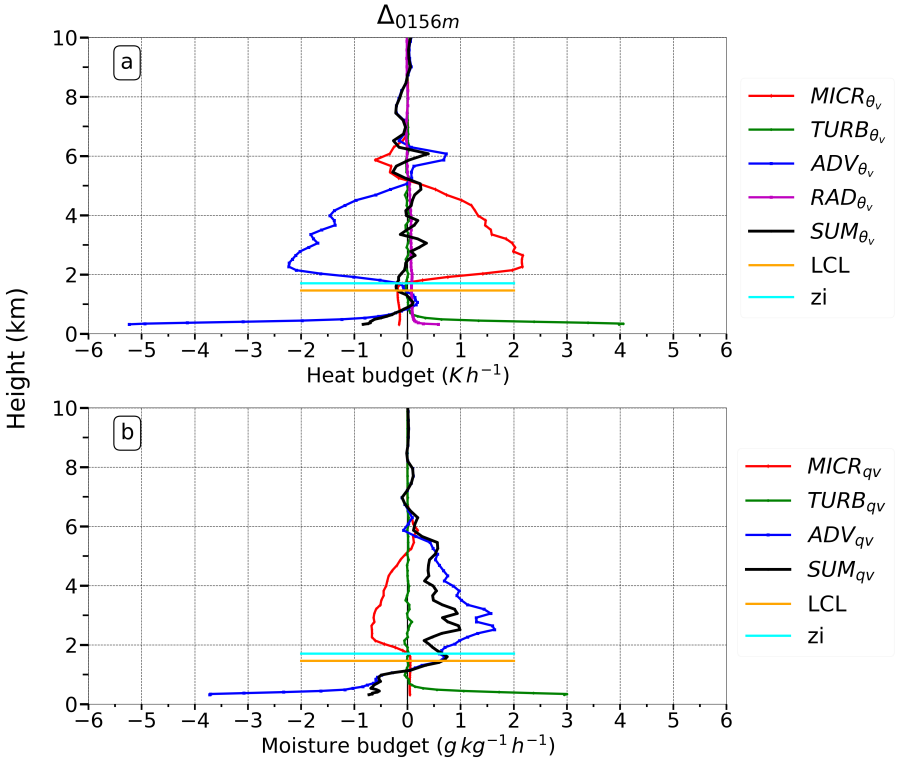

Figure B.20.: Vertical profile of heat (a) and moisture (b) budget terms throughout CBL and free troposphere in Δ_{156m} at 1220 UTC for case over A2, dated 09 June 2018. The horizontal line in orange and cyan colour shows the LCL and mean CBL height (zi), respectively.

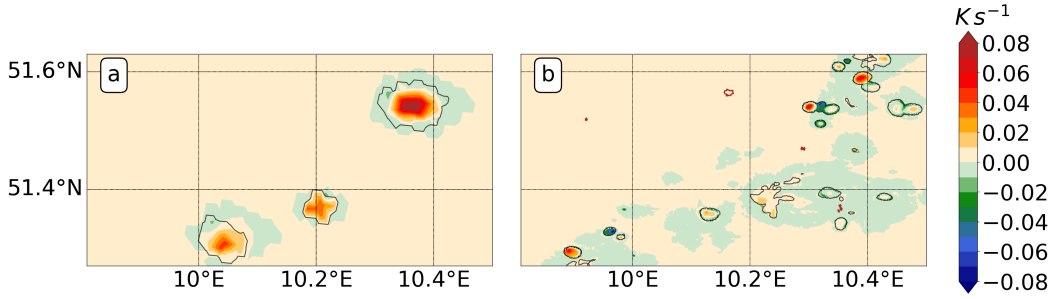

Figure B.21.: Spatial distribution of temperature microphysics tendency (colour coded) ($MICR_{\theta_v}$) in Δ_{1250m} (a) and Δ_{156m} (b) at $\sim$ 6000 m height a.g.l. at 1220 UTC for case over A2, dated 09 June 2018. The black contours are the isolines for cloud liquid water content of 0.1 $g\,kg^{-1}$ at that level and the brown contours encircle the areas of lakes.

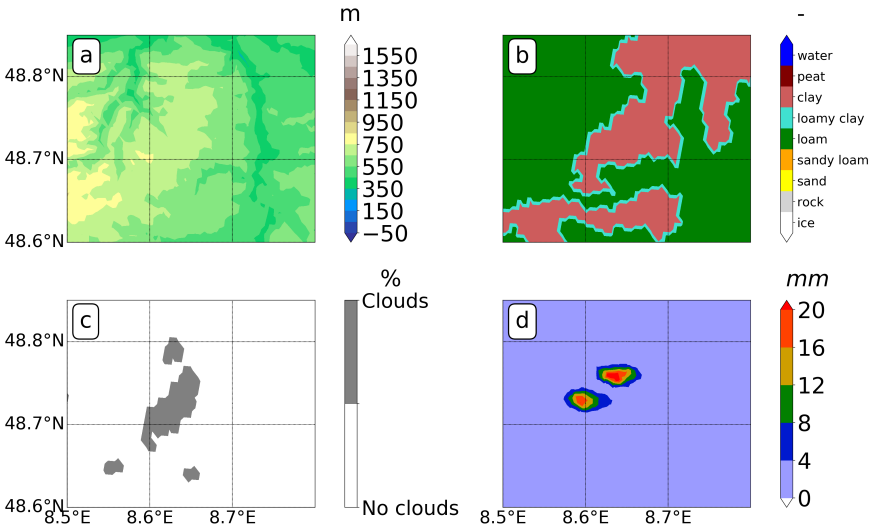

Figure B.22.: Orography (a), soil type (b), cloud cover at 0920 UTC (c), and the resulting accumulated precipitation at 1100 UTC (d) in $\Delta_{625\,m}$ of case over A3, dated 12 Aug 2015.

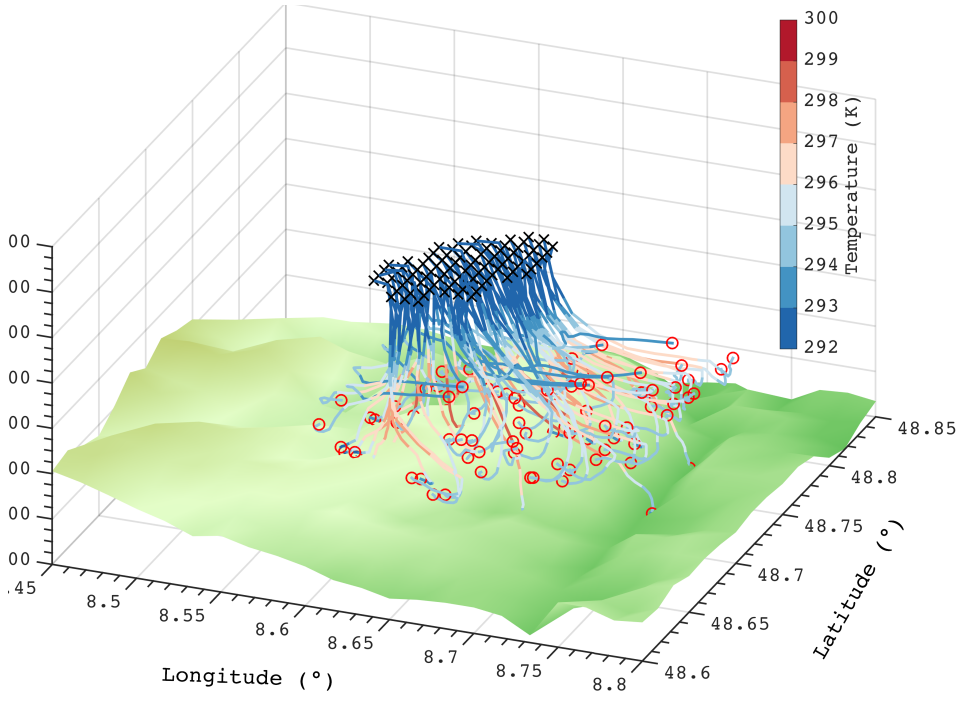

Figure B.23.: Backward Lagrangian trajectories using LAGRANTO in $\Delta_{625\,m}$ of case over A3, dated 12 Aug 2015. The black crosses denote the starting points at the cloud base at 0920 UTC and the red circles denote the end points of trajectory integration until 0600 UTC. The colours along the trajectories indicate the air temperature (K) and the colour in the xy plane denotes orography.

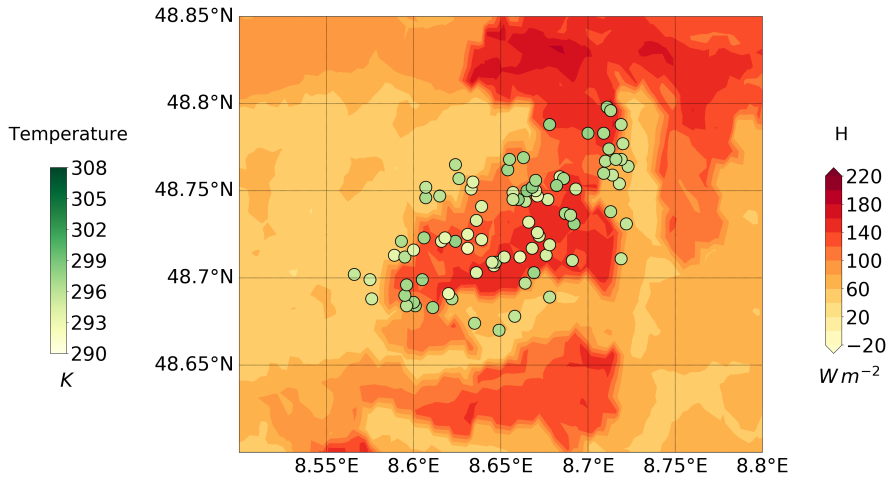

Figure B.24.: Surface sensible heat flux (colour shaded) and the trajectory points (circles with air temperature in the colour shade) at 0820 UTC, in $\Delta_{625\,m}$ of case over A3, dated 12 Aug 2015. The lakes and water bodies are indicated by surface sensible heat flux value (H) of $\sim$-20 $W\,m^{-2}$.

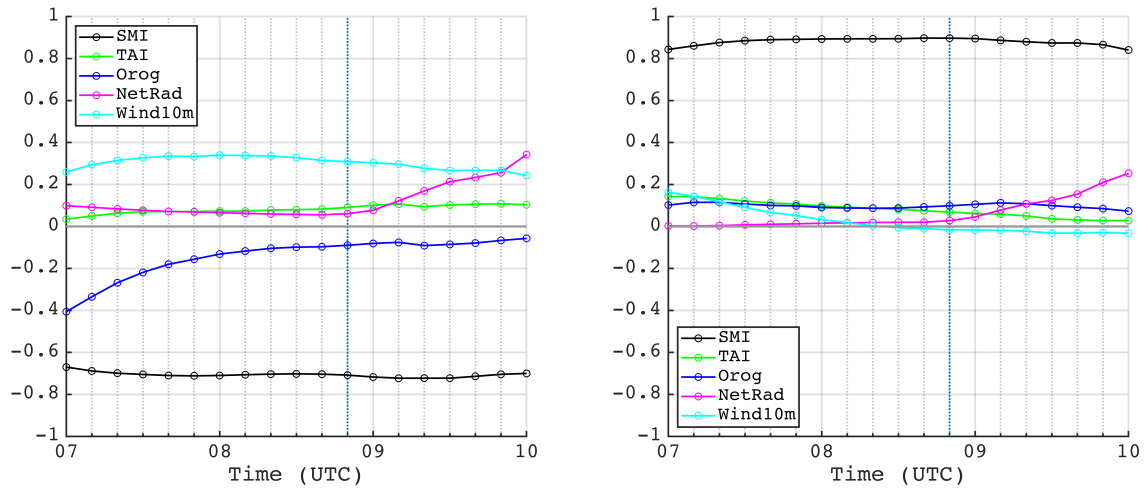

Figure B.25.: The areal mean SMRC for SMI in black, TAI in green, orography (Orog) in blue, net radiation (NetRad) in pink, and horizontal wind at 10 m (Wind10m) in cyan with respect to H (a) and E (b), respectively for $\Delta_{625\,m}$ of case over A3, dated 12 Aug 2015. The vertical dotted line shows the onset of first cloud in the investigation region.

Budget terms

B.1. Heat budgets

Heat budgets physically represent the conservation of heat. According to Stull (1988), it is based on the First Law of Thermodynamics which basically describes the conservation of enthalpy. The different components represent the processes contributing to instantaneous heating (or cooling) of the atmosphere. This includes the contributions from sensible and latent heat energy transport. The basic heat conservation equation is:

$$\frac{\partial \theta}{\partial t} + U_j \frac{\partial \theta}{\partial x_j} = \nu_\theta \frac{\partial^2 \theta}{\partial x_j^2} - \frac{1}{\rho C_p}\left(\frac{\partial Q_j^*}{\partial x_j}\right) - \frac{L_p E}{\rho C_p} \tag{B.1}$$

$$SUM_{\theta_v} \quad ADV_{\theta_v} \qquad DIFF_{\theta_v} \qquad RAD_{\theta_v} \qquad MICR_{\theta_v}$$

where U_j is the wind vector having three components (u,v, w), ν_θ is the thermal diffusivity, C_p is the specific heat for moist air at constant pressure, which is related with the specific heat of dry air according to the equation B.2, Q_j^* is the component of the net radiation in the j^{th} direction, E is the mass of water vapour per unit volume per unit time which is being created by a phase change from liquid to solid phase, and L_p is the latent heat associated with the phase change of E. Depending upon different phase changes, the values for latent heat at 0° are $L_v = 2.50 \times 10^6 J/kg$ (gas$\rightarrow$ liquid), $L_f = 3.34 \times 10^5 J/kg$ (liquid$\rightarrow$ solid), and $L_s = 2.83 \times 10^6 J/kg$ of water (gas $\rightarrow$ solid).

$$C_p = C_{pd}(1 + 0.84q) \tag{B.2}$$

In equation B.1, SUM_{θ_v} denotes the local storage of heat. The other terms represent the heat advection by mean wind (ADV_{θ_v}), the mean molecular conduction of heat ($DIFF_{\theta_v}$) (which is relatively small), and the mean net body source term associated with radiation flux convergence (RAD_{θ_v}) respectively. $MICR_{\theta_v}$ repres-

ents the microphysics contribution mainly the LHR due to condensation of water vapour and also evaporation of clouds and rain. Now, in order to represent the mean and turbulent parts of the designated variables in the model, the dependent variables in the equation B.1 is expanded into mean and turbulent parts. After applying the Reynolds averaging and putting the turbulent advection term into flux form gives equation B.3.

$$\underbrace{\frac{\partial \overline{\theta}}{\partial t}}_{SUM_{\theta_v}} = \underbrace{-\overline{U_j}\frac{\partial \overline{\theta}}{\partial x_j}}_{ADV_{\theta_v}} \underbrace{+\nu_\theta \frac{\partial^2 \overline{\theta}}{\partial x_j^2}}_{DIFF_{\theta_v}} \underbrace{-\frac{1}{\overline{\rho} C_p}\left(\frac{\partial \overline{Q_j^*}}{\partial x_j}\right)}_{RAD_{\theta_v}} \underbrace{-\frac{\overline{L_v E}}{\overline{\rho} C_p}}_{MICR_{\theta_v}} \underbrace{-\frac{\partial \overline{u_j'' \theta''}}{\partial x_j}}_{TURB_{\theta_v}} \tag{B.3}$$

The equation B.3 is similar to the equation of basic conservation of heat B.1, if we replace the instantaneous heat with the mean forcing in the following equation, and then add the turbulence term ($TURB_{\theta_v}$) at the end. This additional term represents the convergence of turbulent heat flux (unresolved).

B.2. Moisture budgets

The formulation of moisture (q_v) budget terms are shown here as per Stull (1988). Following the same steps as B.1, the conservation of moisture can be written (assuming incompressibility) as,

$$\frac{\partial q_v}{\partial t} + U_j \frac{\partial q_v}{\partial x_j} = \nu_{q_v} \frac{\partial^2 q_v}{\partial x_j^2} + \frac{S_{qv}}{\rho_{air}} + \frac{E}{\rho_{air}} \tag{B.4}$$

$$SUM_{q_v} \quad ADV_{q_v} \quad DIFF_{q_v} \quad MIS_{q_v} \quad MICR_{q_v}$$

The terms SUM_{q_v} represents the net water vapour storage tendency, ADV_{q_v} denotes water vapour advection, $DIFF_{q_v}$ is the diffusion terms (which is again very small relative to the other terms). MIS_{q_v} represents the convergence of falling liquid or solid water, for example precipitation, which is not advecting with the wind. It is a net body source term. Term $MICR_{q_v}$ represents the microphysics contribution due to the conversion of solid or liquid into water vapour and vice versa, basically microphysical water vapour source (or sink) rates. Now, splitting the dependent variables into mean and turbulent parts, averaging the equation and apply Reyn-

old's averaging rules, and using the turbulent continuity equation to transform the turbulent advection term into flux form, the resultant equation would be:

$$\underbrace{\frac{\partial \overline{q_v}}{\partial t}}_{SUM_{q_v}} = \underbrace{-\overline{U_j}\frac{\partial \overline{q_v}}{\partial x_j}}_{ADV_{q_v}} \underbrace{+\nu_{q_v}\frac{\partial^2 \overline{q_v}}{\partial x_j^2}}_{DIFF_{q_v}} \underbrace{+\frac{\overline{S_{qv}}}{\overline{\rho}_{air}}}_{MICR_{q_v}} \underbrace{-\frac{\partial \overline{u_j'' q_v''}}{\partial x_j}}_{TURB_{q_v}} \tag{B.5}$$

Similar to before, equation B.5 represent the respective terms except for the addition of the turbulence term at the end (TURB), which represents the convergence of turbulent moisture flux. In the atmosphere, the turbulent diffusion is on several orders of magnitude more than the molecular diffusion. In this study, the area-averaged vertical profiles have been analysed to understand the exchange of heat and moisture between surface and boundary layer, and further the exchange between CBL and free troposphere. The terms in equation B.3 and B.5 are calculated in the model using the given prognostic variables. For more theoretical and formulation details see Stull (1988); Langhans et al. (2012).

Grid-scale and subgrid scale flux

Another important formulation used in this study involves the decomposition of the total advection (ADV_{θ_v}) into a horizontal ($HADV_{\theta_v}$) and vertical ($ZADV_{\theta_v}$) parts. Starting with the equation B.5:

$$\underbrace{U_j\frac{\partial \theta_v}{\partial x_j}}_{ADV_{\theta_v}} = \underbrace{u\frac{\partial \theta_v}{\partial x} + v\frac{\partial \theta_v}{\partial y}}_{HADV_{\theta_v}} + \underbrace{w\frac{\partial \theta_v}{\partial z}}_{ZADV_{\theta_v}} \tag{B.6}$$

From the continuity equation which states the conservation of mass, we have:

$$\frac{\partial U_j}{\partial x_j} = 0 \tag{B.7}$$

If we multiply the continuity equation B.7 by ξ (which denotes any variable, such as temperature, specific humidity), we get: $\xi\frac{\partial U_j}{\partial x_j} = 0$. As an example for θ_v:

$$\theta_v\frac{\partial U_j}{\partial x_j} = 0 \tag{B.8}$$

Since this term is equal to zero, adding it to the total ADV term of the equation B.6 will be also equal to zero.

$$ADV_{\theta_v} = U_j \frac{\partial \theta_v}{\partial x_j} + \theta_v \frac{\partial U_j}{\partial x_j} \tag{B.9}$$

$$ADV_{\theta_v} = \frac{\partial \theta_v U_j}{\partial x_j} \tag{B.10}$$

Equation B.10 is also called as the flux form of the advection term or an expression from anelastic approximation. Since any resolved variable can be decomposed into horizontally averaged part and a resolved deviation from the spatial average. For example θ_v can be decomposed as:

$$\theta_v = \overline{\theta_v} + \theta_v{}' \tag{B.11}$$

This way, the θ_v and vertical wind velocity w in the terms $ZADV_{\theta_v}$ of equation B.6 can be decomposed as:

$$ZADV_{\theta_v} = w \frac{\partial \theta_v}{\partial z} = (\overline{w} + w') \frac{\partial (\overline{\theta_v} + \theta_v{}')}{\partial z} \tag{B.12}$$

After simplifying and applying Reynold's averaging, which states that $[\overline{(A.B)} = \overline{A}\,\overline{B} + \overline{a'b'}]$

$$ZADV_{\theta_v} = \underbrace{\frac{\partial \overline{w}\,\overline{\theta_v}}{\partial z}}_{\mathrm{ZA_{m\_divg}}} + \underbrace{\frac{\partial \overline{w'\theta_v{}'}}{\partial z}}_{\mathrm{ZA_{GS\_divg}}} \tag{B.13}$$

where ZA_{m_divg} and ZA_{GS_divg} are the mean vertical- and grid scale- sensible heat flux divergence, respectively. The turbulent components of $ZADV_{\theta_v}$ has been used extensively in the analysis of turbulent exchange processes. The grid-scale sensible heat fluxes, $ZADV_{GS}$ have been calculated using the model output fields of w and θ_v.

$$ZADV_{GS} = (w - \overline{w})(\theta_v - \overline{\theta_v}).\rho \tag{B.14}$$

where w, θ_v, and ρ are vertical velocity in $m\,s^{-1}$, virtual potential temperature in K and density in $kg\,m^{-3}$ at each grid points, respectively. $\overline{w}$ and $\overline{\theta_v}$ are the areal mean over the considered domain. Further, subgrid sensible heat fluxes are calculated using the model output fields, turbulent diffusion coefficients for heat K_h ('$tkvh'$), θ_v, and the geometric height of model levels above sea level (NN) z ('HHL') (Neske, 2017).

$$ZADV_{SGS} = -K_h \frac{d\theta_v}{dz} \tag{B.15}$$

where K_h is in $m^2\,s^{-1}$ and θ_v is in K, and z is in metres.

C. List of Figures

D. List of Tables

E. Bibliography

Adler, B., N. Kalthoff, and L. Gantner, 2011: Initiation of deep convection caused by land-surface inhomogeneities in West Africa: a modelled case study. *Meteorology and Atmospheric Physics*, **112 (1-2)**, 15–27.

Antonelli, M. and R. Rotunno, 2007: Large-eddy simulation of the onset of the sea breeze. *Journal of the Atmospheric Sciences*, **64 (12)**, 4445–4457.

Arnold, D., D. Morton, I. Schicker, P. Seibert, M. Rotach, K. Horvath, T. Dudhia, T. Satomura, M. Müller, G. Zängl, et al., 2012: Issues in high-resolution atmospheric modeling in complex topography—The HiRCoT workshop. *Hrvatski meteorološki časopis*, **47 (47)**, 3–11.

Asensio, H., M. Messmer, D. Lüthi, and K. Osterried, 2018: External Parameters for Numerical Weather Prediction and Climate Application (EXTPAR). *User and implementation guide* available at www.cosmo-model.org/content/support/software/ethz/extpar-userManual-v5.0-a.pdf. 48.

ASTER, 2011: ASTER Global Digital Elevation Map Announcement. `https://asterweb.jpl.nasa.gov/gdem.asp`, accessed: 20 Aug 2017.

Atkins, N. T., R. M. Wakimoto, and C. L. Ziegler, 1998: Observations of the finescale structure of a dryline during VORTEX 95. *Monthly Weather Review*, **126 (3)**, 525–550.

Atkinson, B. W., 1981: *Meso-scale atmospheric circulations*. Academic press, London, 495 pp.

Avissar, R. and F. Chen, 1993: Development and analysis of prognostic equations for mesoscale kinetic energy and mesoscale (subgrid scale) fluxes for large-scale atmospheric models. *Journal of the Atmospheric Sciences*, **50 (22)**, 3751–3774.

Avissar, R. and Y. Liu, 1996: Three-dimensional numerical study of shallow convective clouds and precipitation induced by land surface forcing. *Journal of Geophysical Research: Atmospheres*, **101 (D3)**, 7499–7518.

Avissar, R. and T. Schmidt, 1998: An evaluation of the scale at which ground-surface heat flux patchiness affects the convective boundary layer using large-eddy simulations. *Journal of the Atmospheric Sciences*, **55 (16)**, 2666–2689.

Babić, K., N. Kalthoff, B. Adler, J. F. Quinting, F. Lohou, C. Dione, and M. Lothon, 2019: What controls the formation of nocturnal low-level stratus clouds over southern West Africa during the monsoon season? *Atmospheric Chemistry and Physics*, **19 (21)**, 13 489–13 506.

Banta, R. M., 1990: The role of mountain flows in making clouds. *Atmospheric processes over complex terrain*, Springer, Boston, MA, 229–283.

Bartels, H., E. Weigl, T. Reich, P. Lang, A. Wagner, O. Kohler, N. Gerlach, et al., 2004: Projekt RADOLAN–Routineverfahren zur Online-Aneichung der Radarniederschlagsdaten mit Hilfe von automatischen Bodenniederschlagsstationen (Ombrometer). *Deutscher Wetterdienst, Hydrometeorologie*, **5**.

Barthlott, C., R. Burton, D. Kirshbaum, K. Hanley, E. Richard, J.-P. Chaboureau, J. Trentmann, B. Kern, H.-S. Bauer, T. Schwitalla, et al., 2011: Initiation of deep convection at marginal instability in an ensemble of mesoscale models: a case-study from COPS. *Quarterly Journal of the Royal Meteorological Society*, **137 (S1)**, 118–136.

Barthlott, C. and N. Kalthoff, 2011: A numerical sensitivity study on the impact of soil moisture on convection-related parameters and convective precipitation over complex terrain. *Journal of the Atmospheric Sciences*, **68 (12)**, 2971–2987.

Baur, F., 2019: Soil moisture-precipitation coupling over Central Europe. Ph.D. thesis, lmu.

Berrisford, P., D. Dee, P. Poli, R. Brugge, K. Fielding, M. Fuentes, P. Kallberg, S. Kobayashi, S. Uppala, and A. Simmons, 2011: The ERA-Interim archive, version 2.0. *ERA Report Series*, **1**, 23.

Bjerknes, V., R. Rubenson, and A. Lindstedt, 1898: *Über einen hydrodynamischen Fundamentalsatz und seine Anwendung besonders auf die Mechanik der Atmosphäre und des Weltmeeres*, Vol. 31. Kungl. Boktryckeriet. PA Norstedt & Söner, Stockholm, Sweden, 1–35 pp.

Bluestein, H. B., E. W. McCaul Jr, G. P. Byrd, R. L. Walko, and R. Davies-Jones, 1990: An observational study of splitting convective clouds. *Monthly Weather Review*, **118 (6)**, 1359–1370.

Böing, S. J., H. J. Jonker, A. P. Siebesma, and W. W. Grabowski, 2012: Influence of the subcloud layer on the development of a deep convective ensemble. *Journal of the Atmospheric Sciences*, **69 (9)**, 2682–2698.

Bonaventura, L. and T. Ringler, 2005: Analysis of discrete shallow-water models on geodesic Delaunay grids with C-type staggering. *Monthly Weather Review*, **133 (8)**, 2351–2373.

Bony, S. and J.-L. Dufresne, 2005: Marine boundary layer clouds at the heart of tropical cloud feedback uncertainties in climate models. *Geophysical Research Letters*, **32 (20)**, L20 806.

Boucher, O., D. Randall, P. Artaxo, C. Bretherton, G. Feingold, P. Forster, V.-M. Kerminen, Y. Kondo, H. Liao, U. Lohmann, et al., 2013: Clouds and aerosols. *Climate change 2013: the physical science basis. Contribution of Working Group I to the Fifth Assessment Report of the Intergovernmental Panel on Climate Change*, Cambridge University Press, Cambridge, UK, 571–657.

Browning, K. A., A. M. Blyth, P. A. Clark, U. Corsmeier, C. J. Morcrette, J. L. Agnew, S. P. Ballard, D. Bamber, C. Barthlott, L. J. Bennett, et al., 2007: The convective storm initiation project. *Bulletin of the American Meteorological Society*, **88 (12)**, 1939–1956.

Brücher, W., 1997: Numerische Studien zum Mehrfachnesting mit einem nichthydrostatischen Modell. *Mitteilungen aus dem Institut für Geophysik und Meteorologie der Universität zu Köln*, **119**.

Bryan, G. H., J. C. Wyngaard, and J. M. Fritsch, 2003: Resolution requirements for the simulation of deep moist convection. *Monthly Weather Review*, **131 (10)**, 2394–2416.

Charba, J., 1974: Application of gravity current model to analysis of squall-line gust front. *Monthly Weather Review*, **102 (2)**, 140–156.

Chen, F. and R. Avissar, 1994: The impact of land-surface wetness heterogeneity on mesoscale heat fluxes. *Journal of Applied Meteorology*, **33 (11)**, 1323–1340.

Chow, F. K., C. Schär, N. Ban, K. A. Lundquist, L. Schlemmer, and X. Shi, 2019: Crossing multiple gray zones in the transition from mesoscale to microscale simulation over complex terrain. *Atmosphere*, **10 (5)**, 274.

Chow, F. K., A. P. Weigel, R. L. Street, M. W. Rotach, and M. Xue, 2006: High-resolution large-eddy simulations of flow in a steep Alpine valley. Part I: Methodology, verification, and sensitivity experiments. *Journal of Applied Meteorology and Climatology*, **45 (1)**, 63–86.

Courault, D., P. Drobinski, Y. Brunet, P. Lacarrere, and C. Talbot, 2007: Impact of surface heterogeneity on a buoyancy-driven convective boundary layer in light winds. *Boundary-Layer Meteorology*, **124 (3)**, 383–403.

Couvreux, F., E. Bazile, G. Canut, M. Lothon, F. Lohou, F. Guichard, and E. Nilsson, 2016: Boundary-layer turbulent processes and mesoscale variability represented by numerical weather prediction models during the BLLAST campaign. *Atmospheric Chemistry and Physics Discussions*, **16 (14)**, 8983–9002.

Crosman, E. T. and J. D. Horel, 2010: Sea and lake breezes: A review of numerical studies. *Boundary-Layer Meteorology*, **137 (1)**, 1–29.

Cuxart, J., 2015: When can a high-resolution simulation over complex terrain be called LES? *Frontiers in Earth Science*, **3**, 87.

Deardorff, J. W., 1972: Numerical investigation of neutral and unstable planetary boundary layers. *Journal of the Atmospheric Sciences*, **29 (1)**, 91–115.

Dee, D. P., S. M. Uppala, A. Simmons, P. Berrisford, P. Poli, S. Kobayashi, U. Andrae, M. Balmaseda, G. Balsamo, d. P. Bauer, et al., 2011: The ERA-Interim reanalysis: Configuration and performance of the data assimilation system. *Quarterly Journal of the Royal Meteorological Society*, **137 (656)**, 553–597.

Déqué, M., D. Rowell, D. Lüthi, F. Giorgi, J. Christensen, B. Rockel, D. Jacob, E. Kjellström, M. De Castro, and B. van den Hurk, 2007: An intercomparison

of regional climate simulations for Europe: assessing uncertainties in model projections. *Climatic Change*, **81 (1)**, 53–70.

Deutscher Wetterdienst (DWD), 2016: Regional model COSMO-DE. https://www.dwd.de/EN/research/weatherforecasting/num_modelling/01_num_weather_prediction_modells/regional_model_cosmo_de.html?nn=484060, accessed: 23 Aug 2019.

Dipankar, A., B. Stevens, R. Heinze, C. Moseley, G. Zängl, M. Giorgetta, and S. Brdar, 2015: Large eddy simulation using the general circulation model ICON. *Journal of Advances in Modeling Earth Systems*, **7 (3)**, 963–986.

Doms, G., J. Förstner, E.Heise, H.-J. Herzog, D. Mironov, M. Raschendorfer, T. Reinhardt, B. Ritter, R. Schrodin, J.-P. Schulz, and G. Vogel, 2011: *A Description of the Nonhydrostatic Regional COSMO Model, Part II: Physical parameterization*. Available at http://www.cosmo-model.org, accessed: 22 Feb 2017.

Doswell III, C. A., 1987: The distinction between large-scale and mesoscale contribution to severe convection: A case study example. *Weather and Forecasting*, **2 (1)**, 3–16.

Drager, A. J. and S. C. van den Heever, 2017: Characterizing convective cold pools. *Journal of Advances in Modeling Earth Systems*, **9 (2)**, 1091–1115.

Draxler, R. R. and G. Hess, 1998: An overview of the HYSPLIT_4 modelling system for trajectories. *Australian Meteorological Magazine*, **47 (4)**, 295–308.

DWD-PAMORE, 2015: PArallel MOdel data REtrieve from Oracle Databases (PAMORE). https://www.dwd.de/DE/leistungen/pamore/pamore.html, accessed: 20 May 2017.

Emanuel, K. A., 1994: *Atmospheric Convection*. Oxford University Press, Oxford, 580 pp.

Entekhabi, D., I. Rodriguez-Iturbe, and F. Castelli, 1996: Mutual interaction of soil moisture state and atmospheric processes. *Journal of Hydrology*, **184 (1-2)**, 3–17.

Findell, K. L. and E. A. Eltahir, 1997: An analysis of the soil moisture-rainfall feedback, based on direct observations from Illinois. *Water Resources Research*, **33 (4)**, 725–735.

Fischer, G., F. Nachtergaele, S. Prieler, H. Van Velthuizen, L. Verelst, and D. Wiberg, 2008: Global agro-ecological zones assessment for agriculture (GAEZ 2008). *IIASA, Laxenburg, Austria and FAO, Rome, Italy*, **10**.

Gal-Chen, T. and R. C. Somerville, 1975: Numerical solution of the Navier-Stokes equations with topography. *Journal of Computational Physics*, **17 (3)**, 276–310.

Gantner, L. and N. Kalthoff, 2010: Sensitivity of a modelled life cycle of a meso-scale convective system to soil conditions over West Africa. *Quarterly Journal of the Royal Meteorological Society*, **136 (S1)**, 471–482.

Gantner, L., V. Maurer, N. Kalthoff, and O. Kiseleva, 2017: The impact of land-surface parameter properties and resolution on the simulated cloud-topped atmospheric boundary layer. *Boundary-Layer Meteorology*, **165 (3)**, 475–496.

Garcia-Carreras, L., D. J. Parker, and J. H. Marsham, 2011: What is the mechanism for the modification of convective cloud distributions by land surface–induced flows? *Journal of the Atmospheric Sciences*, **68 (3)**, 619–634.

Gassmann, A., 2011: Inspection of hexagonal and triangular C-grid discretizations of the shallow water equations. *Journal of Computational Physics*, **230 (7)**, 2706–2721.

Gassmann, A. and H.-J. Herzog, 2008: Towards a consistent numerical compressible non-hydrostatic model using generalized Hamiltonian tools. *Quarterly Journal of the Royal Meteorological Society*, **134 (635)**, 1597–1613.

Giorgetta, M., P. Korn, and C. Reick, 2015: ICON (ICOsahedral nonhydrostatic) - Earth System Models. `http://www.mpimet.mpg.de/en/science/models/icon-esm.html`, accessed: 20 Aug 2019.

Giorgetta, M., P. Korn, and G. Zängl, 2017: ICON - developing a new generation of climate and weather forecasting models. `http://www.mpimet.mpg.de/en/communication/news/focus-on-overview/icon-development/`, accessed: 19 Aug 2019.

Giorgi, F. and R. Avissar, 1997: Representation of heterogeneity effects in Earth system modeling: Experience from land surface modeling. *Reviews of Geophysics*, **35 (4)**, 413–437.

GlobCover, 2009: ESA GlobCover 2009 Project. `http://due.esrin.esa.int/page_globcover.php`, accessed: 20 Aug 2017.

Golden, J. S., 2004: The built environment induced urban heat island effect in rapidly urbanizing arid regions–a sustainable urban engineering complexity. *Environmental Sciences*, **1 (4)**, 321–349.

Heinemann, G. and M. Kerschgens, 2005: Comparison of methods for area-averaging surface energy fluxes over heterogeneous land surfaces using high-resolution non-hydrostatic simulations. *International Journal of Climatology*, **25 (3)**, 379–403.

Heinze, R., A. Dipankar, C. C. Henken, C. Moseley, O. Sourdeval, S. Trömel, X. Xie, P. Adamidis, F. Ament, H. Baars, et al., 2017: Large-eddy simulations over Germany using ICON: A comprehensive evaluation. *Quarterly Journal of the Royal Meteorological Society*, **143 (702)**, 69–100.

Heise, E., B. Ritter, and R. Schrodin, 2006: Operational implementation of the multilayer soil model. *Consortium for Small-Scale Modeling (COSMO) Technical Report*, **9**, 20, accessed: 20 Aug 2018.

Henderson-Sellers, A., Z.-L. Yang, and R. Dickinson, 1993: The project for intercomparison of land-surface parameterization schemes. *Bulletin of the American Meteorological Society*, **74 (7)**, 1335–1350.

Hohenegger, C., P. Brockhaus, and C. Schaer, 2008: Towards climate simulations at cloud-resolving scales. *Meteorologische Zeitschrift*, **17 (4)**, 383–394.

Honnert, R. and V. Masson, 2014: What is the smallest physically acceptable scale for 1D turbulence schemes? *Frontiers in Earth Science*, **2**, 27.

Imamovic, A., L. Schlemmer, and C. Schär, 2017: Collective impacts of orography and soil moisture on the soil moisture-precipitation feedback. *Geophysical Research Letters*, **44 (22)**, 11–682.

Inoue, T., M. Satoh, H. Miura, and B. Mapes, 2008: Characteristics of cloud size of deep convection simulated by a global cloud resolving model over the western tropical Pacific. *Journal of the Meteorological Society of Japan. Ser. II*, **86**, 1–15.

Iribarne, J. V. and W. L. Godson, 2012: *Atmospheric thermodynamics*, Vol. 6. Springer Science & Business Media, Dordrecht, the Netherlands, 141–142 pp.

Jeevanjee, N. and D. M. Romps, 2015: Effective buoyancy, inertial pressure, and the mechanical generation of boundary layer mass flux by cold pools. *Journal of the Atmospheric Sciences*, **72 (8)**, 3199–3213.

Kalthoff, N., B. Adler, C. Barthlott, U. Corsmeier, S. Mobbs, S. Crewell, K. Träumner, C. Kottmeier, A. Wieser, V. Smith, et al., 2009: The impact of convergence zones on the initiation of deep convection: A case study from COPS. *Atmospheric Research*, **93 (4)**, 680–694.

Kalthoff, N., F. Fiedler, M. Kohler, O. Kolle, H. Mayer, and A. Wenzel, 1999: Analysis of energy balance components as a function of orography and land use and comparison of results with the distribution of variables influencing local climate. *Theoretical and Applied Climatology*, **62 (1-2)**, 65–84.

Kalthoff, N., M. Kohler, C. Barthlott, B. Adler, S. Mobbs, U. Corsmeier, K. Träumner, T. Foken, R. Eigenmann, L. Krauss, et al., 2011: The dependence of convection-related parameters on surface and boundary-layer conditions over complex terrain. *Quarterly Journal of the Royal Meteorological Society*, **137 (S1)**, 70–80.

Kang, S.-L. and G. H. Bryan, 2011: A large-eddy simulation study of moist convection initiation over heterogeneous surface fluxes. *Monthly Weather Review*, **139 (9)**, 2901–2917.

Khodayar, S., N. Kalthoff, and G. Schädler, 2013: The impact of soil moisture variability on seasonal convective precipitation simulations. Part I: Validation, feedbacks, and realistic initialisation. *Meteorologische Zeitschrift*, **22 (4)**, 489–505.

Khodayar, S. and G. Schädler, 2013: The impact of soil moisture variability on seasonal convective precipitation simulations. Part II: Sensitivity to land-

surface models and prescribed soil type distributions. *Meteorologische Zeitschrift*, **22 (4)**, 507–526.

Knote, C., G. Heinemann, and B. Rockel, 2010: Changes in weather extremes: Assessment of return values using high resolution climate simulations at convection-resolving scale. *Meteorologische Zeitschrift*, **19 (1)**, 11–23.

Koster, R. D., P. A. Dirmeyer, Z. Guo, G. Bonan, E. Chan, P. Cox, C. Gordon, S. Kanae, E. Kowalczyk, D. Lawrence, et al., 2004: Regions of strong coupling between soil moisture and precipitation. *Science*, **305 (5687)**, 1138–1140.

Kottmeier, C., N. Kalthoff, C. Barthlott, U. Corsmeier, J. Van Baelen, A. Behrendt, R. Behrendt, A. Blyth, R. Coulter, S. Crewell, et al., 2008: Mechanisms initiating deep convection over complex terrain during COPS. *Meteorologische Zeitschrift*, **17 (6)**, 931–948.

Kunz, M., U. Blahak, J. Handwerker, M. Schmidberger, H. J. Punge, S. Mohr, E. Fluck, and K. M. Bedka, 2018: The severe hailstorm in southwest Germany on 28 July 2013: characteristics, impacts and meteorological conditions. *Quarterly Journal of the Royal Meteorological Society*, **144 (710)**, 231–250.

Langhans, W., J. Schmidli, and C. Schär, 2012: Bulk convergence of cloud-resolving simulations of moist convection over complex terrain. *Journal of the Atmospheric Sciences*, **69 (7)**, 2207–2228.

Leary, L. A. and E. A. Ritchie, 2009: Lightning flash rates as an indicator of tropical cyclone genesis in the eastern North Pacific. *Monthly Weather Review*, **137 (10)**, 3456–3470.

Leuenberger, D., M. Koller, O. Fuhrer, and C. Schär, 2010: A generalization of the SLEVE vertical coordinate. *Monthly Weather Review*, **138 (9)**, 3683–3689.

Leung, L. R., Y.-H. Kuo, and J. Tribbia, 2006: Research needs and directions of regional climate modeling using WRF and CCSM. *Bulletin of the American Meteorological Society*, **87 (12)**, 1747–1752.

Lilly, D. K., 1962: On the numerical simulation of buoyant convection. *Tellus*, **14 (2)**, 148–172.

Linardakis, L., D. Reinert, and A. Gassmann, 2011: ICON grid documentation. Tech. rep., Hamburg, Germany.

Liu, G., J. Sun, and L. Yin, 2011: Turbulence characteristics of the shear-free convective boundary layer driven by heterogeneous surface heating. *Boundary-Layer Meteorology*, **140 (1)**, 57–71.

Liu, S., Y. Shao, A. Kunoth, and C. Simmer, 2017: Impact of surface-heterogeneity on atmosphere and land-surface interactions. *Environmental Modelling & Software*, **88**, 35–47.

Mahfouf, J.-F., E. Richard, and P. Mascart, 1987: The influence of soil and vegetation on the development of mesoscale circulations. *Journal of Climate and Applied Meteorology*, **26 (11)**, 1483–1495.

Mansell, E. R., C. L. Ziegler, and D. R. MacGorman, 2007: A lightning data assimilation technique for mesoscale forecast models. *Monthly Weather Review*, **135 (5)**, 1732–1748.

Markowski, P. and Y. Richardson, 2011: *Mesoscale meteorology in midlatitudes*, Vol. 2. John Wiley & Sons, Chichester, United Kingdom, 407 pp.

Marsham, J., C. Morcrette, K. Browning, A. Blyth, D. Parker, U. Corsmeier, N. Kalthoff, and M. Kohler, 2007: Variable cirrus shading during CSIP IOP 5. I: Effects on the initiation of convection. *Quarterly Journal of the Royal Meteorological Society*, **133 (628)**, 1643–1660.

Maurer, V., N. Kalthoff, A. Wieser, M. Kohler, M. Mauder, and L. Gantner, 2016: Observed spatiotemporal variability of boundary-layer turbulence over flat, heterogeneous terrain. *Atmospheric Chemistry and Physics*, **16 (3)**, 1377–1400.

McKee, T. B. and R. D. O'Neal, 1989: The role of valley geometry and energy budget in the formation of nocturnal valley winds. *Journal of Applied Meteorology*, **28 (6)**, 445–456.

Meißner, C., N. Kalthoff, M. Kunz, and G. Adrian, 2007: Initiation of shallow convection in the Black Forest mountains. *Atmospheric Research*, **86 (1)**, 42–60.

Mellado, J.-P., C. Bretherton, B. Stevens, and M. Wyant, 2018: DNS and LES for simulating stratocumulus: better together. *Journal of Advances in Modeling Earth Systems*, **10 (7)**, 1421–1438.

Metzger, J., C. Barthlott, and N. Kalthoff, 2014: Impact of upstream flow conditions on the initiation of moist convection over the island of Corsica. *Atmospheric Research*, **145**, 279–296.

Miller, S., B. Keim, R. Talbot, and H. Mao, 2003: Sea breeze: Structure, forecasting, and impacts. *Reviews of Geophysics*, **41 (3)**, 1011.

Miura, H., 2007: An upwind-biased conservative advection scheme for spherical hexagonal–pentagonal grids. *Monthly Weather Review*, **135 (12)**, 4038–4044.

Mlawer, E. J., S. J. Taubman, and S. A. Clough, 1995: RRTM: A Rapid Radiative Transfer Model. *Conference on Atmospheric Transmission Models, 6-8 June 1995*, 150.

Morton, B., G. I. Taylor, and J. S. Turner, 1956: Turbulent gravitational convection from maintained and instantaneous sources. *Proceedings of the Royal Society of London. Series A. Mathematical and Physical Sciences*, **234 (1196)**, 1–23.

Nakayama, T. and T. Fujita, 2010: Cooling effect of water-holding pavements made of new materials on water and heat budgets in urban areas. *Landscape and Urban Planning*, **96 (2)**, 57–67.

Namelist Overview, 2015: *Guide stored in ICON model folder*.

Neske, S., 2017: Towards an improved Turbulence Closure Scheme by analysing ICON Model Simulations. Ph.D. thesis, Universität zu Köln.

Oke, T. R., 1987: *Boundary layer climates*. Routledge, London, 435 pp.

Orlanski, I., 1975: A rational subdivision of scales for atmospheric processes. *Bulletin of the American Meteorological Society*, **56**, 527–530.

Pal, J. S. and E. A. Eltahir, 2001: Pathways relating soil moisture conditions to future summer rainfall within a model of the land–atmosphere system. *Journal of Climate*, **14 (6)**, 1227–1242.

Peixoto, P. S. and S. R. Barros, 2014: On vector field reconstructions for semi-Lagrangian transport methods on geodesic staggered grids. *Journal of Computational Physics*, **273**, 185–211.

Pielke Sr, R. A., 2001: Influence of the spatial distribution of vegetation and soils on the prediction of cumulus convective rainfall. *Reviews of Geophysics*, **39 (2)**, 151–177.

Piper, D. and M. Kunz, 2017: Spatiotemporal variability of lightning activity in Europe and the relation to the North Atlantic Oscillation teleconnection pattern. *Natural Hazards & Earth System Sciences*, **17 (8)**, 1319–1336.

Pohjola, H. and A. Mäkelä, 2013: The comparison of GLD360 and EUCLID lightning location systems in Europe. *Atmospheric Research*, **123**, 117–128.

Porson, A., D. G. Steyn, and G. Schayes, 2007: Sea-breeze scaling from numerical model simulations, Part I: Pure sea breezes. *Boundary-Layer Meteorology*, **122 (1)**, 17–29.

Prein, A. F., W. Langhans, G. Fosser, A. Ferrone, N. Ban, K. Goergen, M. Keller, M. Tölle, O. Gutjahr, F. Feser, et al., 2015: A review on regional convection-permitting climate modeling: Demonstrations, prospects, and challenges. *Reviews of Geophysics*, **53 (2)**, 323–361.

Prill, F., 2014: *DWD ICON Tools Documentation*. Deutscher Wetterdienst (DWD).

Raschendorfer, M., 2001: The new turbulence parameterization of LM. *In COSMO newsletter no. 1*, 89–97.

Rieck, M., C. Hohenegger, and P. Gentine, 2015: The effect of moist convection on thermally induced mesoscale circulations. *Quarterly Journal of the Royal Meteorological Society*, **141 (691)**, 2418–2428.

Rieck, M., C. Hohenegger, and C. C. van Heerwaarden, 2014: The influence of land surface heterogeneities on cloud size development. *Monthly Weather Review*, **142 (10)**, 3830–3846.

Rotach, M. W., I. Stiperski, O. Fuhrer, B. Goger, A. Gohm, F. Obleitner, G. Rau, E. Sfyri, and J. Vergeiner, 2017: Investigating exchange processes over complex

topography: the Innsbruck Box (i-Box). *Bulletin of the American Meteorological Society*, **98 (4)**, 787–805.

Rotunno, R., J. B. Klemp, and M. L. Weisman, 1988: A theory for strong, long-lived squall lines. *Journal of the Atmospheric Sciences*, **45 (3)**, 463–485.

Sadourny, R., A. Arakawa, and Y. Mintz, 1968: Integration of the nondivergent barotropic vorticity equation with an icosahedral-hexagonal grid for the sphere. *Monthly Weather Review*, **96 (6)**, 351–356.

Schär, C., D. Lüthi, U. Beyerle, and E. Heise, 1999: The soil–precipitation feedback: A process study with a regional climate model. *Journal of Climate*, **12 (3)**, 722–741.

Schneider, L., C. Barthlott, A. I. Barrett, and C. Hoose, 2018: The precipitation response to variable terrain forcing over low mountain ranges in different weather regimes. *Quarterly Journal of the Royal Meteorological Society*, **144 (713)**, 970–989.

Schrodin, R. and E. Heise, 2002: A new multi-layer soil model. *In COSMO newsletter no. 2*, 149–151.

Schulz, W., G. Diendorfer, S. Pedeboy, and D. R. Poelman, 2016: The European lightning location system EUCLID–Part 1: Performance analysis and validation. *Natural Hazards and Earth System Sciences*, **16 (2)**, 595–605.

Segal, M. and R. Arritt, 1992: Nonclassical mesoscale circulations caused by surface sensible heat-flux gradients. *Bulletin of the American Meteorological Society*, **73 (10)**, 1593–1604.

Seifert, A. and K. D. Beheng, 2001: A double-moment parameterization for simulating autoconversion, accretion and selfcollection. *Atmospheric Research*, **59**, 265–281.

Shao, Y., M. Sogalla, M. Kerschgens, and W. Brücher, 2001: Effects of land-surface heterogeneity upon surface fluxes and turbulent conditions. *Meteorology and Atmospheric Physics*, **78 (3-4)**, 157–181.

Shuttleworth, W. J., 1991: Evaporation models in hydrology. *Land surface evaporation*, Springer, 93–120.

Siegel, A., 2016: *Practical business statistics (Seventh Edition)*. Academic Press, 642 pp.

Silvers, L. G., B. Stevens, T. Mauritsen, and M. Giorgetta, 2016: Radiative convective equilibrium as a framework for studying the interaction between convection and its large-scale environment. *Journal of Advances in Modeling Earth Systems*, **8 (3)**, 1330–1344.

Simon, J. S., B. Zhou, J. D. Mirocha, and F. K. Chow, 2019: Explicit filtering and reconstruction to reduce grid dependence in convective boundary layer simulations using WRF-LES. *Monthly Weather Review*, **147 (5)**, 1805–1821.

Simpson, J. E., 1994: *Sea breeze and local winds*. Cambridge University Press, Cambridge, UK, 234 pp.

Smagorinsky, J., 1963: General circulation experiments with the primitive equations: I. The basic experiment. *Monthly Weather Review*, **91 (3)**, 99–164.

Smith, R. B., 1989: Hydrostatic airflow over mountains. *Advances in Geophysics*, Elsevier, New York, Vol. 31, 1–41.

Sprenger, M. and H. Wernli, 2015: The Lagrangian analysis tool LAGRANTO-version 2.0. *Geoscientific Model Development Discussions*, **8 (2)**.

Steinacker, R., 1984: Area-height distribution of a valley and its relation to the valley wind. *Beiträge zur Physik der Atmosphäre*, **57 (1)**, 64–71.

Steinfeld, D. and S. Pfahl, 2019: The role of latent heating in atmospheric blocking dynamics: a global climatology. *Climate Dynamics*, **53 (9-10)**, 6159–6180.

Stevens, B., C. Acquistapace, A. Hansen, R. Heinze, C. Klinger, D. Klocke, H. Rybka, W. Schubotz, J. Windmiller, P. Adamidis, et al., 2020: The Added Value of Large-Eddy and Storm-Resolving Models for Simulating Clouds and Precipitation. *Journal of the Meteorological Society of Japan. Ser. II*, **98 (2)**.

Steyn, D., 1998: Scaling the vertical structure of sea breezes. *Boundary-Layer Meteorology*, **86 (3)**, 505–524.

Stohl, A., 1999: The FLEXTRA Trajectory Model Version 3.0 User Guide. *University of Munich, Am Hochanger*, **13**, 85 354.

Stull, R. B., 1988: *An introduction to boundary layer meteorology*, Vol. 13. Kluwer Academic Publication, Dordrecht, the Netherlands, 666 pp.

Taylor, C. M., D. J. Parker, and P. P. Harris, 2007: An observational case study of mesoscale atmospheric circulations induced by soil moisture. *Geophysical Research Letters*, **34 (15)**.

Taylor, D. M., F. K. Chow, M. Delkash, and P. T. Imhoff, 2016: Numerical simulations to assess the tracer dilution method for measurement of landfill methane emissions. *Waste Management*, **56**, 298–309.

Thorpe, A. J., H. Volkert, and M. J. Ziemiański, 2003: The Bjerknes' circulation theorem: A historical perspective. *Bulletin of the American Meteorological Society*, **84 (4)**, 471–480.

Tompkins, A. M., 2001: Organization of tropical convection in low vertical wind shears: The role of cold pools. *Journal of the Atmospheric Sciences*, **58 (13)**, 1650–1672.

Torri, G., Z. Kuang, and Y. Tian, 2015: Mechanisms for convection triggering by cold pools. *Geophysical Research Letters*, **42 (6)**, 1943–1950.

Turner, J., 1963: The motion of buoyant elements in turbulent surroundings. *Journal of Fluid Mechanics*, **16 (1)**, 1–16.

Van Weverberg, K., N. P. van Lipzig, L. Delobbe, and D. Lauwaet, 2010: Sensitivity of quantitative precipitation forecast to soil moisture initialization and microphysics parametrization. *Quarterly Journal of the Royal Meteorological Society*, **136 (649)**, 978–996.

Wan, H., M. A. Giorgetta, G. Zängl, M. Restelli, D. Majewski, L. Bonaventura, K. Fröhlich, D. Reinert, P. Rípodas, L. Kornblueh, et al., 2013: The ICON-1.2 hydrostatic atmospheric dynamical core on triangular grids, Part I: Formulation and performance of the baseline version. *Geoscientific Model Development*, **6**, 735–763.

Weckwerth, T. M., 2000: The effect of small-scale moisture variability on thunderstorm initiation. *Monthly Weather Review*, **128 (12)**, 4017–4030.

Weisman, M. L. and R. Rotunno, 2004: "A theory for strong long-lived squall lines" revisited. *Journal of the Atmospheric Sciences*, **61 (4)**, 361–382.

Weisman, M. L., W. C. Skamarock, and J. B. Klemp, 1997: The resolution dependence of explicitly modeled convective systems. *Monthly Weather Review*, **125 (4)**, 527–548.

Wernli, B. H. and H. C. Davies, 1997: A Lagrangian-based analysis of extratropical cyclones. I: The method and some applications. *Quarterly Journal of the Royal Meteorological Society*, **123 (538)**, 467–489.

Western, A. W., R. B. Grayson, and G. Blöschl, 2002: Scaling of soil moisture: A hydrologic perspective. *Annual Review of Earth and Planetary Sciences*, **30 (1)**, 149–180.

Weusthoff, T., D. Leuenberger, C. Keil, and G. C. Craig, 2011: Best member selection for convective-scale ensembles. *Meteorologische Zeitschrift*, **20 (2)**, 153–164.

Whiteman, C. D., 1990: Observations of thermally developed wind systems in mountainous terrain. *Atmospheric processes over complex terrain*, Springer, Boston,MA, 5–42.

———, 2000: *Mountain meteorology: fundamentals and applications*. Oxford University Press, Oxford, 355 pp.

Wilson, J. W. and W. E. Schreiber, 1986: Initiation of convective storms at radar-observed boundary-layer convergence lines. *Monthly Weather Review*, **114 (12)**, 2516–2536.

Wulfmeyer, V., A. Behrendt, C. Kottmeier, U. Corsmeier, C. Barthlott, G. C. Craig, M. Hagen, D. Althausen, F. Aoshima, M. Arpagaus, et al., 2011: The Convective and Orographically-induced Precipitation Study (COPS): the scientific strategy, the field phase, and research highlights. *Quarterly Journal of the Royal Meteorological Society*, **137 (S1)**, 3–30.

Wyngaard, J. C., 2004: Toward numerical modeling in the "Terra Incognita". *Journal of the Atmospheric Sciences*, **61 (14)**, 1816–1826.

Zängl, G., D. Reinert, P. Rípodas, and M. Baldauf, 2015: The ICON (ICOsahedral Non-hydrostatic) modelling framework of DWD and MPI-M: Description of the non-hydrostatic dynamical core. *Quarterly Journal of the Royal Meteorological Society*, **141 (687)**, 563–579.

Zardi, D. and C. D. Whiteman, 2013: Diurnal mountain wind systems. *Mountain weather research and forecasting*, Springer, Dordrecht, 35–119.

Zhang, F., Y. Q. Sun, L. Magnusson, R. Buizza, S.-J. Lin, J.-H. Chen, and K. Emanuel, 2019: What is the predictability limit of midlatitude weather? *Journal of the Atmospheric Sciences*, **76 (4)**, 1077–1091.

Zhu, P., B. A. Albrecht, V. P. Ghate, and Z. Zhu, 2010: Multiple-scale simulations of stratocumulus clouds. *Journal of Geophysical Research*, **115 (D23)**.